Improved Reynolds-Stress Modeling for Adverse-Pressure-Gradient Turbulent Boundary Layers in Industrial Aeronautical Flow

Gustave Sporschill

Improved Reynolds-Stress Modeling for Adverse-Pressure-Gradient Turbulent Boundary Layers in Industrial Aeronautical Flow

Gustave Sporschill

THÈSE

pour l'obtention du grade de

Docteur

de l'Université de Pau et des Pays de l'Adour

École Doctorale ED 211
Sciences Exactes et leurs Applications

Spécialité : mécanique des fluides

Présentée et soutenue publiquement par

Gustave Sporschill

le 4 juin 2021

Improved Reynolds-Stress Modelling for Adverse-Pressure-Gradient Turbulent Boundary Layers in Industrial Aeronautical Flow

Amélioration des modèles au second ordre pour les couches limites turbulentes en gradient de pression adverse dans les écoulements aéronautiques

---

Directeur de thèse : Rémi Manceau
Encadrant industriel : Flavien Billard

Jury:

G. A.	Gerolymos	Professeur, Sorbonne Université	Rapporteur
C.	Rumsey	Research Scientist, NASA Langley	Rapporteur
H.	Bézard	Ingénieur de recherche, ONERA	Examinateur
F.	Billard	Ingénieur, Dassault Aviation	Examinateur
J.-P.	Laval	Directeur de recherche CNRS, Lille	Examinateur
R.	Manceau	Directeur de recherche CNRS, Pau	Examinateur

Acknowledgements

First and foremost, I would like to thank Flavien Billard, my supervisor at Dassault Aviation, and Rémi Manceau, my PhD supervisor at the University of Pau, for their patience and confidence for the past three years.

This work benefited from the kind guidance of Flavien. His constant enthusiasm and his ability to always see the bright side in my results, when I lacked perspective, kept me motivated despite regular yet usual setbacks. It would also have been much more difficult without his extensive efforts to modernise and improve the turbulence solver in Aether before and during my PhD.

The regular follow-up of Rémi provided an outside perspective to ensure that the thesis followed its broad outlines. He also helped me to better communicate my work, in this thesis as well as in articles and at international conferences.

Thanks to Georges Gerolymos and Christopher Rumsey for reporting on my thesis and for their valuable feedback, which helped me to improve the present manuscript. I am also grateful to the other members of my thesis committee, Hervé Bézard and Jean-Philippe Laval, who gave me the honour of assessing my work.

This PhD was made possible by the funding of Dassault Aviation and the ANRT. In particular, I would like to thank Michel Mallet, deputy head of the Department of Models, Methods and Tools (MMO), for giving the opportunity to conduct this research in his department.

More generally, my thanks go to both aerodynamics teams, MMO and AERAC, for their availability, help and advice. On their side, I could find out more about various aerodynamics topics more or less closely related to turbulence modelling and CFD, allowing me to better understand the tools I used as well as some of the activities they carry out and that my work might affect in the future. But most importantly I am thankful for the great environment they provided.

Finally, I would like to thank my family and my friends. They continuously supported me during this whole adventure and let me take my mind off things.

Contents

List of Symbols

Latin letters

a_1	Constant in Bradshaw's relation (3.4)
a_{ij}	Turbulence anisotropy
B	Log-law intercept
$\overline{B}$	Apparent log-law intercept
C_D	Drag coefficient, see Eq. (2.7)
$C_{D,0}$	Zero-lift drag coefficient
$C_{D,L}$	Drag-due-to-lift coefficient
C_f	Skin friction coefficient, see Eq. (2.7)
C_L	Lift coefficient, see Eq. (2.7)
C_μ	Eddy-viscosity factor, $C_\mu = a_1^2$
C_p	Pressure coefficient, see Eq. (2.7)
d	Wall distance
D_{friction}	Friction drag
D_{pressure}	Pressure drag
D_ϕ^{cd2}	Mixed cross-diffusion term of ϕ
D_ϕ^p	Pressure diffusion of ϕ
D_k^p	Pressure diffusion of k
D_{ij}^ν	Molecular diffusion of Reynolds stresses
D_{ij}^p	Pressure diffusion of Reynolds stresses
D_{ij}^T	Turbulent transport of Reynolds stresses
f_b	Blending function
E	Specific total energy
E_i	Specific internal energy

$\underline{\mathbf{f}}_{\text{vol}}$	Body forces per unit volume exerted on the fluid
$\underline{\mathbf{g}}$	Gravity vector
H	Shape factor, $H = \delta^*/\theta$
k	Turbulent kinetic energy
$\underline{\mathbf{n}}$	Wall-normal unit vector
P	Pressure
p	Fluctuating pressure
p^+	Pressure-gradient parameter in wall-units, $p^+ = (\delta_\nu/\tau_w)\,\mathrm{d}P_w/\mathrm{d}x$
P_w	Pressure at the wall
P_{ij}	Production of Reynolds stresses
P_k	Production of turbulent kinetic energy
$\underline{\mathbf{q}}$	Thermal flux vector
Re	Reynolds number, $Re = U_\infty L/\nu$
Re_c	Reynolds number based on chord, $Re_c = U_\infty c/\nu$
Re_T	Turbulent Reynolds number, $Re_T = k^2/(\varepsilon\nu)$
Re_{δ^*}	Reynolds number based on displacement thickness, $Re_{\delta^*} = U_e\delta^*/\nu$
Re_τ	Reynolds number based on wall friction, $Re_\tau = u_\tau\delta/\nu$
Re_θ	Reynolds number based on momentum thickness, $Re_\theta = U_e\theta/\nu$
$\underline{\underline{\mathbf{S}}}$	Strain-rate tensor
S_{ij}	Strain-rate tensor components
T	Turbulent time scale
$\overline{u_i u_j}$	Reynolds stresses
$\underline{\mathbf{U}}$	Velocity vector
U, V, W	Mean velocity components
u, v, w	Fluctuating velocity components
U_e	Velocity at the edge of the boundary layer (edge velocity)
U_∞	Velocity at infinity in external flows
u_p	Pressure velocity, $u_p = \sqrt[3]{(\nu/\rho)\,\mathrm{d}P_w/\mathrm{d}x}$
u_τ	Friction velocity, $u_\tau = \sqrt{\tau_w/\rho}$

$\underline{\mathbf{x}}$ Position vector

y_c Sublayer thickness (Nickels's analysis)

Greek letters

β_p Clauser's pressure-gradient parameter, $\beta_p = (\delta^*/\tau_w)\,\mathrm{d}P_w/\mathrm{d}x$

δ Boundary layer thickness

δ^* Displacement thickness

δ_v Viscous length scale, $\delta = \nu/u_\tau$

δ_{ij} Kronecker symbol

η Kolmogorov length scale, similarity variable (in the context of Section 2.3.1), spanwise coordinate (in the context of Chapter 7)

ε Dissipation rate of k

ε_{ij} Dissipation rate of Reynolds stresses

κ Wave number (in the context of Section 1.2) or von Kármán constant

$\overline{\kappa}$ Apparent von Kármán constant

κ_0 Universal von Kármán constant

κ_1 First-order coefficient in the von Kármán parameter expansion for $p^+y^+ \ll 1$, see Eq. (5.7)

κ_c Corrected von Kármán parameter, see Eq. (5.28)

κ_l Mixing-length factor

κ_p Nickels's von Kármán parameter

μ Dynamic viscosity

μ_t Eddy viscosity (dynamic)

ν Kinematic viscosity, $\nu = \mu/\rho$

ν_t Eddy viscosity (kinematic), $\nu_t = \mu_t/\rho$

ω Specific dissipation rate of k, $\omega = \varepsilon/(C_\mu k)$

ϕ Fluctuating part of Φ^* (in the context of Section 1.3) or length-scale providing quantity ($\phi = k^m\varepsilon^n$)

ϕ_{ij} Pressure strain-rate correlation

ϕ^*_{ij} Velocity pressure-gradient correlation

ϕ^1_{ij} Slow part of ϕ_{ij}

ϕ_{ij}^2	Rapid part of ϕ_{ij}
ρ	Density
$\underline{\underline{\boldsymbol{\sigma}}}$	Total stress tensor
$\underline{\underline{\boldsymbol{\tau}}}^{\text{visc}}$	Viscous stress tensor
τ	Total shear-stress
τ_w	Shear-stress at the wall
θ	Momentum thickness
Ξ_{log}	Diagnostic function for the log-law
Ξ_{sqrt}	Diagnostic function for the sqrt-law

Superscripts

$(\cdot)^+$	Scaled in wall-units (u_τ, ν)
$\widehat{(\cdot)}$	Scaled with the pressure velocity (u_p, ν) or modified variable of the Spalart-Allmaras model (Section 3.1.2)
$\check{(\cdot)}$	Instantaneous quantity

Acronyms

APG	Adverse Pressure Gradient
CFD	Computational Fluid Dynamics
DNS	Direct Numerical Simulation
EVM	Eddy-Viscosity Model
FPG	Favourable Pressure Gradient
GGDH	Generalised Gradient Diffusion Hypothesis, see Eq. (3.45)
LES	Large Eddy Simulation
LRR	Launder Reece and Rodi (model, [58])
QCR	Quadratic Constitutive Relation
RANS	Reynolds-Averaged Navier-Stokes
RSM	Reynolds-Stress Model
SGDH	Simple Gradient Diffusion Hypothesis, see Eqs. (3.7) & (3.47)
SSG	Speziale Sarkar and Gatski (model, [107])
ZPG	Zero Pressure Gradient

Introduction

In the last decades, numerical simulation has taken a significant role in many industrial sectors with the development of digital twins, such as Dassault's Falcon 7X, which has been the first aircraft to be entirely designed on a virtual platform. More particularly, *Computational Fluid Dynamics* (CFD) has become indispensable to the aeronautical sector, as it enables more efficient aircraft through the emergence of disruptive designs and technologies, in a highly competitive sector and society's growing environmental awareness. This efficiency is especially called for by the Paris Agreement (2016) and Europe's ambition to reach a net zero CO_2 emissions aviation by 2050 (*Destination 2050* [78]), along with new flying habits and new motorisations.

The progress in numerical methods and the growth of computing power over the past half-century has led to faster CFD computations, carried out on larger and more complex configurations (Rossow & Cambier [89], Chalot *et al.* [19]). It allows for today's simulations of a full aircraft to be run in less than one hour during design cycles, and makes it possible to explore many different new geometries in combination with optimisation processes. Hence, numerical simulation has become a valuable alternative to wind-tunnel and in-flight tests. In parallel, CFD gives access to a detailed description of the flow around the aircraft and provides thus an insight on the physical phenomena at work. However, contrary to experiments, numerical simulations in the industry only represent an approximation of the physics due to the complexity of the considered geometries and phenomena, which need to be simplified and modelled.

Indeed, industrial flows are often turbulent and result in non-linearities in the fluid motion equations and the superimposition of unsteady vortices spread on a wide range of sizes and frequencies. Solving the flow physics exactly would require extremely fine computational grids and time steps to capture the tiniest turbulent structures. Such exact computations (Direct Numerical Simulation – DNS), for now restricted to academic research with flows at low Reynolds numbers, are not expected to be handled by supercomputers for a full aircraft before 2080 (Spalart [102]). Therefore simulations rely on models that describe the turbulent scales they cannot capture (Large Eddy Simulation – LES) or the statistical impact of turbulence of the mean flow (Reynolds-Averaged Navier-Stokes – RANS). Despite considerable research activity for several decades, turbulence modelling remains one of the major scientific problems of the century and has been designated as one of the main requirements to increase impact of CFD, in NASA's *CFD Vision 2030* study [100].

More particularly, RANS models are indispensable for predicting the boundary layer, a very thin region in the immediate vicinity of solid walls where the flow is affected by fluid viscosity and intense turbulence. Indeed, this region involves very small scales preventing from using even the LES approach with the available computing power. Accurate models are all the more important that quantities of interest for aeronautical engineering, such as lift and drag, are determined at the wall and therefore largely dictated by the boundary

layer. The accuracy of models also strongly affects the location of shock-waves at the surface of a wing and flow separations. The latter is a critical phenomenon occurring at the limit of the flight domain, where the boundary layer is slowed down by adverse pressure gradients (APGs), and causes unsteady loads, structural vibrations and stall.

To enable less conservative and more efficient aircraft designs, and thus to reduce the incorporated safety margins, it is necessary to further improve the fidelity in near-wall turbulence modelling at the limit of flight envelop, in particular for flows subjected to APGs. To that end, reference data are crucial as they improve the understanding of the near-wall physics and help calibrate the models. However, most of today's models have been calibrated under the zero-pressure-gradient (ZPG) assumption and are not able to correctly predict the growth and the separation of a decelerated boundary layer. Indeed, reference data for APG flows have only recently been made available, with experimental studies, including the Skåre & Krogstad experiment [99], DNSs from Coleman *et al.* [23] and Kitsios *et al.* [49, 50] and international projects, *e.g.* the European projects WALLTURB[1] and EuHit[2]. In particular, these flows are actively investigated at the DLR, which has produced high-quality experimental data as part of its RETTINA[3] and VicToria[4] projects.

Objectives

This thesis aims to address the aforementioned limitations of turbulence modelling in strong adverse-pressure-gradient boundary layers and to propose generic corrections for RANS models.

The recent developments in the in-house CFD code Aether at Dassault Aviation has made it possible to consider second-order closures, called Reynolds-stress models (RSMs). These advanced RANS models rely on fewer simplifying hypotheses, and especially dispense with the turbulent viscosity concept, which let them reproduce the physics of turbulence more accurately. Moreover, near-wall treatments have been developed to ensure a correct asymptotic prediction down to the wall, such as the elliptic blending from Manceau & Hanjalić [69] which accounts for non-local effects. Consequently, they implicitly account for complex three-dimensional phenomena in boundary layers and in corner flows, for instance at the junction between wings and fuselage.

The implemented RSMs, including the Elliptic Blending Reynolds-Stress Model [69, 67], will be benchmarked against the current industrial reference, the Spalart-Allmaras model [104] to assess their predictions and identify their limitations, especially in APG flows. This will serve as a basis to determine the improvements to be brought to the models. Specific corrections will then be developed and validated, in order to propose a new turbulence model for aeronautical design.

Outline of the thesis

The physics and the numerical description of turbulent flows is first introduced in Chapter 1.

[1] *A European synergy for the assessment of wall turbulence*
[2] *European High-Performance Infrastructure in Turbulence*
[3] *Reliable Turbulence and Transition Modelling for Industrial Aerodynamics*
[4] *Virtual Aircraft Technology Integration Platform*

Chapter 2 describes the turbulent boundary layer and its impact on aerodynamics, before presenting the influence of adverse pressure gradients. In particular, the resulting alteration of the inner layer of the boundary layer is detailed.

Chapter 3 presents the classical RANS modelling, focusing on two-equation eddy-viscosity models and Reynolds-stress models, and details more particularly the models considered in this thesis.

Chapter 4 assesses the performance and differences of three recent RSMs on academic cases: the ZPG flat plate and the equilibrium APG boundary layer from Skåre & Krogstad [99]. The models are compared to the Spalart-Allmaras model, representing the industrial reference model.

Chapter 5 explores corrections for the log-law region, in which the velocity gradient is observed to increase with the pressure-gradient. To account for this phenomenon, a local recalibration is developed for the Spalart-Allmaras model using a NACA 4412 profile.

Chapter 6 investigates the compatibility of the models with the sqrt layer, which progressively grows at the outer end of the log layer. Corrections are developed with the Skåre & Krogstad test case for the RSMs and leads to the definition of a new Reynolds-stress model, the EB-RSM-dP, which includes additional terms activated locally.

This newly developed model is finally validated in Chapter 7 on an industrial application case, the Common Research Model, developed for the AIAA CFD Drag Prediction Workshop and representative of a commercial aircraft.

Chapter 1

Turbulent flows

1.1 Navier-Stokes equations

The dynamic of a viscous fluid is mathematically described by the Navier-Stokes equations, which arise from the transposition of Newton's Second Law to fluid motion in Eulerian formalism. They consist in three conservation equations for mass, momentum and total energy.

1.1.1 Continuity equation

The mass conservation accounts for the continuity of the fluid and ensures that no fluid parcel appears or disappears in the fluid volume. Considering any volume of fluid $\mathcal{V}$ defined by its border surface Σ, and assuming there is no injection or suction of matter inside of it, the variation of mass of fluid in the volume is equal to the quantity of fluid entering or leaving the volume. This translates as

$$\int_{\mathcal{V}} \frac{\partial \check{\rho}}{\partial t} \, \mathrm{dv} + \oint_{\Sigma} \check{\rho} \underline{\check{\mathbf{U}}} \cdot \mathrm{d}\underline{\mathbf{s}} = 0 \tag{1.1}$$

where $\check{\rho}$ stands for the fluid density and $\underline{\check{\mathbf{U}}}$ its velocity. Using the divergence theorem, the surface integral can be transformed into an integral on the volume, leading to the local mass balance in the fluid, also called continuity equation

$$\frac{\partial \check{\rho}}{\partial t} + \underline{\nabla} \cdot \left(\check{\rho} \underline{\check{\mathbf{U}}} \right) = 0 \tag{1.2}$$

or in the convective form, using the material derivative $\frac{\mathrm{D}}{\mathrm{D}t} = \partial_t + \underline{\check{\mathbf{U}}} \cdot \underline{\nabla}$,

$$\frac{\mathrm{D}\check{\rho}}{\mathrm{D}t} + \check{\rho} \underline{\nabla} \cdot \underline{\check{\mathbf{U}}} = 0. \tag{1.3}$$

For incompressible flows, the material derivative of density cancels out and the continuity equation simplifies to $\underline{\nabla} \cdot \underline{\check{\mathbf{U}}} = 0$.

1.1.2 Momentum equation

Regarding the momentum of the fluid in the volume $\mathcal{V}$, its variations is balanced by the creation of momentum from body forces per unit volume $\underline{\check{\mathbf{f}}}_{\mathrm{vol}}$ and the exchange of

momentum with the neighbourhood of the considered fluid element due to surface forces $\underline{\underline{\check{\boldsymbol{\sigma}}}}$ and convection through Σ. The conservation of momentum reads therefore

$$\int_{\mathcal{V}} \frac{\partial \check{\rho} \underline{\check{\mathbf{U}}}}{\partial t} \, \mathrm{dv} + \oint_{\Sigma} \left(\check{\rho} \underline{\check{\mathbf{U}}} \right) \underline{\check{\mathbf{U}}} \cdot \mathrm{d}\underline{\mathbf{s}} = \int_{\mathcal{V}} \underline{\check{\mathbf{f}}}_{\mathrm{vol}} \, \mathrm{dv} + \oint_{\Sigma} \underline{\underline{\check{\boldsymbol{\sigma}}}} \cdot \mathrm{d}\underline{\mathbf{s}}. \tag{1.4}$$

In the case of external air flows around aircraft, the body forces are restricted to gravity, $\underline{\check{\mathbf{f}}}_{\mathrm{vol}} = \check{\rho} \underline{\mathbf{g}}$, which can be neglected. The surface forces correspond to the local total stress applied to the fluid, defined as follow

$$\underline{\underline{\check{\boldsymbol{\sigma}}}} = -\check{P} \underline{\underline{\mathbf{1}}} + \underline{\underline{\check{\boldsymbol{\tau}}}}^{\mathrm{visc}}. \tag{1.5}$$

The first term represents the static pressure exerted on the fluid volume and the second term is the viscous stress arising from the friction between fluid parcels, which can be written

$$\underline{\underline{\check{\boldsymbol{\tau}}}}^{\mathrm{visc}} = \check{\mu} \left(\underline{\underline{\nabla \check{\mathbf{U}}}} + \underline{\underline{\nabla \check{\mathbf{U}}}}^{T} \right) + \check{\zeta} \, \mathrm{tr}\left[\underline{\underline{\nabla \check{\mathbf{U}}}} \right] \underline{\underline{\mathbf{1}}}, \tag{1.6}$$

where $\check{\mu}$ is the dynamic viscosity and $\check{\zeta}$ the second coefficient of viscosity. For Newtonian fluids such as air, Stokes's hypothesis implies $3\check{\zeta} + 2\check{\mu} = 0$, leading to the viscous stress being proportional to the deviatoric part of the strain-rate $\underline{\underline{\check{\mathbf{S}}}} = \frac{1}{2}(\underline{\underline{\nabla \check{\mathbf{U}}}} + \underline{\underline{\nabla \check{\mathbf{U}}}}^{T})$

$$\underline{\underline{\check{\boldsymbol{\tau}}}}^{\mathrm{visc}} = 2\check{\mu} \underline{\underline{\check{\mathbf{S}}}}^{D}, \qquad \text{with} \quad \underline{\underline{\check{\mathbf{S}}}}^{D} = \underline{\underline{\check{\mathbf{S}}}} - \frac{1}{3} \mathrm{tr}\left[\underline{\underline{\check{\mathbf{S}}}} \right] \underline{\underline{\mathbf{1}}} \tag{1.7}$$

Substituting Eqs. (1.5) & (1.7) into Eq. (1.4), the local momentum conservation becomes

$$\check{\rho} \left(\frac{\partial \underline{\check{\mathbf{U}}}}{\partial t} + \left(\underline{\check{\mathbf{U}}} \cdot \underline{\nabla} \right) \cdot \underline{\check{\mathbf{U}}} \right) = -\underline{\nabla} \check{P} + \underline{\nabla} \cdot \left(2\check{\mu} \underline{\underline{\check{\mathbf{S}}}}^{D} \right). \tag{1.8}$$

1.1.3 Energy equation

Using the same reasoning, two quantities contribute to the specific total energy $\check{E}$ conservation, the energy flux produced by the total stress applied to the fluid $\underline{\underline{\check{\boldsymbol{\sigma}}}} \cdot \underline{\check{\mathbf{U}}}$ and the thermal flux $\underline{\check{\mathbf{q}}}$, the body forces $\underline{\check{\mathbf{f}}}_{\mathrm{vol}}$ being neglected. This leads to the last conservation equation

$$\check{\rho} \left(\frac{\partial \check{E}}{\partial t} + \left(\underline{\check{\mathbf{U}}} \cdot \underline{\nabla} \right) \cdot \check{E} \right) = -\underline{\nabla} \cdot \left(\check{P} \underline{\check{\mathbf{U}}} \right) + \underline{\nabla} \cdot \left(2\check{\mu} \underline{\underline{\check{\mathbf{S}}}}^{D} \cdot \underline{\check{\mathbf{U}}} \right) - \underline{\nabla} \cdot \underline{\check{\mathbf{q}}}. \tag{1.9}$$

The thermal flux is modelled with Fourier's law

$$\underline{\check{\mathbf{q}}} = -\lambda \underline{\nabla} \check{T} \tag{1.10}$$

where $\check{T}$ is the temperature and λ the thermal conductivity of the fluid. To link the temperature to the specific total energy, the latter can be decomposed into internal and kinetic energies

$$\check{E} = \check{E}_i(\check{T}) + \frac{1}{2} \underline{\check{\mathbf{U}}} \cdot \underline{\check{\mathbf{U}}}. \tag{1.11}$$

1.1.4 Summary

Finally the full set of Navier-Stokes equations describing the fluid motion is expressed as

$$\begin{cases} \dfrac{\mathrm{D}\check{\rho}}{\mathrm{D}t} &= -\check{\rho}\underline{\nabla}\cdot\underline{\check{\mathbf{U}}} \\ \check{\rho}\dfrac{\mathrm{D}\underline{\check{\mathbf{U}}}}{\mathrm{D}t} &= -\underline{\nabla}\check{P} + \underline{\nabla}\cdot\left(2\check{\mu}\underline{\underline{\check{\mathbf{S}}}}^{D}\right) \\ \check{\rho}\dfrac{\mathrm{D}\check{E}}{\mathrm{D}t} &= -\underline{\nabla}\cdot\left(\check{P}\underline{\check{\mathbf{U}}}\right) + \underline{\nabla}\cdot\left(2\check{\mu}\underline{\underline{\check{\mathbf{S}}}}^{D}\cdot\underline{\check{\mathbf{U}}}\right) - \underline{\nabla}\cdot\underline{\check{\mathbf{q}}} \end{cases} \tag{1.12}$$

In three-dimensional cases, the system contains 5 equations for 7 unknowns and needs therefore two additional relations to be closed. Two state equations are introduced to described the thermodynamic behaviour of the fluid. For aircraft studies, the air behaviour is correctly modelled by the thermally perfect gas law

$$\check{P} = \check{\rho}R_{\text{air}}\check{T} \tag{1.13}$$

$$\mathrm{d}\check{E}_i = c_{v,\text{air}}(\check{T})\ \mathrm{d}\check{T} \tag{1.14}$$

where $R_{\text{air}} = 287.1\,\mathrm{J\,kg^{-1}\,K^{-1}}$ is the specific gas constant and $c_{v,\text{air}} = 718.0\,\mathrm{J\,kg^{-1}\,K^{-1}}$ is the isochoric specific heat capacity at 300 K for dry air.

To simplify the study, the energy transport equation (1.9) will not be further considered. Indeed, the variation of internal energy is negligible in the current application cases and the turbulence around an aircraft, up to supersonic velocities, is mainly driven by the fluctuations of velocity. Using Cartesian coordinates and Einstein's summation convention, the Navier-Stokes equation set (1.12) in conservative form reduces to

$$\frac{\partial\check{\rho}}{\partial t} + \frac{\partial\check{\rho}\check{U}_j}{\partial x_j} = 0 \tag{1.15a}$$

$$\frac{\partial\check{\rho}\check{U}_i}{\partial t} + \frac{\partial\check{\rho}\check{U}_j\check{U}_i}{\partial x_j} = -\frac{\partial\check{P}}{\partial x_i} + 2\frac{\partial\check{\mu}\check{S}_{ij}^{D}}{\partial x_j} \tag{1.15b}$$

1.2 Turbulence

1.2.1 Phenomenon and scales of turbulence

Turbulence arises from the non-linearity of the convection term in the momentum transport equation (1.8), when it is not damped enough by diffusion due to the viscosity of the fluid. This is characterised by the dimensionless Reynolds number Re, named after one of the first scientists to study the phenomenon and its origins and defined as

$$Re = \frac{\rho L U}{\mu} \tag{1.16}$$

where L and U are characteristic length and velocity scales of the considered flow. It represents the ratio of the diffusion time over the convection time. The transition between laminarity and turbulence occurs when the Reynolds number exceeds a critical value that depends on the flow configuration.

The turbulent motion is intrinsically three-dimensional and unsteady, as it corresponds to a deterministic chaotic motion, which contains vortex structures whose time and length scales spread on several orders of magnitude at high Reynolds numbers. The relation between the turbulent structures is described by the Kolmogorov energy cascade [55], illustrated in Figure 1.1. In this process, turbulence is produced by the largest eddies, resulting from the mean flow gradients and determined by the flow geometry. Smaller scales are then generated from the interaction of these eddies with the other turbulent structures: large eddies break down into several smaller eddies, to which they pass on their kinetic energy. The smaller eddies undergo the same process until the cascade reaches the smallest scales, called the Kolmogorov scales or dissipative scales, where the energy is dissipated into heat by the fluid viscosity.

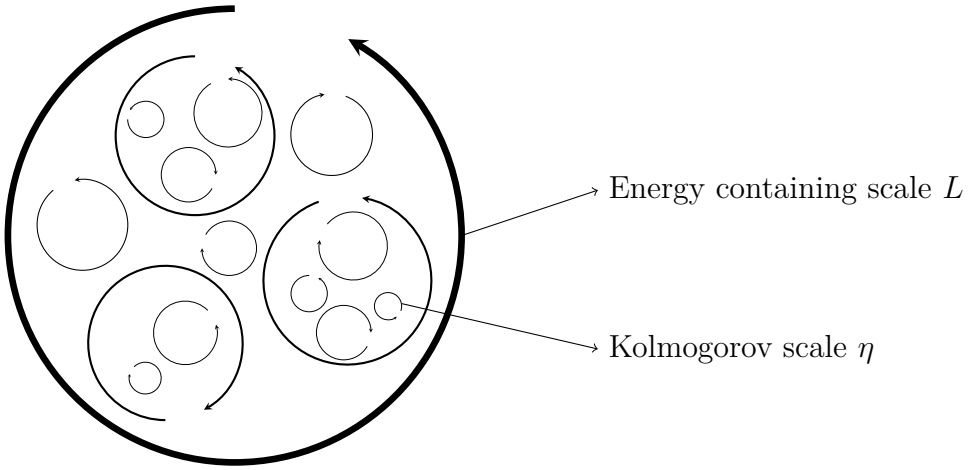

Figure 1.1: *Illustration of the energy cascade*

According to the Kolmogorov hypothesis, for a sufficiently high Reynolds number, the mean flow information is progressively lost in the cascade process, so that the dissipative scales are isotropic and only depend on the dissipation rate ε and the kinematic viscosity $\nu = \mu/\rho$. As a result, the Kolmogorov scales η (length), u_η (velocity) and τ_η (time) are defined by dimensional analysis as

$$\eta = \left(\frac{\nu^3}{\varepsilon}\right)^{1/4}, \qquad u_\eta = (\nu\varepsilon)^{1/4}, \qquad \tau_\eta = \left(\frac{\nu}{\varepsilon}\right)^{1/2} \tag{1.17}$$

Assuming the equilibrium of the energy cascade, meaning that the transfer rate of energy from the largest scales balances the dissipation rate at the smallest scales, it leads to

$$\frac{U^2}{T} \sim \varepsilon \quad \Rightarrow \qquad \frac{L}{\eta} \sim Re^{3/4}, \qquad \frac{T}{\tau_\eta} \sim Re^{1/2} \tag{1.18}$$

where $T = L/U$. This shows that the range of scales depends on the Reynolds number.

In the inertial subrange, formed by the intermediate scales $\eta \ll l \ll L$, the eddies are self-similar, meaning that they display a universal behaviour. Relying on a dimensional analysis, Kolmogorov's K41 theory [55] describes this behaviour with the famous '$-5/3$' law for the energy spectrum (Figure 1.2)

$$E(\kappa) \sim \varepsilon^{2/3}\kappa^{-5/3} \tag{1.19}$$

where κ corresponds to the wave number associated to the scale $l = 2\pi\kappa$.

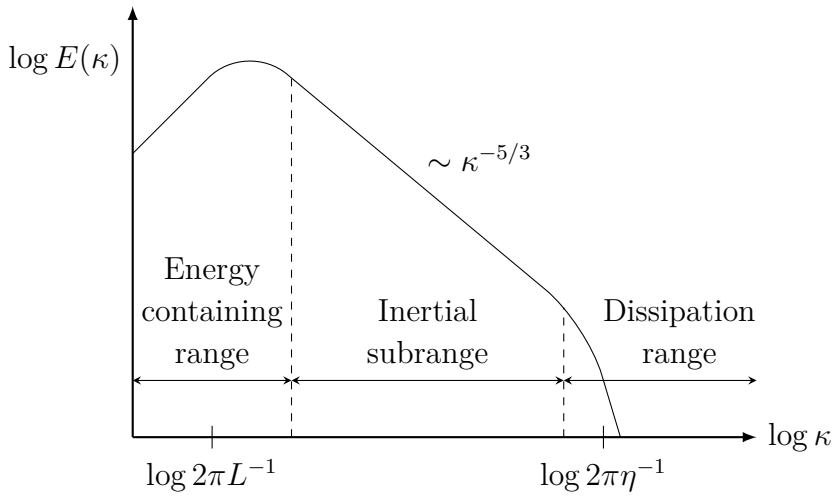

Figure 1.2: *The energy spectrum in log-log plot according to Kolmogorov's '$-5/3$' law*

1.2.2 Numerical resolution of turbulent flows

When considering the resolution of turbulence, three main approaches can be distinguished, classified in Figure 1.3

- Direct Numerical Simulation, where the physics is entirely resolved
- Large Eddy Simulation, where the smallest scales are filtered out and modelled
- Reynolds-Averaged Navier-Stokes, where all the scales are modelled statistically

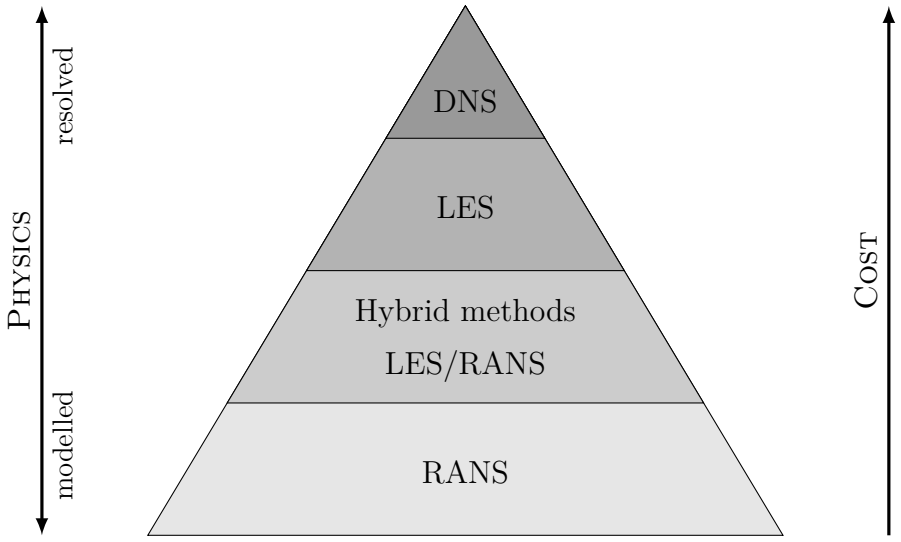

Figure 1.3: *Turbulence resolution approaches*

Direct Numerical Simulation (DNS)

Direct Numerical Simulations correspond to numerical experiments. The Navier-Stokes equations are accurately solved without any modelling, by resolving all the turbulent structures in the flow. The difference to the actual represented flow are due to the

assumptions made when deriving the equations, *e.g.* neglected terms and ideal gas state equations, and numerical errors. To reduce these errors, high order numerical schemes or spectral methods are used.

The spatial and temporal discretisations must be fine enough to capture all the scales down to the Kolmogorov scales, leading to heavy meshes and extremely costly computations. The dependence of the scale range on the Reynolds number, Eq. (1.18), strongly limits DNS to low Reynolds number simulations. Indeed, for the computation of a decaying isotropic turbulence, considering a mesh with a spatial step h and N points in each direction, the mesh must satisfy

$$Nh > L, \quad h \leq \eta \qquad i.e. \qquad N^3 \geq Re^{9/4}. \tag{1.20}$$

The number of points therefore exponentially increases with the Reynolds number. Similarly, the temporal refinement leads to an increase of time steps proportional to $Re^{1/2}$. Finally, the computational cost grows approximately as Re^3.

Considering the current growth of computing power, this approach will not be affordable for the aeronautical industry before the end of this century. It is for now only used as a research tool to gain in-depth understanding of the physics, for instance in incompressible turbulent boundary layers under zero pressure gradient (Schlatter *et al.*) and adverse pressure gradients (Coleman *et al.* [23], Kitsios *et al.* [49, 50]), in supersonic turbulent boundary layers (Pirozzoli *et al.* [82]), and in adverse pressure-gradient channel flows (Laval & Marquillie [61]).

Large Eddy Simulation (LES)

The LES approach addresses the high-computation-cost issue of DNS by reducing the required grid and time resolutions. The largest scales of turbulence, containing most of the energy and anisotropy of the flow, are explicitly solved, whereas the scales below a cut-off wave number κ_c in the inertial subrange, including the dissipative scales, can be assumed to be in an equilibrium state, thus to have a universal isotropic behaviour and are modelled (Figure 1.4).

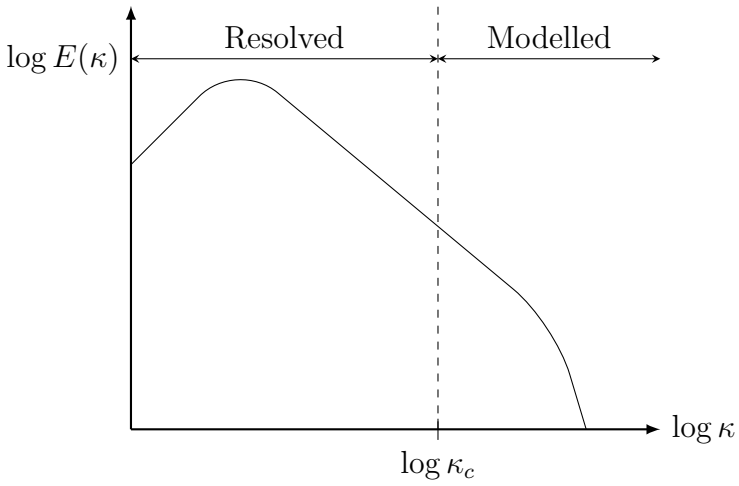

Figure 1.4: *LES spectrum cut-off*

To that effect, the velocity is filtered and decomposed into a resolved component and a residual, or sub-grid-scale, component. The residual scales influence the resolved

ones by introducing a residual-stress tensor into the momentum equations of the filtered Navier-Stokes equations. The residual-stress tensor is then modelled with a sub-grid-scale viscosity, as first suggested by Smagorinsky [101].

Since the smallest scales are not explicitly computed, meshes can be defined coarser compared to the ones required for DNS, only to capture the resolved scales usually defined to contain 80 % of energy. In particular, the dependency of the grid size on the Reynolds number is strongly reduced, so that LES enables a significant gain in computation costs for high-Re cases. However, close to the walls, the size of the largest eddies is constrained by the wall-distance and results in a narrowed energy spectrum. Consequently, the cut-off wave-number κ_c gets closer to the dissipative scales and the required grid resolution drops closer to DNS, preventing LES from being used for aeronautical configurations.

Reynolds-averaged Navier-Stokes (RANS)

To further reduce computation costs, the last approach offers to completely model the turbulence and all the scales involved, meaning that the evolution of the turbulent structures in the flow is no longer simulated over time. In most engineering applications, it is the mean force exerted by the fluid on the designed device or the heat transfers between them that are of interest, so the prediction of the mean flow, alongside with the turbulence influence on it, is often enough.

Reynolds-averaged Navier-Stokes (RANS), further detailed in Section 1.3, consists therefore in considering a statistically averaged system of equations, where the turbulence effects appear as additional terms impacting the momentum and the energy conservation laws. Since the turbulent scales are not simulated anymore, the spatial discretisation can be much coarser than the ones needed for DNS and LES. Therefore, RANS models are far cheaper compared to the two other approaches.

Their limitation lies in the accuracy achieved for rendering turbulence, which directly impacts the accuracy of the predicted mean flow, leading to the development and the use of always more complete and complex models, in a trade-off with computational cost.

Hybrid methods

Finally, hybrid methods coupling LES and RANS have been developed to retain the accuracy and time-dependence of LES in the regions remote from walls while reducing its computational cost, by using RANS models where LES requires too fine grid resolutions, especially close to walls. In particular, this approach is considered for engineering applications where the unsteadiness of turbulence has to be considered, for instance noise propagation and dynamic load predictions in the aeronautical industry.

Different coupling strategies have been suggested regarding the type and the activation of the RANS model. Among them, some approaches switch modelling methods based on turbulent length-scale or geometric criteria, *e.g.* the Detached Eddy Simulation (DES) of Spalart [103] and its variants Delayed Detached Eddy Simulation (DDES) [105], Zonal Detached Eddy Simulation (ZDES) [26]. Other approaches seamlessly adjust the cut-off wave number κ_c (with $\kappa_c \to \infty$ in RANS regions), such as the Very Large Eddy Simulation (VLES) of Speziale [106], the Partially-Averaged Navier-Stokes (PANS) of Girimaji [37] and the Partially Integrated Turbulence Model (PITM) of Schiestel & Dejoan [92]. Alternatively, the Hybrid Temporal LES (HTLES) of Manceau [68] considers a cut-off frequency ω_c in the temporal domain of the energy spectrum.

1.3 Reynolds-Averaged Navier-Stokes

1.3.1 The closure problem

The RANS equations are based on a statistical approach, consisting in decomposing any instantaneous physical quantity $\check{\Phi}$ into its mean value $\overline{\check{\Phi}}$ and a fluctuating value ϕ,

$$\check{\Phi} = \overline{\check{\Phi}} + \phi \qquad \text{with} \quad \begin{cases} \overline{\overline{\check{\Phi}}} = \overline{\check{\Phi}} \\ \overline{\phi} = 0 \end{cases}. \tag{1.21}$$

When considering a stationary flow, the statistical average can be assimilated to a time average on a long period

$$\overline{\check{\Phi}}\left(\underline{\mathbf{x}}\right) = \lim_{T\to\infty} \frac{1}{T} \int_{t_0}^{t_0+T} \check{\Phi}\left(\underline{\mathbf{x}}, t\right) \, \mathrm{d}t \tag{1.22}$$

Assuming an incompressible flow, *i.e.* $\check{\rho} = \rho_0 = const$, and taking the average of the Navier-Stokes equations (1.15) written with the Reynolds decomposition leads to

$$\frac{\partial \overline{\check{U}_i}}{\partial x_i} = 0 \tag{1.23a}$$

$$\frac{\partial \rho_0 \overline{\check{U}_i}}{\partial t} + \frac{\partial \rho_0 \overline{\check{U}_j}\,\overline{\check{U}_i}}{\partial x_j} = -\frac{\partial \overline{\check{P}}}{\partial x_i} + \frac{\partial}{\partial x_j}\left(2\overline{\check{\mu}}\overline{\check{S}_{ij}^D} - \rho_0 \, \overline{u_i u_j}\right) \tag{1.23b}$$

The new system involves the symmetric Reynolds-stress tensor $\rho_0 \, \overline{u_i u_j}$, corresponding to the correlations of the fluctuating velocities, which adds 6 unknowns. The problem is therefore not closed anymore and needs additional relations to be solved. Note that a similar closing problem arises with the energy equation, resulting in three additional unknowns, the turbulent heat fluxes $\overline{u_i e}$.

1.3.2 Favre average

In compressible flows, the density cannot be assumed constant. The application of the Reynolds decomposition to the density $\check{\rho} = \overline{\check{\rho}} + \varrho$ in the averaging process of the Navier-Stokes equations yields numerous non-linear terms. To simplify the study of such turbulent flows, Favre [32] introduced a density-weighted statistical average $\widetilde{\cdot}$

$$\check{\Phi} = \widetilde{\check{\Phi}} + \phi'' \qquad \text{with} \qquad \widetilde{\check{\Phi}} = \frac{\overline{\check{\rho}\check{\Phi}}}{\overline{\check{\rho}}}. \tag{1.24}$$

ϕ'', the fluctuation with respect to the density-weighted time average, satisfies the following auxiliary relations

$$\overline{\check{\rho}\phi''} = 0 \qquad \text{and} \qquad \overline{\phi''} = -\frac{\overline{\varrho\phi''}}{\overline{\check{\rho}}}. \tag{1.25}$$

The Favre decomposition is applied to the velocity[1] and the Reynolds decomposition to density and pressure, leading to a new set of equations similar to Eq. (1.23),

$$\frac{\partial \overline{\check{\rho}}}{\partial t} + \frac{\partial \overline{\check{\rho}}\widetilde{\check{U}_i}}{\partial x_i} = 0 \tag{1.26a}$$

$$\frac{\partial \overline{\check{\rho}}\widetilde{\check{U}_i}}{\partial t} + \frac{\partial \overline{\check{\rho}}\widetilde{\check{U}_j}\widetilde{\check{U}_i}}{\partial x_j} = -\frac{\partial \overline{\check{P}}}{\partial x_i} + \frac{\partial}{\partial x_j}\left(2\overline{\check{\mu}\check{S}_{ij}^D} - \overline{\check{\rho}u_i''u_j''}\right) \tag{1.26b}$$

where $\overline{\check{\rho}u_i''u_j''} = \overline{\check{\rho}}\,\widetilde{u_i''u_j''}$ and $\overline{\check{\mu}\check{S}_{ij}^D} \approx \widetilde{\check{\mu}}\widetilde{\check{S}_{ij}^D}$.

1.3.3 Morkovin hypothesis

Morkovin [73] showed that the density fluctuations ϱ are small compared to the mean density $\overline{\check{\rho}}$ close to the walls in non-hypersonic flows ($M < 5$), so that the compressibility effects are negligible for the turbulence dynamics. Hence, the resulting equations for mean flow and turbulence take the same form as for incompressible flows, written with the Reynolds average.

Noting that most results in the literature are given for incompressible flows and since most of the cases studied here are incompressible as well, the developments will be presented using the Reynolds average introduced in the previous section. They will then be assumed directly applicable to compressible cases, such as the Common Research Model in Chapter 7 by applying the same modelling to the Favre-average equations.

To simplify the notation, the mean values are written as upper case variables without any symbol above

$$\overline{\check{U}_i} = U_i, \qquad \overline{\check{\rho}} = \rho, \qquad \overline{\check{\mu}} = \mu, \qquad \overline{\check{P}} = P, \qquad \overline{\check{S}_{ij}^D} = S_{ij}^D. \tag{1.27}$$

Moreover, the incompressibility hypothesis results in a traceless strain-rate tensor, so that the notation can be further simplified into $S_{ij}^D = S_{ij}$.

1.3.4 Transport of the Reynolds stresses

To close the RANS equations (1.23), six additional transport equations can be derived for the Reynolds stresses by averaging a combination of the Navier-Stokes momentum equation Eq. (1.15b), noted as the $\mathcal{NS}$ operator

$$\overline{u_i\,\mathcal{NS}\left(\check{U}_j\right) + u_j\,\mathcal{NS}\left(\check{U}_i\right)} = 0$$

This yields

$$\begin{aligned}\frac{\partial \rho\overline{u_iu_j}}{\partial t} + \underbrace{\frac{\partial \rho U_k\overline{u_iu_j}}{\partial x_k}}_{\rho C_{ij}} = &\underbrace{-\rho\overline{u_iu_k}\frac{\partial U_j}{\partial x_k} - \rho\overline{u_ju_k}\frac{\partial U_i}{\partial x_k}}_{\rho P_{ij}} \quad \underbrace{-\overline{u_i\frac{\partial p}{\partial x_j}} - \overline{u_j\frac{\partial p}{\partial x_i}}}_{\rho\phi_{ij}^*} \\ &+ \underbrace{\mu\frac{\partial^2\overline{u_iu_j}}{\partial x_k\partial x_k}}_{\rho D_{ij}^\nu} \quad \underbrace{-\frac{\partial \rho\overline{u_iu_ju_k}}{\partial x_k}}_{\rho D_{ij}^T} \quad \underbrace{-2\mu\overline{\frac{\partial u_i}{\partial x_k}\frac{\partial u_j}{\partial x_k}}}_{\rho\varepsilon_{ij}}\end{aligned} \tag{1.28}$$

[1] and to thermal quantities when considering energy transport

where C_{ij}, P_{ij}, ϕ^*_{ij}, D^ν_{ij}, D^T_{ij} and ε_{ij} are the convection of stress, the production, the velocity pressure-gradient correlation, the molecular diffusion, the turbulent transport and the dissipation rate, respectively. To improve physical understanding, the velocity pressure-gradient correlation can be split into a pressure diffusion term D^p_{ij} and a traceless term ϕ_{ij}

$$\rho D^p_{ij} = -\frac{\partial}{\partial x_k}\left(\overline{u_i p}\delta_{jk} + \overline{u_j p}\delta_{ik}\right) \tag{1.29}$$

$$\rho\phi_{ij} = 2\overline{p s_{ij}} \qquad \text{with} \quad s_{ij} = \frac{1}{2}\left(\frac{\partial u_i}{\partial x_j} + \frac{\partial u_j}{\partial x_i}\right) \tag{1.30}$$

The pressure strain-rate correlation ϕ_{ij} is then interpreted as the part of ϕ^*_{ij} that redistributes without loss the energy between the Reynolds stresses. However, such a decomposition to extract the trace of ϕ^*_{ij} is not unique and thus the physical meaning of the newly introduced terms is ambiguous.

Eq. (1.28) introduces new unknowns in the terms ϕ^*_{ij}, D^T_{ij} and ε_{ij}, for which new transport equations can be derived. For instance, the dissipation rate ε_{ij} leads to six exact transport equations, further investigated by Gerylomos & Vallet [35]. Assuming the Reynolds-stress dissipation rate to be isotropic, Daly & Harlow [24] restricted the derivation to the exact transport equation for its contraction $\varepsilon = \frac{1}{2}\varepsilon_{ii}$, starting from

$$2\mu\overline{\frac{\partial u_i}{\partial x_j}\frac{\partial}{\partial x_j}\left[\mathcal{NS}\left(\check{U}_i\right)\right]} = 0. \tag{1.31}$$

Using Mansour *et al.* notation [70], it reads

$$\rho\frac{\mathrm{D}\varepsilon}{\mathrm{D}t} = P_1 + P_2 + P_3 + P_4 + D^T_\varepsilon + D^p_\varepsilon + D^\nu_\varepsilon - Y \tag{1.32}$$

where the different terms are defined as:

$$P_1 = -2\mu\,\overline{\frac{\partial u_i}{\partial x_k}\frac{\partial u_j}{\partial x_k}}\frac{\partial U_i}{\partial x_j} \qquad \text{Production by mean velocity}$$

$$P_2 = -2\mu\,\overline{\frac{\partial u_k}{\partial x_i}\frac{\partial u_k}{\partial x_j}}\frac{\partial U_i}{\partial x_j} \qquad \text{Mixed production}$$

$$P_3 = -2\mu\,\overline{u_i\frac{\partial u_j}{\partial x_k}}\frac{\partial^2 U_j}{\partial x_i \partial x_k} \qquad \text{Gradient production}$$

$$P_4 = -2\mu\,\overline{\frac{\partial u_i}{\partial x_j}\frac{\partial u_i}{\partial x_k}\frac{\partial u_j}{\partial x_k}} \qquad \text{Turbulent production}$$

$$D^T_\varepsilon = -\frac{\partial}{\partial x_k}\left(\rho\overline{u_k\varepsilon}\right) \qquad \text{Turbulent transport}$$

$$D^p_\varepsilon = -\frac{\partial}{\partial x_k}\left(\frac{2\mu}{\rho}\overline{\frac{\partial p}{\partial x_i}\frac{\partial u_k}{\partial x_i}}\right) \qquad \text{Pressure transport}$$

$$D^\nu_\varepsilon = \frac{\partial}{\partial x_k}\left(\mu\frac{\partial \varepsilon}{\partial x_k}\right) \qquad \text{Viscous diffusion}$$

$$Y = 2\mu\,\overline{\frac{\partial^2 u_i}{\partial x_j \partial x_k}\frac{\partial^2 u_i}{\partial x_j \partial x_k}} \qquad \text{Viscous destruction}$$

This transport equation involves again many unknowns, such as the triple velocity-gradient correlations or the pressure-gradient velocity-gradient correlation.

In fact, each new transport equation derived for a given unknown introduces new correlations. Therefore the RANS equations cannot be solved exactly and need modelling. The RANS models will be presented in Chapter 3.

Chapter 2

The boundary layer

On a solid wall, a fluid experiences a strong friction due to its viscosity. This is mathematically translated into a no-slip condition: the fluid elements adjacent to the surface adhere to the wall. In 1904, Prandtl [84] theorised that the viscosity of a fluid in a high-Reynolds number flow acts on a restricted thin region near the surface, called the boundary layer. Outside of this region, the flow can be assumed to be inviscid and only geometrically influenced by the wall through the deviation of its streamlines. Concentrating all the viscous effects of the fluid, the boundary layer is a key-phenomenon in understanding and quantifying the performance of an aircraft.

2.1 General description

2.1.1 Aeronautical considerations

The aerodynamic force exerted on a solid body, *e.g.* a wing or the whole aircraft, is related to pressure distribution on the body and the friction on its walls.

The integration of the pressure around the solid body yields

$$\underline{\mathbf{F}}_{\text{total}} = L\,\underline{\mathbf{k}} + D_{\text{pressure}}\,\underline{\mathbf{i}} = \oint_{\Sigma} P\underline{\mathbf{n}}\,\mathrm{d}s \tag{2.1}$$

where $\underline{\mathbf{i}}$ and $\underline{\mathbf{k}}$ are the wind-wise and wind-normal directions respectively. Besides, the boundary layer developing on the solid body consists in a viscous shear layer at the wall, resulting in a skin friction expressed as

$$\tau_w = \mu \underline{\nabla}_{\underline{\mathbf{n}}} U\Big|_w \tag{2.2}$$

which essentially yields an opposing force, called the friction drag D_{friction}, once integrated. From a mechanical point of view, the total drag is thus written

$$D = D_{\text{pressure}} + D_{\text{friction}}. \tag{2.3}$$

Both the lift L and the total drag D strongly rely on the boundary layer. Indeed, it slightly deflects the streamlines close to the walls and alters the pressure distribution. The boundary layer can also be susceptible to separating from the wall, *i.e.* when slowed down by an adverse pressure gradient. In the case of a wing, the separation typically appears at the trailing edge and move upstream with increasing angle of attack, while the pressure distribution on the fore part intensifies and increases the lift. Past a critical angle

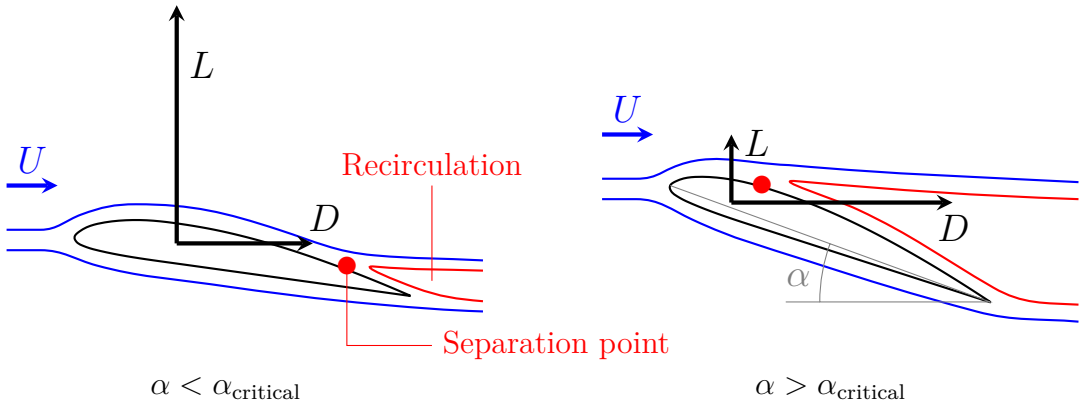

Figure 2.1: *Lift and drag on a wing profile*

of attack, the wing stalls as the lift abruptly falls, the remaining lift-producing surface of the wing becoming too small. This phenomenon is illustrated in Figure 2.1.

Correctly predicting the boundary layer behaviour on the body walls is therefore important for accurately estimating the lift and pressure drag, as well as anticipating the separation point.

The drag decomposition Eq (2.3) is referred to as *near-field*, as opposed to the *far-field* decomposition [113, 27], which relies on the conservation of a dynalpy-type vector $\underline{\mathbf{f}}$ defined as

$$\underline{\mathbf{f}} = -\rho\left[(\underline{\mathbf{U}} - \underline{\mathbf{U}}_\infty)\cdot\underline{\mathbf{i}}\right]\underline{\mathbf{U}} - (P - P_\infty)\,\underline{\mathbf{i}} + \underline{\underline{\boldsymbol{\tau}}}^{\text{visc}}\cdot\underline{\mathbf{i}} \tag{2.4}$$

to integrate the drag in the volume around the solid body and split it phenomenologically

$$D = D_{\text{viscous}} + D_{\text{wave}} + D_{\text{lift-induced}}. \tag{2.5}$$

The first two terms gather the drag due to irreversible thermodynamic phenomena, the second specifically targeting the drag increment due to the shock wave that forms on wings in transonic flights. The lift-induced term corresponds to the reversible phenomena, for instance the vortices created downstream an aircraft by the flow deflection on the wings.

In an ideal case, both approaches Eqs. (2.3) & (2.5) yield the same drag. However, the numerical integration introduces a small discrepancy

$$D_{\text{near-field}} = D_{\text{far-field}} + D_{\text{spurious}}. \tag{2.6}$$

The spurious drag account for the parasitic artificial drag, detected as the irreversible phenomena drag produced outside the viscous and wave drag regions.

Figure 2.2 illustrates the decompositions. The form drag D_{form}, defined as the part of the viscous drag due to pressure, specifically depends on the shape of the solid body and the boundary layer thickness.

To assess an aircraft performance, the lift, drag, pressure and skin friction are directly analysed using their dimensionless coefficients

$$C_L = \frac{L}{\frac{1}{2}\rho U_e^2 A_L}, \qquad C_D = \frac{D}{\frac{1}{2}\rho U_e^2 A_D}, \qquad C_p = \frac{P - P_0}{\frac{1}{2}\rho U_e^2}, \qquad C_f = \frac{\tau_w}{\frac{1}{2}\rho U_e^2}, \tag{2.7}$$

where A_L and A_D are reference areas for lift and drag, and P_0 is a reference pressure.

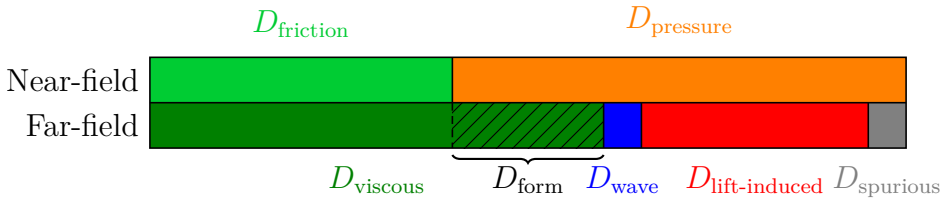

Figure 2.2: *Near-field and far-field drag decompositions*

2.1.2 Thin shear layer approximation

In the boundary layer, the flow evolves slowly in the streamwise direction but undergoes strong velocity gradients in the wall-normal direction to recover the velocity at the outer edge of the boundary layer, U_e. Introducing the boundary layer thickness δ as the wall-normal length-scale and L as the streamwise length-scale, it can be expressed as

$$\delta \ll L. \tag{2.8}$$

Thanks to this condition and dimensional analysis, the Navier-Stokes equations can be simplified. Approximating locally the solid wall to an infinite flat plate, the study is restricted to a two-dimensional steady flow. Further detailed in Pope [83], the boundary layer approximation leads to

$$\frac{\partial \rho U}{\partial x} + \frac{\partial \rho V}{\partial y} = 0 \tag{2.9a}$$

$$\frac{\partial \rho U^2}{\partial x} + \frac{\partial \rho UV}{\partial y} = -\frac{\partial P}{\partial x} + \frac{\partial}{\partial y}\left(\mu \frac{\partial U}{\partial y}\right) - \frac{\partial \rho \overline{uv}}{\partial y} \tag{2.9b}$$

$$0 = -\frac{\partial P}{\partial y} - \frac{\partial \rho \overline{v^2}}{\partial y} \tag{2.9c}$$

where U and V denote the streamwise and wall-normal components of the mean velocity, u and v those of the velocity fluctuations.

Since the fluctuations vanish at the wall, the normal momentum Eq. (2.9c) integrates to

$$P + \rho \overline{v^2} = P_w \tag{2.10}$$

so that the pressure gradient in the streamwise momentum Eq. (2.9b) becomes

$$\frac{\partial P}{\partial x} = \frac{\mathrm{d}P_w}{\mathrm{d}x} - \frac{\partial \rho \overline{v^2}}{\partial x} \approx \frac{\mathrm{d}P_w}{\mathrm{d}x}. \tag{2.11}$$

Note that the velocity fluctuations also vanish at the outer edge of the boundary layer, which results in $P_w = P_e$ using Eq. (2.10).

The boundary layer is characterised by its thickness. However, since it is defined as the length scale required to enable the self-similarity of velocity profiles plotted as $U/U_e = f(y/\delta)$, δ is difficult to determine exactly, either experimentally or numerically, and is conventionally replaced by the thickness yielding 99 % of the edge velocity, sometimes written δ_{99}.

Alternatively, the boundary layer can also be described as a loss in mass-flow rate and in momentum due to the presence of the wall. Two more length scales are therefore

introduced

$$\delta^* \equiv \delta_1 = \int_0^\infty \left(1 - \frac{\rho U}{\rho_e U_e}\right) \, \mathrm{d}y, \tag{2.12}$$

$$\theta \equiv \delta_2 = \int_0^\infty \frac{\rho U}{\rho_e U_e}\left(1 - \frac{U}{U_e}\right) \, \mathrm{d}y. \tag{2.13}$$

The displacement thickness δ^* measures the section corresponding to the mass-flow rate lost in the boundary layer. It is equivalent to the distance the wall should be shifted toward the free-stream to conserve the mass-flow rate if considering a perfect inviscid flow, for which the no-slip condition does not apply and no boundary layer develops (see Figure 2.3). Similarly, the momentum thickness θ corresponds to the shift of the wall needed to conserve the total momentum.

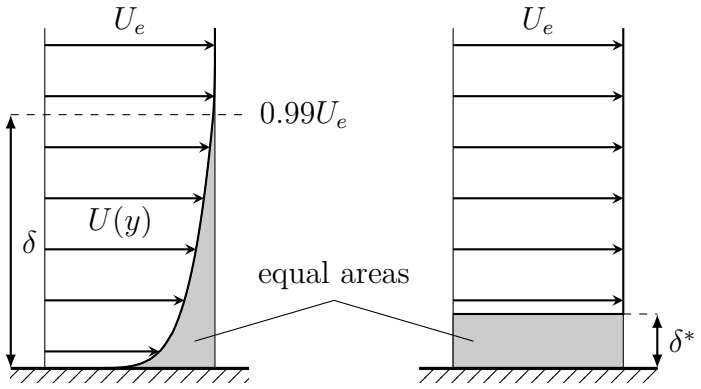

Figure 2.3: *The boundary layer thickness δ and the displacement thickness δ^**

These thicknesses help to further determine the nature of the flow in the boundary layer through the shape factor $H = \delta^*/\theta$, giving an insight on the velocity distribution and its fragility regarding flow separation. As illustrated in Figure 2.4, lower values describe *fuller* profiles, characterising turbulent boundary layer ($H \approx 1.3$), whereas the highest values are typical of laminar profiles ($H \approx 2.6$) or turbulent profiles near separation.

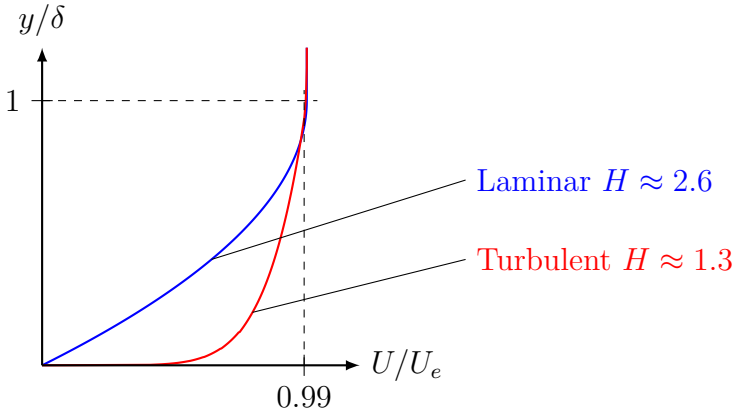

Figure 2.4: *Shape factor comparison for two flat plate boundary layer profiles*

2.2 Law of the wall without pressure gradient

At high Reynolds numbers, von Kármán [118] demonstrated that the flow behaviour in a turbulent boundary layer becomes universal. Yet it cannot be described with a similarity solution, contrary to the laminar case with the Blasius solution for the flow on a Zero-Pressure-Gradient (ZPG) flat plate, or the Falkner-Skan solutions for APG flows.

Indeed, turbulence leads to a scale separation. In the outer region, the turbulent motion is mostly affected by convection as in the free-stream region, and can thus be characterised by an outer scaling related to the free-stream conditions, including δ and U_e. However, in the inner region, the turbulent structures are damped as their sizes are bounded by the wall-distance and convection becomes negligible. An inner scaling is therefore defined with the conditions close to the wall, using the dynamic viscosity ν and the skin-friction τ_w. Both scales being independent, the profiles can only be compared with one of them at the time, resulting in partial similarities.

The structure of wall-bounded flows has been exhaustively described by Tennekes & Lumley [109] and Pope [83], and is briefly summarized in the following.

2.2.1 The inner layer

In the vicinity of the wall, it can be demonstrated that the velocity U and the wall distance y are related to the friction velocity $u_\tau = \sqrt{\tau_w/\rho}$ and to the dynamic viscosity ν. Forming the inner scales, respectively the velocity scale u_τ and the length scale $\delta_\nu = \nu/u_\tau$, a dimensional analysis leads to

$$U^+ = f_{\text{in}}\left(y^+\right) \tag{2.14}$$

where $U^+ = U/u_\tau$ and $y^+ = y/\delta_\nu$. Similarly, all the flow quantities in the inner layer can be written $\phi^+ = f_{\text{in},\phi}\left(y^+\right)$. Their dimensionless counterparts are independent of the mean flow Reynolds number and thus universal.

More particularly, turbulence and convection fade at the wall, hence Eq. (2.9b) integrates to

$$0 = -y\frac{\mathrm{d}P_w}{\mathrm{d}x} + \mu\frac{\partial U}{\partial y} - \rho\overline{uv} - \tau_w. \tag{2.15}$$

If no pressure gradient is applied, then it reduces at the wall to

$$\mu\frac{\partial U}{\partial y} = \tau_w. \tag{2.16}$$

Integrating and scaling Eq. (2.16) leads to the sublayer wall-law, valid for $y^+ < 5$

$$U^+ = y^+. \tag{2.17}$$

2.2.2 The defect layer

In the outer region, the turbulence structures are no longer shrunk by their proximity to the wall. Defining the outer scales with the boundary layer thickness δ, a dimensional analysis for the mean velocity yields

$$\frac{U - U_e}{u_\tau} = f_{\text{out}}\left(\frac{y}{\delta}\right). \tag{2.18}$$

This region is called the defect layer, as the relation f here corresponds to the loss of velocity compared to the flow outside the boundary layer[1].

2.2.3 The overlap region

When the Reynolds number is large enough so that the inner and outer scales are widely separated $\delta_\nu \ll \delta$, an overlap region where both scaling are valid exists and Eqs. (2.14) & (2.18) can be matched

$$u_\tau f_{\text{in}}\left(y^+\right) = u_\tau f_{\text{out}}\left(Y\right) + U_e \qquad \text{for} \qquad y^+ \gg 1 \quad \text{and} \quad Y = \frac{y}{\delta} \ll 1 \tag{2.19}$$

Differentiating Eq. (2.19) with respect to y, and multiplying it by y/u_τ, leads to

$$y^+ \frac{\mathrm{d}f_{\text{in}}}{\mathrm{d}y^+} = Y \frac{\mathrm{d}f_{\text{out}}}{\mathrm{d}Y} \tag{2.20}$$

Since the left hand side depends only on y^+ and the right hand side only on Y, and noting that these two quantities are independent due to the scale separation, both sides of the equation are constant. Writing this constant $1/\kappa_0$, where κ_0 is called the von Kármán constant, the velocity profile in the overlap region is described by

$$U^+ = \frac{1}{\kappa_0} \log\left(y^+\right) + B \tag{2.21}$$

Experimentally, $\kappa_0 \approx 0.41$ and $B \approx 5$. This overlap region is often referred to as the logarithmic region, or log-region, and extends from $y^+ \approx 30$ up to $10-20\,\%$ of the boundary layer thickness.

The blending of the viscous sublayer and the log layer gives rise to the buffer layer, where both viscosity and turbulence affect the flow. Figure 2.5 shows the stratification of the different layers described above, applied to a ZPG flat plate DNS yielding a canonical boundary layer. The outer layer is also often referred to as the wake region.

Some authors proposed alternative overlap region laws, experimentally calibrated, to account for finite-Reynolds-number effects when charactering boundary layers, in the form of a power law, *e.g.* Barenblatt [5] and Zagarola *et al.* [122], or a generalized log law, *e.g.* Buschmann & Gad-el-Hak [13]. Wilcox [120] provides a more detailed discussion on the different approaches for the overlap region.

2.3 Influence of the adverse pressure gradient

The pressure gradient greatly affects the behaviour of the boundary layer. Assuming an incompressible steady inviscid flow, the Bernoulli relation applies outside the boundary layer and yields

$$U_e \frac{\mathrm{d}U_e}{\mathrm{d}x} = -\frac{1}{\rho}\frac{\mathrm{d}P_e}{\mathrm{d}x} = -\frac{1}{\rho}\frac{\mathrm{d}P_w}{\mathrm{d}x} \tag{2.22}$$

As for laminar boundary layers, an adverse pressure gradient (APG, $\mathrm{d}P_w/\mathrm{d}x > 0$) causes a deceleration of the flow, the fluid meeting progressively more resistance on its path,

[1] a defect law can also be defined for channel and pipe flows, replacing the free-stream velocity U_e with the centerline velocity U_c

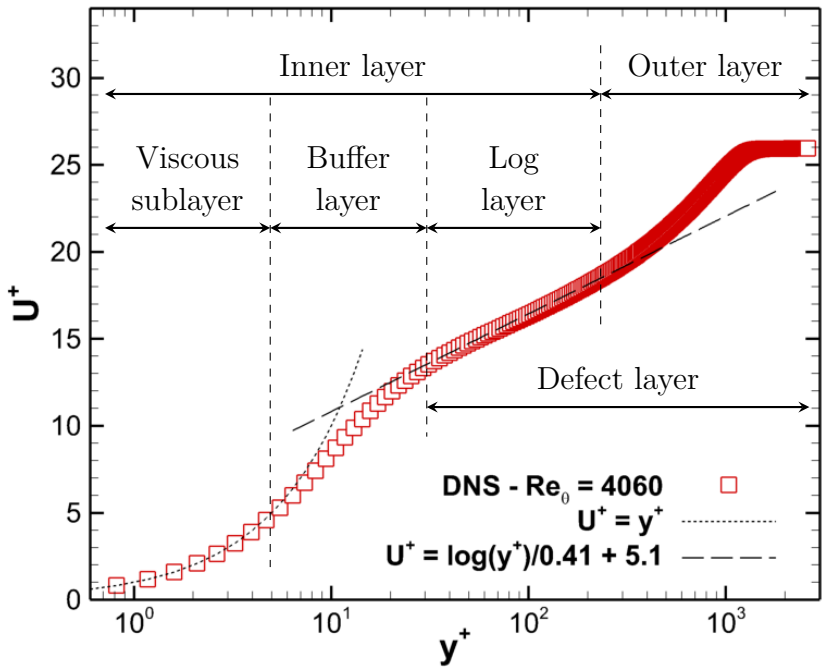

Figure 2.5: *Law of the wall illustrated with a ZPG flat plate DNS (Schlatter* et al. *[93])*

and can lead to flow separation, as shown in Figure 2.6. On the other hand, a favourable pressure gradient (FPG, $\mathrm{d}P_w/\mathrm{d}x < 0$) corresponds to an acceleration and stabilises the flow along the wall. Strong FPGs can also make a turbulent boundary layer transition back to a laminar regime.

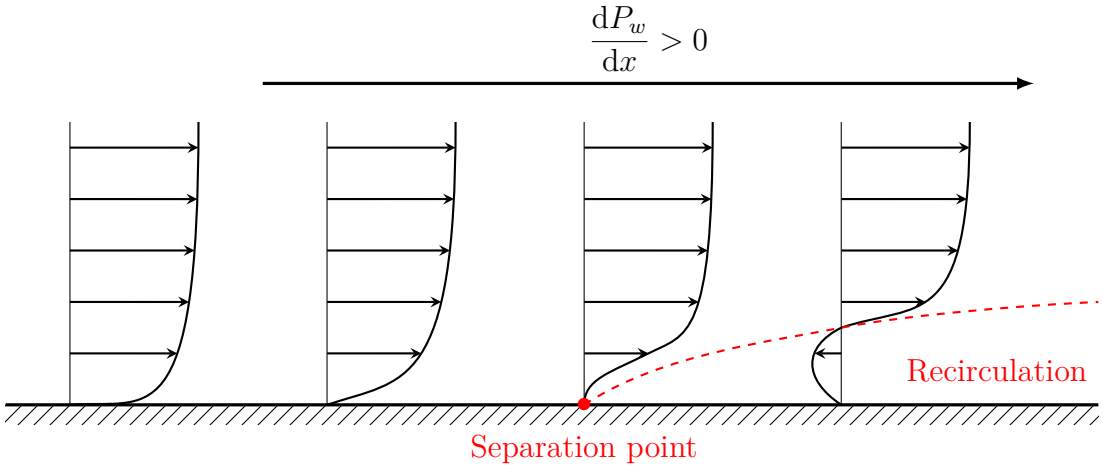

Figure 2.6: *Pressure-gradient effects on the streamwise evolution of the boundary layer*

Under APG, the boundary layer grows faster, its friction decreases, and the mean velocity profile departs from the ZPG case described in the section above. In inner scaling, the pressure gradient mainly affects the outer region, as illustrated in Figure 2.7. Turbulence is also strongly impacted and, in particular, its intensity increases in the outer layer, as further discussed in section 2.3.5.

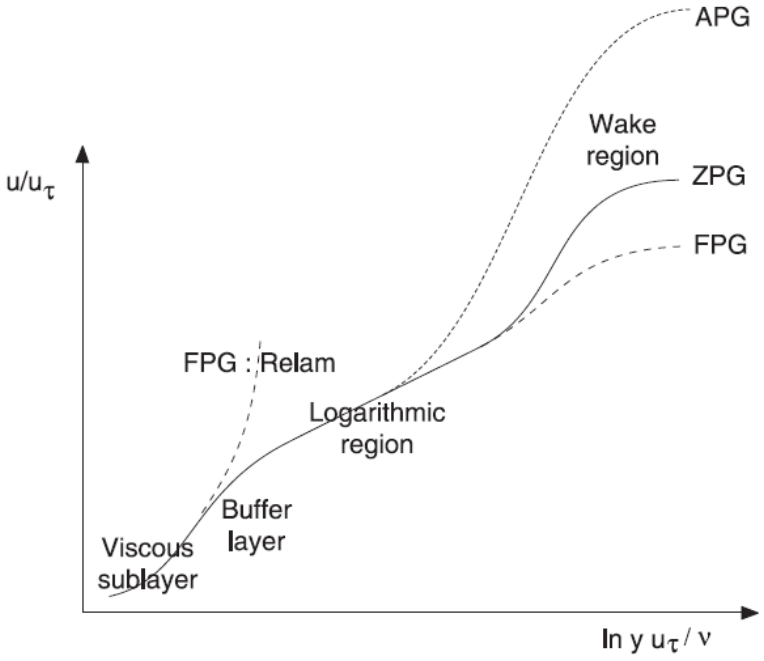

Figure 2.7: *Pressure-gradient effects on the mean velocity profile (reproduced from Catris & Aupoix [16])*

2.3.1 Equilibrium defect layer

The presence of an APG is all the more problematic as it comes with history effects, *i.e.* the profiles for a given pressure gradient are conditioned to its evolution upstream (see for instance Bobke *et al.* [8] or Vinuesa *et al.* [117]). The study of APG boundary layers, to correctly predict their behaviour with turbulence models, requires to separate these history effects from the ones due to the pressure gradient. Such flows are referred to as *equilibrium APG boundary layers* and enable partial similarity of profiles under APG.

Justifying that history effects are caused by the evolution of the perceived pressure gradient, which slowly changes the streamwise momentum balance, Clauser [21] defines a dimensionless pressure-gradient parameter to quantify the evolution

$$\beta_p = \frac{\delta^*}{\tau_w}\frac{\mathrm{d}P_w}{\mathrm{d}x}. \tag{2.23}$$

An equilibrium boundary layer is then characterised by a constant β_p parameter. Moreover, he introduces a new thickness $\Delta = \delta^*\sqrt{2/C_f}$ to scale the velocity profiles.

Townsend [111] derived conditions on scaling parameters to reach self-similar defect layers. Integrating and substituting Eq (2.9c) along with the Bernoulli relation Eq. (2.22) into Eq (2.9b), and simplifying the demonstration to the incompressible case, the turbulent boundary layer momentum equation reads

$$U\frac{\partial U}{\partial x} - \frac{\partial U}{\partial y}\int_0^y \frac{\partial U}{\partial x}(x,\widetilde{y})\,\mathrm{d}\widetilde{y} = U_e\frac{\mathrm{d}U_e}{\mathrm{d}x} + \nu\frac{\partial^2 U}{\partial y^2} - \frac{\partial \overline{uv}}{\partial y} \tag{2.24}$$

Defining the similarity variable $\eta = y/L_0(x)$ and the similarity functions f and g

$$U(x,y) = U_e(x) + U_0(x)f(\eta) \tag{2.25}$$

$$\overline{uv}(x,y) = U_0(x)^2 g(\eta) \tag{2.26}$$

where L_0 and U_0 are length and velocity scales depending only on the streamwise position x, Eq. (2.24) becomes

$$\frac{\mathrm{d}\left(U_0 U_e\right)}{\mathrm{d}x} f - \frac{U_0}{L_0}\frac{\mathrm{d}\left(L_0 U_e\right)}{\mathrm{d}x}\eta\frac{\mathrm{d}f}{\mathrm{d}\eta} + U_0\frac{\mathrm{d}U_0}{\mathrm{d}x} f^2 - \frac{U_0}{L_0}\frac{\mathrm{d}\left(L_0 U_0\right)}{\mathrm{d}x}\frac{\mathrm{d}f}{\mathrm{d}\eta}\int_0 f\ \mathrm{d}\eta - \frac{U_0^2}{L_0}\frac{\mathrm{d}g}{\mathrm{d}\eta} = 0 \quad (2.27)$$

To achieve self-similarity, Eq. (2.27) has to be an ordinary differential equation of the variable η, *i.e.* its coefficients must have the same x-dependency. This yields the following constraints

$$\frac{U_0}{U_e} = const, \qquad \frac{\mathrm{d}L_0}{\mathrm{d}x} = const, \qquad \frac{L_0}{U_0}\frac{\mathrm{d}U_0}{\mathrm{d}x} = const. \quad (2.28)$$

Replacing the scales L_0 and U_0 with δ^* and u_τ, the constraints translate into

$$C_f = const, \qquad \frac{\mathrm{d}\delta^*}{\mathrm{d}x} = const, \qquad \beta_p = const. \quad (2.29)$$

Note that using $L_0 \equiv \Delta$ leads to the same constraints. Wilcox [120] details a similar approach and adds an infinite-Reynolds-number condition to further simplify the condition (2.29) down to $\beta_p = const$.

More recently, alternative pressure-gradient parameters have been introduced by Castillo & George [14] and Maciel *et al.* [64]. The former suggests the equilibrium notion for an APG boundary layer can be broaden to flows only observing

$$\Lambda = \frac{\delta}{\rho U_e^2 \frac{\mathrm{d}\delta}{\mathrm{d}x}}\frac{\mathrm{d}P_w}{\mathrm{d}x} = const, \quad (2.30)$$

while the latter prefers the parameter

$$\beta_{ZS} = -\frac{\delta}{U_{ZS}}\frac{\mathrm{d}U_e}{\mathrm{d}x} \quad (2.31)$$

where $U_{ZS} = U_e\delta^*/\delta$ is a velocity scale introduced by Zagarola & Smits [123] to improve the collapse of profiles in channel flows.

2.3.2 Viscous sublayer

The pressure gradient can also be scaled for the inner layer, resulting in

$$p^+ = \frac{\delta_\nu}{\tau_w}\frac{\mathrm{d}P_w}{\mathrm{d}x} = \frac{\nu}{\rho u_\tau^3}\frac{\mathrm{d}P_w}{\mathrm{d}x}. \quad (2.32)$$

Considering a non-zero pressure gradient in the viscous sublayer, the integration of the streamwise momentum in the inner layer, Eq. (2.15), reduces to

$$\mu\frac{\partial U}{\partial y} = \tau_w + \frac{\mathrm{d}P_w}{\mathrm{d}x}y \qquad i.e. \qquad \frac{\tau}{\tau_w} = \frac{\mathrm{d}U^+}{\mathrm{d}y^+} = 1 + p^+y^+. \quad (2.33)$$

Integrating further leads to a generalised expression for the viscous sublayer law

$$U^+ = y^+\left(1 + \frac{1}{2}p^+y^+\right). \quad (2.34)$$

From Eq. (2.34), it can be deduced that the sublayer is slightly accelerated in wall-units under adverse pressure gradient ($p^+ > 0$). However, it is important to remember that the skin friction is also greatly affected by the pressure gradient, decreasing down to $\tau_w = 0$ at the separation point. The apparent acceleration is thus artificially caused by the inner scaling.

The APG influence can be clearly observed in Figure 2.8, where the generalised sublayer law Eq. (2.34) is assessed with the 2D separation bubble DNS from Coleman *et al.* [23]. The case consists in a flat plate boundary layer which undergoes a separation and reattachment, using velocity transpiration at the upper domain condition to impose the pressure gradient. The low Reynolds number (around $Re_\theta = 2{,}000$ at the inlet) results in large p^+ values. The correct asymptotic behaviour comes however with a reduced validity domain, meaning that the turbulent shear-stress $\overline{uv}$ starts affecting the inner layer closer to the wall as the pressure gradient increases.

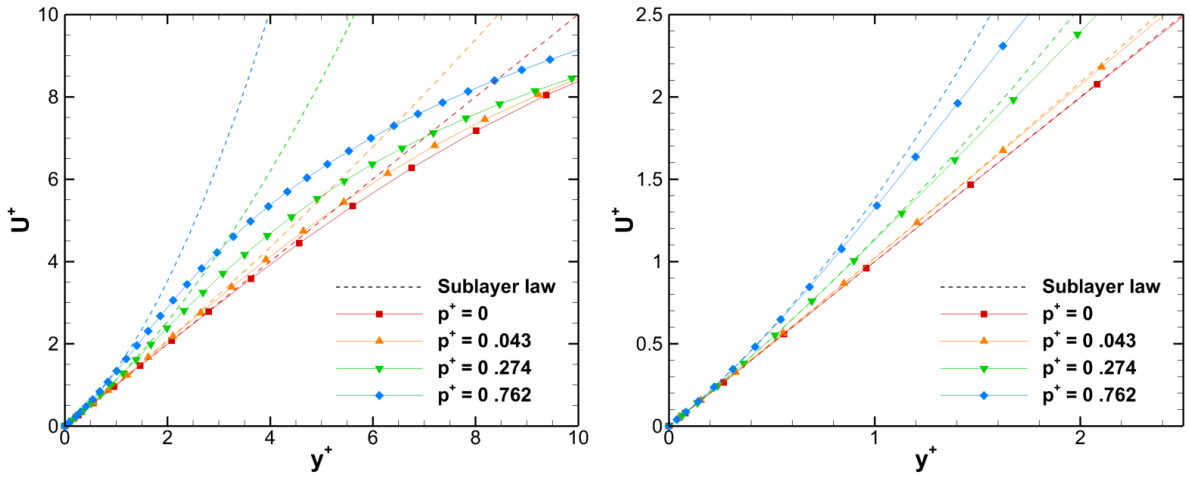

(a) *Viscous sublayer* **(b)** *Asymptotic behaviour at the wall*

Figure 2.8: *Agreement of the DNS of Coleman* et al. *[23] with the generalised viscous sublayer law Eq.* (2.34)

2.3.3 The logarithmic region

Universality?

The universality of the log-law and of the von Kármán constant is often questioned, especially in APG boundary layers. From the assumptions used for its derivation, the validity of this law is restricted to infinite-Reynolds-number flows, but it is used in practice to characterise finite-high-Reynolds-number flows.

Many authors consider that the universality holds despite pressure gradients, for instance Brown & Joubert [12], Huang & Bradshaw [45] and Aupoix *et al.* [4], reporting only a reduction of its extent as the velocity in the wake region increases. Clauser [21] and Nagano *et al.* [74] observed experimentally the alteration of the log-law intercept, B in Eq. (2.21), which undergoes a downward shift as p^+ rises without changing κ_0, and relate this phenomenon to the decrease of the sublayer thickness.

Finally, Nickels [77], Nagib & Chauhan [75] and Knopp [54] describe a general departure of the infinite Reynolds number log-law. Studying low-Reynolds-number APG turbulent

boundary layers, thus with strong p^+, Nickels noticed indeed the alteration of both κ_0 and the intercept, as well as the dependence of the sublayer thickness to the pressure gradient, and suggests a variable slope for the log-region.

These discrepancies in the experimental observations can be related to differences in Reynolds numbers. Eqs. (2.23) and (2.32) combined yield

$$\frac{p^+}{\beta_p} = \frac{\delta_\nu}{\delta^*} = \sqrt{\frac{2}{C_f}} Re_{\delta^*}^{-1} \tag{2.35}$$

so that when the Reynolds number tends to infinity, β_p being constant, the wall pressure-gradient parameter p^+ tends to zero, and the log-law recovers its universal behaviour. Nickels's slope alteration, described in the following section, can be therefore restricted to finite-Reynolds-number cases and complies with the universality of the log-law at infinite Reynolds numbers.

Slope alteration

From his experimental observations, Clauser [22] states that the viscous sublayer behaves as a laminar layer under constant shear stress, growing until it is disturbed by the structures from the outer turbulence. These structures being vigorous, their influence takes effect at a critical wall-distance y_c for which the local Reynolds number crosses the lowest critical Reynolds number for laminar-to-turbulent transition. Neglecting the impact of pressure gradient on the viscous sublayer compared to the shear-stress, Clauser uses Eq. (2.17) to deduce

$$Re_{\text{critical}} = \frac{U_c y_c}{\nu} = U_c^+ y_c^+ \approx 150 \qquad i.e. \qquad U_c^+ = y_c^+ \approx \sqrt{150} \approx 12 \tag{2.36}$$

which coincides with the maximum production distance, according to flat plate DNSs. This critical distance y_c is referred to as sublayer thickness by Nickels [77], in the sense that the influence of viscosity becomes negligible beyond.

As for a laminar-to-turbulent boundary layer transition, Nickels assumes that the addition of an adverse pressure gradient reduces the critical Reynolds number for instability, resulting in a smaller y_c in APG flows. Rather than modifying Re_{critical}, he suggests transferring the pressure-gradient effects to the scales so that the critical value can be kept constant. He thus introduces a constant critical Reynolds number based on the total shear-stress and the corresponding velocity scale

$$R_c = \frac{u_T \; y_c}{\nu} = 12 \tag{2.37}$$

$$u_T = \sqrt{\frac{\tau(y = y_c)}{\rho}} = u_\tau \sqrt{1 + p^+ y_c^+} \tag{2.38}$$

The sublayer thickness y_c^+ can be found by substituting Eq. (2.38) into Eq. (2.37)

$$p^+ {y_c^+}^3 + {y_c^+}^2 - R_c^2 = 0 \tag{2.39}$$

The smallest root of Eq (2.39) is retained as y_c^+, resulting in a sublayer thickness decreasing with p^+. Nickels shows in Figure 2.9 the good agreement of the theoretical solution with different boundary layer data sets, for which he computed the y_c by fitting the law of the wall defined in [77]. For a ZPG boundary layer, $u_T = u_\tau$ and $y_c^+ = 12$ so that Eq. (2.37) is compatible with Clauser's critical Reynolds number Eq. (2.36).

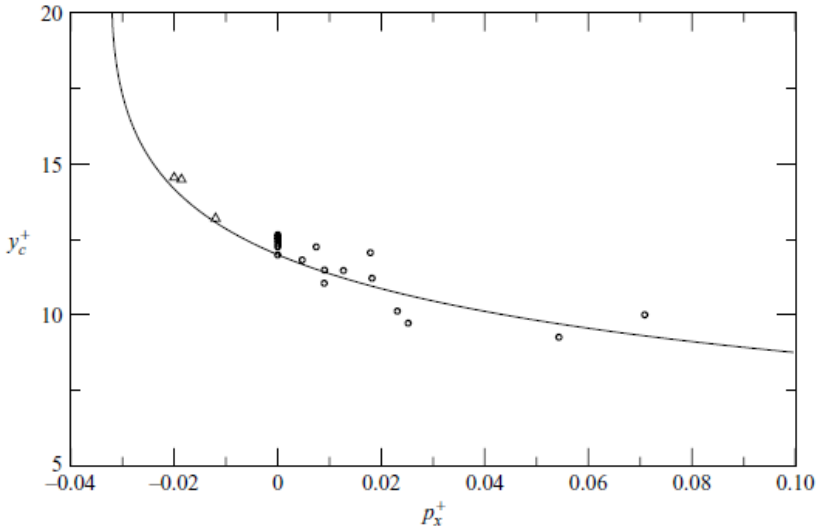

Figure 2.9: *Solution of Eq (2.39) compared to boundary layers data (reproduced from Nickels [77])*

Finally, he suggests to derive the log-law as in Section 2.2.3 with u_T for the inner velocity scale, which leads to

$$\frac{\mathrm{d}U}{\mathrm{d}y} = \frac{u_T}{\kappa_0 y} = \frac{u_\tau\sqrt{1+p^+y_c^+}}{\kappa_0 y} \tag{2.40}$$

Reverting back to the usual inner scaling

$$\frac{\mathrm{d}U^+}{\mathrm{d}y^+} = \frac{\sqrt{1+p^+y_c^+}}{\kappa_0 y^+} = \frac{1}{\kappa_p y^+}, \qquad \text{with} \quad \kappa_p = \frac{\kappa_0}{\sqrt{1+p^+y_c^+}} \tag{2.41}$$

Therefore, the log-law according to Nickels [77] becomes

$$U^+ = \frac{1}{\kappa_p}\log\left(y^+\right) + B' \tag{2.42}$$

where the slope depends on the pressure-gradient parameter p^+. More particularly, since κ_p decreases with increasing p^+, the velocity profile steepens in APG log layers.

Numerical simulations analysis

Recent numerical results are consistent with Nickels's log-law slope alteration. Figure 2.10 shows the velocity profiles at different positions and p^+ values for the flat plate separation bubble DNS from Coleman *et al.* [23] on the left, and for a NACA 4412 profile [116] on the right. The wing profile is computed with a wall-resolved LES for a chord Reynolds number $Re_c = 1\,\mathrm{M}$ at an angle of attack $\alpha = 5°$, and turbulence is triggered at 10 % of chord-wise position on both sides of the wing. The viscous sublayer in these velocity profiles reduces with the increasing p^+, while the log region progressively steepens, following Eq. (2.42).

This slope behaviour can be further analysed with the mean velocity slope diagnostic function, see for instance Österlund *et al.* [79] and Knopp [51], defined as

$$\Xi_{\log} = \left(y^+\frac{\mathrm{d}U^+}{\mathrm{d}y^+}\right)^{-1}. \tag{2.43}$$

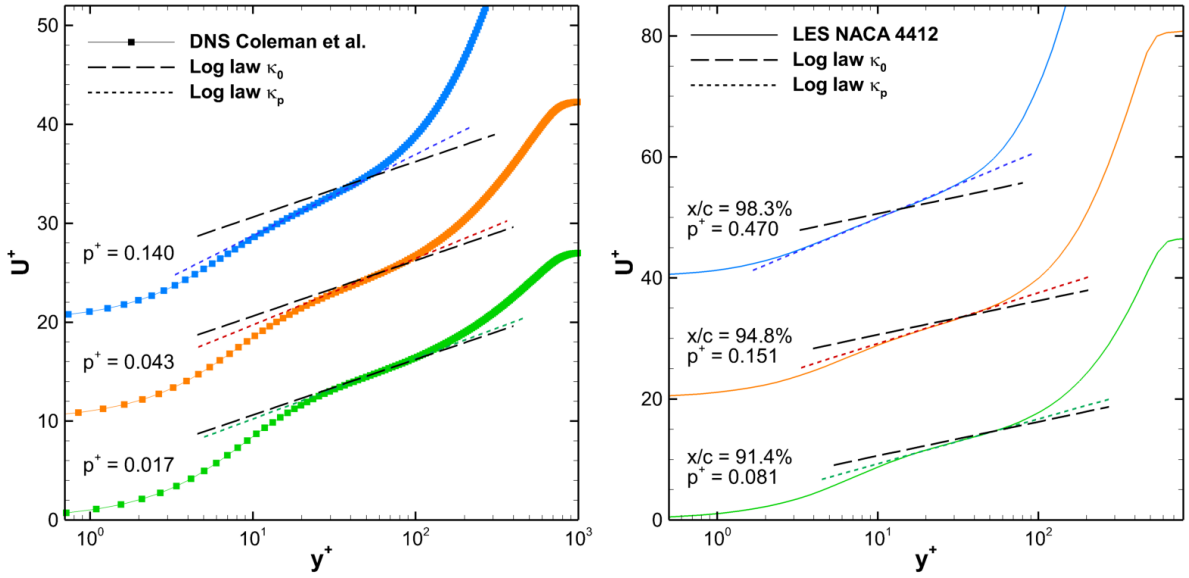

(a) *Separation bubble DNS (Coleman* et al. *[23])* **(b)** *NACA 4412 LES (Vinuesa* et al. *[116])*

Figure 2.10: *Velocity profiles in APG low-Reynolds-number flows*

This function yields the apparent von Kármán coefficient across the profile, and is shown in Figure 2.11 for the corresponding velocity profiles plotted in Figures 2.10. The κ_p value is reached in the logarithmic region as a local maximum of $\Xi_{\log}$ and thus directs the log-law in the vicinity of the inflection point of the velocity profile in log scale.

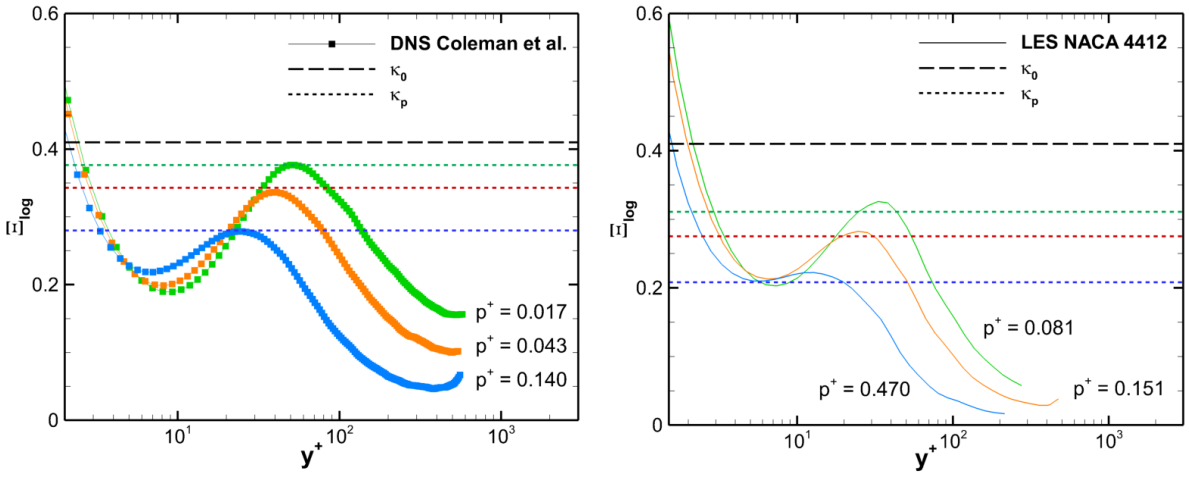

(a) *Separation bubble DNS (Coleman* et al. *[23])* **(b)** *NACA 4412 LES (Vinuesa* et al. *[116])*

Figure 2.11: *Log region diagnostic function*

Despite being visually appreciable on the velocity profiles of Figure 2.10, the logarithmic region cannot be observed as a region with a constant von Kármán coefficient with $\Xi_{\log}$ since the exact log law behaviour is only expected for infinite Reynolds numbers. Rather, the diagnostic function tends to indicate that the log region is too shrunk by the low-Reynolds-number effects, with a wake region departing closer to the wall, to achieve the ideal κ_0 slope value.

2.3.4 The square-root region

In a ZPG boundary layer, the inner layer can be assumed to be a constant-stress layer: when moving away from the wall, the decreasing viscous stress applied to the fluid is progressively compensated by the turbulent stress. The addition of pressure gradient results in a linear-stress layer. As turbulence becomes predominant, Eq. (2.33) becomes

$$-\overline{uv}^+ \approx \tau^+ = 1 + p^+ y^+ \tag{2.44}$$

The concept of square-root region, also called half-power law region, has been introduced by Townsend [111, 112] as an outcome of the analytical derivation of the velocity profile in a linear stress layer, and experimentally observed by Perry [81] and Brown & Joubert [12].

In the overlap region where both the viscosity and the advection are negligible, the production of turbulent energy balances its dissipation rate

$$\frac{\tau}{\rho}\frac{\mathrm{d}U}{\mathrm{d}y} = \varepsilon. \tag{2.45}$$

Since the size l of the turbulent structures is constrained by the wall distance in the overlap region, Townsend uses the mixing-length hypothesis, $l = \kappa_l y$, to scale the dissipation as $\varepsilon = (\tau/\rho)^{3/2} / (\kappa_l y)$, which leads to

$$\frac{\mathrm{d}U}{\mathrm{d}y} = \frac{\sqrt{\tau/\rho}}{\kappa_l y} \tag{2.46}$$

Note that the mixing-length factor is given by $\kappa_l = \kappa_0$ in ZPG conditions.

Substituting Eq. (2.44) into Eq. (2.46) scaled in wall-units, the velocity gradient in the overlap region becomes

$$\frac{\mathrm{d}U^+}{\mathrm{d}y^+} = \frac{\sqrt{1 + p^+ y^+}}{\kappa_l y^+} \tag{2.47}$$

which then integrates into the generalised sqrt-law for the overlap region

$$U^+ = \frac{2}{\kappa_l}\sqrt{1 + p^+ y^+} + \frac{1}{\kappa_l}\log\left(\frac{\sqrt{1 + p^+ y^+} - 1}{\sqrt{1 + p^+ y^+} + 1}\right) + const. \tag{2.48}$$

Alternatively, the generalised law Eq. (2.48) can equivalently be written

$$U^+ = \frac{2}{\kappa_l}\left(\sqrt{1 + p^+ y^+} - 1\right) + \frac{1}{\kappa_l}\log\left(y^+\right) + \frac{2}{\kappa_l}\log\left(\frac{2}{\sqrt{1 + p^+ y^+} + 1}\right) + const \tag{2.49}$$

as suggested by Knopp [51] to highlight the log-law behaviour when p^+ vanishes or for sufficiently small y^+ so that $p^+ y^+ \ll 1$.

On the contrary, when $p^+ y^+ \gg 1$, Eq. (2.48) simplifies into

$$U^+ = \frac{2}{\kappa_l}\sqrt{p^+ y^+} + const \tag{2.50}$$

and corresponds to the sqrt-law usually referred to, first introduced by Stratford [108] for flows at the verge of separation due to pressure gradient. Defining the pressure velocity u_p

as velocity scale for APG flows to prevent the singularity as u_τ vanishes, new dimensionless quantities are introduced

$$u_p = \sqrt[3]{\frac{\nu}{\rho}\frac{\mathrm{d}P_w}{\mathrm{d}y}} = u_\tau \sqrt[3]{p^+}, \qquad \widehat{U} = \frac{U}{u_p}, \qquad \widehat{y} = \frac{y u_p}{\nu}. \tag{2.51}$$

The sqrt-law can then be written as independent from the pressure-gradient parameter p^+

$$\widehat{U} = \frac{2}{\kappa_l}\sqrt{\widehat{y}} + const. \tag{2.52}$$

While the generalised law Eq. (2.48) is valid in the whole overlap region, where the shear-stress is given by Eq. (2.33), the sqrt-law Eq. (2.50) validity domain is restricted to the end of the overlap region, where $p^+ y^+ \gg 1$. Therefore, the square-root behaviour is expected in a region just above the logarithmic layer, which extent is progressively reduced to the benefit of the sqrt layer as p^+ grows.

In Figure 2.12, both the generalised law Eq. (2.48) and the asymptotic law Eq. (2.50) are plotted for the Skåre & Krogstad experiment [99], corresponding to an equilibrium APG boundary layer at $\beta_p = 20$ ($p^+ \approx 0.013$), at the last two available stations in the equilibrium region to ensure the absence of history effects. The generalised sqrt-law extends the validity of the traditional log law Eq. (2.21) from $y^+ \approx 300$ to $y^+ \approx 800$. This extension corresponds to the sqrt layer, described by the asymptotic law, which directly follows the log layer.

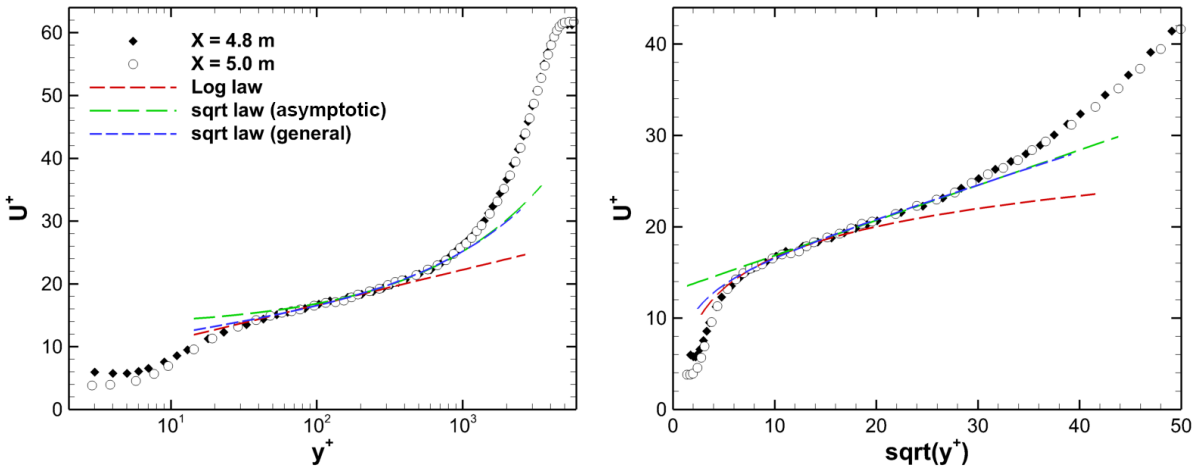

(a) *Mean velocity profile in log-scale* **(b)** *Mean velocity profile in sqrt-scale*

Figure 2.12: *Square-root laws for the Skåre & Krogstad experiment [99]*

In these figures, κ_l differs from the von Kármán constant κ_0 and is here adjusted to 0.6 to best fit the profiles. The diagnostic function for the generalised sqrt-law region Ξ_{sqrt} can be defined similarly to Eq. (2.43)

$$\Xi_{\mathrm{sqrt}} = \sqrt{1 + p^+ y^+}\left(y^+ \frac{\mathrm{d}U+}{\mathrm{d}y+}\right)^{-1} \tag{2.53}$$

and is plotted in Figure 2.13 for the Skåre & Krogstad experiment [99] at the positions considered in Figure 2.12. The uncertainty in the experimental mean velocity measurements

results in a large dispersion of the computed value for the velocity gradient in the inner layer. However, it can be seen that the diagnostic function Ξ_{sqrt} fluctuates around $\kappa_l \approx 0.6$ for $\sqrt{y^+} \in [8; 25]$. The increase of κ_l in APG is in agreement with the conclusions of Glowacki & Chi [38], who studied the mixing length for several experimental flows under pressure gradients.

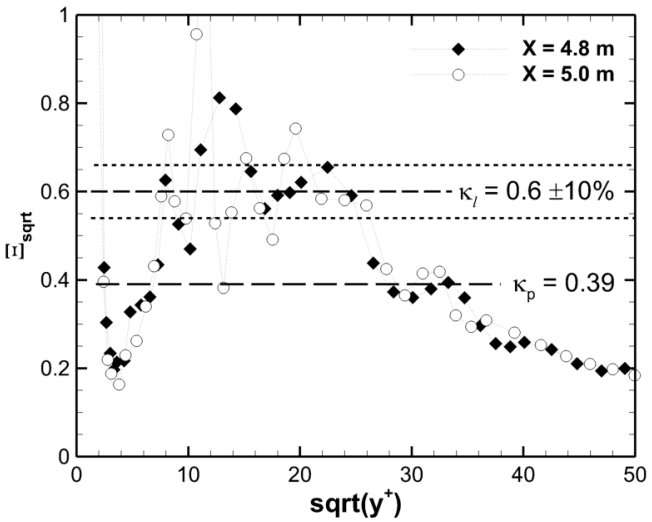

Figure 2.13: *Square-root region diagnostic function for the Skåre & Krogstad experiment [99]*

Some authors, including Perry [81], Daris [25] and Knopp [51], consider the sqrt layer as a disconnected region from the log layer and separated by a buffer layer. This is a consequence of the authors using a different von Kármán constant in the sqrt-law instead of κ_l, which results in the region designated by the sqrt-law being further away from the wall. Indeed, Perry and Daris derived the asymptotic sqrt-law Eq. (2.50) using the universal von Kármán constant κ_0, whereas Knopp [51] more recently fitted the generalised law Eq. (2.49) to several experimental data sets and retained Nickels's parameter κ_p [77]. Figure 2.13 exhibits a secondary plateau in the diagnostic function for the equilibrium region in the Skåre & Krogstad experiment [99], at $\Xi_{\text{sqrt}} \approx \kappa_p$, in the vicinity of $\sqrt{y^+} = 30$, which justifies this approach.

2.3.5 Effects on the Reynolds stresses

The rise of the outer layer in the mean velocity profile of APG boundary layers comes with the alteration of the turbulent structures. Indeed, in addition to the peak of turbulent kinetic energy in the buffer layer in ZPG conditions, a second peak grows with the pressure gradient in the outer layer, located just below the middle of the boundary layer. Similarly to Bradshaw [9], Krogstad & Skåre [57] also observe an outer peak in the shear-stress, which reaches in their wind-tunnel experiment [99] an intensity 17 times larger than the maximum shear-stress in ZPG boundary layers.

Figure 2.14 presents the Reynolds-stress profiles in the outer layer for the APG boundary layer of Skåre & Krogstad [99] and the ZPG boundary layer of Schlatter *et al.* [93], with the locations of the outer edge of the log layer and of the sqrt layer, estimated by curve fitting on the velocity profiles. The figure on the left highlights the outer peak of Reynolds stress for $y/\delta \approx 0.45$ due to the pressure gradient, and indicates that the sqrt layer corresponds

to an increase of turbulence intensity with wall-distance. For the ZPG profiles on the right, turbulence gradually fades beyond the log layer.

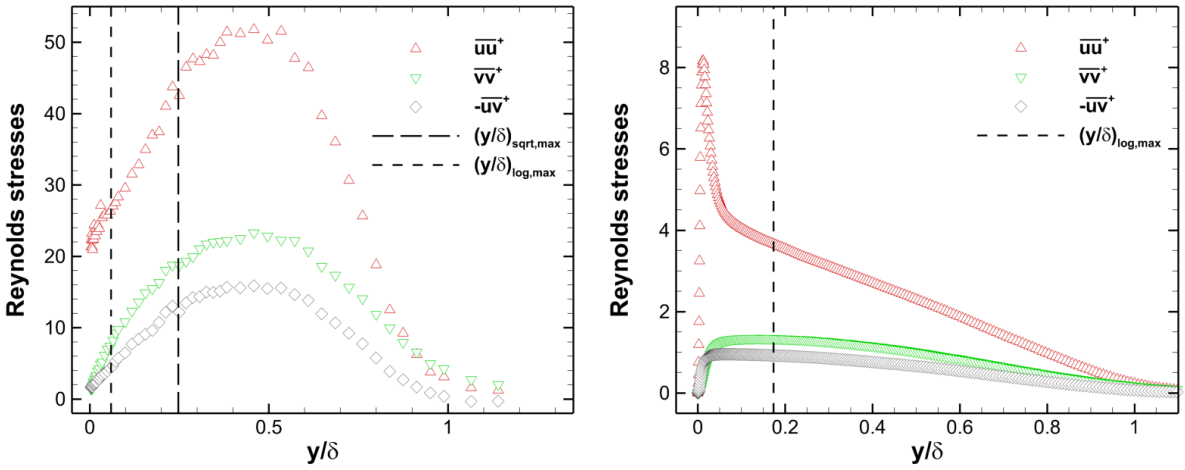

(a) *Skåre & Krogstad experiment [99]* **(b)** *Flat plate DNS (Schlatter* et al. *[93])*

Figure 2.14: *Reynolds stresses in the outer layer*

According to Monty *et al.* [72], the increase in turbulence intensity in the outer layer is due to large-scale structures that grow stronger with the pressure gradient. Harun *et al.* [42] exhibits this phenomenon using a spectral analysis. In particular, Monty *et al.* [72] observed on several experimental data sets ($0 \leqslant \beta_p < 5$) that for a given friction Reynolds number $Re_\tau = u_\tau \delta/\nu$, the peak of turbulence intensity $\overline{uu}^+$ in the buffer layer was only slightly increased with the pressure gradient, whereas the outer peak appeared and grew sharply.

Using three flat plate DNSs with $\beta_p \in \{0, 1, 39\}$, Kitsios [50] noted the same behaviour, adding that the outer peak coincides with a mean streamwise velocity inflection point, indicating that the fluctuations in the outer region are produced by a shear flow instability. According to the author, the growth of the outer peak beyond the height of the inner peak suggests that the boundary layer in APG progressively behaves more like a free shear layer and less like a ZPG boundary layer as the pressure gradient increases.

Bobke *et al.* [8] analysed several flows with different simple history of β_p to show that the heights of both peaks are strongly related to the flow history. In Figure 2.15, the rise of the outer peak in the $\overline{uu}^+$-profile is highlighted by comparing the APG flows studied by Bobke *et al.* [8] to the ZPG flat plate DNS of Schlatter *et al.* [93] at the same Re_τ. The solid lines correspond to (nearly) constant β_p flows and dashed lines to decreasing β_p flows.

The outer peak of turbulent kinetic energy can also be illustrated with its production, defined as the half-trace of the Reynolds-stress production $P_k = \frac{1}{2}P_{ii}$. Figure 2.16 shows the progressive increase in the outer layer of turbulence production rate in inner scaling at $Re_\tau = 670$.

Krogstad & Skåre [57] also point out that the outer peak strongly affects the dissipation rate and the turbulent transport in the outer layer by amplifying them. In particular, they noticed that the turbulent diffusion velocity, defined as

$$v_k = \frac{\frac{1}{2}\left(\overline{u^2 v} + \overline{v^3} + \overline{v w^2}\right)}{k}, \tag{2.54}$$

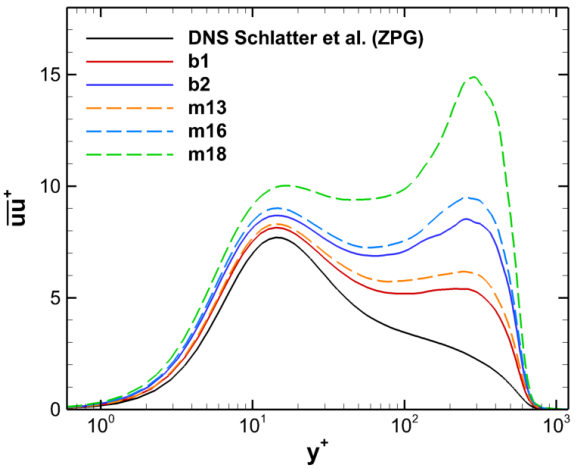

Case	p^+	β_p
Schlatter *et al.*	0	0
b1	0.006	0.9
b2	0.011	2.0
m13	0.006	1.0
m16	0.011	2.1
m18	0.016	3.4

Figure 2.15: *APG effects on* $\overline{u^2}^+$ *at* $Re_\tau = 670$

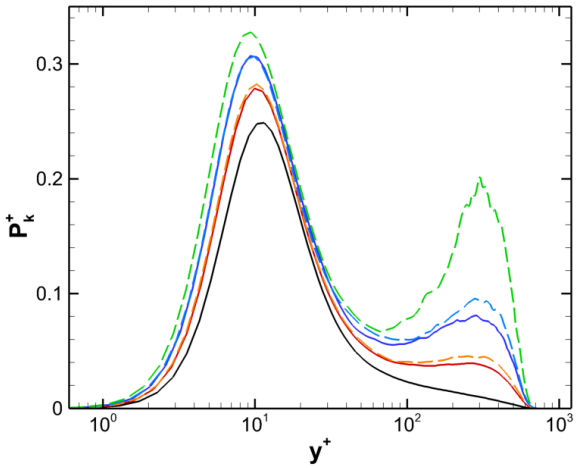

Figure 2.16: *Turbulence production across APG boundary layers (*cf. *Figure 2.15 for legend)*

is considerably negative below the outer peak, and significantly increased beyond, compared to a ZPG boundary layer.

2.4 Conclusions

This chapter has described the boundary layer developing on a solid wall, and the influence of adverse pressure gradients on its canonical ZPG form. In particular, two effects have been presented, the modification of the slope of the log layer in the velocity profile, characterised by Nickels [77], and the formation of a sqrt layer between the log layer and the outer layer, while an outer peak grows in the Reynolds-stress profiles.

To correctly predict APG boundary layers, turbulent models must therefore correctly account for these alterations.

Chapter 3

Turbulence modelling

As discussed in Section 1.3.4, the resolution of the Reynolds-stress tensor in the RANS equations implies many unknown high-order correlations, and complex coupled transport equations. It is therefore necessary to model these equations.

Two classes of turbulence models are presented in this chapter. Eddy-Viscosity Models (EVMs) simplify turbulence down to a single quantity in the momentum equations, the turbulent viscosity, in place of the six Reynolds stresses, to reduce the number of unknown variables and coupled equations, and thus to reduce numerical stiffness. On the contrary, Reynolds-Stress Models (RSMs) aim to accurately render the impact of the Reynolds-stress tensor and its anisotropy on the mean flow.

This chapter also introduces the models considered in this thesis, the one-equation Spalart-Allmaras model and three Reynolds-stress models.

3.1 Eddy-Viscosity Models

To avoid the numerical stiffness of the Reynolds-stress models due to their many coupled variables, the simplest RANS models use an analogy between the molecular random motion, described by the fluid viscosity, and the turbulent effects on the mean flow. Indeed, the turbulent motion diffuses fluid particles across the layers with different momentums, just as the molecular diffusion. Introducing a turbulent viscosity μ_t, also called eddy viscosity, the Boussinesq hypothesis relates the deviatoric part of the Reynolds-stress tensor to the strain-rate tensor

$$\rho\overline{u_i u_j} - \frac{2}{3}\rho k\delta_{ij} = -2\mu_t S_{ij} \tag{3.1}$$

where the contraction $k = \frac{1}{2}\overline{u_i u_i}$ represents the turbulent kinetic energy. Note that in compressible flow, S_{ij} should be replaced by its deviatoric part S_{ij}^D (see Section 1.3.3).

However, Tennekes & Lumley [109] recall that the turbulent viscosity μ_t is only a phenomenological concept and depends on the flow conditions, contrary to the viscosity μ which is a physical property of the fluid. Also, the Boussinesq relation Eq. (3.1) can be criticized because the hypothesis of scale separation needed for the diffusive phenomenon description is not verified[1].

[1] In the case of viscous diffusion, the scale separation is verified with the continuity assumption, *i.e.* a small Knudsen number $Kn = l_{mfp}/L \ll 1$, with l_{mfp} the mean free path of a molecule in the fluid and L the characteristic length scale of the mean flow.

The turbulent viscosity has the dimension of the fluid viscosity. When considering its dynamic definition $\nu_t = \mu_t/\rho$, its dimension is therefore $\mathrm{L}^2\mathrm{T}^{-1}$, which can be described as the product of a turbulent length scale L_{tur} and a turbulent velocity scale U_{tur}

$$\nu_t \sim L_{\text{tur}} \times U_{\text{tur}} \tag{3.2}$$

These scales characterise the mixing process due to the turbulence and allow for an easier physical interpretation.

To model ν_t, Eddy-Viscosity Models (EVMs) can either prescribe these turbulent scales, compute them using algebraic relations, as *e.g.* mixing-length models, or solve them with transport equations. However, the first two classes are limited to specific flow configurations for which they have been calibrated.

Some of the most-common EVMs are described below.

3.1.1 Two-equation models

The two-equation models are designated as *complete*, because they overcome the limitation mentioned above and can be used for all kind of flow configurations. They solve transport equations for two turbulent quantities, from which the turbulent scales L_{tur} and U_{tur} can be formed to compute the turbulent viscosity. They are usually referred to as $k-\phi$ models, where k is the turbulent kinetic energy solved to form the velocity scale $U_{\text{tur}} \sim \sqrt{k}$, and $\phi = k^m \varepsilon^n$ a length-scale providing turbulent quantity, with $\varepsilon = \frac{1}{2}\varepsilon_{ii}$ the dissipation rate. The most common expressions for ϕ are gathered in [62] (Table 9.1). The turbulent viscosity is then given by

$$\mu_t = \rho C_\mu \sqrt[n]{\frac{k^{2n+m}}{\phi}}. \tag{3.3}$$

where C_μ is a constant determined with Bradshaw's hypothesis [10], assuming the shear-stress proportional to the turbulent kinetic energy in equilibrium shear layers

$$-\overline{uv} = a_1 k, \qquad a_1 = \sqrt{C_\mu} \approx 0.3 \tag{3.4}$$

The k-equation

The k-equation comes as a simplification of the Reynolds-stress transport equations Eq. (1.28). Indeed, taking half the trace of this equation system yields

$$\rho \frac{\mathrm{D}k}{\mathrm{D}t} = \rho P_k + \rho \phi_k^* + \frac{\partial}{\partial x_j}\left(\mu \frac{\partial k}{\partial x_j}\right) - \frac{\partial \rho \overline{u_j u_i u_i}}{\partial x_j} - \rho\varepsilon \tag{3.5}$$

where

$$P_k = \frac{1}{2}P_{ii} = -\overline{u_i u_j}\frac{\partial U_i}{\partial x_j}, \qquad \rho\phi_k^* \equiv \rho D_k^p = -\frac{\partial \overline{u_j p}}{\partial x_j}, \qquad \varepsilon = \frac{1}{2}\varepsilon_{ii}.$$

It can be noted the velocity pressure-gradient correlation ϕ_k^* reduces to the pressure diffusion term, as the pressure strain-rate correlation is traceless by definition.

The Reynolds stresses in the production of turbulent kinetic energy P_k are replaced by applying the Boussinesq relation

$$P_k = 2\nu_t S_{ij} S_{ij}, \tag{3.6}$$

while the turbulent and pressure diffusion are modelled together with a Simple Gradient Diffusion Hypothesis (SGDH), by analogy with the molecular diffusion

$$-\frac{\partial}{\partial x_j}\left(\rho\overline{u_j u_i u_i} + \overline{u_j p}\right) = \frac{\partial}{\partial x_j}\left(\frac{\mu_t}{\sigma_k}\frac{\partial k}{\partial x_j}\right). \tag{3.7}$$

The Schmidt number σ_k is usually taken equal to one. The dissipation rate of the turbulent kinetic energy ε is modelled with the length-scale providing equation.

The modelled equation for k becomes

$$\rho\frac{\mathrm{D}k}{\mathrm{D}t} = \rho P_k - \rho\varepsilon + \frac{\partial}{\partial x_j}\left[\left(\mu + \frac{\mu_t}{\sigma_k}\right)\frac{\partial k}{\partial x_j}\right] \tag{3.8}$$

The $k-\varepsilon$ model

The dissipation rate ε, given by Eq. (1.32), is often solved as the second turbulent quantity to form the turbulent length scale. However, the term-by-term modelling of this equation is quite difficult due to the lack of data available for its calibration and to the complexity of the physics involved. It is therefore simplified using a form similar to Eq. (3.8)

$$\rho\frac{\mathrm{D}\varepsilon}{\mathrm{D}t} = C_{\varepsilon 1}\rho P_k\frac{\varepsilon}{k} - C_{\varepsilon 2}\rho\frac{\varepsilon^2}{k} + \frac{\partial}{\partial x_j}\left[\left(\mu + \frac{\mu_t}{\sigma_\varepsilon}\right)\frac{\partial \varepsilon}{\partial x_j}\right]. \tag{3.9}$$

Leschziner [62] provides a correspondence between the exact terms in Eq. (1.32) and the terms in Eq. (3.9).

The constant $C_{\varepsilon 2}$ is calibrated with the study of the decay of the homogeneous and isotropic turbulence generated by a grid, for which Eq. (3.9) reduces to the dissipation term of ε and the unsteady term. The constant $C_{\varepsilon 1}$ is then tuned to correctly predict the turbulence growth rate in an homogeneous shear flow, with the constraint that $C_{\varepsilon 2} > C_{\varepsilon 1}$. Eventually, the constant σ_ε is adjusted to return the correct log-law region, yielding

$$\sigma_\varepsilon = \frac{\kappa_0^2}{(C_{\varepsilon 2} - C_{\varepsilon 1})\sqrt{C_\mu}}. \tag{3.10}$$

An exhaustive description of the calibration process can be found in [83, 62].

At the wall, convection and turbulent shear-stress become negligible, so that the k-equation (3.8) simplifies into

$$\varepsilon_0 = \nu\left.\frac{\partial^2 k}{\partial y^2}\right|_{y=0}. \tag{3.11}$$

Due to the numerical difficulty to correctly enforce a second-order derivative at the wall, this boundary condition is usually replaced by asymptotic equivalences

$$\varepsilon_0 = 2\nu\left(\left.\frac{\partial\sqrt{k}}{\partial y}\right|_{y=0}\right)^2 \qquad \text{or} \qquad \varepsilon_0 = 2\nu\lim_{y\to 0}\frac{k}{y^2} \tag{3.12}$$

The dependence on k motivated some models to rather solve the so-called isotropic form [62], or reduced form, $\widetilde{\varepsilon} = \varepsilon - \partial_j\left(\nu\partial_j k\right)$, which vanishes at the wall, while recovering to ε outside the viscous sublayer.

Nevertheless, the basic form of the $k-\varepsilon$ model does not behave correctly in the near-wall region, as turbulence cannot be assumed isotropic anymore, leading to the development of many near-wall extensions to account for the increased turbulence dissipation in the buffer layer and the selective damping of the velocity scale due to a two-component turbulence at the wall. This is done by using damping functions f_μ for μ_t and $f_{\varepsilon 2}$ for the destruction of ε (*e.g.* Launder & Sharma [59]), and for some models amplifying functions $f_{\varepsilon 1}$ for the production of ε or extra source terms (*e.g.* Chien [20]). Further variants are detailed in [62].

The general $k-\phi$ model

The transport equation for the general length-scale providing variable $\phi = k^m \varepsilon^n$ can be derived by combining Eqs. (3.8) & (3.9) and yields

$$\begin{aligned}\rho\frac{\mathrm{D}\phi}{\mathrm{D}t} = {} & C_{\phi 1}\rho P_k\frac{\phi}{k} - C_{\phi 2}\rho\varepsilon\frac{\phi}{k} + \frac{\partial}{\partial x_j}\left[\left(\mu+\frac{\mu_t}{\sigma_\phi}\right)\frac{\partial\phi}{\partial x_j} + \frac{\mu_t}{\sigma_{\phi k}}\frac{\phi}{k}\frac{\partial k}{\partial x_j}\right] \\ & + C_{kk}\frac{\mu_t\phi}{k^2}\frac{\partial k}{\partial x_j}\frac{\partial k}{\partial x_j} + C_{k\phi}\frac{\mu_t}{k}\frac{\partial k}{\partial x_j}\frac{\partial\phi}{\partial x_j} + C_{\phi\phi}\frac{\mu_t}{\phi}\frac{\partial\phi}{\partial x_j}\frac{\partial\phi}{\partial x_j} \\ & + C_{kk}^{\mathrm{visc}}\frac{\mu\phi}{k^2}\frac{\partial k}{\partial x_j}\frac{\partial k}{\partial x_j} + C_{k\phi}^{\mathrm{visc}}\frac{\mu}{k}\frac{\partial k}{\partial x_j}\frac{\partial\phi}{\partial x_j} + C_{\phi\phi}^{\mathrm{visc}}\frac{\mu}{\phi}\frac{\partial\phi}{\partial x_j}\frac{\partial\phi}{\partial x_j}\end{aligned} \tag{3.13}$$

where the new model constants are functions of m, n and the $k-\varepsilon$ model constants. Detailed expressions of these constants can be found in [11, 43].

Therefore, the conversion from ε to ϕ introduces in Eq. (3.13) an additional diffusion term with $\sigma_{\phi k}$ on the first line and cross-diffusion terms on the second and third lines. The absence or the modification of these terms is the reason for $k-\phi$ models to behave differently from the $k-\varepsilon$ model.

In particular, the viscous cross-diffusion terms on the third line in Eq. (3.13) are almost always neglected, as they lead to stiff boundary conditions. Similarly, the additional diffusion term, which is a second-order derivative of k, is neglected to prevent numerical instability.

However, some cross-diffusion terms must necessarily be kept to ensure the physical behaviour of the model. Indeed, the log-law calibration Eq. (3.10) becomes

$$\sigma_\phi = \left(\frac{(C_{\phi 2}-C_{\phi 1})\sqrt{C_\mu}}{\kappa_0^2 n^2} - C_{\phi\phi}\right)^{-1}, \tag{3.14}$$

and the conversion yields $C_{\phi 2}-C_{\phi 1} = n\,(C_{\varepsilon 2}-C_{\varepsilon 1})$. Without the $C_{\phi\phi}$ cross-diffusion term, the turbulent transport constant σ_ϕ has the sign of n. Hence, $k-\phi$ models with $n<0$ must be defined with $C_{\phi\phi}<0$ to ensure $\sigma_\phi>0$ and a physical consistency.

Alternatively, the ϕ-equation can be defined independently of the $k-\varepsilon$ model, on the format of Eqs. (3.8) & (3.9), *i.e.* without any additional or cross-diffusion term. In that case, the model constants $C_{\phi 1}$ and $C_{\phi 2}$ are calibrated with the constraint $C_{\phi 2}>C_{\phi 1}$, regardless of the sign of n (see *e.g.* the $k-kl$ model of Adbol-Hamid [1], based on Rotta's formulation [90]).

The $k-\omega$ model

The widely used alternative to the $k-\varepsilon$ forms the turbulent length-scale using the specific dissipation rate[2] $\omega = \varepsilon/(C_\mu k)$. First suggested by Kolmogorov [56], the version formulated by Wilcox [119] gained in popularity due to its improved behaviour in the near-wall region, especially in APG boundary layers. Expecting a universal log-region, Huang & Bradshaw [45] justify this improved behaviour from the mathematical consistency of the ω-equation with an unchanged von Kármán constant κ_0 for a small perturbation of the shear-stress Eq. (2.44), $-\overline{uv} = 1 + p^+ y^+$, with $p^+ y^+ \ll 1$. This will be further discussed in Section 5.1.1.

The $k-\omega$ model differs from the $k-\varepsilon$ model due to the absence of all or most of the cross-diffusion terms in Eq. (3.13). For instance, the Wilcox 1988 model [119] is written without extra-terms in the ω-equation. To prevent the strong dependence of the model on the free-stream turbulence value, the author thus proposed in his 2006 model [120] to add a corrective cross-diffusion term. Alternatively, Menter [71] suggested to blend the Wilcox 1988 $k-\omega$ model in the near-wall region with the Standard $k-\varepsilon$ model [59] far from the wall to combine the good properties of both models. As it is written using the ω formalism, the second equation in Menter's BSL (BaSeLine) $k-\omega$ model is expressed by

$$\rho\frac{\mathrm{D}\omega}{\mathrm{D}t} = \alpha\rho P_k\frac{\omega}{k} - \beta\rho\omega^2 + \frac{\partial}{\partial x_j}\left[\left(\mu + \mu_t\sigma^*\right)\frac{\partial\omega}{\partial x_j}\right] + \rho\frac{\sigma_d}{\omega}\frac{\partial k}{\partial x_j}\frac{\partial\omega}{\partial x_j} \tag{3.15}$$

where the introduced cross-diffusion term results from the conversion from the Standard $k-\varepsilon$ model and disappears in the inner region of the boundary layer. The corresponding constant set is given in Table 3.1. Note that in Wilcox's notation, $\sigma = 1/\sigma_k$ and $\sigma^* = 1/\sigma_\omega$.

Table 3.1: *BSL $k-\omega$ model constants*

	α	β	β^*	σ	σ^*	κ_0	σ_d
Inner	5/9	0.0750	0.09	0.5	0.5	0.41	0
Outer	0.44	0.0828	0.09	1	0.856	0.41	$2\sigma^{*(\varepsilon)}$

To switch between the inner and outer models, the model constants are blended according to

$$c = F_1\, c^{(\omega)} + (1 - F_1)\; c^{(\varepsilon)} \tag{3.16}$$

where F_1 is the baseline function, going from one at the wall to zero in the free-stream region. It is defined as

$$F_1 = \tanh\left(\arg_1^4\right) \tag{3.17}$$

with

$$\arg_1 = \min\left[\max\left(\frac{\sqrt{k}}{\beta^*\omega d}; \frac{500\mu}{\rho\omega d^2}\right); \frac{4\sigma^{*(\varepsilon)}k}{\mathrm{CD}_{k\omega}\, d^2}\right], \tag{3.18}$$

$$\mathrm{CD}_{k\omega} = \max\left(\frac{2\sigma^{*(\varepsilon)}}{\omega}\frac{\partial k}{\partial x_j}\frac{\partial\omega}{\partial x_j}; 10^{-20}\right). \tag{3.19}$$

[2] the definition used by Wilcox is here used instead of $\omega = \varepsilon/k$

Menter further improved this model to yield the SST (Shear-Stress-Transport) model detailed in [71], which adds a correction in the turbulent viscosity expression to limit the strain-rate in accordance with Bradshaw's relation (3.4) and prevent the overprediction of the shear-stress. The inner model constants are slightly recalibrated.

The drawback of $k-\omega$ models comes from its boundary condition, since ω tends to infinity at the wall. Wilcox suggests to enforce the correct asymptotic behaviour on the closest points to the wall

$$\omega = \frac{6\nu}{\beta d^2}, \qquad y^+ < 2.5 \tag{3.20}$$

Menter [71] simplified this condition to a Dirichlet boundary condition at the wall

$$\omega_0 = 10\frac{6\nu}{\beta\left(\Delta y_1\right)^2} \tag{3.21}$$

where Δy_1 is the distance to the next point away from the wall, and correctly reproduced the wall behaviour as long as $\Delta y_1^+ < 3$.

The $k-kl$ model

To further improve the behaviour of two-equation models, Daris [25] proposed a $k-kl$ model, at the conclusion of a general study with $k-\phi$ models. In particular, the model has been designed with constraints on the coefficients to reproduce the behaviour in APG boundary layers, in both log and sqrt layers, as further discussed in Sections 5.1.1 & 6.1.1. The equation for $\phi \equiv kl$, $\{m,n\} = \{1, {}^{-5}/_{2}\}$, is written

$$\begin{aligned}\rho\frac{\mathrm{D}kl}{\mathrm{D}t} = {} & C_{kl1}\rho P_k\frac{kl}{k} - C_{kl2}\rho k^{3/2} + \frac{\partial}{\partial x_j}\left[\left(\mu + \frac{\mu_t}{\sigma_{kl}}\right)\frac{\partial kl}{\partial x_j}\right] \\ & + C_{kk}\frac{\mu_t kl}{k^2}\frac{\partial k}{\partial x_j}\frac{\partial k}{\partial x_j} + C_{k\,kl}\frac{\mu_t}{k}\frac{\partial k}{\partial x_j}\frac{\partial kl}{\partial x_j} + C_{kl\,kl}\frac{\mu_t}{kl}\frac{\partial kl}{\partial x_j}\frac{\partial kl}{\partial x_j}.\end{aligned} \tag{3.22}$$

3.1.2 The Spalart-Allmaras model

The Spalart-Allmaras model is one of the most widely used models in aerodynamics for the good trade-off accuracy/cost it offers. It is also one of the few EVMs able to reproduce a fair approximation of the sqrt-law behaviour according to Catris [15] and Catris & Aupoix [16].

Proposed by Spalart & Allmaras [104], it directly transports the turbulent viscosity with an equation build empirically. Based on the general expression of a transport equation, the model is defined with dimensional analysis and Galilean invariance arguments, and calibrated with a selection of experiments to isolate the terms of the equation.

More precisely, the model transports a modified turbulent viscosity $\widehat{\nu}$ for which the log-law behaviour extends to the wall, resulting in the following equation

$$\frac{\mathrm{D}\widehat{\nu}}{\mathrm{D}t} = c_{b1}\widehat{S}\widehat{\nu} - c_{w1}f_w\left(\frac{\widehat{\nu}}{d}\right)^2 + \frac{1}{\sigma}\left[\frac{\partial}{\partial x_j}\left(\left(\nu+\widehat{\nu}\right)\frac{\partial\widehat{\nu}}{\partial x_j}\right) + c_{b2}\frac{\partial\widehat{\nu}}{\partial x_j}\frac{\partial\widehat{\nu}}{\partial x_j}\right] \tag{3.23}$$

where d is the distance to the closest wall. The viscous sublayer behaviour of the turbulent viscosity is then retrieved with $\nu_t = f_{v1}\widehat{\nu}$. The strain-rate is also altered in the near-wall

region

$$\widehat{S} = \max\left[\sqrt{2\Omega_{ij}\Omega_{ij}} + \frac{\widehat{\nu} f_{v2}}{(\kappa_0 d)^2}\,;\, 0\right], \qquad \Omega_{ij} = \frac{1}{2}\left(\frac{\partial U_i}{\partial x_j} - \frac{\partial U_j}{\partial x_i}\right) \tag{3.24}$$

The damping functions of the two near-wall alterations are given by

$$f_{v1} = \frac{\chi^3}{\chi^3 + c_{v1}^3}, \qquad f_{v2} = 1 - \frac{\chi}{1 + f_{v1}\chi} \qquad \text{with} \qquad \chi = \frac{\widehat{\nu}}{\nu} \tag{3.25}$$

Similarly to the constraint Eq. (3.10), the destruction is calibrated to reproduce the log-region with $\kappa_0 = 0.41$

$$c_{w1} = \frac{c_{b1}}{\kappa_0^2} + \frac{1 + c_{b2}}{\sigma} \tag{3.26}$$

Finally the destruction term is also damped according to

$$f_w = \left[\frac{1 + c_{w3}^6}{1 + \left(\frac{c_{w3}}{g}\right)^6}\right]^{1/6}, \qquad g = r + c_{w2}\left(r^6 - r\right), \qquad r = \frac{\widehat{\nu}}{\widehat{S}\,(\kappa_0 d)^2} \tag{3.27}$$

All the constants of the model are gathered in Table 3.2.

Table 3.2: *Spalart-Allmaras model constants*

c_{b1}	c_{b2}	c_{v1}	c_{w2}	c_{w3}	σ
0.1355	0.622	7.1	0.3	2	2/3

Many variants of this model have been developed to address some limitations of the original model and can be found on NASA's Turbulence Modeling Resource website[3]. For example, the Spalart-Allmaras RC model [98] provides a correction for rotating and curved flow by multiplying the production term with a rotation function.

Another widely used correction is the Quadratic Constitutive Relation (QCR) [102, 91], initially developed with the Spalart-Allmaras model but applicable to any EVM. This correction completes the linear Boussinesq relation Eq. (3.1) with nonlinear terms to improve the prediction of anisotropy in corner flows, *e.g.* at the wing and fuselage junction. The first version of the QCR [102] reads

$$\tau_{ij}^{QCR} = \tau_{ij} - C_{cr1}\left(O_{ik}\tau_{jk} + O_{jk}\tau_{ik}\right) \tag{3.28}$$

where $\tau_{ij} = \rho\overline{u_i u_j}$ is the Reynolds-stress tensor as computed from the Boussinesq relation and O_{ij} is a normalized rotation tensor defined as

$$O_{ij} = \frac{2\Omega_{ij}}{\sqrt{\partial_l U_m \partial_l U_m}} \tag{3.29}$$

The latest version [91] adds a term in Eq. (3.28) to account for the $^{-2}/_3\, k\delta_{ij}$ term in Eq. (3.1) and replaces the constants C_{cr1} and C_{cr2} with variable parameters, distinguishing a near-wall constant set.

[3] https://turbmodels.larc.nasa.gov/spalart.html

3.2 Reynolds-Stress Models

The second-moment closures of the RANS equations, called Reynolds-Stress Models (RSM), directly solve the transport equations for the Reynolds stresses to avoid simplifying hypotheses like the Boussinesq relation and to dispense with most corrections (SST, rotating flows, QCR). The anisotropy of turbulence is implicitly rendered by modelling the turbulence in all directions independently. Moreover, the mean flow equations are exactly solved due to the absence of the eddy viscosity.

The modelling of the three unclosed terms in the Reynolds-stress transport equations, indicated in Section 1.3.4, is detailed in the following sections.

3.2.1 Pressure term modelling

The pressure term ϕ^*_{ij} must be carefully modelled. Indeed, the shear-stress $\overline{uv}$ driving the turbulence in the boundary layer is produced by the wall-normal stress $\overline{v^2}$, but the latter has no production rate itself: it is generated by the redistribution of energy from the other Reynolds stresses.

To model ϕ^*_{ij}, it is decomposed into the pressure diffusion D^p_{ij} and the redistribution ϕ_{ij}. The pressure diffusion is only significant in the near-wall region and is usually modelled with the turbulent transport term D^T_{ij}, as for the k-equation in EVMs. The redistributive part ϕ_{ij} can be of the same order as production. It is modelled starting from the fluctuating pressure Poisson equation, obtained by taking the divergence of the Navier-Stokes equations

$$\nabla^2 p = -2\rho \frac{\partial U_i}{\partial x_j}\frac{\partial u_j}{\partial x_i} - \rho \frac{\partial^2}{\partial x_i \partial x_j}\left(u_i u_j - \overline{u_i u_j}\right) \tag{3.30}$$

which yields for an integration domain Ω of border $\partial\Omega$

$$p(\underline{\mathbf{x}}) = \int_\Omega \frac{\nabla^2 p(\underline{\tilde{\mathbf{x}}})}{4\pi \left\|\underline{\tilde{\mathbf{x}}} - \underline{\mathbf{x}}\right\|} \,\mathrm{dv}(\underline{\tilde{\mathbf{x}}}) - \int_{\partial\Omega} \left[p(\underline{\tilde{\mathbf{x}}}) \frac{\partial}{\partial \underline{\tilde{\mathbf{n}}}} \left(\frac{1}{4\pi \left\|\underline{\tilde{\mathbf{x}}} - \underline{\mathbf{x}}\right\|} \right) - \frac{\partial p(\underline{\tilde{\mathbf{x}}})}{\partial \underline{\mathbf{n}}} \frac{1}{4\pi \left\|\underline{\tilde{\mathbf{x}}} - \underline{\mathbf{x}}\right\|} \right] \mathrm{ds}(\underline{\tilde{\mathbf{x}}}). \tag{3.31}$$

From this, it comes

$$\begin{aligned} \rho\phi_{ij}(\underline{\mathbf{x}}) = &- \int_\Omega \frac{2\overline{\nabla^2 p(\underline{\tilde{\mathbf{x}}}) s_{ij}(\underline{\mathbf{x}})}}{4\pi \left\|\underline{\tilde{\mathbf{x}}} - \underline{\mathbf{x}}\right\|} \,\mathrm{dv}(\underline{\tilde{\mathbf{x}}}) \\ &- \int_{\partial\Omega} 2\overline{p(\underline{\tilde{\mathbf{x}}}) s_{ij}(\underline{\mathbf{x}})} \frac{\partial}{\partial \underline{\tilde{\mathbf{n}}}} \left(\frac{1}{4\pi \left\|\underline{\tilde{\mathbf{x}}} - \underline{\mathbf{x}}\right\|} \right) \mathrm{ds}(\underline{\tilde{\mathbf{x}}}) \\ &+ \int_{\partial\Omega} 2\overline{\frac{\partial p(\underline{\tilde{\mathbf{x}}})}{\partial \underline{\mathbf{n}}} s_{ij}(\underline{\mathbf{x}})} \frac{\mathrm{ds}(\underline{\tilde{\mathbf{x}}})}{4\pi \left\|\underline{\tilde{\mathbf{x}}} - \underline{\mathbf{x}}\right\|}. \end{aligned} \tag{3.32}$$

The volume integral can be split using the Laplacian of the pressure in Eq. (3.30), yielding

$$\phi^1_{ij} = \int_\Omega \overline{\frac{\partial^2 u_l u_m}{\partial x_l \partial x_m}(\underline{\tilde{\mathbf{x}}}) s_{ij}(\underline{\mathbf{x}})} \frac{\mathrm{dv}(\underline{\tilde{\mathbf{x}}})}{2\pi \left\|\underline{\tilde{\mathbf{x}}} - \underline{\mathbf{x}}\right\|}, \tag{3.33}$$

$$\phi^2_{ij} = \int_\Omega \frac{\partial U_l}{\partial x_m}(\underline{\tilde{\mathbf{x}}}) \overline{\frac{\partial u_m}{\partial x_l}(\underline{\tilde{\mathbf{x}}}) s_{ij}(\underline{\mathbf{x}})} \frac{\mathrm{dv}(\underline{\tilde{\mathbf{x}}})}{\pi \left\|\underline{\tilde{\mathbf{x}}} - \underline{\mathbf{x}}\right\|}. \tag{3.34}$$

The terms ϕ^1_{ij} and ϕ^2_{ij} are respectively called the slow part and the rapid part. Indeed, while the latter instantaneously reacts to a sudden mean-flow gradient by affecting the

turbulence, the former only steps in indirectly, reacting to the resulting anisotropy of the turbulence. The surface integrals in Eq. (3.32) represent the wall-echo terms, due to the reflection of the pressure fluctuations on the solid wall, and can be neglected far from the walls[4].

From Eqs. (3.33) & (3.34), it can be noticed that both redistribution terms are non-local, *i.e.* they depend on the whole fluid domain. Nevertheless, they are both modelled locally, *i.e.* it is assumed that the integral can be modelled as a function of quantities taken in $\underline{\mathbf{x}}$ only.

Model for the slow part ϕ_{ij}^1

The experience of an homogeneous turbulence field initially anisotropic decaying in time shows that the turbulence tends to an isotropic state as it decays. In this case, the Reynolds-stress transport equations simplify into

$$\frac{\partial \overline{u_i u_j}}{\partial t} = \phi_{ij}^1 - \varepsilon_{ij}, \tag{3.35}$$

and it can be deduced that both ϕ_{ij}^1 and dissipation take part in the return to isotropy, the latter being also responsible for the turbulence energy decay. Decomposing the dissipation as $\varepsilon_{ij} = \varepsilon_{ij}^D + \frac{2}{3}\varepsilon\delta_{ij}$, the deviatoric part ε_{ij}^D which is affecting the anisotropy of the turbulence field is modelled alongside with ϕ_{ij}^1, as the whole return-to-isotropy term.

A simple model has been proposed by Rotta [90] considering the turbulence tends to isotropy with a constant rate:

$$\phi_{ij}^1 = -C_1 \frac{1}{T}\left(\overline{u_i u_j} - \frac{2}{3}k\delta_{ij}\right) = -C_1 \varepsilon a_{ij} \tag{3.36}$$

with $C_1 = 1.8$, $T = k/\varepsilon$ the turbulent time scale and $a_{ij} = \frac{\overline{u_i u_j}}{k} - \frac{2}{3}\delta_{ij}$ the turbulence anisotropy tensor. Other models introduce non-linearities in order to take into account the resistance of ϕ_{ij}^1 to strong anisotropy. A more general expression for the slow part is therefore written

$$\phi_{ij}^1 = -C_1 \varepsilon a_{ij} + C_2 \varepsilon \left(a_{ik}a_{kj} - \frac{1}{3}A_2\delta_{ij}\right), \tag{3.37}$$

where the coefficients C_1 and C_2 can depend on the turbulent Reynolds number Re_T and on the second and third invariants of the anisotropy tensor, $A_2 = a_{ij}a_{ji}$ and $A_3 = a_{ij}a_{jk}a_{ki}$ respectively. The model of Speziale *et al.* [107], for example, uses the constants $C_1 = 1.7$ and $C_2 = 1.05$.

Model for the rapid part ϕ_{ij}^2

The rapid part of the redistribution arises from a distortion of the mean flow. In the particular case of rapid distortion, the turbulence is mainly affected by the mean velocity gradient and the Reynolds-stress transport equations reduce to

$$\frac{\partial \overline{u_i u_j}}{\partial t} = P_{ij} + \phi_{ij}^2. \tag{3.38}$$

[4] They must however be taken into account in near-wall models

It is experimentally observed that ϕ_{ij}^2 partially counteracts the increase of anisotropy due to production.

The rapid part modelling relies on the quasi-homogeneity hypothesis for the mean flow. This allows to consider the mean velocity gradient independent of the integration point and therefore, to simplify Eq. (3.34) by taking it out of the integral. The modelling then focuses on a fourth-order tensor A_{ijkl} such that

$$\phi_{ij}^2 = \frac{\partial U_k}{\partial x_l} \left(A_{ijkl} + A_{jikl} \right). \tag{3.39}$$

The IP (isotropisation of production) model, introduced by Naot *et al.* [76], stands as the simplest model for ϕ_{ij}^2 and reads

$$\phi_{ij}^2 = -C_2 \left(P_{ij} - \frac{2}{3} P_k \delta_{ij} \right), \tag{3.40}$$

to partially balance the anisotropy of the production tensor. Using the Caley-Hamilton theorem to limit the expansion of A_{ijkl}, it has been shown [40] that the general expression for the rapid part of the redistribution is

$$\begin{aligned} \phi_{ij}^2 = \; & C_1^* P_k a_{ij} + C_3 k S_{ij} \\ & + C_4 k \left(a_{il} S_{jl} + a_{jl} S_{il} - \frac{2}{3} a_{mn} S_{mn} \delta_{ij} \right) \\ & + C_5 k \left(a_{il} \Omega_{jl} + a_{jl} \Omega_{il} \right) \\ & + C_6 k \left(a_{il} a_{lm} S_{jm} + a_{jl} a_{lm} S_{im} - 2 a_{lj} a_{mi} S_{lm} - 3 a_{ij} a_{ml} S_{ml} \right) \\ & + C_7 k \left(a_{il} a_{lm} \Omega_{jm} + a_{jl} a_{lm} \Omega_{im} \right) \\ & + C_8 k \left[a_{mn} a_{mn} \left(a_{il} \Omega_{jl} + a_{jl} \Omega_{il} \right) + \frac{3}{2} a_{mi} a_{nj} \left(a_{ml} \Omega_{nl} + a_{nl} \Omega_{ml} \right) \right] \end{aligned} \tag{3.41}$$

where $S_{ij} = \frac{1}{2} \left(\partial_j U_i + \partial_i U_j \right)$ and $\Omega_{ij} = \frac{1}{2} \left(\partial_j U_i - \partial_i U_j \right)$ are the mean strain-rate tensor and the mean rotation tensor respectively. The constants are then chosen in order to respect some mathematical constraints, such as the realisability[5].

Amongst the most popular models, both the LRR model (Launder *et al.* [58], for which the rapid part corresponds to the IP model Eq. (3.40)) and the SSG model (Speziale *et al.* [107]) restrain Eq. (3.41) to its linear terms, *i.e.* $C_6 = C_7 = C_8 = 0$, the SSG introducing non-linearities directly into the C_3 constant through the second invariant of the anisotropy tensor. Table 3.3 gathers the constants of these models. Note however that these two models have been calibrated on experimental, numerical and theoretical data rather than on realisability criteria.

Near-wall model

The decomposition of the redistribution ϕ_{ij} modelled above does not apply when considering the turbulence in the vicinity of solid walls. Indeed, the surface integrals in Eq. (3.32) can no longer be neglected any more, the assumptions of quasi-homogeneity and locality are no longer valid and the pressure diffusion D_{ij}^p can no longer be modelled with the turbulent transport D_{ij}^T, see for instance Manceau [67].

[5] Realisability refers to a physically acceptable state, which requires the Reynolds-stress tensor to be positive semidefinite

Table 3.3: *Constants sets for the ϕ_{ij}^2 model*

	C_1^*	C_3	C_4	C_5	c_2
LRR	0	0.8	$\frac{9c_2+6}{11}$	$\frac{-7c_2+10}{11}$	0.52
SSG	0.9	$0.8-0.625\sqrt{A_2}$	0.625	0.2	

It has been experimentally observed that the wall presence damps the redistribution of the turbulent energy from the streamwise component $\overline{u^2}$ towards the others. Launder *et al.* [58] explained this behaviour with the phenomenon of wall-echo, which is caused by the reflection of the pressure fluctuations on the solid boundary.

However, according to Manceau [66], the wall-echo leads on the contrary to an amplification of the redistribution, the overall damping being due to the blocking effect of the wall. Near a solid boundary, its impermeability imposes a damping that applies as much to the wall-normal velocity fluctuation v as to the mean value V, in particular $v=0$ at the wall. Added to the adherence conditions ($u=w=0$), the impermeability condition simplifies the continuity equation to the constraint $\partial_y v = 0$. Considering a Taylor-series expansion of the Reynolds stresses, these conditions translate into

$$\overline{u^2} \sim y^2, \qquad \overline{v^2} \sim y^4, \qquad \overline{w^2} \sim y^2. \tag{3.42}$$

Thus, the wall-normal velocity fluctuation is strongly damped compared to the wall-parallel components, leading to a two-component turbulence near the wall.

The pressure intervenes here to redirect immediately any wall-normal fluctuation that is blocked towards the tangential components.

To account for the near-wall damping, several models add corrective terms, referred to as 'wall-echo terms', for instance those proposed by Gibson & Launder [36]

$$\phi_{ij}^{1p} = C_1^p \frac{\varepsilon}{k}\left(\overline{u_l u_m} n_l n_m \delta_{ij} - \frac{3}{2}\left(\overline{u_l u_i} n_l n_j + \overline{u_l u_j} n_l n_i\right)\right) f\left(\frac{\ell}{d}\right) \tag{3.43a}$$

$$\phi_{ij}^{2p} = C_2^p \frac{\varepsilon}{k}\left(\phi_{lm}^2 n_l n_m \delta_{ij} - \frac{3}{2}\left(\phi_{li}^2 n_l n_j + \phi_{lj}^2 n_l n_i\right)\right) f\left(\frac{\ell}{d}\right) \tag{3.43b}$$

where $\underline{\mathbf{n}}$ is the local wall-normal unit vector, $\ell = k^{3/2}/\varepsilon$ is the integral turbulent length-scale, d is the distance to the wall, and f is defined so that $f=1$ in the log-law region and $f=0$ in a free-stream region.

However, these corrective terms are not sufficient to correctly predict the asymptotic behaviour of the near-wall redistribution, and are then coupled with damping functions dependent on the wall-distance, the turbulent Reynolds number and/or the anisotropy tensor invariants.

In order to closely match the asymptotic behaviour at the wall, Manceau & Hanjalić [69] introduced a new model for the whole redistribution term, valid in the viscous sublayer

$$\phi_{ij}^{w} = -5\frac{\varepsilon}{k}\left(\overline{u_i u_l} n_j n_l + \overline{u_j u_l} n_i n_l - \frac{1}{2}\overline{u_l u_m} n_l n_m \left(n_i n_j + \delta_{ij}\right)\right), \tag{3.44}$$

To switch from this near-wall model to the slow and rapid part modelling described above, the redistribution term uses a blending function, presented in Section 3.2.4.

3.2.2 Turbulent transport modelling

Instead of deriving equations for the triple velocity correlations, the turbulent transport is usually modelled with the Generalised Gradient Diffusion Hypothesis (GGDH) from Daly & Harlow [24]

$$\rho D_{ij}^T = -\frac{\partial}{\partial x_l}\left(C_s \rho \frac{k}{\varepsilon}\overline{u_l u_m}\frac{\partial \overline{u_i u_j}}{\partial x_m}\right). \tag{3.45}$$

To ensure the symmetry of the term, Hanjalić & Launder [41] suggested as an alternative

$$\rho D_{ij}^T = -\frac{\partial}{\partial x_l}\left(C_s \rho \frac{k}{\varepsilon}\left(\overline{u_i u_m}\frac{\partial \overline{u_j u_l}}{\partial x_m} + \overline{u_j u_m}\frac{\partial \overline{u_i u_l}}{\partial x_m} + \overline{u_l u_m}\frac{\partial \overline{u_i u_j}}{\partial x_m}\right)\right). \tag{3.46}$$

However, it does not significantly improve the results compared to Eq. (3.45) while introducing more terms, explaining why the GGDH prevails in industrial and commercial codes [62].

On the contrary, some RSMs aim to simplify and to reduce numerical stiffness. In that case, they rely on the Simple Gradient Diffusion Hypothesis (SGDH)

$$\rho D_{ij}^T = -\frac{\partial}{\partial x_m}\left(D_{\text{SGDH}}\ \mu_t \frac{\partial \overline{u_i u_j}}{\partial x_m}\right). \tag{3.47}$$

which assumes an isotropic turbulence in the boundary layer.

3.2.3 Dissipation rate modelling

As the deviatoric contribution of the dissipation rate ε_{ij}^D is already modelled with the slow part of pressure term ϕ_{ij}^1, the dissipation rate is only modelled with its isotropic part

$$\varepsilon_{ij} = \frac{2}{3}\varepsilon\delta_{ij}. \tag{3.48}$$

Reynolds-stress Models still need an expression for ε. This is done by adding a length-scale providing transport equation as Eq. (3.13) from the two-equation eddy-viscosity models, usually an equation for ε directly.

In the near-wall region, the dissipation rate ε_{ij} is highly anisotropic and must be correctly modelled to ensure the balance of the Reynolds-stress budgets. Whereas some authors consider that the deviatoric part is still absorbed in the redistribution ϕ_{ij} down to the wall, most models blend the isotropic dissipation model in the free-stream region with a specific near-wall dissipation ε_{ij}^w

$$\varepsilon_{ij} = \frac{2}{3}\varepsilon\delta_{ij} f_b + \varepsilon_{ij}^w (1 - f_b) \tag{3.49}$$

where f_b switches from 0 at the wall to 1 far from the wall.

The simplest model is due to Rotta [90]

$$\varepsilon_{ij}^w = \frac{\overline{u_i u_j}}{k}\varepsilon. \tag{3.50}$$

However, its does not accurately reproduce the asymptotic behaviour, which can be found with the Taylor-series expansion of the Reynolds stresses at the wall

$$\varepsilon_{11}^w = \frac{\overline{u^2}}{k}\varepsilon, \qquad \varepsilon_{22}^w = 4\frac{\overline{v^2}}{k}\varepsilon, \qquad \varepsilon_{33}^w = 2\frac{\overline{w^2}}{k}\varepsilon, \qquad \varepsilon_{12}^w = \frac{\overline{uv}}{k}\varepsilon. \tag{3.51}$$

Several authors developed new models to solve this issue, for instance Launder & Tselepidakis [60] formulated theirs as

$$\varepsilon_{ij}^{w} = \left(\overline{u_i u_j} + \overline{u_i u_l} n_j n_l + \overline{u_j u_l} n_i n_l + \overline{u_l u_m} n_l n_m n_i n_j\right) \frac{\varepsilon}{k} F \tag{3.52}$$

$$F = \left(1 + \frac{3}{2} \frac{\overline{u_l u_m}}{k} n_l n_m\right)^{-1} \tag{3.53}$$

where F is a correction function so that ε_{ij}^{w} correctly contracts into ε and $\underline{\mathbf{n}}$ is the wall-normal unit vector.

3.2.4 Blending for wall modelling

The near-wall behaviour of turbulence is due to the fluid viscosity, which damps the Reynolds stresses in the vicinity of the wall, and the blocking effect of the wall, an inviscid mechanism that affects the turbulence anisotropy even beyond the viscous sublayer.

As discussed above, some models account for these effects by activating near-wall corrections, such as the 'wall-echo' terms Eq. (3.43) for ϕ_{ij}, or using specific models close to the wall, as Rotta's dissipation tensor Eq. (3.50) or the near-wall redistribution Eq. (3.44) of Manceau & Hanjalić [69].

The transition between free-stream and near-wall modelling is gradually performed with a blending function f_b

$$\psi_{ij} = f_b \psi_{ij}^{h} + (1 - f_b)\, \psi_{ij}^{w} \tag{3.54}$$

where f_b takes values between zero (at the wall) and one (free-stream). Since free-stream models are assumed valid down to the log region, the transition usually occurs in this region, although the blocking effect remains significant [62].

Analytical blending

Some RSMs, such as the SSG-ω model from the ATAAC project [97, 3] and those of Jakirlić & Hanjalić [47] and Gerolymos *et al.* [34], rely on analytical functions that depends on the wall distance d (or y^+), the local turbulent Reynolds number $Re_T = k^2/(\varepsilon\nu)$ or both of them, just like the damping functions in low-Reynolds $k-\varepsilon$ models.

However, the use of the wall distance to impose the validity of near-wall modelling can lead to inaccurate results in complex geometries, for instance in corner flows where the boundary layers do not necessarily have the same thickness on both sides.

Elliptic relaxation and elliptic blending

The hypothesis of quasi-homogeneity and the local modelling of the non-local pressure term are no longer valid in the near-wall region, subjected to strong mean-velocity gradients. To overcome this limitation that impacts boundary layer predictions, Durbin [29, 30] suggested a new approach, assuming an exponential decrease in two-point correlations with the distance

$$\Psi_{ij}(\underline{\mathbf{x}}, \widetilde{\underline{\mathbf{x}}}) = \Psi_{ij}(\widetilde{\underline{\mathbf{x}}}, \widetilde{\underline{\mathbf{x}}}) \exp\left(\frac{\|\widetilde{\underline{\mathbf{x}}} - \underline{\mathbf{x}}\|}{L}\right) \tag{3.55}$$

where $\Psi_{ij}(\underline{\mathbf{x}}, \underline{\tilde{\mathbf{x}}}) = 2\overline{\nabla^2 p(\underline{\tilde{\mathbf{x}}}) s_{ij}(\underline{\mathbf{x}})}$ is the integrand of the volumetric integral in Eq. (3.32) and L is the characteristic distance of correlation. With this new hypothesis, ϕ becomes solution of an equation, called *elliptic relaxation equation*

$$\phi_{ij} - L^2 \nabla^2 \phi_{ij} = \phi^h_{ij} \tag{3.56}$$

Far from the wall, $L^2\nabla^2\phi_{ij}$ vanishes, so that ϕ_{ij} equals the RHS in Eq. (3.56), where the quasi-homogeneity hypothesis applies. Thus, ϕ^h_{ij} can be modelled with the usual models presented in Section 3.2.1.

Despite the improved physics of the models due to less restricting assumptions, the elliptic relaxation adds 6 equations, resulting in a 13-equation model (Durbin [30]), and proved to be numerically unstable. However, it has been simplified by Manceau & Hanjalić [69] into an unique additional equation, the *elliptic blending equation*

$$\alpha - L^2 \nabla^2 \alpha = 1 \tag{3.57}$$

The dimensionless elliptic variable α, which is zero at the wall and tends to one in the quasi-homogeneous region, is then used to form a blending function $f_b = \alpha^3$ to switch between near-wall and free-stream modelling without explicitly relying on the distance to the wall.

The correlation distance L is modelled as proportional to the local largest eddies

$$L = C_L \max\left[\, \ell \,;\; C_\eta \eta \,\right] \tag{3.58}$$

with $\ell = k^{3/2}/\varepsilon$ the turbulent integral length-scale, bounded by the Kolmogorov scale η to prevent L to vanish at the wall as suggested by Durbin [29].

Note that Durbin [29] also applied the elliptic relaxation to a two-equation EVM, as a simplification of the RSM with elliptic relaxation. This model generated a new class of EVMs, called $\overline{v^2} - f$ models, which add an equation for the wall-normal stress $\overline{v^2}$, representing a second turbulent velocity scale used for the eddy viscosity, and its corresponding elliptic equation (3.56). The main advantage of this model is to correctly reproduce the near-wall damping of turbulence without any analytical damping function, contrary to $k-\varepsilon$ models discussed in Section 3.1.1. Billard [7] adapted the elliptic blending of Manceau & Hanjalić [69] to improve the code-friendliness of these models, introducing the BL-$\overline{v^2}/k$ model. An exhaustive analysis of the $\overline{v^2} - f$ models is provided by Billard [6].

3.3 Implemented Reynolds-Stress Models

At Dassault Aviation, the simulations are carried out with the in-house CFD tool Aether (for AEro-THERmodynamics). It solves the compressible Navier-Stokes equations (1.12) for multi-species flows on unstructured meshes, using a finite element methods stabilized with the Streamline Upwind Petrov-Galerkin (SUPG) method, and takes advantage of the entropic formulation, presented in Appendix A. More detailed descriptions of Aether, its finite elements methods implementation and its stabilisation method can be found in [18, 63, 121].

The Navier-Stokes solver is coupled to a turbulence solver, which enables RANS, LES, and hybrid methods modelling. However, the entropy formulation is not easily transposed to turbulent variables. The turbulence solver thus relies on a matrix formulation with the primitive variables, meaning that the models presented in the present work are implemented without further transformation.

In addition to a few EVMs, three RSMs have been implemented in AETHER and are described in this section:

- the Elliptic Blending Reynolds Stress Model (EB-RSM) [69, 67], which aims to model the near-wall behavior with high-fidelity,
- the SSG/LRR-ω RSM [31, 17], a robustness-oriented RSM without specific near-wall modelling developed by the DLR (*Deutsches Zentrum für Luft- and Raumfahrt* – German Aerospace Center),
- the SSG-ω RSM from the European ATAAC project [97, 3], which combines both approaches.

3.3.1 EB-RSM

As most RSMs, the EB-RSM relies on an ε-equation. Eq (3.9) is here slightly altered and expressed as

$$\rho\frac{\mathrm{D}\varepsilon}{\mathrm{D}t} = \frac{\rho}{T}\left(C'_{\varepsilon 1}P_k - C_{\varepsilon 2}\varepsilon\right) + \frac{\partial}{\partial x_j}\left(\mu\frac{\partial\varepsilon}{\partial x_j}\right) + \rho D^T_\varepsilon. \tag{3.59}$$

The production and destruction terms in Eq. (3.9) using the ratio ε/k are rewritten with the turbulent integral time scale T, bounded by the Kolmogorov time scale, following Durbin [30]

$$T = \max\left(\frac{k}{\varepsilon}; C_T\left(\frac{\nu}{\varepsilon}\right)^{1/2}\right) \tag{3.60}$$

with $C_T = 6$. This prevents the singularity at the wall, as k vanishes.

Moreover, the constant $C_{\varepsilon 1}$ for the production term is replaced with a variable coefficient $C'_{\varepsilon 1}$ in the near-wall region, to robustly account for the P_3 term in the exact dissipation rate Eq. (1.32). The peak of P_3 in the buffer layer is thus here reproduced as a amplification of the production term $C_{\varepsilon 1}$. Several formulations have been suggested (see [67]) and the following expression has been retained

$$C'_{\varepsilon 1} = C_{\varepsilon 1}\left(1 + A_1\left(1-\alpha^3\right)\sqrt{\frac{k}{\overline{u_iu_j}n_in_j}}\right) \tag{3.61}$$

with $A_1 = 0.019$. The remaining coefficients are calibrated as $C_{\varepsilon 1} = 1.44$, $C_{\varepsilon 2} = 1.83$ and $\sigma_\varepsilon = 1.15$.

The EB-RSM uses the GGDH, consistently in the Reynolds-stress equations and in Eq.(3.59), to improve the prediction of the anisotropy of the turbulent transport in the boundary layer

$$\rho D^T_{ij} = \frac{\partial}{\partial x_l}\left(C_s\rho T\,\overline{u_lu_m}\frac{\partial\overline{u_iu_j}}{\partial x_m}\right), \qquad \rho D^T_\varepsilon = \frac{\partial}{\partial x_l}\left(\frac{C_s}{\sigma_\varepsilon}\rho T\,\overline{u_lu_m}\frac{\partial\varepsilon}{\partial x_m}\right). \tag{3.62}$$

with $C_s = 0.21$.

The pressure term is modelled with a modified SSG model where the nonlinear return C_2 term is suppressed to prevent numerical stiffness. It is blended to the Manceau & Hanjalić near-wall model Eq. (3.44), and the isotropic dissipation model Eq. (3.48) to Rotta's dissipation model Eq. (3.50), using the Elliptic Blending Eq. (3.57). The correlation distance L is calibrated with $C_L = 0.133$ and $C_\eta = 80$.

3.3.2 SSG/LRR-ω RSM

The good predictions of Menter's $k-\omega$ model [71] in aeronautical applications, due to its improved behaviour in APG flows, motivated a new second-moment closure that combines the Reynolds-stress transport equations to the BSL ω-equation, during the European FLOMANIA project [39].

Unlike the EB-RSM, the SSG/LRR-ω RSM does not try to correctly reproduce the near-wall behaviour and rather focuses on numerical robustness. The Reynolds-stress dissipation rate tensor is modelled isotropically down to the wall with Eq. (3.48), where the turbulent kinetic energy specific dissipation rate is converted according to

$$\varepsilon = \beta^* k\omega, \qquad \text{with} \qquad \beta^* = 0.009. \tag{3.63}$$

As the model's name indicates, the redistribution term is modelled with a blending of both the SSG and the LRR models. Indeed, Wilcox [120] showed that the ω-equation provides a better behaviour in association with the LRR model, written without 'wall-echo' terms. The RSM thus switches from the SSG model in the free-stream region to the LRR model close to the wall when the BSL equation switches from the ε to the ω-equation. Since both redistribution models can be cast into the same mathematical expression, Eqs. (3.37) & (3.41), the blending is simply applied on their coefficients, similarly to the BSL ω-equation,

$$C = F_1 C^{(\omega)} + (1 - F_1) C^{(\varepsilon)} \tag{3.64}$$

where F_1 is the baseline function defined in Eq. (3.17).

Although the SSG/LRR-ω model has been defined with a GGDH to model the turbulent transport in the latest communications (*e.g.* in [17]), it is here implemented with the SGDH in all seven equations, with $\mu_t = \rho k/\omega$.[6] The diffusion coefficient in the Reynolds-stress equations is defined as

$$D_{\text{SGDH}} = \frac{1}{2} F_1 + \frac{2}{3} \frac{C_s}{\beta^*} (1 - F_1), \qquad \text{with} \quad C_s = 0.22. \tag{3.65}$$

3.3.3 SSG-ω RSM 'ATAAC'

The SSG-ω RSM ATAAC also combines the BSL ω-equation to the SGDH turbulent transport, the SSG redistribution and the isotropic dissipation Eq. (3.48). However, the ω-equation coefficients are adjusted, the new values are gathered in Table 3.4.

Table 3.4: *Recalibrated constants in the ω-equation for the SSG-ω RSM ATAAC*

	α	β	σ^*
Inner	5/9	0.075	0.605
Outer	0.664	0.0828	0.65

Contrary to the SSG/LRR-ω RSM, it intends to reproduce the near-wall behaviour. To that end, it blends the above modelling to the Manceau & Hanjalić redistribution Eq. (3.44)

[6] hence, the model corresponds to the `SSG/LRR-RSM-w2012-SD` in https://turbmodels.larc.nasa.gov/rsm-ssglrr.html

and Rotta's dissipation Eq. (3.50) in the vicinity of the wall using an analytic function. After testing different parameters, including the Reynolds numbers $Re_T = k^2/(\varepsilon\nu)$ and $Re_d = d\sqrt{k}/\nu$, with DNS data, the following blending function was retained

$$f_b = 1 - \exp\left(-\left[\frac{\frac{\omega d^2}{\nu} - \frac{6}{\beta}}{225}\right]^2\right) \tag{3.66}$$

where $\omega d^2/\nu$ is a dimensionless parameter based on the specific dissipation rate and the wall distance.

To account for wall blocking in the turbulent transport, a damping function f_w is introduced in the diffusion coefficient of the SGDH model

$$D_{\text{SGDH}} = \frac{2}{3}\frac{C_s}{\beta^*} f_w \tag{3.67}$$

where $C_s = 0.22$ and $\beta^* = 0.09$. Considering the model behaviour in the inner layer, *i.e.* neglecting convection, the damping function is determined by trial and error and yields

$$f_w = 1 - \exp\left(-\left[\frac{\omega d^2}{250\nu}\right]^{2.5}\right). \tag{3.68}$$

Similarly, the ε-to-ω conversion is adapted to ensure consistent values of the dissipation rate in the near-wall region. In the wall region, convection, production and turbulent transport are negligible. The k-equation, *i.e.* half the trace of the Reynolds-stress transport equations, reduces to

$$\varepsilon = \beta^* k\omega = \nu\frac{\mathrm{d}^2 k}{\mathrm{d}y^2}, \tag{3.69}$$

and replacing ω with its near-wall solution, Eq. (3.20), yields

$$k \propto y^{3.23}. \tag{3.70}$$

Hence, dissipation is too strong in this region and results in a slower growth of k compared to the expected y^2 behaviour. Using an *a priori* analysis on DNS data, a damping function for ε is thus defined as

$$f_\varepsilon = \frac{5}{18} + \frac{13}{18}\tanh\left(\left[\frac{y}{42}\left(\frac{\omega k}{\nu^3}\right)^{1/4}\right]^3\right), \tag{3.71}$$

where $y\sqrt[4]{\omega k/\nu^3}$ is the ratio of the wall distance and the Kolmogorov length scale.

To anticipate the effect of pressure gradient on the log-law prediction, Aupoix [3] limits the turbulent length scale using a Yap-like correction. He applies this limitation only to the Reynolds-stress transport equations to prevent any interference with the numerical solution of the ω-equation, resulting in

$$\varepsilon = f_\varepsilon \max\left(\beta^* k\omega\,;\left(\frac{k}{k_0^+}\right)^{3/2}\frac{1}{\kappa_0 y}\right), \tag{3.72}$$

where $k_0^+ = 3.118{,}556$ is the zero-th order approximation of k in wall-units in the log layer.

3.3.4 Summary

In the free-stream region, all three RSMs behave similarly. Indeed, they all rely on the SSG model for the velocity pressure-gradient modelling, with an isotropic dissipation and the use of an ε-equation to transport the dissipation rate.

However, they differ in their near-wall modelling. Both the SSG/LRR-ω RSM and the SSG-ω RSM ATAAC switch to a ω-equation, the latter adjusting the conversion to ε to conserve a coherent behaviour at the wall. While the SSG/LRR-ω switches ϕ_{ij}^* models only out of compatibility reason with its BSL ω-equation, the others ensure a correct asymptotic behaviour for ε_{ij} and ϕ_{ij}^* by using a specific asymptotic near-wall model. Finally, all models have their own blending functions to activate their near-wall modelling. Table 3.5 sums up the near-wall differences.

Table 3.5: *Differences between the implemented models in the near-wall region*

	EB-RSM	SSG-ω RSM ATAAC	SSG/LRR-ω RSM
Length-scale	ε	ω BSL (recalibrated) near-wall corrected ε	ω BSL $\varepsilon = \beta^* \omega k$
ε_{ij}^w	Rotta	Rotta	isotropic
ϕ_{ij}^w	Manceau & Hanjalić	Manceau & Hanjalić	LRR
D_{ij}^T	GGDH	SGDH	SGDH
f_b	elliptic blending	analytic blending	BSL function F_1

The different modelling strategies used in these Reynolds-stress models will be assessed in the next chapter, along with the overall performance of RSMs compared to the Spalart-Allmaras model on two academic cases, yielding zero-pressure-gradient and adverse-pressure-gradient boundary layers, respectively. The four considered models will also be assessed on an industrial application case, representing a transonic commercial aircraft, in Chapter 7.

Chapter 4

Assessment of the implemented Reynolds-stress models

In this chapter, the three Reynolds-stress models presented in Section 3.3, the SSG/LRR-ω RSM, the SSG-ω ATAAC RSM and the EB-RSM, are benchmarked against the Spalart-Allmaras model and reference data to assess their behaviour and their limitations in both zero-pressure-gradient and adverse-pressure-gradient flows.

4.1 Zero-pressure-gradient boundary layer

The first case analysed is the flat plate, on which a ZPG boundary layer develops. This is a canonical case, which must be correctly predicted by all turbulence models. The present study offers a closer look to the fundamental differences between the considered RSMs, especially regarding their Reynolds-stress profiles.

4.1.1 Case description

Computations are run at $M = 0.2$ over an adiabatic wall. The two-dimensional computational domain, shown in Figure 4.1, starts upstream of the leading edge with a free-stream region. This enables the imposition of a uniform velocity profile with a low isotropic turbulence level at the inlet and to ensure that turbulence settles before reaching the plate leading edge. The free-stream velocity is determined by the Reynolds number, set at $Re_L = 5\,\mathrm{M}$, where $L = 1\,\mathrm{m}$ is the characteristic length scale of the case.

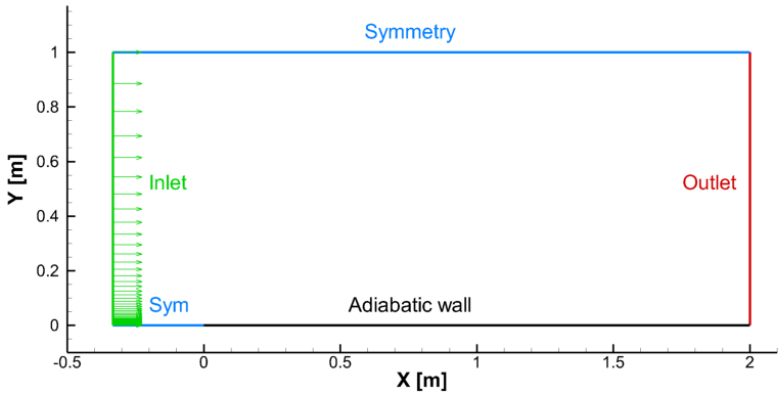

Figure 4.1: *Computational domain of the flat plate*

The mesh convergence study has been carried out using the different meshes provided by NASA[1], whose characteristics are gathered in Table 4.1.

Table 4.1: *Meshes characteristics*

Mesh	Resolution	Total nodes
M1	35 × 25	875
M2	69 × 49	3,381
M3	137 × 97	13,289
M4	273 × 193	52,689
M5	545 × 385	209,825

Figure 4.2 shows the friction coefficient predicted by the models for the different meshes, at two different Reynolds numbers based on the momentum thickness, $Re_\theta = U_\infty \theta/\nu$. Note that the convergence is assessed at a given Re_θ rather than at a fixed position, as proposed by NASA. The comparison position is thus defined with respect to the predicted boundary layer rather than to the flat plate geometry. Hence, the boundary layer growth rates on the different refined meshes are accounted for.

It can be seen from the figure that the third mesh offers a satisfactory refinement for all the models. Unlike the EB-RSM and the SSG/LRR-ω RSM, the SSG-ω ATAAC model already yields a good estimate of the skin friction on the coarsest mesh, with a maximum relative error of 1 % at the lower Re_θ station in Figure 4.2(a) for the mesh M1 and of 0.8 % at the higher Re_θ station for the mesh M2 in Figure 4.2(b). The resolution needed to properly converge the different RSMs appears similar to the one needed for Spalart-Allmaras model. In the following, the four models are compared on mesh M3.

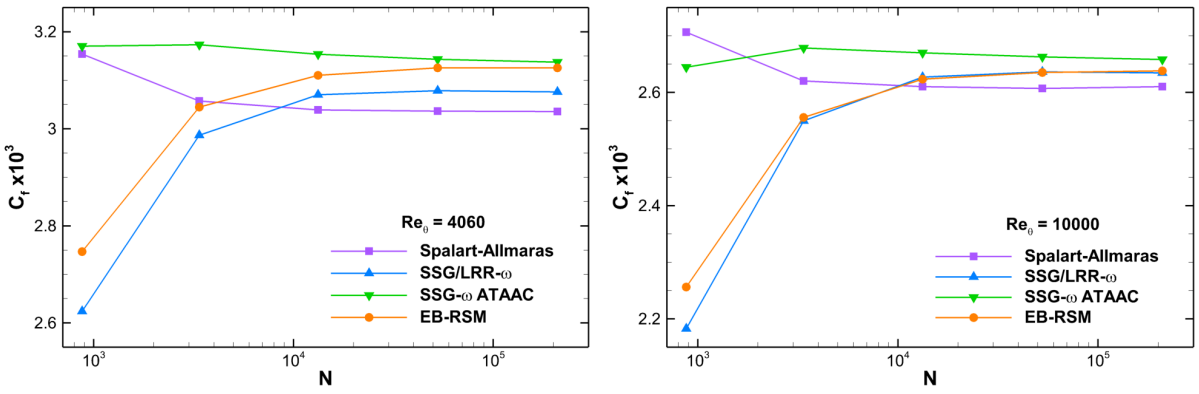

(a) $Re_\theta = 4{,}060$ **(b)** $Re_\theta = 10{,}000$

Figure 4.2: *Mesh convergence for the flat plate*

4.1.2 Integral quantities

The evolution of the integral quantities in the boundary layer is assessed using empirical laws. Using the von Kármán integral equation without pressure gradient, $\frac{d\theta}{dx} = \frac{1}{2}C_f$, with

[1] https://turbmodels.larc.nasa.gov/flatplate_grids.html

the experimentally calibrated $^1/_{7^{\text{th}}}$-power-law velocity profile (see Schlichting [95]), the displacement and the momentum thicknesses are expressed as

$$\delta^* \approx \frac{0.048x}{Re_x^{1/5}}, \qquad \theta \approx \frac{0.037x}{Re_x^{1/5}}, \tag{4.1}$$

and are valid for $Re_x < 10^7$ for a boundary layer turbulent from the leading edge.

Figure 4.3 shows the good agreement of the Reynolds-stress models with these empirical laws. In particular, the RSMs seem to better predict θ compared to the Spalart-Allmaras model, which slightly underpredicts the integral thicknesses.

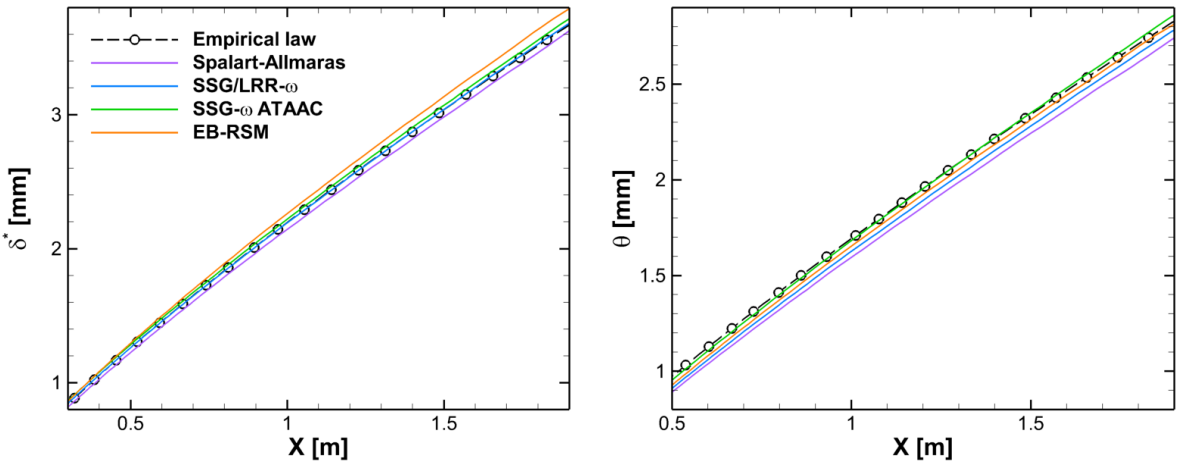

(a) *Displacement thickness* **(b)** *Momentum thickness*

Figure 4.3: *Boundary layer thicknesses on the flat plate*

The local skin friction is shown in Figure 4.4. The models are benchmarked against the Kármán-Schoenherr relation [96]

$$C_f = \frac{1}{17.08\,(\log_{10} Re_\theta)^2 + 25.11 \log_{10} Re_\theta + 6.012}, \tag{4.2}$$

for $4{,}000 < Re_\theta < 13{,}000$ as suggested by NASA.

The RSMs improve the predictions over the Spalart-Allmaras model on a large range of Reynolds numbers. In Figure 4.4, both the EB-RSM and the SSG/LRR-ω model closely follow the empirical relation. The Spalart-Allmaras model tends to the target skin friction at the highest Re_θ, reducing the relative error from 2.8 % at $Re_\theta = 4{,}000$ down to 0.4 % at $Re_\theta = 12{,}000$. Despite a correct trend over the entire flat plate, the SSG-ω ATAAC model systematically overestimates the skin friction of about 2 %.

4.1.3 Profiles

The results are compared with the DNS of Schlatter *et al.* [93], obtained with a fully spectral method and a tripping of turbulence from a Blasius laminar inflow. The profiles are extracted at the same Reynolds numbers Re_θ as in the DNS.

Figure 4.5 shows the profiles in wall-units for $Re_\theta = 4{,}060$, the highest Reynolds number available in the reference.

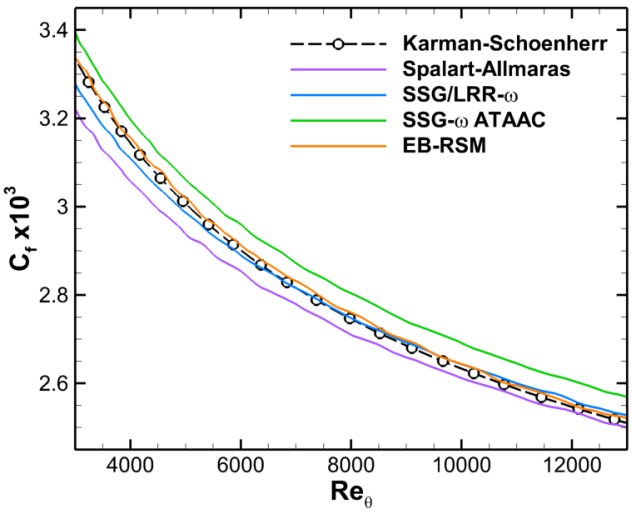

Figure 4.4: *Skin friction coefficient on the flat plate*

As expected, the mean velocity profile is correctly predicted by all the models in Figure 4.5(a). It can be noted though that the SSG-ω ATAAC model underestimates the velocity in the wake region, whereas the EB-RSM and the SSG/LRR-ω model tend to underestimate the buffer layer velocity. These observations are confirmed by the turbulent shear-stress, which directly affects the mean velocity. Figure 4.5(b) indeed shows good overall predictions, but the SSG-ω ATAAC model returns to zero in the free-stream region more gradually than the DNS, and the other RSMs amplify the shear-stress in the vicinity of $y^+ \approx 10$ by 10 % with a slightly steeper gradient. The stronger shear-stress in these regions increases the mixing between the low-momentum fluid closer to the wall and the higher-momentum fluid further away, resulting in a smoothing of the velocity profile where $|\overline{uv}|$ is too large compared to the DNS.

Figures 4.5(c)–(e) highlight the difference in the modelling approaches. Both the EB-RSM and the SSG-ω ATAAC model correctly reproduce the two-component turbulence at the wall by means of the near-wall model Eq. (3.44) of Manceau & Hanjalić [69], with $\overline{u^2}$ and $\overline{w^2}$ decreasing in y^2 whereas $\overline{v^2}$ decreases in y^4. They also predict the peaks in the buffer layer for $\overline{u^2}$ and $\overline{w^2}$. This can be related to the ε-equation in the EB-RSM and the improved ω-to-ε conversion Eq. (3.72) of the SSG-ω ATAAC model, which points out here its effectiveness by yielding a non-zero constant dissipation rate in the viscous sublayer, as shown in Figure 4.5(f).

This behaviour is to be compared to the vanishing dissipation rate with the SSG/LRR-ω model and its exaggerated peak in the buffer layer. Indeed, without the corrected conversion, the SSG/LRR-ω model is unable to reproduce any peak for $\overline{u^2}$ and $\overline{w^2}$. Moreover, the absence of near-wall modelling results in the model predicting a three-component turbulence at the wall, with all the Reynolds stresses decreasing as y^3.

4.1.4 Turbulence budgets

The models can be further analysed by looking at the budget of the Reynolds stresses. Figure 4.6 compares the different source terms of the transport equations for $\overline{u^2}$ and $\overline{v^2}$.

The vanishing of ε at the wall for the SSG/LRR-ω model shown in Figure 4.5(f) results in the component ε_{11} of the dissipation tensor tending to zero as well in Figure 4.6(c). At

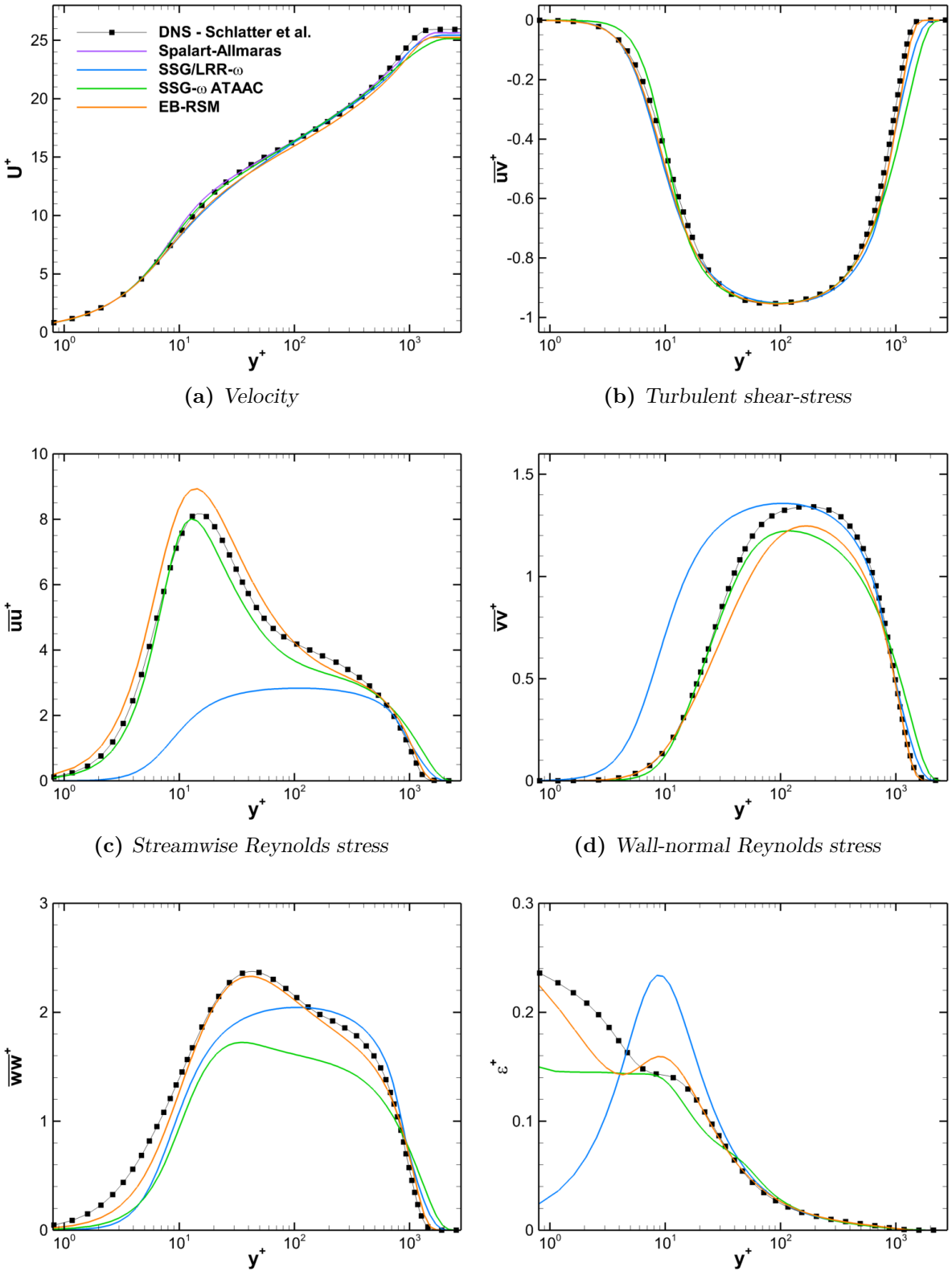

(a) *Velocity*

(b) *Turbulent shear-stress*

(c) *Streamwise Reynolds stress*

(d) *Wall-normal Reynolds stress*

(e) *Spanwise Reynolds stress*

(f) *Dissipation rate*

Figure 4.5: *Profiles on the flat plate at* $Re_\theta = 4{,}060$

the wall, it is compensated by a vanishing total dissipation $D^{\nu}_{11} + D^{T}_{11}$ in Figure 4.6(g), which explains the asymptotic behaviour $\overline{u^2} \propto y^3$ with a vanishing second-order derivative.

The near-wall modelling in the EB-RSM and the SSG-ω ATAAC model improves this behaviour. In particular, the blending of the SSG model with the near-wall model Eq. (3.44) of Manceau & Hanjalić [69] corrects the amplitude of their redistribution terms ϕ^*_{11} and ϕ^*_{22}. The near-wall modelling also damps the source terms for $\overline{v^2}$ in the viscous sublayer and in the buffer layer, so that the wall-normal stress correctly decreases as $\propto y^4$ at the wall.

Figures 4.6(g) & (h) highlight the differences between the GGDH model used in the EB-RSM and the SGDH in the other RSMs. In particular, the SGDH overpredicts the peaks of turbulent transport in the buffer layer. Despite an improved amplitude, the GGDH does not correctly predict the negative diffusion of $\overline{v^2}$ for $y^+ \approx 30$.

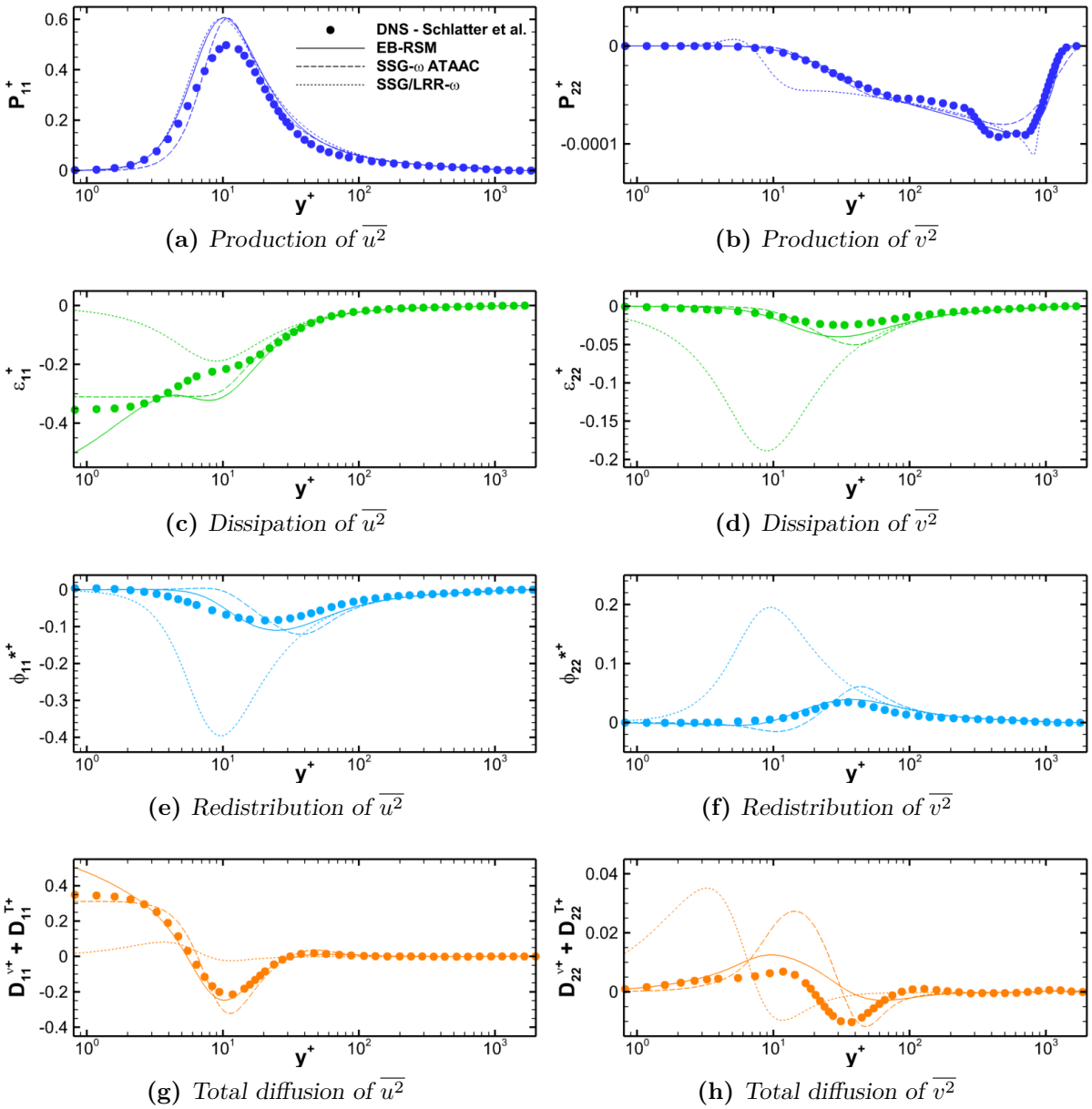

(a) *Production of* $\overline{u^2}$ **(b)** *Production of* $\overline{v^2}$

(c) *Dissipation of* $\overline{u^2}$ **(d)** *Dissipation of* $\overline{v^2}$

(e) *Redistribution of* $\overline{u^2}$ **(f)** *Redistribution of* $\overline{v^2}$

(g) *Total diffusion of* $\overline{u^2}$ **(h)** *Total diffusion of* $\overline{v^2}$

Figure 4.6: *Reynolds-stress source terms on the flat plate at* $Re_\theta = 4{,}060$

To observe the relative behaviour of the different terms as they vanish, Figure 4.7 presents the budgets in a proportional way, as proposed by Billard [6]. The terms are decomposed into to their positive and negative contributions, so that the transport equation can be written

$$\frac{\partial \overline{u_i u_j}}{\partial t} = \sum_k T_k^+ + \sum_k T_k^-, \qquad \text{with} \quad T_k^+ = \max\left(T_k, 0\right), \quad T_k^- = \min\left(T_k, 0\right). \tag{4.3}$$

The flow considered is stationary, thus $\partial_t \overline{u_i u_j} = 0$ and the balance of the transport equation imposes $\sum_k T_k^+ = -\sum_k T_k^-$. The terms are then rescaled according to the budget amplitude $\sum_k T_k^+$ at each point of the boundary layer to indicate the proportion of each term at a given distance to the wall.

Using a DNS, this presentation enables an understanding of the physical phenomena at play. With Reynolds-stress models, it illustrates their ability to reproduce these phenomena. Figure 4.7 especially highlights the main regions of the boundary layer.

The logarithmic layer corresponds to the range where the molecular diffusion D_{ij}^{ν} vanishes and the convection C_{ij} does not yet intervene. For infinite Reynolds numbers, turbulent transport is also expected to vanish, which is not entirely the case in the considered DNS with $Re_\theta = 4{,}060$. One third of the production of $\overline{u^2}$ is dissipated, whereas the rest is redistributed to the other stresses. In particular, this redistribution feeds $\overline{v^2}$ and is almost entirely dissipated in the log layer. This behaviour is well reproduced by all models. Similarly, the models correctly predict the balance between turbulent transport and convection in the outer region, as observed in the DNS (a) & (b).

The main discrepancies appear as expected in the near-wall region. The viscous sublayer in the SSG/LRR-ω model displays the wrong redistribution, ϕ_{11}^* taking energy from $\overline{u^2}$ at the wall to feed $\overline{v^2}$, in the continuation of the log layer behaviour for which the LRR model has been calibrated. Consequently, ϕ_{22}^* does not reproduces the wall-blockage effect, which leads to redistribute the wall-normal stress energy towards all others stresses.

This phenomenon is on the contrary visible for the EB-RSM (d) and the SSG-ω ATAAC model (f). The distribution between ϕ_{22}^* and ε_{22} is however different from the $^2/_5 - {}^3/_5$ distribution in the DNS. As explained in [69], the near-wall model aims at correctly predicting the difference $\phi_{22}^* - \varepsilon_{22}$ at the wall, which impacts the budget, rather than each term individually, and compensates especially for the asymptotic shortcomings of Rotta's near-wall dissipation Eq. (3.50) [90]. For these two models, the spatial extent of the negative ϕ_{22}^* is larger than what is observed for the DNS (b). This extended region towards the buffer layer balances the turbulent transport D_{22}^T and is larger for the SSG-ω ATAAC model as the SGDH modelling exaggerates the turbulent transport D_{22}^T in the buffer layer, observed in Figure 4.6(h).

4.2 APG test case - Skåre & Krogstad

4.2.1 Case presentation and numerical considerations

The Skåre & Krogstad experiment [99], briefly introduced in Section 2.3.4, was aimed to gather data on an APG boundary layer at equilibrium. The setup, shown in Figure 4.8, consists in a diverging wind-tunnel with a 6 m long and 1.4 m wide test section. The upper-wall profile $h(x)$ was iteratively adjusted to let the lower boundary layer reach an equilibrium state under pressure gradient, where the boundary layer becomes independent of the flow history and the velocity profiles are self-similar.

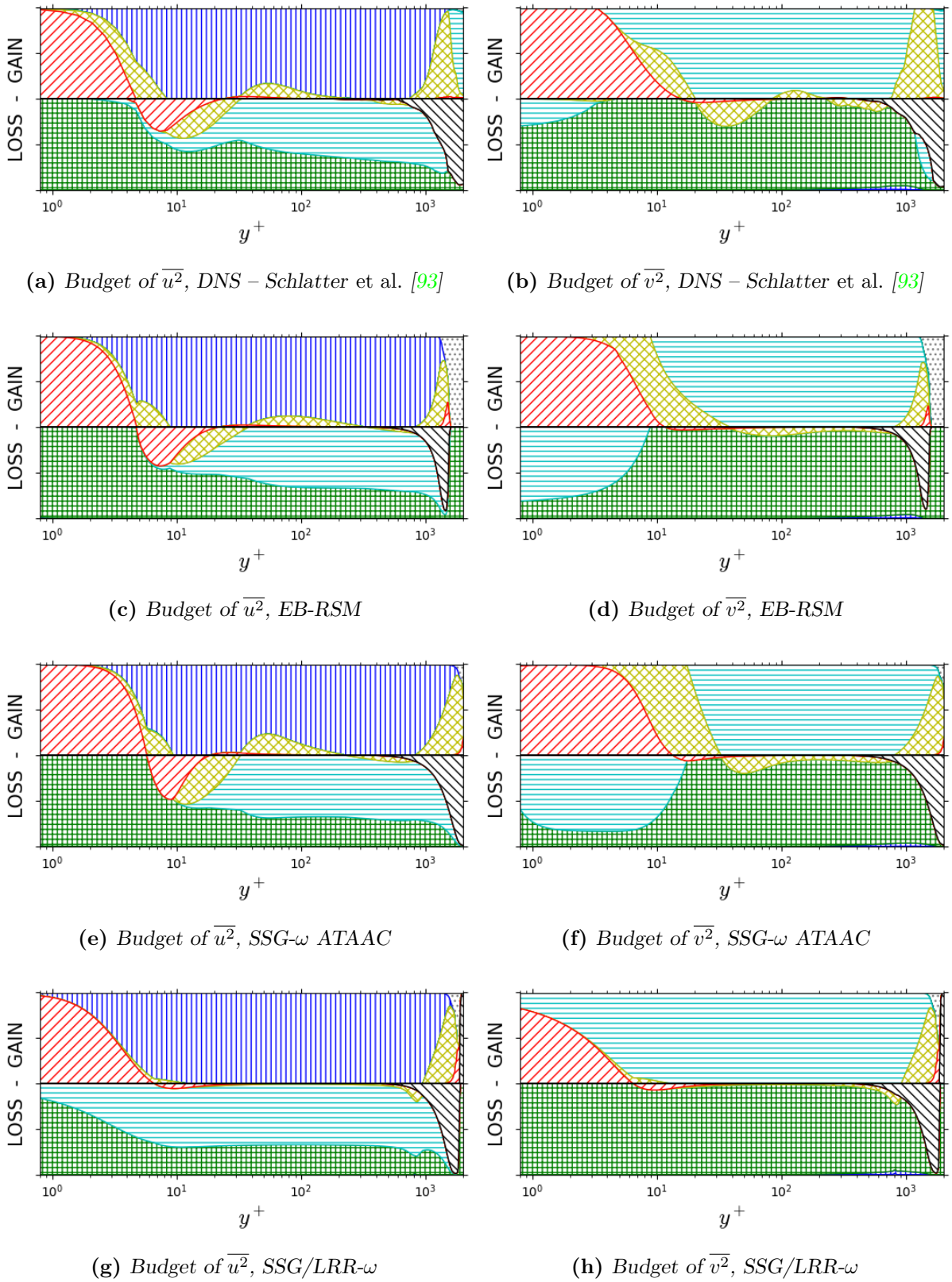

(a) *Budget of* $\overline{u^2}$*, DNS – Schlatter* et al. *[93]*

(b) *Budget of* $\overline{v^2}$*, DNS – Schlatter* et al. *[93]*

(c) *Budget of* $\overline{u^2}$*, EB-RSM*

(d) *Budget of* $\overline{v^2}$*, EB-RSM*

(e) *Budget of* $\overline{u^2}$*, SSG-ω ATAAC*

(f) *Budget of* $\overline{v^2}$*, SSG-ω ATAAC*

(g) *Budget of* $\overline{u^2}$*, SSG/LRR-ω*

(h) *Budget of* $\overline{v^2}$*, SSG/LRR-ω*

Figure 4.7: *Proportional budgets on the flat plate at* $Re_\theta = 4{,}060$

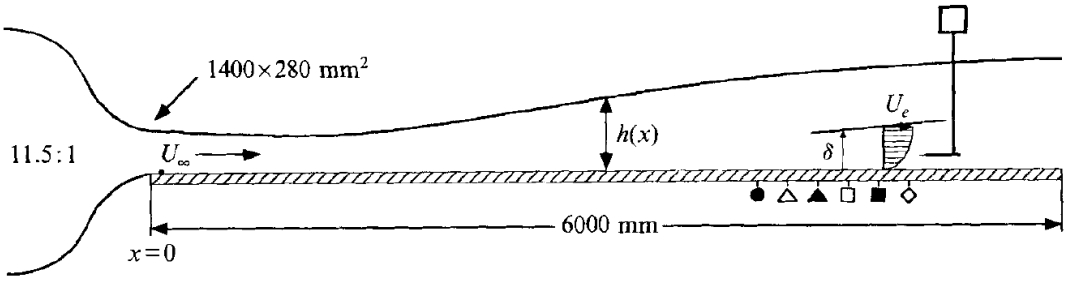

Figure 4.8: *Skåre & Krogstad experiment configuration (reproduced from Skåre & Krogstad [99])*

The equilibrium region is achieved for $4.0\,\mathrm{m} \leqslant x \leqslant 5.0\,\mathrm{m}$ and is characterised by

$$\beta_p = 20, \qquad Re_\theta \in [39{,}000\,;51{,}000]\,. \tag{4.4}$$

This experiment is therefore an interesting case for the aeronautical industry as it is representative of the strong pressure gradients and high Reynolds numbers found at the trailing edge of wings, as shown for instance in Figure 4.9 for NASA's Common Research Model (detailed in Chapter 7).

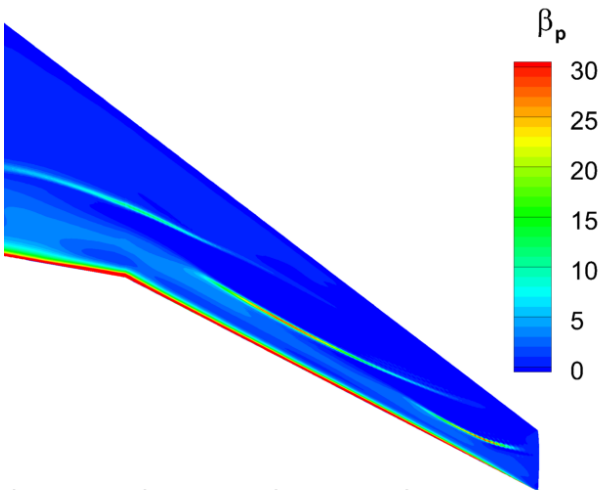

Figure 4.9: *Predicted β_p on the wing of the CRM with the Spalart-Allmaras model ($Re_c = 30\,\mathrm{M}$, $C_L = 0.4$)*

The measurements include the wall static pressure distribution using wall taps along the test section and velocity profiles using hot wires within $x \in [3.0\,\mathrm{m}\,;5.0\,\mathrm{m}]$. The measurements are performed on the lower wall and the authors conclude that the boundary layer is two-dimensional.

To confirm this observation, the computations have been run on 2D and 3D configurations, representing the test section up to $x = 6.0\,\mathrm{m}$, with a free-stream inlet at $x = -0.5\,\mathrm{m}$. The 3D geometry corresponds to half of the test section with a symmetry condition at $z = 0.7\,\mathrm{m}$, z being the spanwise coordinate. The 2D configuration restricts the domain to the symmetry plane. A third configuration, extending the 3D geometry to $x = 9.0\,\mathrm{m}$ with a straight channel, has also been considered to avoid instabilities due to transient phenomena during convergence and speed up the convergence. A grid convergence study [80] led to

meshes with a first-cell height of $y^+ < 0.5$ and a size of 13 M nodes for the extended 3D configuration.

Despite an apparent 2D behaviour of the boundary layer on the lower wall, the numerical simulations point out the deficiency of the two-dimensionality hypothesis and the influence of the side wall leading to non-negligible three-dimensional effects. Contrary to the computations run on the full 3D domain, the ones on the 2D domain fail to reproduce the flow conditions of the experiment, especially the pressure coefficient distribution shown in Figure 4.10 for the Spalart-Allmaras model, which is important to ensure a pressure gradient comparable to the experiment. In particular, the reduced pressure in 3D is explained by the strong recirculation that develops in the upper corner and compresses the flow in the symmetry plane in Figure 4.11 and blocks the free-stream flow expansion.

Note that the Spalart-Allmaras model in the 3D configuration has been run with the first version of the QCR correction [102] to improve the behaviour of the model in corner flows (see Section 3.1.2). Indeed, it enables the model to predict a secondary flow in the corner by adding anisotropy in the stream-normal plane, and results in an increased mixing and moderation of the corner flow separation.

The pressure coefficient distribution plotted in Figure 4.10 for the three tested geometries with the Spalart-Allmaras model indicates that the extension does not affect the flow

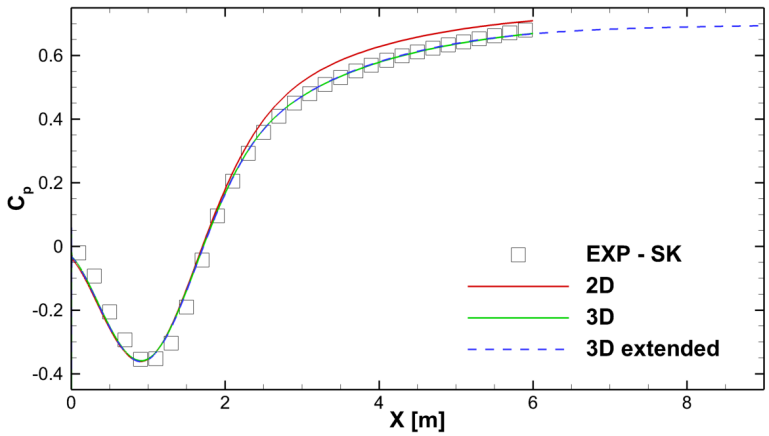

Figure 4.10: *Pressure coefficient for the Spalart-Allmaras model on the different configurations*

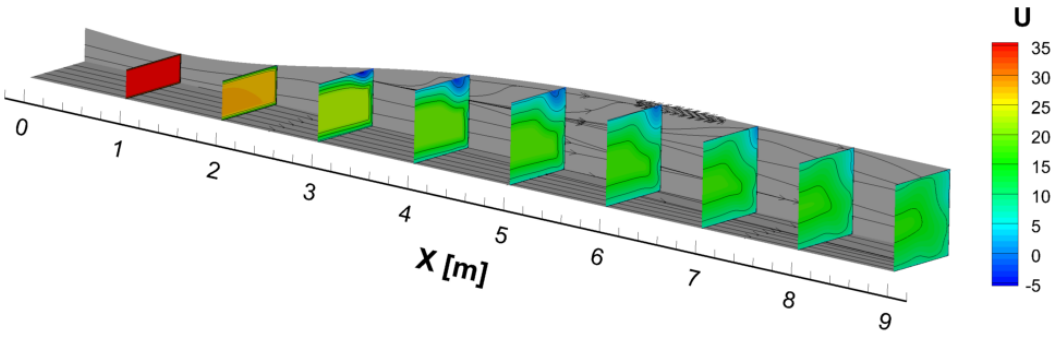

Figure 4.11: *Flow topology for the Spalart-Allmaras QCR model. The lines indicate the skin friction direction.*

behaviour in the test section. Hence, the extended 3D geometry is chosen for the APG test case, as it improves numerical stability.

The resulting C_p for all the models are shown in Figure 4.12, where the SSG/LRR-ω model and the EB-RSM coincide. The SSG-ω ATAAC model overpredicts the recirculation in the upper corner and fails to converge. Its results on this case will therefore not be presented.

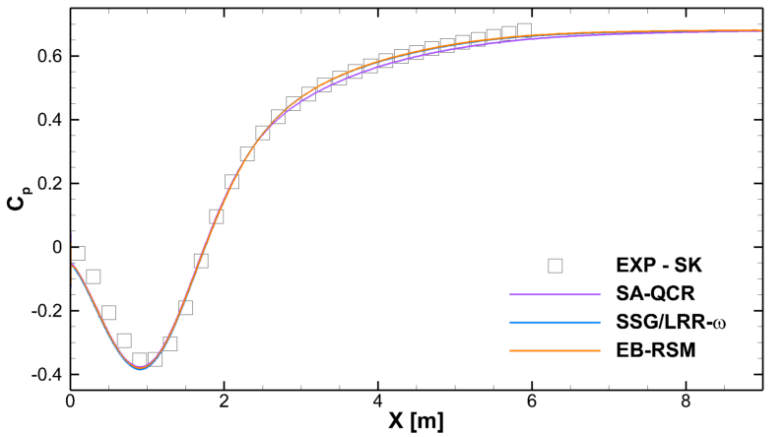

Figure 4.12: *Pressure coefficients of the different models on the extended 3D geometry*

4.2.2 Integral quantities

The boundary layer quantities are shown in Figure 4.13. The experimental equilibrium region is clearly visible in Figures 4.13(a) & 4.13(b), displaying respectively a constant pressure-gradient parameter β_p and a constant skin friction within $x \in \{4.0\,\text{m}\,; 5.0\,\text{m}\}$.

On the other hand, none of the models achieve the equilibrium flow, according to Figure 4.13(b). Instead of a plateau of β_p starting from $x = 4.0\,\text{m}$, all three models decrease after reaching a peak between $x = 3.5\,\text{m}$ and $x = 4.0\,\text{m}$. The β_p-distribution upstream the peak for the RSMs is consistent with the upstream experimental measurements.

Both RSMs yield good predictions of the skin friction at $x = 3.0\,\text{m}$ but overpredict it downstream, resulting in a relative error to the experiment of 42 % and 67 % at $x = 5.0\,\text{m}$ for the EB-RSM and the SSG/LRR-ω model respectively. The Spalart-Allmaras model here exhibits a better prediction for C_f in the equilibrium region, despite the exaggerated drop in the upstream region, for $x \leqslant 3.0\,\text{m}$. Still, the skin friction is relatively constant over the experimental equilibrium range for the one-equation model and the EB-RSM.

The discrepancy observed with the pressure-gradient parameter is explained by the deviation of the displacement thickness, which enters the parameter definition Eq. (2.23), $\beta_p = (\delta^*/\tau_w)\,\frac{\mathrm{d}P}{\mathrm{d}x}$. Figure 4.13(c) shows indeed that for the RSMs, δ^*, and to a lesser extent θ, progressively deviate from the measurements around the predicted peak of β_p. The figure also highlights the correct growth of their boundary layers upstream, as they reach the experimental values for $x = 3.0\,\text{m}$. In contrast, the Spalart-Allmaras model underpredicts both thicknesses downstream of $x = 3.0\,\text{m}$, which explains the poor prediction of the pressure-gradient parameter despite the equilibrium condition fulfilled for the skin friction.

The underprediction of the boundary layer growth of the Spalart-Allmaras model also results in a less accurate shape factor $H = \delta^*/\theta$, plotted in Figure 4.13(d). The RSMs improve the minimum relative error of H to the measurements in the equilibrium

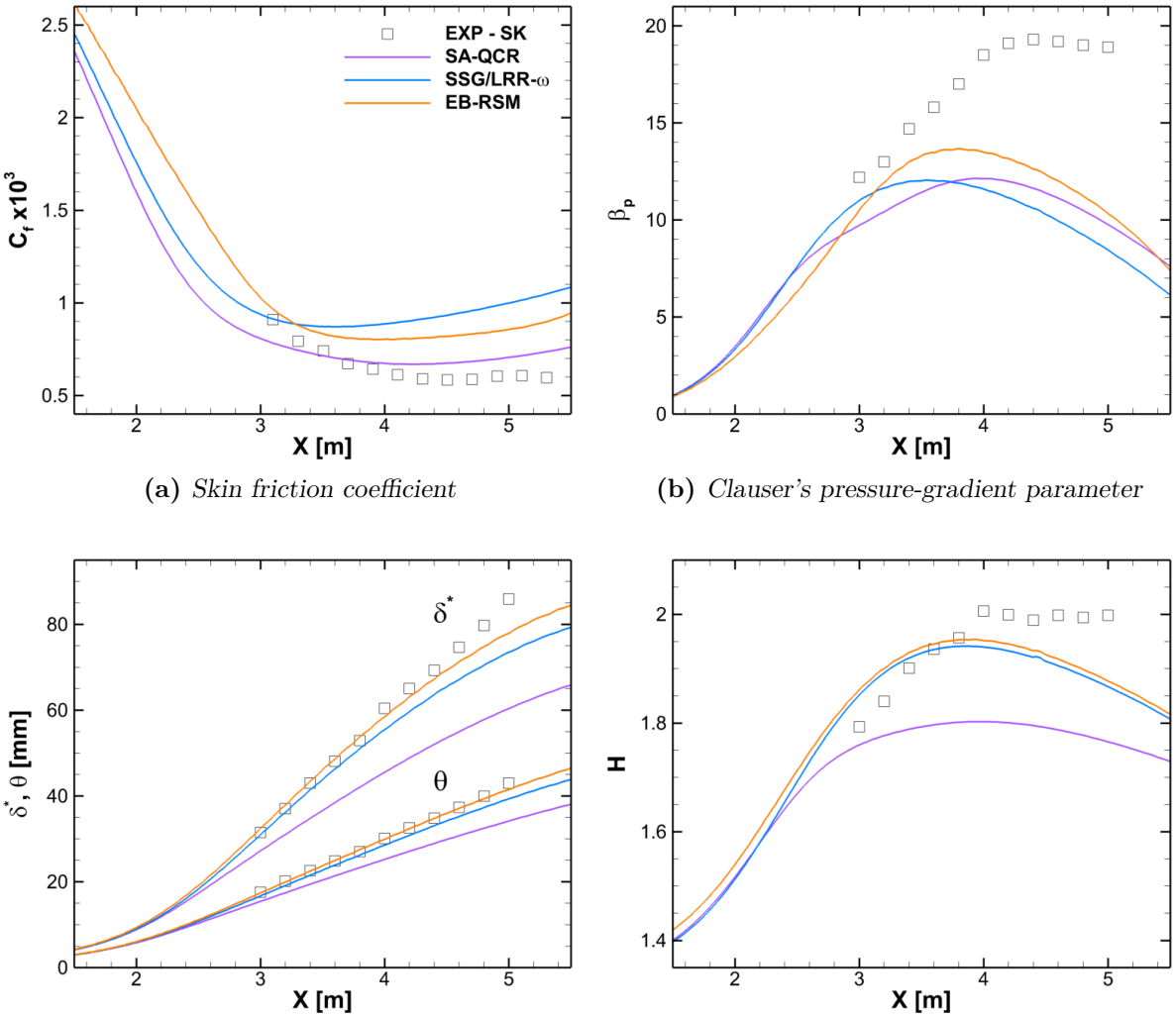

(a) *Skin friction coefficient*

(b) *Clauser's pressure-gradient parameter*

(c) *Displacement and momentum thicknesses*

(d) *Shape factor*

Figure 4.13: *Integral quantities in the instrumented region of the Skåre & Krogstad wind-tunnel*

region from 10 % for the Spalart-Allmaras model down to 2.5 %. However, the decrease of the shape factor after $x = 4.0\,\mathrm{m}$ indicates that their displacement thicknesses deviate faster from the reference than their momentum thicknesses. Thus it can be expected that their wake region progressively displays a smaller amplitude between the log-layer and free-stream velocities, preventing the profile similarity characterising equilibrium.

4.2.3 Profiles

Three profiles in the experimental equilibrium region are compared in Figure 4.14, for $x \in \{4.2\,\mathrm{m}\,; 4.6\,\mathrm{m}\,; 5.0\,\mathrm{m}\}$. Figure 4.14(a) shows the mean velocity profiles in wall-units, which indicates a better agreement of the Spalart-Allmaras model to the experiment. Indeed, the EB-RSM and the SSG/LRR-ω model both predict a thick and abnormally flat logarithmic layer, with an apparent von Kármán constant of $\kappa \approx 0.60$, to be compared to Nickels's constant $\kappa_p = 0.38$. Conversely, the velocity profiles in Figure 4.14(b), plotted in a linear scale, support the RSMs against the one-equation model. Keeping the dimension

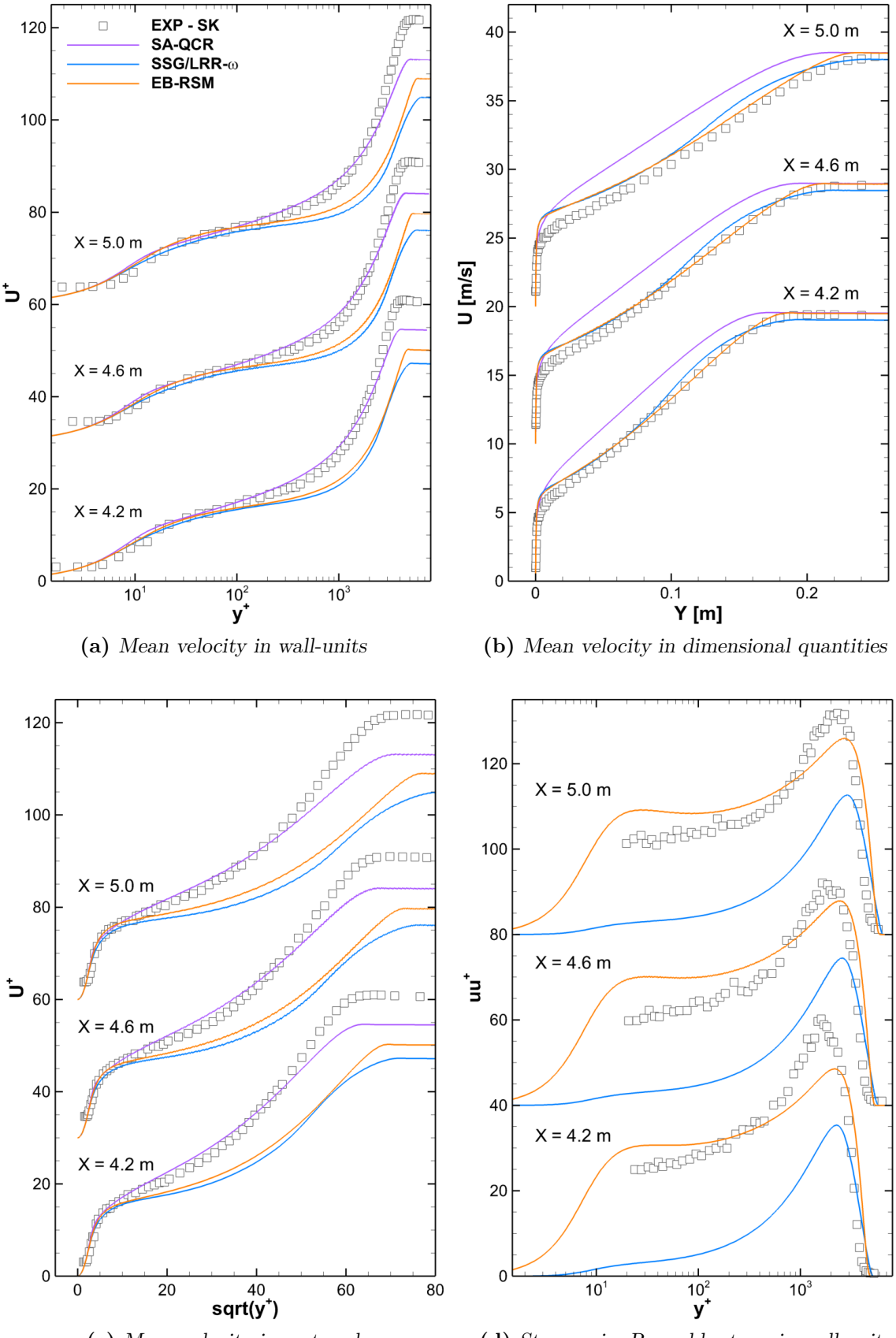

(a) *Mean velocity in wall-units*

(b) *Mean velocity in dimensional quantities*

(c) *Mean velocity in sqrt-scale*

(d) *Streamwise Reynolds stress in wall-units*

Figure 4.14: *Profiles in the equilibrium region for the Skåre & Krogstad wind-tunnel*

of the quantities here make it possible to combine the information of the outer boundary layer shape with the accuracy of the boundary layer thickness. Therefore, as expected from the previous section, the RSMs correctly predict the outer layer, especially the EB-RSM which yields a satisfactory velocity profile at the interface between the boundary layer and the free-stream region. The decrease in H from Figure 4.13(d) is here explained by an overprediction of the velocity in the inner region ($y < 0.05\,\mathrm{m}$). This reflects the inability of these models to correctly slow down in the inner layer, and is related to the overprediction of the skin friction in Figure 4.13(a).

Figure 4.14(c) confirms the satisfying sqrt-law behaviour of the Spalart-Allmaras model, though its slope is slightly too steep in the upstream profiles. It also shows how the model fails to predict the outer region coming after, the velocity profiles remaining almost linear in this scaling up to the free-stream border. The Reynolds-stress models do not present a clear sqrt-law behaviour, probably due to flat log-law prediction.

The Reynolds-stress profiles point out, once again, the difference between the modelling approaches. The streamwise stress in Figure 4.14(d) highlights in particular the ability of the EB-RSM to predict the two peaks: the first one in the buffer layer, the second one rising with the adverse pressure gradient in the outer region. The accuracy of the inner peak under APG cannot be assessed here with the experiment, which lacks measurement points in the viscous sublayer. However, the amplitude of the outer peak with respect to the inner region appears clearly underpredicted. It can be concluded that the diffusion of the turbulence is too strong, leading turbulence to level across the region below the outer peak, and thus of the sqrt region.

4.3 Conclusions

This section highlighted the difference between Reynolds-stress models enforcing the correct near-wall stress behaviour through an asymptotic approach, and the SSG/LRR-ω model, which does not. The near-wall modelling greatly improves the Reynolds-stress profiles, and especially helps the models to reproduce the physical features of turbulence at the wall, such as the two-component limit and the peaks in the buffer layer. However, the lack of this specific modelling does not prevent the SSG/LRR-ω RSM to yield satisfactory results regarding the mean flow, close to the other RSMs.

In particular, the SSG/LRR-ω model yields similar results to the EB-RSM in the Skåre & Krogstad test case, with an overall improvement of the mean flow prediction of the outer layer and of the boundary layer growth compared to the one-equation Spalart-Allmaras model, widely used in the industry. Both considered RSMs can therefore be expected to improve the prediction of the form drag, as presented in Section 2.1.1. On the other hand, the adverse pressure gradient affects their accuracy in the inner layer, pointing out the shortcomings of the term-by-term modelling calibrated in ZPG conditions. They especially overpredict the skin friction, unlike the Spalart-Allmaras model, which yields a satisfactory estimation of C_f at the lower wall. Hence, the one-equation model is expected to yield a better prediction of friction drag compared to the EB-RSM and SSG/LRR-ω model.

Unfortunately, the SSG-ω ATAAC model did not converge in the Skåre & Krogstad test case. This may be related to its systematic exaggeration of the skin friction, highlighted on the flat plate. Therefore, the benefit of solving the ω-equation, supposed to improve flow predictions in APG, with a near-wall modelling could not be assessed. Due to its convergence difficulty on the APG test case, this model will not be considered for APG corrections in the following chapters.

Chapter 5

Log-law correction

It has been seen with the Skåre & Krogstad benchmark in the previous chapter that turbulence models fail to predict the slope of the log-law in adverse pressure gradients. A first approach to improve the overall behaviour of these models consists therefore in ensuring the correct velocity gradient in the logarithmic region. Such a modification has to account for the natural deviation of the model, but also for the impact of the pressure gradient on the log-law slope, as observed in experiments and DNSs and described by Nickels [77]. To account for the latter, Knopp [51] introduced a κ-correction in the $k-\omega$ model and Knopp *et al.* [52] applied it to the SSG/LRR-ω RSM. In this chapter, the von Kármán constant alteration in turbulence models and its application are further investigated.

5.1 Local recalibration of the log-law slope

5.1.1 Two-equation and Reynolds-stress models

Direct application of Nickels's $\kappa_p\left(p^+\right)$ relation

As seen in Section 3.1.1, the slope of the log-law in ZPG boundary layers for two-equation and Reynolds-stress models is imposed through the calibration of the coefficients in the length-scale providing equation with Eq. (3.14), recalled below for the general quantity $\phi = k^m \varepsilon^n$

$$\left(\frac{\left(C_{\phi 2} - C_{\phi 1}\right)\sqrt{C_\mu}}{\kappa_0^2 n^2} - C_{\phi\phi} \right) \sigma_\phi = 1. \tag{5.1}$$

To account for the pressure gradient in the boundary layer, Nickels's analysis [77] suggests to sensitise the von Kármán constant to p^+ with

$$\kappa_p\left(p^+\right) = \frac{\kappa_0}{\sqrt{1 + p^+ y_c^+(p^+)}}, \tag{5.2}$$

which is equivalent to sensitise and locally recalibrate one of the model constants to the local pressure-gradient parameter using Eq. (5.1).

At this point, the modification can be applied to any of the constants and always results in an increase of the dissipation rate ε, hence a decrease of turbulent mixing and a steepening of the velocity profile in the log layer. However, the different choices regarding

the modified coefficient do not affect the model equations identically. Indeed, assuming a model with $C_{\phi\phi} \geqslant 0$, an increase in p^+ leads either to

- $C_{\phi 1}\left(p^+\right)$: increasing the production of ϕ,
- $C_{\phi 2}\left(p^+\right)$: reducing the dissipation of ϕ,
- $C_{\phi\phi}\left(p^+\right)$: increasing the cross-diffusion of ϕ,
- $\sigma_\phi\left(p^+\right)$: reducing the diffusion of ϕ.

Moreover, the four options are not equivalent, since the relation Eq. (5.1) is valid only for the infinite-Reynolds-number log-law region, and no experimental data make it possible to guide the choice.

The common practice for calibration is to set at first $C_{\phi 2}$ and $C_{\phi 1}$ for decaying isotropic turbulence and free-shear flows respectively, then σ_ϕ by following Eq. (5.1). It is therefore natural to consider the ϕ Schmidt number as the adjusted quantity

$$\sigma_\phi\left(p^+\right) = \left(\left(C_{\phi 2} - C_{\phi 1}\right) \frac{\sqrt{C_\mu}}{\kappa_p \left(p^+\right)^2 n^2} - C_{\phi\phi} \right)^{-1}, \tag{5.3}$$

which exhibits a singularity when κ_p is equal to

$$\kappa_p^{\text{singular}} = \sqrt{\frac{\left(C_{\phi 2} - C_{\phi 1}\right)\sqrt{C_\mu}}{C_{\phi\phi} n^2}}. \tag{5.4}$$

For Daris's $k-kl$ model [25], it restricts the amplitude of correction to $\kappa_p > 0.27$, *i.e.* $p^+ < 0.16$. This singularity only exists when $C_{\phi\phi} \neq 0$, so that no restriction applies for the usual two-equation eddy-viscosity models and the considered Reynolds-stress models. In particular, Menter's $k-\omega$ SST and BSL [71], hence also the SSG/LRR-ω RSM [17], only use the mixed cross-diffusion term ($C_{k\phi} \neq 0$) and do not have any singularity.

Alternatively, Knopp [51] and Knopp *et al.* [52] adjust the production term for the ω-equation Eq. (3.15) in the $k-\omega$ and the SSG/LRR-ω models respectively, which becomes

$$C_{\omega 1} \equiv \alpha\left(p^+\right) = \frac{\beta}{\beta^*} - \frac{\left[\kappa_p\left(p^+\right)\right]^2 \sigma}{\sqrt{\beta^*}}. \tag{5.5}$$

Natural deviation

In addition to Nickels's [77] von Kármán-constant correction, the models also have to compensate for a natural deviation of the log-law slope, due to pressure-gradient effects. Indeed, the log layer has been calibrated for the models under ZPG assumptions that are not applicable to APG conditions. As a result, the models do not yield the calibrated value of κ_0 in APG boundary layers. It can be especially observed in Section 4.2 for the EB-RSM and the SSG/LRR-ω model.

This deviation was first investigated by Huang & Bradshaw [45] for a $k-\phi$ model without cross-diffusion terms, Catris [15] extended their work to $k-\phi$ models with cross-diffusion terms and to the Spalart-Allmaras model and Daris [25] to thermal turbulent models $k-\phi$, $k_\theta-\phi_\theta$. Their approach is briefly summarised here.

To find the slope deviation of the model, the von Kármán constant κ_0 is replaced by an unknown κ^* in the log-law

$$\frac{\mathrm{d}U^+}{\mathrm{d}y^+} = \frac{1}{\kappa^* y^+} \tag{5.6}$$

A perturbation method is applied for small pressure gradients $p^+y^+ \ll 1$ and yields

$$\kappa^* = \kappa_0 + \kappa_1 p^+ y^+, \tag{5.7}$$

where κ_1 is the coefficient of the alteration due to the pressure gradient. Note that it differs from κ_p in Eq. (5.2), which describes the whole parameter up to large values of p^+. With the perturbation method and Eq. (5.7), Eq. (5.6) becomes

$$\frac{\mathrm{d}U^+}{\mathrm{d}y^+} = \frac{1}{\left(\kappa_0 + \kappa_1 p^+ y^+\right) y^+} \approx \frac{1}{\kappa_0 y^+} - \frac{\kappa_1}{\kappa_0^2} p^+. \tag{5.8}$$

It can be seen that the ratio of κ_1/κ_0^2 directly quantifies the deviation of velocity profile in the log layer for the considered model in APG flows. Using the APG shear-stress Eq. (2.44), $-\overline{uv}^+ = 1 + p^+y^+$, with Boussinesq's hypothesis,

$$\begin{aligned} \nu_t^+ &= -\overline{uv}^+ \left(\frac{\mathrm{d}U^+}{\mathrm{d}y^+}\right)^{-1} = \left(1 + p^+y^+\right)\left(\kappa_0 + \kappa_1 p^+ y^+\right) y^+ \\ &\approx \kappa_0 y^+ \left[1 + \left(1 + \frac{\kappa_1}{\kappa_0}\right) p^+ y^+\right] \end{aligned} \tag{5.9}$$

The remaining turbulent quantities are also expanded up to the first order in p^+y^+, noting that $\epsilon^+ = \varepsilon^+ y^+$ is constant in the ZPG log layer as a consequence of the equilibrium $\varepsilon^+ = P_k^+$,

$$k^+ = k_0^+ + k_1^+ p^+ y^+, \tag{5.10}$$

$$\epsilon^+ = \epsilon_0^+ + \epsilon_1^+ p^+ y^+, \qquad i.e. \qquad \varepsilon^+ = \frac{\epsilon^+}{y^+} = \frac{\epsilon_0^+}{y^+} + \epsilon_1^+ p^+, \tag{5.11}$$

where k_0^+, k_1^+, ϵ_0^+ and ϵ_1^+ are constant coefficients to be determined. The equilibrium in the log layer at leading order is expressed with Bradshaw's hypothesis Eq. (3.4), $-\overline{uv} = a_1 k$, and gives

$$k_0^+ = \frac{1}{\sqrt{C_\mu}}, \tag{5.12}$$

while combining the expansions (5.10) & (5.11) with the eddy-viscosity relation Eq. (3.3), $\nu_t = C_\mu k^2/\varepsilon$, leads to [15]

$$\epsilon_0^+ = C_\mu \frac{{k_0^+}^2}{\kappa_0} = \frac{1}{\kappa_0}, \tag{5.13}$$

$$\frac{\epsilon_1^+}{\epsilon_0^+} = 2\frac{k_1^+}{k_0^+} - \left(1 + \frac{\kappa_1}{\kappa_0}\right). \tag{5.14}$$

Finally, k_1^+ is determined using the k-equation (see [15, 25]). Substituting all these expressions into the ϕ-equation without cross-diffusion terms, the authors [45, 15, 25] find at first order

$$\frac{\kappa_1}{\kappa_0} = \frac{(n^2 + 2mn - m)\, n\sigma_k + [(n-1)\,(C_{\phi 2} - C_{\phi 1}) + nC_{\phi 2}]\,\sigma_\phi}{(2n-1)\,[2n^2\sigma_k - (C_{\phi 2} - C_{\phi 1})\,\sigma_\phi]}. \tag{5.15}$$

The resulting relation when considering the cross-diffusion terms for ϕ, as well as the equivalent relation for the Spalart-Allmaras model, are detailed in [15]. Note that Eq. (5.1) is recovered as the zero-th order solution.

The calibrated von Kármán constant κ_0 given by Eq. (5.1) and the log-law slope deviation κ_1/κ_0^2 are given in Table 5.1 for various models. It can be seen that the two ε-based models indicate the largest deviations. On the contrary, the $k-kl$ of Daris [25] is expected to predict the universal log-law slope without deviation, due to its design constraints. The Spalart-Allmaras model also deviates little. The conclusions of Huang & Bradshaw [45] regarding the reduced deviation of the $k-\omega$ model compared to the $k-\varepsilon$ model holds for the Reynolds-stress models as well. However, although the SSG/LRR-ω model uses the ω-equation of the Wilcox 1988 $k-\omega$ in the inner layer, the different σ_k constant[1] results in a larger deviation compared to the EVM.

Table 5.1: *Characterisation of the slope deviation in various models*

Model	κ_0	κ_1/κ_0^2
$k-\varepsilon$ Standard	0.433	5.88
$k-\omega$ Wilcox 1988	0.408	1.19
$k-kl$ Daris	0.410	0
EB-RSM	0.408	4.88
SSG/LRR-ω	0.408	2.83
Spalart-Allmaras	0.41	0.36

Note that the EB-RSM uses the GGDH modelling for turbulent transport. The coefficient relation (5.1) for the ε-equation thus becomes

$$\frac{(C_{\varepsilon 2} - C_{\varepsilon 1})\, C_\mu^{3/2}}{\kappa^2 C_s}\sigma_\varepsilon = \frac{\overline{v^2}}{k}, \tag{5.16}$$

where $\overline{v^2}/k$ is assumed constant at leading order through the log layer. In particular, the model has been calibrated with $\overline{v^2}/k = 0.346$. The deviation of the log-law slope for the EB-RSM is computed from Eq. (5.15) by converting σ_k and σ_ε into equivalents in SGDH modelling $\sigma^{\mathrm{GGDH}} = \lambda\sigma^{\mathrm{SGDH}}$ with

$$\lambda = \frac{C_s}{C_\mu}\frac{\overline{v^2}}{k}. \tag{5.17}$$

Huang & Bradshaw [45] also showed that, assuming the exact equilibrium between production and dissipation of k, the $k-\omega$ model yields no deviation. Indeed, in that case,

[1] $\sigma_k = 1$ for the SSG/LRR-ω RSM and $\sigma_k = 2$ in the Wilcox 1988 $k-\omega$ model

the turbulent transport of k is neglected and Eq. (5.15) reduces to

$$\frac{\kappa_1}{\kappa_0} = \frac{n^2 + m\,(2n-1)}{2n\,(2n-1)}. \tag{5.18}$$

Under such conditions, the deviation only depends on m and n, *i.e.* on the length-scale providing quantity $\phi = k^m \varepsilon^n$. In particular,

$$\omega \;\; (m=-1, n=1): \qquad \frac{\kappa_1}{\kappa_0^2} = 0, \tag{5.19}$$

$$\varepsilon \;\; (m=0, n=1): \qquad \frac{\kappa_1}{\kappa_0^2} = \frac{1}{2\kappa_0} \approx 1.22, \tag{5.20}$$

Hence, assuming equilibrium, the SSG/LRR-ω RSM predicts a universal κ_0 in APGs, just as the $k-\omega$ model, whereas the EB-RSM and the $k-\varepsilon$ model still deviate.

Approach limitations

The deviations in Table 5.1 are positive, and thus these models are expected to produce flatter log-law regions in APG boundary layers, as observed for the EB-RSM and the SSG/LRR-ω model in Figure 4.14(a). Hence, the log-law of the considered models deviates in the opposite direction compared to Nickels's analysis [77].

Their deviations are further investigated in Figure 5.1 at $x = 5.0\,\mathrm{m}$, where $p^+ \approx 0.011$. The velocity profiles are shown with respect to the log-law, using both the universal κ_0 and $\kappa_p\,(p^+)$ in Eq. (5.2), and the first-order behaviour given by Eq. (5.15) with $\kappa^* = \kappa_0 + \kappa_1 p^+ y^+$. It can be noticed that for this small value of p^+, the log law with κ_p hardly differs from the universal one. The validity range of expression (5.15) for the natural deviation derived in the previous section reduces to $y^+ \ll 1/p^+ \approx 90$, so that it is not really applicable here, nor in any strong APG flow, more generally. Nonetheless, it can be seen that the models demonstrate the correct trend with a reduction of the log-law slope.

Figure 5.1 also points out that the amplitude of the natural deviation is larger than Nickels's slope alteration [77]. Therefore, the natural deviation of models in APG log layers have to be accounted for first in the slope correction. However, the perturbation method is not valid in strong APG flows and to enforce the correct slope of the log-law for these models, new deviation laws should be investigated first. Note that Knopp [51] and Knopp *et al.* [52] do not use Nickels's von Kármán parameter κ_p as a stand-alone correction but in combination with a sqrt-law correction, analysed in the next chapter, which could provide such an anticipation of the natural deviation.

Finally, this correction raises the question of its application range, whether the sensitised coefficients should be recalibrated locally to the inner layer or across the entire boundary layer.

5.1.2 Spalart-Allmaras model

The Spalart-Allmaras model [104], described in detail in Section 3.1.2, has the advantage of including $\kappa_0 = 0.41$ as a model parameter, which makes it easier to sensitise to the local p^+ and impose Nickels's modified parameter Eq. (5.2). More precisely, the von Kármán constant appears in three distinct terms

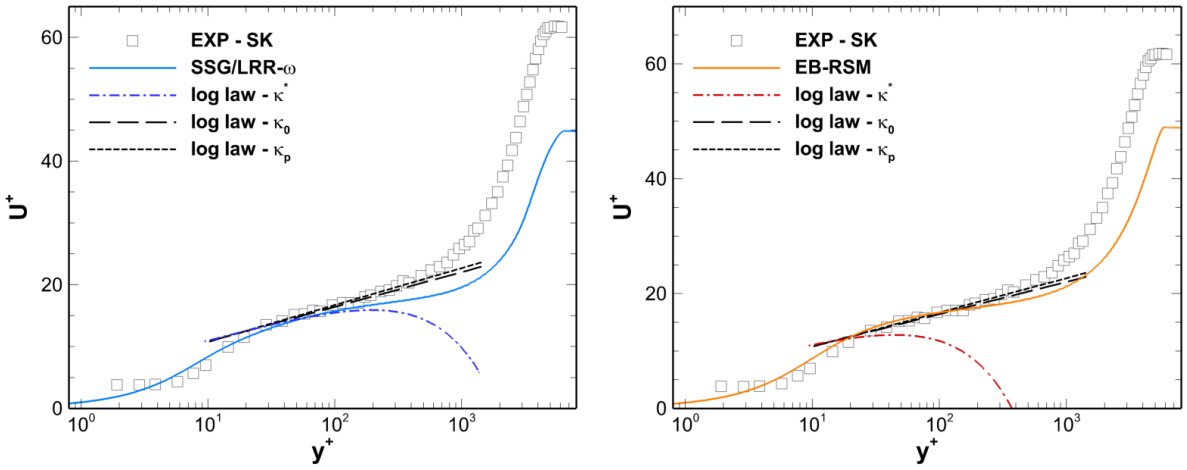

(a) *SSG/LRR-ω RSM* **(b)** *EB-RSM*

Figure 5.1: *Deviation prediction in the Skåre & Krogstad test case at* $x = 5.0\,\mathrm{m}$

- the dissipation constant c_{w1}

$$c_{w1} = \frac{c_{b1}}{\kappa_0^2} + \frac{1 + c_{b2}}{\sigma}, \tag{5.21}$$

  which corresponds to the calibration relation Eq. (5.1) and ensures the log-law slope for $Re \to \infty$,

- the modified strain-rate $\widehat{S}$, Eq. (3.24), which becomes, in the boundary layer approximation,

$$\widehat{S} = \frac{\mathrm{d}U}{\mathrm{d}y} + \frac{\widehat{\nu}}{\kappa_0^2 y^2} f_{v2}. \tag{5.22}$$

  and forces the log-law behaviour to the modified turbulent viscosity $\widehat{\nu}$ down to the wall (see Section 3.1.2),

- the near-wall function f_w for the destruction term, Eq. (3.27), more particularly

$$r = \frac{\widehat{\nu}}{\widehat{S}\,(\kappa_0 y)^2}, \tag{5.23}$$

  which adjusts the destruction term in the buffer layer.

The modified strain-rate $\widehat{S}$ and the near-wall function f_w have a strong impact on the near-wall end of the log-law. They are thus also corrected in the following for consistency across the entire inner layer.

In this chapter, the benefits of the log-law correction, enforcing Nickels's slope coefficient [77], are further investigated using this one-equation model. The different versions of the Spalart-Allmaras model are denoted SA(κ) with κ corresponding to the implemented von Kármán parameter. To simplify its implementation, the correction applies across the entire boundary layer rather than in a delimited range in the inner layer.

5.1.3 Computing p^+ across the boundary layer

To comply with Nickels's log-law [77] and locally sensitise the model coefficients in the boundary layer, the model must have access to the value of the wall pressure-gradient parameter p^+, recalled below

$$p^+ = \frac{\nu}{\rho u_\tau^3} \frac{\mathrm{d}P_w}{\mathrm{d}x}. \tag{5.24}$$

Here, $\mathrm{d}/\mathrm{d}x$ is meant along the wall in the streamwise direction. By definition, it is only defined at the wall, especially due to its dependence on the friction velocity u_τ. Therefore, it has to be propagated into the volume above the wall at each step of the iterative resolution process.

Such a feature is already available in Aether, as some models accounting for the wall-roughness also rely on the friction velocity. The existing algorithm associates each volume-node to the nearest wall-node, so that the value of a skin variable, for instance u_τ or p^+, can be propagated from the wall to the volume. However, the algorithm lacks accuracy since this node association does not correspond to an orthogonal projection on the wall, and is all the more problematic in regions where the volume nodes are not correctly aligned above the wall.

A new algorithm has been developed to address this accuracy issue. It also improves the overall performance of the existing algorithm by taking advantage of parallel computing. Hence, it can be used with limited CPU overhead for applications where the mesh is updated during the simulation, *e.g.* mesh morphing and optimisation processes.

The algorithms are further detailed in Appendix B.1.

5.2 Low-Reynolds number test case

To amplify the effects of the pressure gradient on the log-law slope, APG flows with large p^+ values, *i.e.* $p^+ \geqslant 0.1$, have to be considered. Such strong APG test cases are achieved in low-to-moderate Reynolds-number cases, computed using DNSs or Wall-Resolved LESs. However, equilibrium APG boundary layers, as defined in Section 2.3, have been investigated with DNSs only up to $p^+ \approx 0.016$ (Bobke *et al.* [8]).

Larger p^+ are achieved in the 2D separation bubble DNS from Coleman *et al.* [23], which has been discussed in Section 2.3. The case describes an APG boundary layer developing on a flat plate with a pressure gradient growing until flow separation, for $p^+ = 18$ and its detailed flow statistics are available on NASA's website[2]. Despite its simple geometry, this case requires a velocity transpiration condition on the upper boundary of the computational domain in order to drive the pressure gradient in the flow. This feature is not yet implemented in the CFD code Aether, thus the case cannot be reproduced.

Alternatively, Vinuesa *et al.* [116] provide in KTH's database[3] four Wall-Resolved LESs of a NACA 4412 wing profile computed at an angle of attack of $\alpha = 5°$ for four Reynolds numbers based on the chord c, from $Re_c = 100{,}000$ to $Re_c = 1\,\mathrm{M}$, using a spectral-element method to solve the incompressible Navier-Stokes equations. On the wing suction side, the boundary layer develops in a progressively growing adverse pressure gradient, and

[2] https://turbmodels.larc.nasa.gov/Other_DNS_Data/separation_bubble_2d.html
[3] https://mech.kth.se/~rvinuesa/WingData/

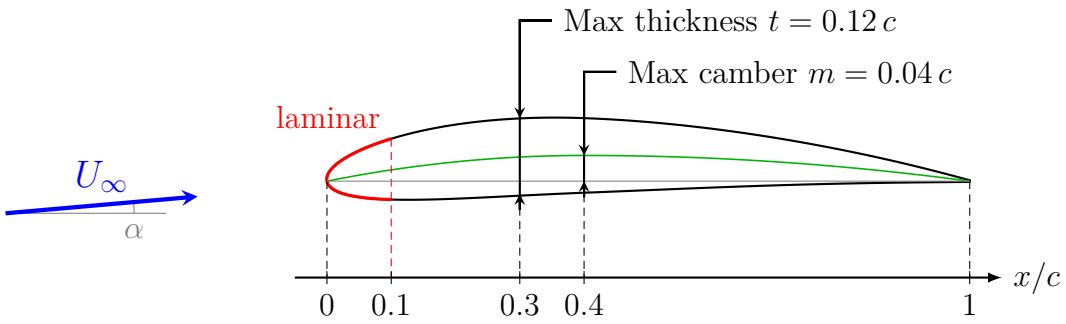

Figure 5.2: *The NACA 4412 wing profile geometry*

reaches $p^+ = 5.9$ and $p^+ = 0.47$ at the trailing edge for $Re_c = 100{,}000$ and $Re_c = 1\,\mathrm{M}$ respectively. To reduce its computational cost, the highest Reynolds-number case uses a coarser grid, with $\Delta x_t^+ < 27$, $\Delta y_n^+ < 0.96$ and $\Delta z^+ < 13.5$. This resolution has been assessed at $Re_c = 400{,}000$ by comparing with the DNS carried out by Hosseini *et al.* [44] on the same geometry (see also Vinuesa *et al.* [115]) and shown to be accurate for the mean flow and the Reynolds shear-stress.

To avoid low-Re effects, the case at $Re_c = 1\,\mathrm{M}$ is here reproduced. The geometry consists in a NACA wing profile with a maximum camber of 4 % located at 40 % chord and a maximum thickness of 12 % achieved at 30 % chord, illustrated in Figure 5.2. In the LES, turbulence is tripped at 10 % chord on both sides of the wing using a volume-force method, detailed in [94], which imitates tripping strips used in wind-tunnel experiments.

The RANS computations are run on a 2D domain, where the wing profile is at the center of a 200c-radius disc. The mesh includes 42,000 nodes, with an average first-cell height of $y^+ < 1$. The far-field pressure is set to $P_\infty = 100\,\mathrm{hPa}$ and the Mach number is set to $M = 0.2$ for the flow to remain incompressible. The tripping is imposed in Aether by forcing the production terms in the model equations to zero for $x/c \leqslant 0.1$ within a distance of 15 % chord above the wall.

5.3 Application to the Spalart-Allmaras model

5.3.1 Impact of the slope modification

The impact of modifying the von Kármán parameter in the Spalart-Allmaras model is assessed by considering SA(κ_0) and SA(κ_p), *i.e.* the original model and the direct implementation with Nickels's parameter.

To compare the resulting log-law slopes, the velocity profiles are extracted at the same p^+ values, since the correction directly depends on this parameter. Therefore, they do not necessarily correspond to the same chordwise position, as indicated in Table 5.2. This alteration in the boundary layer affects the mean flow and the pressure-gradient distribution on the wing. More precisely, from the table it can be seen that the SA(κ_0) predicts progressively stronger APG, especially after $x/c \geqslant 88\,\%$, resulting in the profiles to be extracted upstream of the reference stations. The modified SA(κ_p) is even more affected, the value of p^+ observed at the trailing edge for the reference LES being reached at $x/c = 85\,\%$.

Figure 5.3 shows the influence of the pressure gradient on the velocity profile for both models at $p^+ = 0.151$ on the left and the corresponding log-law diagnostic function

Table 5.2: *Correspondence between the pressure-gradient parameter p^+ and the chordwise position x/c for the LES and the two Spalart-Allmaras model versions on the NACA 4412 profile at $Re_c = 1\,\mathrm{M}$, $\alpha = 5°$*

p^+	x/c		
	LES	SA(κ_0)	SA(κ_p)
0.008	60.0 %	62.2 %	59.1 %
0.024	81.0 %	80.8 %	76.7 %
0.061	89.7 %	88.0 %	80.8 %
0.106	93.1 %	90.8 %	82.6 %
0.151	94.8 %	92.1 %	83.1 %
0.216	96.6 %	93.2 %	83.8 %
0.470	98.3 %	94.8 %	84.8 %

Eq. (2.43) on the right, recalled below

$$\Xi_{\log} = \left(y^+ \frac{\mathrm{d}U^+}{\mathrm{d}y^+} \right)^{-1}. \tag{5.25}$$

The slope of the log-law observed in Figure 5.3(a) can be related to the apparent von Kármán constant, noted $\overline{\kappa}$ and evaluated in the overlap region as

$$\overline{\kappa} = \max_{\text{overlap region}} \Xi_{\log}. \tag{5.26}$$

In addition to the agreement of the LES with the theoretical value κ_p, the diagnostic function in Figure 5.3(b) points out that both models are strongly affected by the pressure gradient, with the modified SA(κ_p) model paradoxically deteriorating the results of the original model. Indeed, the correction is combined to the natural deviation of the SA(κ_0)

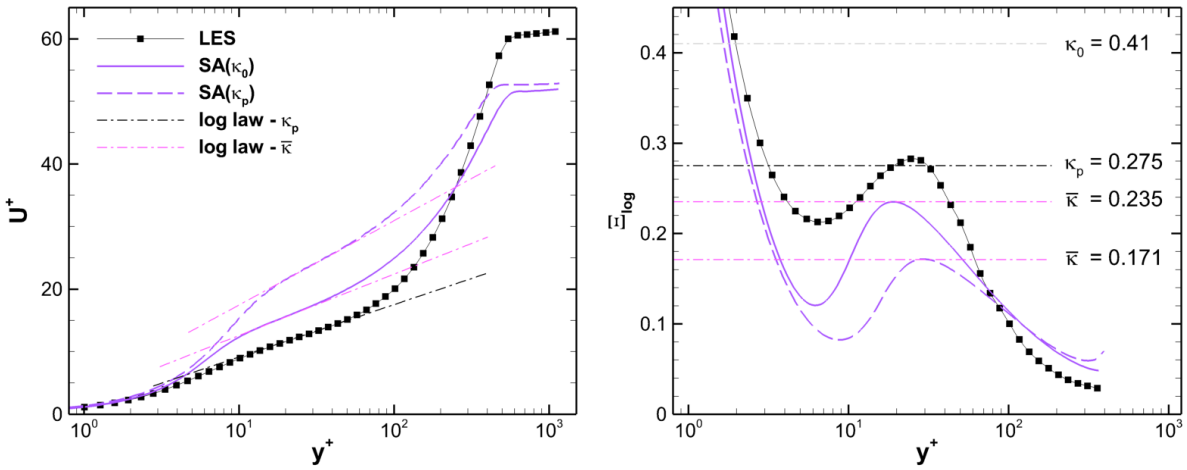

(a) *Velocity* **(b)** *Diagnostic function*

Figure 5.3: *SA(κ_0) and SA(κ_p) models profiles on the NACA 4412 at $p^+ = 0.151$*

model in the log-law and results in a reduction of the apparent slope parameter $\overline{\kappa}$ of the original model, already reduced compared to κ_0. Note that this natural response of the Spalart-Allmaras model to the pressure gradient goes against the perturbation analysis, which predicts an increase of κ instead (see Table 5.1).

To assess the impact of the modification of the von Kármán parameter in the model equation, the ratio between the observed parameters of the modified model $\overline{\kappa}\,[\mathrm{SA}\,(\kappa_p)]$ and of the original model $\overline{\kappa}\,[\mathrm{SA}\,(\kappa_0)]$ has been investigated and is shown in Figure 5.4 for different values of p^+. The influence of the Reynolds number is also tested by extending the NACA 4412 test case to $Re_c = 4\,\mathrm{M}$. The figure displays a satisfactory agreement of the observed ratio with the theoretical ratio κ_p/κ_0, which indicates a correct response of the model to the change of κ directly in the model equation. Thus, the natural deviation and the κ_p-correction are not coupled. The scattering of the data does not show a clear dependence on Re_c, this behaviour can thus be considered insensitive to Re-effects for moderate and high Reynolds numbers.

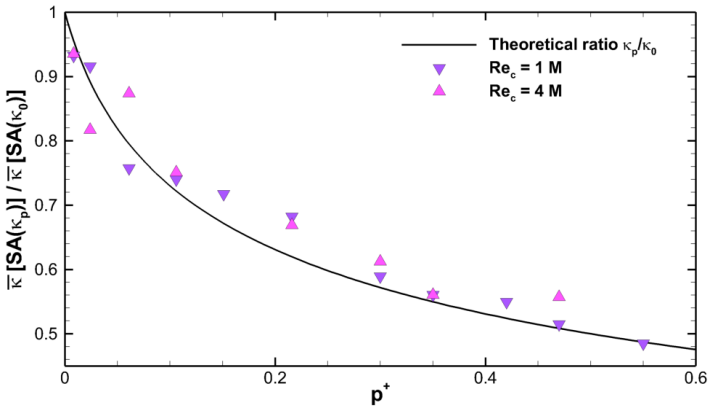

Figure 5.4: *Ratio of the apparent von Kármán constants between the SA(κ_p) and the SA(κ_0) on the NACA 4412 wing profile*

5.3.2 Correction accounting for the natural deviation bias

Since the Spalart-Allmaras model correctly reproduces the modification of the von Kármán parameter in the model equation, the expected log-law slope with $\overline{\kappa} = \kappa_p$ can be enforced by accounting for the natural deviation directly in the model. To that end, this deviation is investigated and quantified using the NACA 4412 test case.

Figure 5.5 presents the natural deviation as the ratio between the von Kármán parameter $\overline{\kappa}$ actually observed in the profiles and the parameter κ involved in the model, respectively κ_0 for the SA(κ_0) model and κ_p for the SA(κ_p) model, at both Reynolds numbers. In particular, it can be seen that the ratio $\overline{\kappa}/\kappa$ only depends on p^+ and is not related to the considered κ, which makes it possible to locally predict the deviation of the model.

Using a regression on the four computed data sets for $\kappa \in \{\kappa_0\,;\kappa_p\}$ and $Re_c \in \{1\,\mathrm{M}\,;4\,\mathrm{M}\}$, the following correction law, shown in Figure 5.5, is proposed

$$r_\kappa\left(p^+\right) = \frac{\overline{\kappa}}{\kappa} = a\log(p^+ + c) + b. \tag{5.27}$$

The best fit is obtained for

$$a \simeq -0.135, \qquad b \simeq 0.344, \qquad c = \exp\left(\frac{1-b}{a}\right) \simeq 0.0077,$$

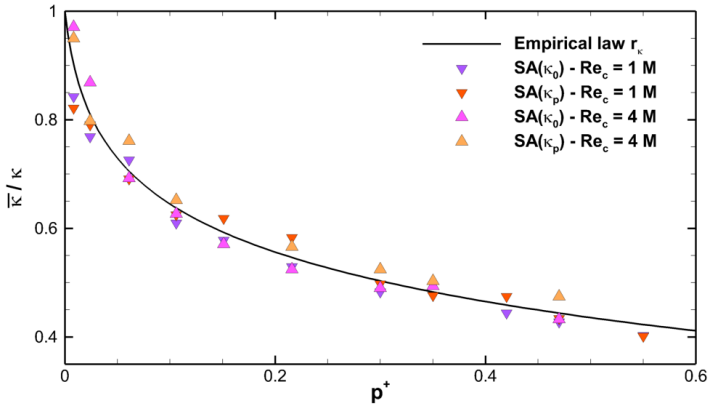

Figure 5.5: *Apparent-to-target κ ratio for the Spalart-Allmaras model*

where the constant c is chosen to ensure $r_\kappa(p^+ = 0) = 1$, *i.e.* no alteration to the original model in ZPG conditions. The coefficient of determination of the regression, $r^2 = 0.98$, indicates a satisfactory correlation of Eq. (5.27) with the CFD results.

A new version of the Spalart-Allmaras model with a corrected slope is proposed, the SA(κ_c) model, defining the new von Kármán parameter as

$$\kappa_c\left(p^+\right) = \frac{\kappa_p\left(p^+\right)}{r_\kappa\left(p^+\right)} = \frac{\kappa_0}{r_\kappa\left(p^+\right)\sqrt{1 + p^+ y_c^+}}. \tag{5.28}$$

Results are shown in Figure 5.6 for $p^+ = 0.061$. The new SA(κ_c) model yields a log-law slope in good agreement with Nickels's analysis and the overprediction of the velocity in the log-law region with respect to the LES, observed for all the models, is reduced. The diagnostic function in Figure 5.6(b) once again points out the correct response to the change of κ in the model equation, the new SA(κ_c) model achieving here the expected apparent value of $\overline{\kappa_c} = \kappa_p$. Although closer to the LES reference, the peak value of $\Xi_{\log}$ is

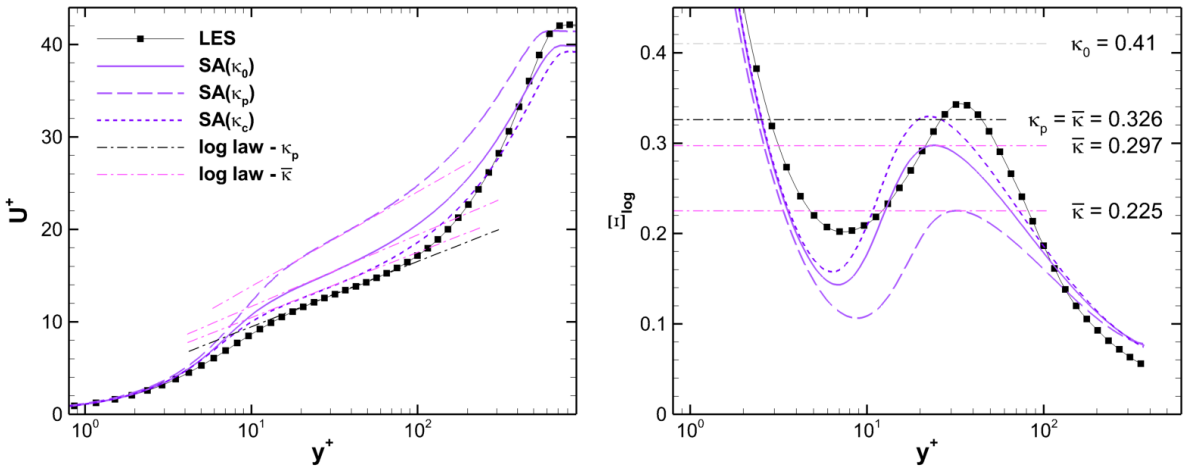

(a) *Velocity* **(b)** *Diagnostic function*

Figure 5.6: *SA(κ_0) and SA(κ_p) models profiles on the NACA 4412 at $p^+ = 0.061$*

reached for smaller y^+ and indicates a shift of the log-law region towards the wall, which is visually confirmed from the velocity profile in Figure 5.6(a). The reduced error on the intercept observed on the velocity profile can also be assessed with $\Xi_{\log}$, whose local minimum value in the buffer layer is increased, indicating a milder slope in this region and thus a more progressive velocity gain below the log layer.

The corrected SA(κ_c) model exhibits overall improved results compared to the original SA(κ_0). In particular, it comes with an improved p^+-distribution on the suction side of the wing, shown in Figure 5.7(a). Indeed, the SA(κ_c) predicts a streamwise distribution of p^+ along the wing that agrees with the LES reference up to $x/c = 93\,\%$, whereas the SA(κ_0) model starts deviating for $x/c = 80\,\%$.

The displacement and momentum thicknesses, plotted in Figure 5.7(b), are however only slightly improved with the new model. This inefficiency can be linked to the defect layer prediction, which is barely improved. Figure 5.6(a) indeed shows that the free-stream velocity is not improved. Therefore, this correction is not sufficient and another one is needed for the outer region to correctly reproduce the mean flow in this test case.

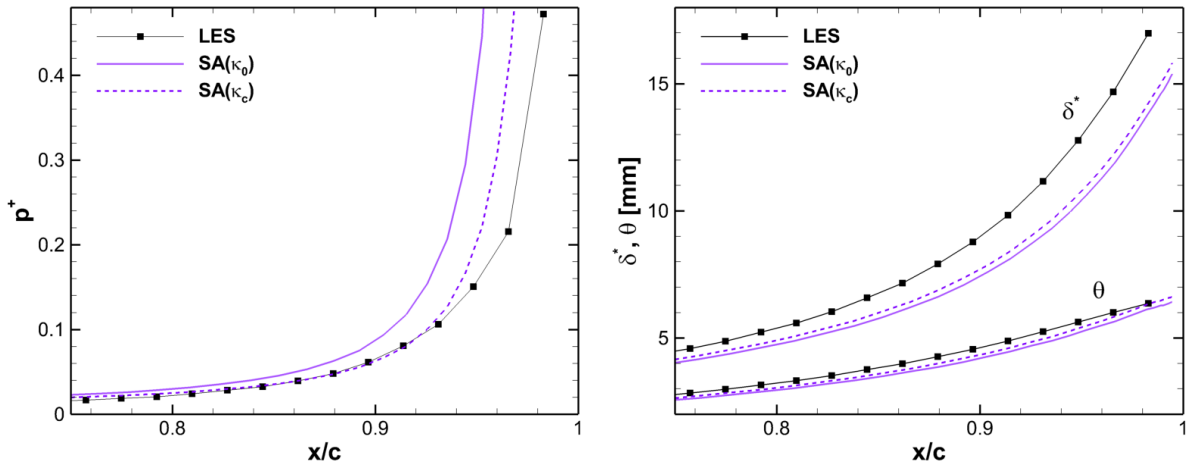

(a) *Pressure-gradient parameter* **(b)** *Displacement and momentum thicknesses*

Figure 5.7: *Integral quantities on the NACA 4412 upper side trailing edge*

5.3.3 Deviation of the log-law intercept

In addition to the slope steepening, Figures 5.3(a) & 5.6(a) also reveal that the intercept value of the log-law does not follow the reference, the results of the SA(κ_0), SA(κ_p) and SA(κ_c) models systematically appearing shifted upwards, even though the amplitude of this shift is reduced with the new κ_c calibration.

The apparent intercept, noted $\overline{B}$, has been computed for the LES and the two models to best fit the velocity profiles using the log-law with the apparent $\overline{\kappa}$. They are compared in Figure 5.8 to the empirical relation introduced by Nagib & Chauhan [75]

$$\overline{\kappa}\overline{B} = 1.6\left(\exp(0.1663\overline{B}) - 1\right), \tag{5.29}$$

which has been determined by fitting several experiments and DNSs of turbulent pipe, channels and boundary layers under different pressure-gradient conditions.

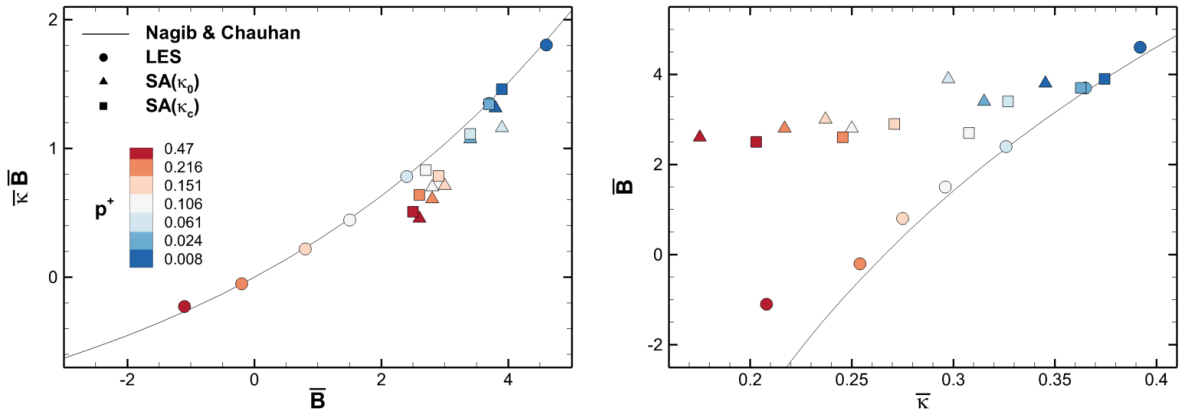

(a) $\overline{\kappa}\overline{B} = f\left(\overline{B}\right)$ **(b)** $\overline{B} = f\left(\overline{\kappa}\right)$

Figure 5.8: *Apparent intercept* $\overline{B}$ *for the LES and the Spalart-Allmaras model variants*

Figure 5.8(a) shows the great agreement of the LES results with the empirical relation. On the contrary, the SA(κ_0) and SA(κ_c) models gradually deviate from the empirical relation, pointing out their misprediction of the intercept, the corrected model improving the predictions and yielding a good agreement up to $p^+ = 0.1$.

This deviation is magnified in Figure 5.8(b), which directly associates the observed intercept $\overline{B}$ to the corresponding observed slope parameter $\overline{\kappa}$. In particular, it can be seen that both models display a similar slope, but the SA(κ_c) model yields improved results over the SA(κ_0) model due to a better prediction of $\overline{\kappa}$ with respect to the pressure-gradient parameter p^+ in comparison with the LES. Note that the LES confirms the experimental observations of a reduction of $\overline{B}$ with increasing APGs (Clauser [21] and Nagano *et al.* [74], Knopp [54], see Section 2.3.3).

Contrary to Figure 5.8(a), Figure 5.8(b) shows a reasonable agreement of the SA(κ_c) model with Eq. (5.29) only up to around $p^+ = 0.024$. Similarly, it can be noted that the LES deviates from the empirical relation in the figure on the right for $p^+ = 0.47$, which is not visible in the figure on the left. This highlights the tolerance of the plot $\overline{\kappa}\overline{B} = f\left(\overline{B}\right)$ to errors in experimental measurements, as stated by Nagib & Chauhan [75].

Figure 5.9 presents velocity profiles at three different values of p^+ for the SA(κ_c) and SA(κ_0) models, compared to LES. In particular, it confirms that the shift of the log-law intercept from the reference occurs for larger APGs with the SA(κ_c) model, which correctly predicts the velocity level in the log layer up to $p^+ \approx 0.03$ as observed in Figure 5.8(b), whereas the SA(κ_0) model starts overpredicting the velocity for $p^+ \approx 0.01$.

The overprediction of the intercept indicates an exaggeration of the viscous sublayer thickness. Figure 5.10 presents the velocity gradient at different p^+ locations, along with the viscous sublayer law (2.34), recalled below,

$$U^+ = y^+\left(1 + \frac{1}{2}p^+y^+\right), \qquad i.e. \qquad \frac{\mathrm{d}U^+}{\mathrm{d}y^+} = 1 + p^+y^+. \tag{5.30}$$

It can be seen here that the models follow this behaviour too far away from the wall. For instance, at $p^+ = 0.47$, both models comply with the sublayer law up to $y^+ \approx 3$, whereas turbulence becomes non-negligible at $y^+ \approx 1$ according to the reference, so that the sublayer law does not apply above this point in the LES. As a result, the velocity gradient presents an overshoot in the buffer layer, which causes the overprediction of the

velocity in the log layer, despite a correct velocity gradient in this region. The improved intercept can here again be noticed, as the velocity gradient is slightly corrected with the SA(κ_c) model.

Therefore, the proposed correction for the von Kármán constant enables the correct prediction of the slope of the log layer, by accounting for the natural deviation of the Spalart-Allmaras model. The overprediction of the log-law intercept $\overline{B}$, which is gradually

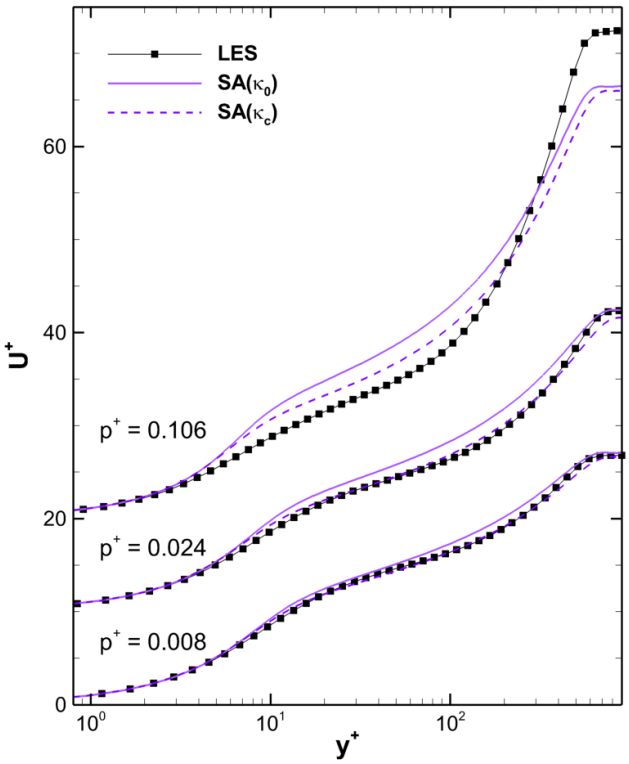

Figure 5.9: *SA(κ_0) and SA(κ_c) models velocity profiles for different adverse pressure gradients*

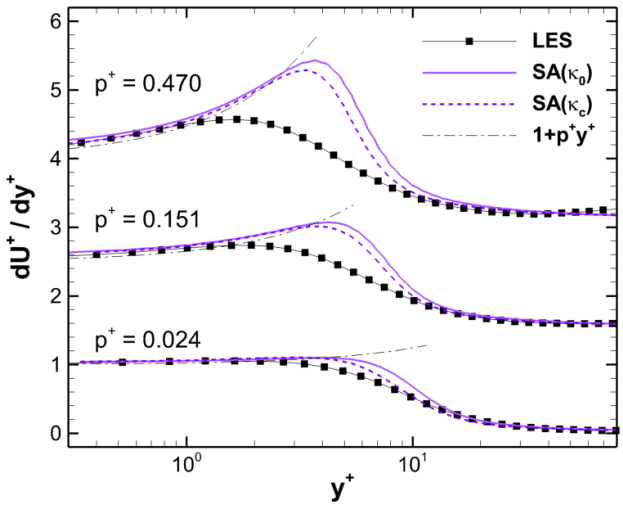

Figure 5.10: *SA(κ_0) and SA(κ_c) models velocity gradients in the buffer layer for different adverse pressure gradients*

observed for the original SA(κ_0) model, is slightly reduced. The SA(κ_c) model thus yields a satisfactory log layer for a larger range of p^+.

To further improve the Spalart-Allmaras model, an additional correction would be required in the buffer layer, by adding correction terms or by sensitising its near-wall blending functions f_{v1}, f_{v2} and f_w, defined in Eqs. (3.25) & (3.27), to strong pressure gradients.

5.4 Application to the Skåre & Krogstad test case

The corrected model SA(κ_c) has been applied on the Skåre & Krogstad configuration, to evaluate the influence of the correction on a higher-Reynolds-number case. As in Section 4.2, the QCR correction is activated.

Due to the increased Reynolds number, the wall pressure gradient and the amplitude of the correction remain small ($p^+ \leqslant 0.013$ *i.e.* $\kappa_p \geqslant 0.38$). The SA(κ_c) model still slightly improves the velocity profiles in Figure 5.11, with the logarithmic layer being more accurately reproduced. On the other hand, the profiles in physical quantities on the right show that the correction, despite going in the expected direction, is far from enough. The change in the von Kármán coefficient seems indeed to have a limited impact on the defect layer. Similarly to the conclusions for the NACA 4412 test case, another correction must here be considered.

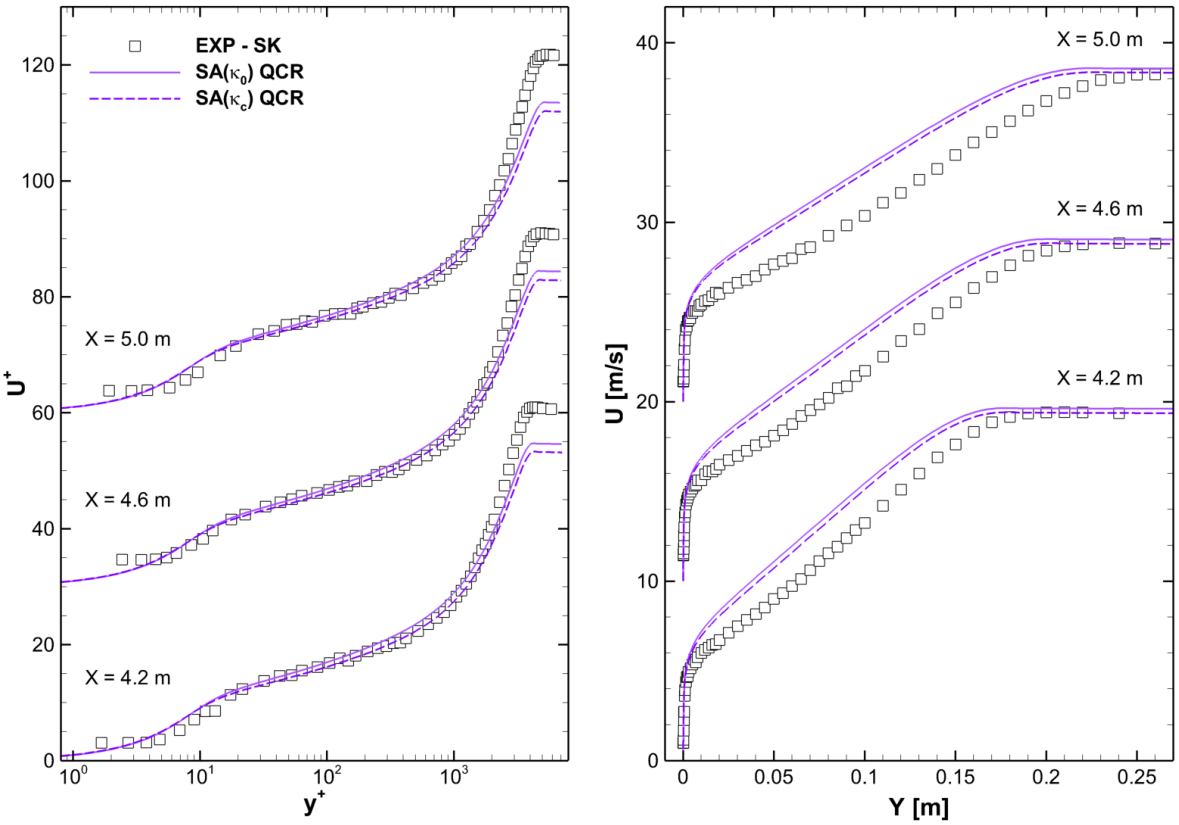

(a) *Wall-units* **(b)** *Dimensional quantities*

Figure 5.11: *Velocity profiles in the Skåre & Krogstad test case for the SA(κ_0) and SA(κ_c) models*

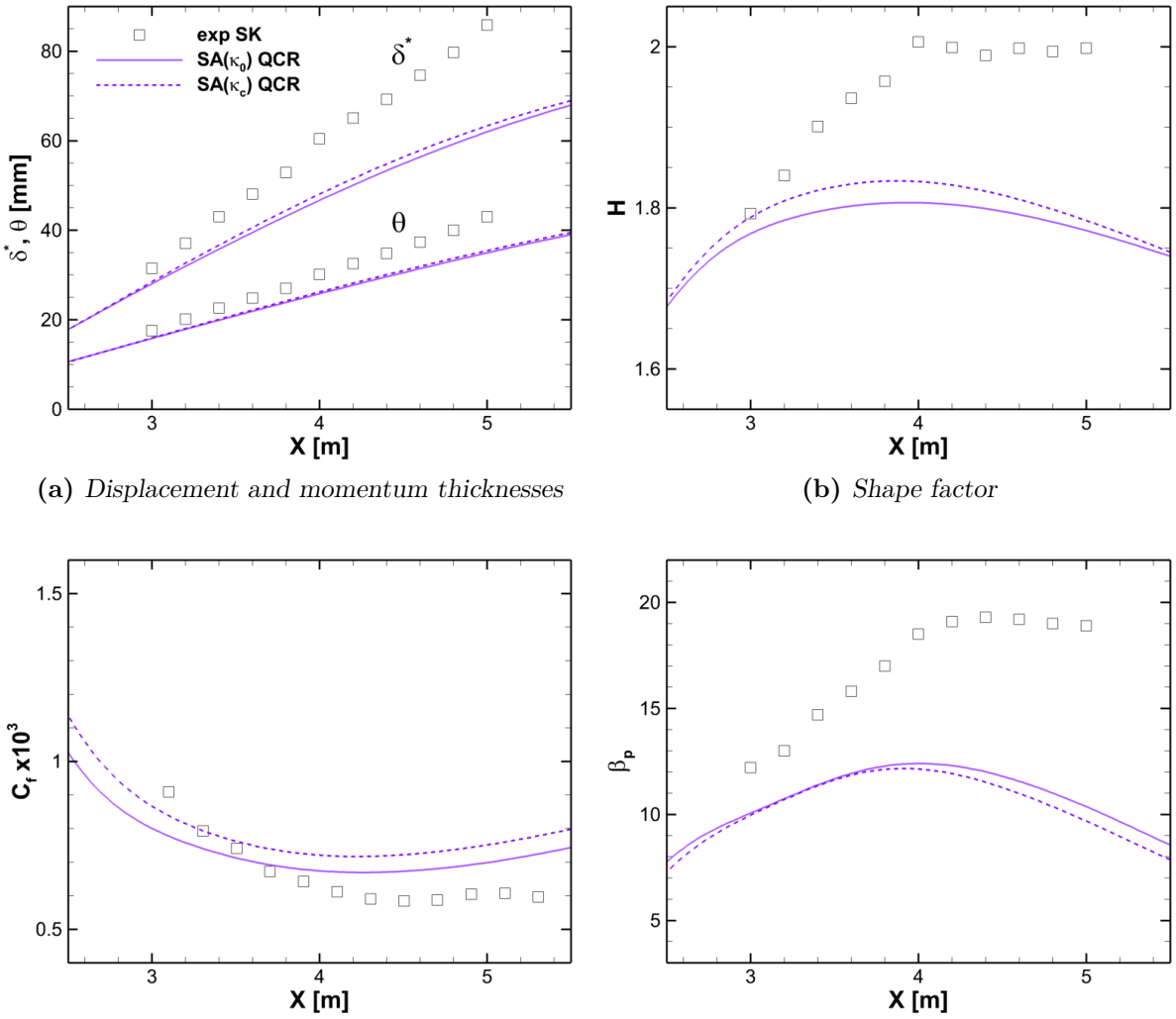

(a) *Displacement and momentum thicknesses*

(b) *Shape factor*

(c) *Skin friction coefficient*

(d) *Clauser's pressure-gradient parameter*

Figure 5.12: *Integral quantities in the Skåre & Krogstad test case for the SA(κ_0) and SA(κ_c) models*

Figure 5.12 shows the small impact of the correction on the integral quantities. The slight improvement in the velocity profiles positively affects the displacement thickness and the shape factor, plotted in Figures 5.12(a) & (b), but the amplitude of the correction on δ^* and H remains hardly significant.

The prediction of the skin friction coefficient, displayed in Figure 5.12(c), is deteriorated and consequently, so is the pressure-gradient parameter β_p in Figure 5.12(d). Indeed, the small improvement of δ^* is compensated by the overprediction of C_f. Paradoxically, according to Knopp [51], the correction is expected to reduce the friction, by decreasing the dissipation rate in the inner layer, *i.e.* by increasing the destruction of ν_t in the Spalart-Allmaras model, hence by decreasing the friction velocity to make the model more susceptible to flow separation. However, the compensated correction with $\kappa_c = \kappa_p / r_\kappa$, anticipating the natural deviation of the Spalart-Allmaras model, actually results in a larger $\overline{\kappa}$ than the original SA(κ_0) model, *i.e.* a milder slope, and therefore explains the increase of the friction.

5.5 Conclusions

A first correction for adverse pressure gradients has been investigated in this chapter, to correctly account for the log-law slope alteration, which is progressively steepened with an increasing p^+.

The local recalibration of the von Kármán coefficient according to Nickels's analysis [77] has been successfully implemented in the Spalart-Allmaras model. For this occasion, a new algorithm has been developed, which computes the wall-distance more efficiently and propagates skin variables such as the pressure-gradient parameter p^+ more accurately in the volume for the model to locally adapt its coefficients. To anticipate the model slope deviation with increasing p^+, an additional empirical law has been proposed. Combined with the κ_p-recalibration, this makes the model able to accurately predict the expected log-law slope.

Indeed, the new model offers a visible improvement in the velocity profiles, correctly reproducing the log-law region. For very strong APGs, the model requires further developments to improve the behaviour of the model in the viscous sublayer, which leads to an exaggerated apparent log-law intercept. Moreover, it has been observed that the correction barely affects the outer region, and as a consequence, does not significantly improves the integral quantities describing the mean flow.

The slope correction has not been generalised to two-equation and Reynolds-stress models. Indeed, it is made complicated by the indirect involvement of the von Kármán constant as a constraint on the model coefficients, but also by the strong natural deviation of the models regarding their slope predictions in APG conditions.

The value of Nickels's κ_p coefficient directly depends on p^+, which decreases as the Reynolds-number increases. Consequently, in aeronautical applications, the behaviour of two-equation and Reynolds-stress models in the log layer appears to be mostly due to the natural deviation of the model. The correction of the model should therefore first address this deviation. This justifies the use of the alteration of the von Kármán parameter according to Nickels's analysis [77] as a secondary correction in the models of Knopp [51] and Knopp *et al.* [52].

Chapter 6

Square-root region correction

Several authors justified the inaccuracy of turbulence models in APG flows by pointing out their shortcomings regarding the predictions of the sqrt layer. A comprehensive analysis of compatibility issue of two-equation EVMs and RSMs is provided in a general form, with the assumed behaviour of the turbulence equations in the square-root region. The existing solutions to alleviate this incompatibility issue are then reviewed. Finally, new developments are applied to the SSG/LRR-ω RSM and the EB-RSM and validated on the Skåre & Krogstad APG case.

6.1 Turbulence budgets

6.1.1 Discrepancies in the square-root region

The sqrt-law is investigated for a general $k-\phi$ model, without cross-diffusion terms to keep the derivation simple and close to the considered ε and ω-based RSMs. The model equations simplify under the boundary layer approximation, *i.e.* steady and two-dimensional flow, and more precisely under the overlap region approximation. Therefore, the flow is assumed far enough from the wall so that viscous diffusion vanishes, yet still in the inner layer where convection is negligible. The transport equations thus read

$$0 = \quad \nu_t \left(\frac{\mathrm{d}U}{\mathrm{d}y}\right)^2 \quad - \quad \varepsilon \quad + \frac{\mathrm{d}}{\mathrm{d}y}\left(\frac{\nu_t}{\sigma_k}\frac{\mathrm{d}k}{\mathrm{d}y}\right) \tag{6.1a}$$

$$0 = C_{\phi 1}\nu_t \left(\frac{\mathrm{d}U}{\mathrm{d}y}\right)^2 \frac{\phi}{k} - C_{\phi 2}\varepsilon\frac{\phi}{k} + \frac{\mathrm{d}}{\mathrm{d}y}\left(\frac{\nu_t}{\sigma_\phi}\frac{\mathrm{d}\phi}{\mathrm{d}y}\right) \tag{6.1b}$$

with $\phi = k^m\varepsilon^n$.

In this chapter, the von Kármán coefficient is simply noted κ, to adapt to the different definitions considered by the authors (Townsend's mixing length slope κ_l for Rao & Hassan [86], universal log-law slope κ_0 for Catris [15] and Daris [25], Nickels's log-law slope κ_p for Knopp [51] and Knopp *et al.* [52]).

Model compatibility with the generalised sqrt-law

The study of Knopp [51] regarding the compatibility of the $k-\omega$ model with the generalised sqrt-law is here extended to the general form of a $k-\phi$ model, Eqs. (6.1). Starting from the shear-stress Eq. (2.44) and the velocity gradient Eq. (2.47) in the overlap region, recalled

below

$$\overline{uv}^+ = 1 + p^+ y^+, \qquad \frac{\mathrm{d}U^+}{\mathrm{d}y^+} = \frac{\sqrt{1+p^+y^+}}{\kappa y^+}, \tag{6.2}$$

Boussinesq's hypothesis yields

$$\nu_t^+ = -\overline{uv}^+ \left(\frac{\mathrm{d}U^+}{\mathrm{d}y^+}\right)^{-1} = \kappa y^+ \sqrt{1+p^+y^+}. \tag{6.3}$$

Assuming that Bradshaw's relation (3.4), $-\overline{uv} = a_1 k$, still holds for equilibrium APG flows, and using the eddy-viscosity definition $\nu_t = C_\mu \sqrt[n]{k^{m+2n}/\phi}$, the behaviour of the turbulent quantities k and ϕ becomes

$$k^+ = \frac{-\overline{uv}^+}{a_1} = \frac{1+p^+y^+}{a_1}, \tag{6.4}$$

$$\phi^+ = C_\mu^n \frac{{k^+}^{m+2n}}{{\nu_t^+}^n} = \frac{1}{a_1^m \kappa^n} \frac{(1+p^+y^+)^{m+\frac{3}{2}n}}{{y^+}^n}. \tag{6.5}$$

As in ZPG conditions, Bradshaw's hypothesis implies equilibrium between production and dissipation rate in the k-equation. Consequently, Eq. (6.1a) reduces to

$$0 = D_k^{T+} = \frac{\kappa}{a_1 \sigma_k} p^+ \frac{1+\frac{3}{2}p^+y^+}{\sqrt{1+p^+y^+}}. \tag{6.6}$$

This relation is verified only if $p^+ = 0$. Hence, the k-equation is not compatible with the APG overlap region described by the generalised sqrt-law.

Similarly, substituting Eqs. (6.3)–(6.5) in the ϕ-equation (6.1b) leads to

$$0 = \frac{a_1^{-m}}{\kappa^{n-1}} \frac{(1+p^+y^+)^{m+\frac{3}{2}n+\frac{1}{2}}}{{y^+}^{n+1}} \left((C_{\phi 1} - C_{\phi 2}) \frac{a_1}{\kappa^2} + \frac{n^2}{\sigma_\phi} \frac{1 + Ap^+y^+ + B{p^+}^2{y^+}^2}{(1+p^+y^+)^2} \right) \tag{6.7}$$

where

$$A = \frac{1}{2n^2}\left(2r\left(1-2n\right)+n\right), \qquad B = \frac{1}{2n^2}\, r\left(2r+1\right), \qquad r = m + \frac{1}{2}n. \tag{6.8}$$

Thus for a generic length-scale providing quantity ϕ, turbulent transport (last term in brackets in Eq. (6.7)) does not have the same dependency on p^+y^+ as production and dissipation. Noting that the model constants are linked through the log-law calibration Eq. (3.14),

$$\frac{(C_{\phi 2} - C_{\phi 1})\, a_1}{\kappa^2 n^2} = \frac{1}{\sigma_\phi}, \tag{6.9}$$

Eq. (6.7) simplifies into

$$0 = (A-2)\, p^+y^+ + (B-1)\, {p^+}^2{y^+}^2. \tag{6.10}$$

The ϕ-equation is compatible with the sqrt-law only if Eq. (6.10) is valid for any value of y^+ and p^+. This implies that the polynomial coefficients must cancel out, *i.e.* $A = 2$ and $B = 1$. The solution corresponds to $m = 0$ and $n = 1/3$. Therefore, the compatibility condition requires $\phi \equiv \sqrt[3]{\varepsilon}$. It does not represent a physical quantity, as its dimension is a length to the ²/₃ per unit time.

This general study shows that usual two-equation models are not able to reproduce the sqrt-law behaviour due to pressure gradients, under the hypotheses used to calibrate them.

Simplification for $p^+y^+ \gg 1$

The compatibility of EVMs with the square-root region has also been investigated by Rao & Hassan [86], Catris [15] and Daris [25], under the additional hypothesis $p^+y^+ \gg 1$. It corresponds to the asymptotic behaviour of the previous section in strong APG, where the sqrt-law reduces to Eq. (2.50), recalled below

$$\widehat{U} = \frac{2}{\kappa}\sqrt{\widehat{y}} + cst \qquad \text{with} \quad \widehat{y} = \frac{yu_p}{\nu}, \quad \widehat{U} = \frac{U}{u_p}. \tag{6.11}$$

It is written with the pressure-velocity scale $u_p = u_\tau \sqrt[3]{p^+}$, defined in Section 2.3.4 to include the pressure-gradient parameter p^+ in the scaling and simplify the notation. The velocity gradient and the shear-stress read

$$\frac{\mathrm{d}\widehat{U}}{\mathrm{d}\widehat{y}} = \frac{1}{\kappa}\widehat{y}^{-1/2}, \qquad \widehat{\overline{uv}} = -\widehat{y}. \tag{6.12}$$

Given these expressions, the solutions are sought as power-laws of $\widehat{y}$

$$\widehat{\nu_t} = A_{\nu_t}\widehat{y}^{\,r_{\nu_t}}, \qquad \widehat{k} = A_k\widehat{y}^{\,r_k}, \qquad \widehat{\phi} = A_\phi\widehat{y}^{\,r_\phi}. \tag{6.13}$$

The definition of the eddy viscosity Eq. (3.3) and Boussinesq's hypothesis Eq. (3.1) impose respectively

$$\widehat{\nu_t} = C_\mu \sqrt[n]{\frac{\widehat{k}^{m+2n}}{\widehat{\phi}}} = C_\mu \sqrt[n]{\frac{A_k^{m+2n}}{A_\phi}}\widehat{y}^{\,\left((m+2n)r_k - r_\phi\right)/n}, \tag{6.14}$$

$$\widehat{\nu_t} = -\widehat{\overline{uv}}\left(\frac{\mathrm{d}\widehat{U}}{\mathrm{d}\widehat{y}}\right)^{-1} = \kappa\widehat{y}^{\,3/2}, \tag{6.15}$$

which leads to

$$A_\phi = \left(\frac{C_\mu}{\kappa}\right)^n A_k^{m+2n}, \tag{6.16}$$

$$r_\phi = (m+2n)\,r_k - \frac{3}{2}n. \tag{6.17}$$

To be compatible with the asymptotic sqrt-law behaviour, each of the model equations must verify two constraints: the exponents of every terms must be equal and the sum of their coefficients must be zero.

Substituting Eqs. (6.12) & (6.13) in Eq. (6.1) yields the following constraints on the exponents

$$\frac{1}{2} = \frac{1}{n}r_\phi - \frac{m}{n}r_k = r_k - \frac{1}{2}, \tag{6.18}$$

$$\frac{1}{2} + r_\phi - r_k = \left(1+\frac{1}{n}\right)r_\phi - \left(1+\frac{m}{n}\right)r_k = r_\phi - \frac{1}{2}, \tag{6.19}$$

which are compatible with Eq. (6.17) and verified for

$$r_k = 1 \qquad \text{and} \qquad r_\phi = m + \frac{1}{2}n. \tag{6.20}$$

These exponents comply with the expressions (6.4) & (6.5) found for the generalised sqrt-law in the previous section when $p^+y^+ \gg 1$.

Similarly, the constraints on the coefficients from Eq. (6.1) read

$$0 = \frac{1}{\kappa} - A_\phi^{1/n} A_k^{-m/n} + r_k \left(r_k + \frac{1}{2}\right) \frac{\kappa}{\sigma_k} A_k \tag{6.21}$$

$$0 = C_{\phi 1} \frac{1}{\kappa} - C_{\phi 2} A_\phi^{1+1/n} A_k^{-1-m/n} + r_\phi \left(r_\phi + \frac{1}{2}\right) \frac{\kappa}{\sigma_\phi} A_\phi \tag{6.22}$$

Using Eq. (6.16), these constraints become

$$0 = C_\mu A_k^2 - \frac{3}{2} \frac{\kappa^2}{\sigma_k} A_k - 1, \tag{6.23}$$

$$0 = C_{\phi 2} C_\mu A_k^2 - r_\phi \left(r_\phi + \frac{1}{2}\right) \frac{\kappa^2}{\sigma_\phi} A_k - C_{\phi 1}. \tag{6.24}$$

Therefore, applying Bradshaw's hypothesis

$$\widehat{k} = \frac{-\widehat{uv}}{a_1} = \frac{1}{a_1} \widehat{y} \qquad i.e. \qquad A_k = \frac{1}{a_1} = \frac{1}{\sqrt{C_\mu}}, \tag{6.25}$$

the constraints on the coefficients cannot be verified, especially since Eq. (6.23) requires $\sigma_k \to \infty$. Once again, the equation of the general form of the $k - \phi$ model are not compatible with the sqrt-law behaviour, even in the limit $p^+y^+ \gg 1$. To assess the ability for a two-equation model to predict a satisfactory sqrt region, Catris [15] derived two constraints on the velocity profile and the turbulent kinetic energy profile respectively. The $k - kl$ model of Daris [25] has been designed using these constraints, for which it yields a fair approximation.

Removing the constraint of Bradshaw's hypothesis Alternatively, Rao & Hassan [86] looked for a solution without using Bradshaw's hypothesis. They considered the Wilcox 1988 $k - \omega$ model [119] and from the constraint on the ϕ-equation, Eq. (6.24), they found

$$A_k = \frac{1}{a_1} \sqrt{\frac{C_{\omega 1}}{C_{\omega 2}}} = \sqrt{\frac{\alpha}{\beta}} \tag{6.26}$$

where the last expression uses Wilcox notations (see Eq. (3.15)). As a result, the constraint on the k-equation, Eq. (6.23), yields

$$0 = \frac{3}{2} \frac{\kappa}{a_1 \sigma_k} \sqrt{\frac{C_{\omega 1}}{C_{\omega 2}}} + \frac{1}{3\kappa} \qquad i.e. \qquad \sigma_k < 0 \tag{6.27}$$

Since the Schmidt number σ_k, already calibrated in ZPG conditions, must be strictly positive, this conclusion exhibits the incompatibility of the k-equation in the $k - \omega$ model. Note that defining A_k with the k-equation first would results in the incompatibility of the ϕ-equation.

Thus, simplifying the behaviour of the turbulent quantities under the asymptotic condition $p^+y^+ \gg 1$ does not lift the incompatibility of two-equation EVMs with the sqrt-law prediction.

6.1.2 Pressure diffusion term

Compatibility of the sqrt-law behaviour with the k-equation

To overcome the discrepancy observed in the turbulence budget, Rao & Hassan [86], followed by by Knopp [51] and Knopp *et al.* [52], suggest to add a term depending on the pressure gradient directly in the k-equation of the Wilcox 1988 $k-\omega$ model. Instead of modelling the pressure velocity correlation $\overline{u_i p}$ together with the triple correlation, they introduce a dedicated term for the pressure diffusion[1] D_k^p

$$\rho D_k^p = -\frac{\partial \overline{u_i p}}{\partial x_i} = -\frac{\partial}{\partial x_i}\left(\frac{\mu_t}{\sigma_k^p}\frac{a_{ij}}{\rho}\frac{\partial P}{\partial x_j}\right). \tag{6.28}$$

In the boundary layer, this expression is equivalent to a GGDH model, Eq.(3.45), applied to the mean pressure and reduces to

$$\rho D_k^p = -\frac{\mathrm{d}}{\mathrm{d}y}\left(\frac{\mu_t}{\sigma_k^p k}\,\overline{uv}\frac{\mathrm{d}P}{\mathrm{d}x}\right) = -\frac{\mathrm{d}}{\mathrm{d}y}\left(C_s^p \rho \frac{k}{\varepsilon}\,\overline{uv}\frac{\mathrm{d}P}{\mathrm{d}x}\right) \tag{6.29}$$

where the eddy viscosity has been rewritten for a $k-\varepsilon$ model in the last term to yield an expression similar to Eq.(3.45), with $C_s^p = C_\mu/\sigma_k^p$. Note that D_k^p vanishes along with the pressure gradient, so that this term does not alter the model in ZPG flows.

To justify the modelling of D_k^p, the authors using it [86, 51, 52] consider its asymptotic behaviour in the sqrt region. Using the generalised sqrt-law Eq. (6.2) alongside with Bradshaw's relation, the pressure diffusion term becomes

$$D_k^{p+} = \frac{a_1}{\sigma_k^p}\,p^+\frac{\mathrm{d}\nu_t^+}{\mathrm{d}y^+} = \frac{a_1\kappa}{\sigma_k^p}\,p^+\frac{1+\frac{3}{2}p^+y^+}{\sqrt{1+p^+y^+}}. \tag{6.30}$$

The pressure Schmidt number σ_k^p can then be determined by balancing the turbulent kinetic energy budget, *i.e.* balancing the pressure diffusion with the turbulent transport due to the pressure gradient Eq. (6.6). Including D_k^p in the k-equation leads to

$$0 = \frac{a_1\kappa}{\sigma_k^p}\left(\frac{1}{a_1^2\sigma_k}+\frac{1}{\sigma_k^p}\right)p^+\frac{1+\frac{3}{2}p^+y^+}{\sqrt{1+p^+y^+}} \tag{6.31}$$

The sqrt-law behaviour for k is therefore achieved with $\sigma_k^p = -a_1^2\sigma_k$. For the Wilcox 1988 $k-\omega$ model,

$$\sigma^{*p} = \frac{1}{\sigma_k^p} \approx -5.56 \tag{6.32}$$

Due to their alternative derivation without Bradshaw's relation and using Wilcox notations, Rao & Hassan [86] found

$$\sigma^{*p} = -\sigma^*\frac{\alpha}{\beta} - \frac{2}{9\kappa^2}\sqrt{\frac{\alpha}{\beta}} \approx -6.03, \tag{6.33}$$

where they retained $\kappa \equiv \kappa_l = 0.51$, as suggested by Townsend [111] for the sqrt-law. The authors then recalibrated the parameter to $\sigma^{*p} = -5.13$ to improve the agreement with experimental data. This value remains close to Eq. (6.32).

The pressure diffusion is a local correction for the overlap region in APG boundary layers and should not alter the free-stream region. The implementation of this correction in the different models proposed in the literature is further detailed in Section 6.2.

[1] written here with the notation defined in this thesis

Compatibility of the sqrt-law behaviour with the ϕ-equation

To solve the incompatibility Eq. (6.10) in the ω-equation, Knopp [51] suggests to renew the operation, introducing a pressure diffusion term for ω, D_ω^p, defined by dimensionally consistent analogy to D_k^p. Knopp's analysis is here extended to a general two-equation model. The pressure diffusion term for the length-scale providing quantity ϕ is thus expressed as

$$\rho D_\phi^p = -\frac{\phi}{k}\frac{\partial}{\partial x_i}\left(\frac{\mu_t}{\sigma_\phi^p}\frac{a_{ij}}{\rho}\frac{\partial P}{\partial x_j}\right), \tag{6.34}$$

This can be expressed under the generalised log-law hypothesis as

$$D_\phi^{p+} = \frac{a_1^{2-m}}{\kappa^{n-1}\sigma_\omega^p} p^+ \left(1+\frac{3}{2}p^+y^+\right)\frac{\left(1+p^+y^+\right)^{m+\frac{3}{2}(n-1)}}{{y^+}^n}. \tag{6.35}$$

Substituting in the ϕ-equation, Eq. (6.7) transforms into

$$0 = \frac{n^2}{\sigma_\phi}\left((A-2)\,p^+y^+ + (B-1)\,{p^+}^2{y^+}^2\right) + \frac{a_1^2}{\sigma_\phi^p}p^+y^+\left(1+\frac{3}{2}p^+y^+\right). \tag{6.36}$$

Eq. (6.10) now becomes

$$c_1\; p^+y^+ + c_2\; {p^+}^2{y^+}^2 = 0 \tag{6.37}$$

with

$$c_1 = \frac{a_1^2}{\sigma_\phi^p} + \frac{n^2}{\sigma_\phi}(A-2), \qquad c_2 = \frac{3}{2}\frac{a_1^2}{\sigma_\phi^p} + \frac{n^2}{\sigma_\phi}(B-1).$$

The constraint can be written as a second-order polynomial in $X = p^+y^+$, for which all the coefficients must by zero. No values of σ_ϕ^p satisfies both $c_1 = 0$ and $c_2 = 0$, *i.e.* the pressure diffusion term D_ϕ^p cannot alone impose the sqrt-law behaviour in the ϕ-equation. Adding the non-viscous cross-diffusion terms from the general ϕ-equation Eq. (3.13)

$$D_\phi^{cd1} = C_{kk}\frac{\nu_t\phi}{k^2}\left(\frac{\mathrm{d}k}{\mathrm{d}y}\right)^2, \qquad D_\phi^{cd2} = C_{k\phi}\frac{\nu_t}{k}\frac{\mathrm{d}k}{\mathrm{d}y}\frac{\mathrm{d}\phi}{\mathrm{d}y}, \qquad D_\phi^{cd3} = C_{\phi\phi}\frac{\nu_t}{\phi}\left(\frac{\mathrm{d}\phi}{\mathrm{d}y}\right)^2, \tag{6.38}$$

Eq. (6.10) now becomes $c_0 + c_1\; p^+y^+ + c_2\; {p^+}^2{y^+}^2 = 0$ with

$$c_0 = C_{\phi\phi}n^2, \tag{6.39}$$

$$c_1 = \frac{a_1^2}{\sigma_\phi^p} + \frac{1}{\sigma_\phi}\left(\left(r+\frac{1}{2}n\right)(1-2n) - n^2\right) - C_{k\phi}n - 2C_{\phi\phi}nr, \tag{6.40}$$

$$c_2 = \frac{3}{2}\frac{a_1^2}{\sigma_\phi^p} + \frac{1}{\sigma_\phi}\left(r\left(r+\frac{1}{2}\right) - n^2\right) + C_{kk} + C_{k\phi}r + C_{\phi\phi}r^2, \tag{6.41}$$

and $r = m + \frac{1}{2}n$, with the same constraints on the coefficients $c_0 = 0$, $c_1 = 0$ and $c_2 = 0$.

The constraint $c_0 = 0$ implies $C_{\phi\phi} = 0$. From the three remaining constants (σ_ϕ^p, C_{kk}, $C_{k\phi}$) involved in c_1 and c_2, only two are needed to solve the constraint $c_1 = 0$ and $c_2 = 0$, so that $C_{kk} = 0$ or $C_{k\phi} = 0$.

Considering $\phi \equiv \omega$, Knopp [51] retains the mixed cross-diffusion term D_ω^{cd2}, already used in several versions of the $k-\omega$ model (*cf.* [71, 120]). More generally, the mixed

cross-diffusion for ϕ has the advantage of being computable together with the implicit convective-flux term of the equation, which becomes

$$\underline{\boldsymbol{\mathcal{F}}}^{\text{conv}} = \rho\underline{\mathbf{U}} - C_{k\phi}\frac{\nu_t}{k}\underline{\nabla}k \tag{6.42}$$

and offers therefore numerical robustness. Keeping the mixed cross-diffusion term D_ϕ^{cd2} in the ϕ-equation, the constraints Eqs. (6.40) & (6.41) yield

$$\sigma_\phi^p = a_1^2\sigma_\phi\frac{4\left(m+2n\right)}{4m\left(m\left(n-1\right)+n\left(3n-2\right)\right)+3n^2\left(3n-1\right)}, \tag{6.43}$$

$$C_{k\phi} = -\frac{1}{\sigma_\phi}\frac{4m\left(m+4n-1\right)+5n\left(3n-1\right)}{4\left(m+2n\right)}. \tag{6.44}$$

Hence, adding both the pressure diffusion and the mixed cross-diffusion in the ϕ-equation, along with D_k^p (Eq. (6.28)) in the k-equation, enables all two-equation models to correctly predict the sqrt-law behaviour. In particular, applying these expressions for the specific dissipation rate ω and the dissipation rate ε,

$$\omega\ \ (m=-1,n=1): \qquad \sigma_\omega^p = 2a_1^2\sigma_\omega, \qquad C_{k\omega} = -\frac{1}{2\sigma_\omega} \tag{6.45}$$

$$\varepsilon\ \ (m=0,n=1): \qquad \sigma_\varepsilon^p = \frac{4}{3}a_1^2\sigma_\varepsilon, \qquad C_{k\varepsilon} = -\frac{5}{4\sigma_\varepsilon} \tag{6.46}$$

Note that the values found for ω are those proposed by Knopp [51].

Impact on the log-law behaviour

To assess the validity range of the pressure diffusion terms introduced in both equations, Knopp [51] also investigates the compatibility in the log layer with APG. It corresponds to the extent of the overlap region where $p^+y^+ \ll 1$ so that the log-law still applies and the velocity gradient can be approximated to

$$\frac{\mathrm{d}U^+}{\mathrm{d}y^+} = \frac{1}{\kappa y^+}. \tag{6.47}$$

However, he keeps the shear-stress as $-\overline{uv}^+ = 1+p^+y^+$ to account for the pressure gradient as a small perturbation.

From Boussinesq's and Bradshaw's hypotheses, the new expressions for the $k-\phi$ model read

$$\nu_t^+ = \kappa y^+\left(1+p^+y^+\right), \qquad k^+ = \frac{1+p^+y^+}{a_1}, \qquad \phi^+ = \frac{1}{a_1^m\kappa^n}\frac{\left(1+p^+y^+\right)^{m+n}}{{y^+}^n} \tag{6.48}$$

The additional terms become

$$D_k^{p+} = \frac{a_1\kappa}{\sigma_k^p}p^+\left(1+2p^+y^+\right), \tag{6.49}$$

$$D_\phi^{p+} = \frac{a_1^{2-m}}{\kappa^{n-1}\sigma_\phi^p}\frac{\left(1+p^+y^+\right)^{m+n+1}}{y^{n+1}}p^+y^+\left(1+2p^+y^+\right), \tag{6.50}$$

$$D_\phi^{cd2+} = C_{k\phi}\frac{a_1^{-m}}{\kappa^{n-1}}\frac{\left(1+p^+y^+\right)^{m+n-1}}{y^{n+1}}p^+y^+\left(n-mp^+y^+\right). \tag{6.51}$$

Substituting the APG log-law behaviour Eqs. (6.47)–(6.48) in Eq. (6.1a) yields

$$0 = D_k^{T+} = \frac{\kappa}{a_1 \sigma_k} p^+ \left(1 + 2p^+ y^+\right) \tag{6.52}$$

thus the constraint

$$D_k^T + D_k^p = 0 \tag{6.53}$$

still holds with the value $\sigma_k^p = -a_1 \sigma_k$ arrived at in the sqrt-law region. Therefore, the k-equation with the new D_k^p pressure diffusion term is compatible in the entire overlap region.

Regarding the ϕ-equation, the additional terms lead to a new second-order polynomial in $p^+ y^+$. Again, the constraint of all coefficients being zero reads

$$0 = c_1 = \left(m\,(1-2n) - n^2\right) \frac{1}{\sigma_\phi} + \frac{a_1^2}{\sigma_\phi^p} + C_{k\phi} n, \tag{6.54}$$

$$0 = c_2 = m\,(m+1)\,\frac{1}{\sigma_\phi} + 2\frac{a_1^2}{\sigma_\phi^p} - C_{k\phi} m, \tag{6.55}$$

which yields

$$\sigma_\phi^p = a_1^2 \sigma_\phi \frac{m+2n}{m\,(m\,(n-1) + n\,(n-1))}, \tag{6.56}$$

$$C_{k\phi} = \frac{1}{\sigma_\phi} \frac{m\,(m+4n-1) + 2n^2}{m+2n}. \tag{6.57}$$

These solutions are compatible with the coefficients found for the sqrt layer Eqs. (6.43) & (6.44) only if $\{m, n\} = \{1, 0\}$, *i.e.* $\phi \equiv k$ which is not a possible length-scale providing quantity, or $\{m, n\} = \left\{-\frac{3}{2}, 1\right\}$, *i.e.* $\phi \equiv 1/l$, corresponding to the inverse of the turbulent length scale.

Alternatively, considering the usual ϕ-equation (6.1b) without correction, the previous system simplifies into

$$0 = m\,(1-2n) - n^2, \qquad 0 = m\,(m+1) \tag{6.58}$$

which yields $\{m, n\} = \{-1, 1\}$, *i.e.* $\phi \equiv \omega$.

Therefore, the $k - 1/l$ and $k - \omega$ models appear to be the only two-equation models able to correctly reproduce the entire overlap region in APG. However, for the $k-\omega$ model, the correction terms D_ω^p and D_ω^{cd2} must be deactivated in the log layer.

Knopp [51] relies once again on blending functions in his $k - \omega$ model, detailed in Section 6.2.1, to restrict the activation range for the additional terms towards the wall.

Summary

The compatibility achieved for each equation is summarised in Table 6.1.

In particular, the dissipation rate ε cannot be entirely corrected, as the ε-equation is not compatible with the log-law either with corrective terms or without. To improve the EB-RSM (Section 6.3.2), this equation will be left unchanged in the log-region, as for the ω-equation.

Table 6.1: *Compatibility of the model equations in the considered regions*

Model variable	log-law	sqrt-law
k	✓ (with D_k^p)	✓ (with D_k^p)
$1/l$	✓ (with $D_{1/l}^p$, $D_{1/l}^{\mathrm{cd2}}$)	✓ (with $D_{1/l}^p$, $D_{1/l}^{\mathrm{cd2}}$)
ω	✓	✓ (with D_ω^p, D_ω^{cd2})
other ϕ	×	✓ (with D_ϕ^p, D_ϕ^{cd2})

6.1.3 Extension of the analysis to Reynolds-stress models

Following the previous asymptotic approach for $p^+y^+ \gg 1$, the investigation for the sqrt-law behaviour is now carried out for the Reynolds-stress transport equations. The Reynolds stresses are written as

$$\widehat{\overline{u^2}} = A_{11}\widehat{y}^{\,r_{11}}, \quad \widehat{\overline{v^2}} = A_{22}\widehat{y}^{\,r_{22}}, \quad \widehat{\overline{w^2}} = A_{33}\widehat{y}^{\,r_{33}}, \quad \widehat{\overline{uv}} = -\widehat{y} \tag{6.59}$$

and substituted into the corresponding transport equations, assuming a 2D boundary layer with no viscosity and no convection,

$$0 = -2\widehat{\overline{uv}}\frac{\mathrm{d}\widehat{U}}{\mathrm{d}\widehat{y}} + \widehat{\phi_{11}} - \frac{2}{3}\widehat{\varepsilon} + \frac{\mathrm{d}}{\mathrm{d}\widehat{y}}\left(D\frac{\mathrm{d}\widehat{\overline{u^2}}}{\mathrm{d}\widehat{y}}\right) \tag{6.60a}$$

$$0 = \widehat{\phi_{22}} - \frac{2}{3}\widehat{\varepsilon} + \frac{\mathrm{d}}{\mathrm{d}\widehat{y}}\left(D\frac{\mathrm{d}\widehat{\overline{v^2}}}{\mathrm{d}\widehat{y}}\right) \tag{6.60b}$$

$$0 = \widehat{\phi_{33}} - \frac{2}{3}\widehat{\varepsilon} + \frac{\mathrm{d}}{\mathrm{d}\widehat{y}}\left(D\frac{\mathrm{d}\widehat{\overline{w^2}}}{\mathrm{d}\widehat{y}}\right) \tag{6.60c}$$

$$0 = -\widehat{\overline{v^2}}\frac{\mathrm{d}\widehat{U}}{\mathrm{d}\widehat{y}} + \widehat{\phi_{12}} + \frac{\mathrm{d}}{\mathrm{d}\widehat{y}}\left(D\frac{\mathrm{d}\widehat{\overline{uv}}}{\mathrm{d}\widehat{y}}\right) \tag{6.60d}$$

where D stands either for $\widehat{\nu_t} = C_\mu\widehat{k}^2/\varepsilon$ if the model uses the SGDH or for $C_s\widehat{\overline{v^2}}\,\widehat{k}/\widehat{\varepsilon}$ if it uses the GGDH, with

$$\widehat{k} = \frac{1}{2}\widehat{\overline{u_iu_j}}\delta_{ij} = A_k\widehat{y}^{\,r_k}, \qquad \widehat{\varepsilon} = \widehat{\phi}^{\,1/n}\widehat{k}^{\,m/n} = A_\varepsilon\widehat{y}^{\,r_\varepsilon} \tag{6.61}$$

Similarly to the k-equation, which corresponds to half the trace of Eq. (6.60), the constraints on the exponents are verified with

$$r_{11} = r_{22} = r_{33} = r_k = 1, \qquad r_\varepsilon = \frac{1}{2}, \tag{6.62}$$

which is consistent with the constraint Eq. (6.20) found for EVMs. Consequently, the anisotropy tensor a_{ij} is constant and

$$a_{ij} = \frac{A_{ij}}{A_k} - \frac{2}{3}\delta_{ij}, \quad a_{12} = \frac{A_{12}}{A_k} = -\frac{1}{A_k}, \qquad \text{with} \quad A_k = \frac{1}{2}\left(A_{11} + A_{22} + A_{33}\right) \tag{6.63}$$

The constraints on the coefficients A_{ij} extracted from Eq. (6.60) are long and complex relations due to the redistribution terms, expressed here using the general form of the SSG

and LRR models (Eqs. (3.37) & (3.41) with $C_6 = C_7 = C_8 = 0$). Noting $\widetilde{A_{ij}} = A_{ij}/A_k$, they reduce to

$$\begin{aligned} 0 = {} & \frac{2C_2}{3}\widetilde{A_{11}}^2 - \left(C_1 + \frac{C_1^*}{\kappa}\frac{1}{A_\varepsilon} + \frac{4C_2}{9} + \frac{3C_D}{2}\frac{1}{{A_\varepsilon}^2\widetilde{A_{12}}^3}\right)\widetilde{A_{11}} \\ & - \frac{C_2}{3}\left(\widetilde{A_{22}}^2 + \widetilde{A_{33}}^2 - \widetilde{A_{12}}^2\right) + \frac{2}{\kappa}\left(1 + \frac{C_1^*}{3} - \frac{C_4}{6} - \frac{C_5}{2}\right)\frac{1}{A_\varepsilon} + \frac{2C_1}{3} + \frac{8C_2}{9} - \frac{2}{3} \end{aligned} \tag{6.64}$$

$$\begin{aligned} 0 = {} & \frac{2C_2}{3}\widetilde{A_{22}}^2 - \left(C_1 + \frac{C_1^*}{\kappa}\frac{1}{A_\varepsilon} + \frac{4C_2}{9} + \frac{3C_D}{2}\frac{1}{{A_\varepsilon}^2\widetilde{A_{12}}^3}\right)\widetilde{A_{22}} \\ & - \frac{C_2}{3}\left(\widetilde{A_{11}}^2 + \widetilde{A_{33}}^2 - \widetilde{A_{12}}^2\right) + \frac{1}{\kappa}\left(\frac{2C_1^*}{3} - \frac{C_4}{3} + C_5\right)\frac{1}{A_\varepsilon} + \frac{2C_1}{3} + \frac{8C_2}{9} - \frac{2}{3} \end{aligned} \tag{6.65}$$

$$\begin{aligned} 0 = {} & \frac{2C_2}{3}\widetilde{A_{33}}^2 - \left(C_1 + \frac{C_1^*}{\kappa}\frac{1}{A_\varepsilon} + \frac{4C_2}{9} + \frac{3C_D}{2}\frac{1}{{A_\varepsilon}^2\widetilde{A_{12}}^3}\right)\widetilde{A_{33}} \\ & - \frac{C_2}{3}\left(\widetilde{A_{11}}^2 + \widetilde{A_{22}}^2 + 2\widetilde{A_{12}}^2\right) + \frac{2}{3\kappa}\left(C_1^* + C_4\right)\frac{1}{A_\varepsilon} + \frac{2C_1}{3} - \frac{8C_2}{9} - \frac{2}{3} \end{aligned} \tag{6.66}$$

$$\begin{aligned} 0 = {} & \left(C_1 + \frac{C_1^*}{\kappa}\frac{1}{A_\varepsilon} + C_2\left(\widetilde{A_{33}} - \frac{2}{3}\right)\right)\widetilde{A_{12}}^2 + \frac{3C_D}{2}\frac{1}{{A_\varepsilon}^2\widetilde{A_{12}}} \\ & - \frac{1}{2\kappa}\left(C_5\widetilde{A_{11}} - \left(C_5 - 2\right)\widetilde{A_{22}} + C_4\widetilde{A_{33}} - C_3 + C_3^*\sqrt{A_2} - \frac{2}{3}\right)\frac{1}{A_\varepsilon} \end{aligned} \tag{6.67}$$

with

$$A_2 = a_{ij}a_{ij} = \widetilde{A_{ij}}\widetilde{A_{ij}} - \frac{4}{3}, \qquad D = \frac{C_D}{A_\varepsilon\widetilde{A_{12}}^2}, \qquad \text{and} \qquad C_D = \begin{cases} C_\mu & \text{SGDH} \\ C_s\widetilde{A_{22}} & \text{GGDH} \end{cases}$$

In the present analysis, the general ϕ-equation, Eq. (6.1b), is considered as the length-scale providing equation. In particular, writing $\widehat{\phi} = \widehat{k}^m\widehat{\varepsilon}^n$ and using the general expression of the diffusion coefficient D, Eq. (6.24) becomes

$$0 = \left(C_{\phi 1}\frac{1}{\kappa} - C_{\phi 2}A_\varepsilon\right)A_\varepsilon\widetilde{A_{12}}^3 + r_\phi\left(r_\phi + \frac{1}{2}\right)C_D \tag{6.68}$$

The resulting system consists in four strongly coupled polynomials, with no analytical solution. To assess the sqrt-law behaviour prediction of RSMs, an *a priori* solution from the Skåre & Krogstad experiment [99] is sought for A_ε, using experimental values for the $\widetilde{A_{ij}}$ constants. In figure 6.1, the sqrt-law behaviour is fitted to the Reynolds stresses and yields

$$\widetilde{A_{11}} = 0.44, \quad \widetilde{A_{22}} = 0.285, \quad \widetilde{A_{33}} = 0.275, \quad \widetilde{A_{12}} = -0.3 \tag{6.69}$$

Condition Eq. (6.63) is verified with $\sum_i \widetilde{A_{ii}} = 1$ and, noting that $\widetilde{A_{12}} = -1/A_k$, this is consistent with $A_k = 1/a_1$, found using Bradshaw's relation for $k-\phi$ models.

The remaining unknown A_ε is solved for each of the four constraints Eqs. (6.64)–(6.67) and its solutions are given in Table 6.2. Since negative solutions for A_ε are not physical, it confirms that neither the SSG/LRR-ω RSM nor the EB-RSM are able to reproduce the sqrt-law behaviour. More particularly, the different equations yield different solutions, indicating their incompatibility between one another and therefore pointing out

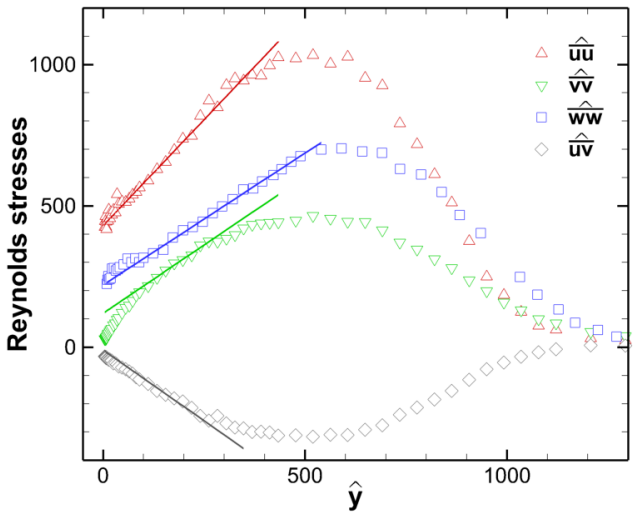

Figure 6.1: *Sqrt-law behaviour of the Reynolds stresses in the Skåre & Krogstad experiment [99] at* $x = 5.0\,\mathrm{m}$

Table 6.2: A priori *solutions for* A_ε

Model	Eq. (6.64)	Eq. (6.65)	Eq. (6.66)	Eq. (6.67)
LRR + SGDH	9.9	−58.2	−55.1	−0.3
SSG + GGDH	−5.1	−0.8	1.0	−1.7

the shortcomings of the Reynolds-stress transport equations in the sqrt region. It was expected from the previous section, as the k-equation corresponds to half their trace.

Note that the model used for the turbulent transport does not affect the conclusion. Using the SGDH modelling with the SSG redistribution instead of the GGDH modelling alters the solutions less than 2.4 %, the maximum variation being found for the turbulent shear-stress equation constraint, Eq. (6.67).

The analysis of the Reynolds stresses in the square-root region makes it possible to show the incompatibility of the transport equations with the expected sqrt-law behaviour. However, the strong coupling between the constraint equations (6.64)–(6.67) makes it difficult to find an analytical definition for correction terms.

6.2 Existing models with pressure diffusion terms

The models proposed in the literature to account for adverse pressure gradients with a pressure diffusion term are summarised below. In particular, the localisation of the correction term is further detailed. Finally, the proposed Reynolds-stress model [52] is assessed on the Skåre & Krogstad test case.

6.2.1 Two-equation models

The implementation of the corrections proposed by Rao & Hassan [86] and Knopp [51] for the Wilcox 1988 $k-\omega$ model [119] and presented in Section 6.1.2 is detailed here.

Rao & Hassan correction

Considering the asymptotic sqrt-law where $p^+y^+ \gg 1$, Rao & Hassan [86] studied the square-root region with Boussinesq's hypothesis and, enforcing the compatibility of the ϕ-equation by dispensing with Bradshaw's hypothesis, concluded a discrepancy in the k-equation only. Noting that the correction should only apply in the inner layer, they introduced the pressure diffusion term D_k^p, Eq. (6.28), using the boundary layer assumption

$$\rho D_k^p = -\frac{\partial}{\partial y}\left(\frac{\mu_t}{\sigma_k^p}\frac{\overline{uv}}{\rho k}\frac{\partial P}{\partial x}\right) = -\frac{\mathrm{d}}{\mathrm{d}y}\left(\sigma^{*p}\frac{k}{\omega^2}\frac{\mathrm{d}U}{\mathrm{d}y}\frac{\mathrm{d}P}{\mathrm{d}x}\right) \tag{6.70}$$

where x and y correspond to the local streamwise and wall-normal coordinates. The last expression is obtained with Boussinesq's hypothesis $\overline{uv} = \nu_t \frac{\mathrm{d}U}{\mathrm{d}y}$ and the eddy-viscosity definition $\nu_t = k/\omega$. As already mentioned in Section 6.1.2, the model is calibrated with $\sigma^{*p} \equiv 1/\sigma_k^p = -5.13$.

To restrict the model correction to the inner layer, the term is only activated when it is negative. According to Eq. (6.30), the corrective term is thus applied in the region where the eddy viscosity ν_t is increasing with the wall-distance, which corresponds to the inner layer according to the mixing-length theory.

The model finally becomes

$$\rho\frac{\mathrm{D}k}{\mathrm{D}t} = \rho P_k - \beta^* k\omega + \frac{\partial}{\partial x_j}\left[(\mu + \mu_t\sigma)\frac{\partial k}{\partial x_j}\right] + \rho\min\left(D_k^p, 0\right) \tag{6.71a}$$

$$\rho\frac{\mathrm{D}\omega}{\mathrm{D}t} = \alpha\rho P_k\frac{\omega}{k} - \beta\rho\omega^2 + \frac{\partial}{\partial x_j}\left[(\mu + \mu_t\sigma^*)\frac{\partial \omega}{\partial x_j}\right] \tag{6.71b}$$

In [86], the correction displays promising results in subsonic conditions, using the Skåre & Krogstad experiment as a reference, but fails to improve the $k-\omega$ model in a supersonic turbulent boundary layer with APG [33]. The authors expected this conclusion, noting that the pressure gradient affects supersonic and subsonic flows differently.

Knopp correction

Knopp [51] analysed the $k-\omega$ model for the generalised sqrt-law Eq. (2.49) using both Boussinesq's and Bradshaw's hypotheses. He corrects the incompatibility in both equations by adding the pressure diffusion and cross-diffusion terms found in Section 6.1.2, with the constants Eqs. (6.32) & (6.45). To restrict the new terms to their domains of validity, he defines three blending functions.

The pressure diffusion term for k should apply in the overlap region whereas it is deactivated in the viscous sublayer and in the buffer layer with

$$f_{b1} = \left(1 - e^{-\frac{y^+}{60}\sqrt{1+23p^+}}\right)^6 \tag{6.72}$$

The additional terms D_ω^p and D_ω^{cd2} in the ω-equation should only intervene in the sqrt layer. Knopp distinguishes the log layer from the sqrt layer by curve fitting the corresponding laws on experimental data, using $\kappa \equiv \kappa_p$. As a result, the two regions are detached from each other and a buffer layer arises in-between, which is characterised by the author with

$$y^+_{\mathrm{log,max}} = 78\left(p^+\right)^{-0.35}, \quad y^+_{\mathrm{incpt}} = 94\left(p^+\right)^{-0.35}, \quad y^+_{\mathrm{sqrt,min}} = 110\left(p^+\right)^{-0.35}, \tag{6.73}$$

where $y^+_{\text{log,max}}$, $y^+_{\text{sqrt,min}}$ and y^+_{incpt} correspond to the outer edge of the log-law region, the inner edge of the sqrt-law region and the intercept of both laws respectively. The parameters have been determined by fitting the log-law and sqrt-law on several experimental data sets at different p^+ values. To enable a smooth transition from 0 at $y^+_{\text{log,max}}$ to 1 at $y^+_{\text{sqrt,min}}$, the blending function for the region below the sqrt layer in the ω-equation is expressed as

$$f_{b2} = \frac{1}{2}\left(1 + \tanh\left(5\zeta\right)\right), \qquad \zeta = \frac{y^+ - y^+_{\text{incpt}}}{y^+_{\text{sqrt,min}} - y^+_{\text{log,max}}}. \tag{6.74}$$

It can be noted that these first two blending functions f_{b1} and f_{b2} are sensitised to the pressure-gradient parameter p^+ and calibrated using experimental data.

As for the outer edge of the square-root region, it is simply defined as the outer edge of the inner layer. Knopp [51] proposes a Klebanoff-type function (see Wilcox [120]) decreasing above $y = 0.15\delta$,

$$f_{b3} = \left(1 + 5.5\left(\frac{y}{0.35\delta}\right)^6\right)^{-4}. \tag{6.75}$$

The boundary layer thickness being an integral quantity of the boundary layer, it is not directly accessible as a field variable. Hence, Knopp relies on a specific data structure of the TAU Code, the unstructured compressible flow solver developed by the DLR, to probe the flow in boundary layers and estimate δ during computations (see Appendix B.2).

Finally, the corrected $k-\omega$ model reads

$$\rho\frac{\mathrm{D}k}{\mathrm{D}t} = \rho P_k - \beta^* k\omega + \frac{\partial}{\partial x_j}\left[\left(\mu + \mu_t\sigma\right)\frac{\partial k}{\partial x_j}\right] + f_{b1}f_{b3}\rho D^p_k \tag{6.76a}$$

$$\rho\frac{\mathrm{D}\omega}{\mathrm{D}t} = \alpha\rho P_k\frac{\omega}{k} - \beta\rho\omega^2 + \frac{\partial}{\partial x_j}\left[\left(\mu + \mu_t\sigma^*\right)\frac{\partial \omega}{\partial x_j}\right] + f_{b2}f_{b3}\rho\left(D^p_\omega + D^{\text{cd2}}_\omega\right) \tag{6.76b}$$

The *a priori* blending functions are plotted for the Skåre & Krogstad experiment [99] in Figure 6.2 at the first station available, $x = 3.0\,\text{m}$, and at the last two stations in the equilibrium region, $x \in [4.8\,\text{m}\,;5.0\,\text{m}]$. It can be seen that the blending function f_{b1} progressively switches after the buffer layer so that the pressure diffusion term only fully contributes to the turbulence budget at the end of the log layer. It is surprising as the correction is expected to be already activated at the beginning of the log layer, according to Section 6.1.2 and Knopp's derivation [51]. Indeed, as seen in Section 6.1.2, the presence of D^p_k in the log layer is important to ensure compatibility with the log-law in APG (constraint Eq. (6.53). The second inner blending function f_{b2} steeply activates at the intercept of log and sqrt laws. Regarding the outer blending, the progressive transition of f_{b3} already starts at the inner edge of the sqrt-law region, preventing the resulting function $f_{b2}f_{b3}$ from fully activating in short sqrt layers, *e.g.* for $x = 3.0\,\text{m}$.

Note that in [51], Knopp applies the correction to the SST $k-\omega$ [71], and also considers a variant combining Eq. (6.76) to the κ-correction discussed in Chapter 5. The models show improved velocity profiles and friction coefficient on the RETTINA-II experimental case (see Knopp & Reuther [53], Reuther *et al.* [88]). They also slightly improve integral quantity profiles on aerofoils, such as the NACA 4412. The effect of the κ-correction is mostly visible in friction coefficient distributions, the slope correction reducing the skin friction and moving the separation point upstream. The additional terms D^p_k, D^p_ω and D^{cd2}_ω are the largest contributors to the observed improvement.

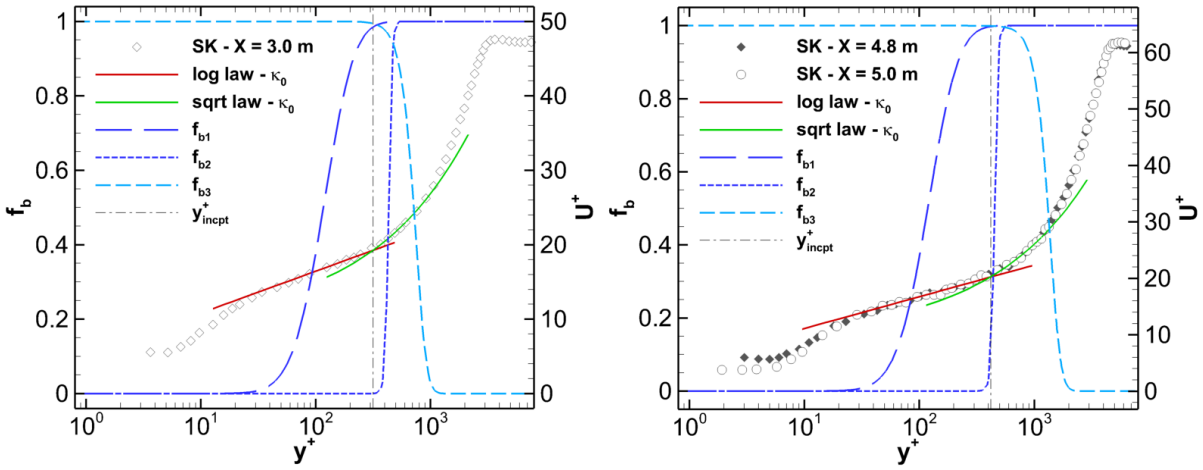

(a) $x = 3.0\,\mathrm{m}$ **(b)** $x = 5.0\,\mathrm{m}$

Figure 6.2: A priori *blending functions defined by Knopp for the Skåre & Krogstad experiment [99]*

6.2.2 Modified SSG/LRR-ω RSM – Knopp *et al.* [52]

To take advantage of the benefits offered by Reynolds-stress models, Knopp *et al.* [52] apply a simplified version of the $k-\omega$ modification developed in [51] to the SSG/LRR-ω RSM [17]. In this model, the Reynolds-stress equations remain unchanged, the authors considering the pressure diffusion for the Reynolds stresses already accounted for by the usual turbulent transport and only the ω-equation is altered.

Despite justifying the correction in the ω-equation with the same analysis as for the $k-\omega$ model, they do not mention the mixed cross-diffusion term $D_\omega^{\mathrm{cd}2}$, necessary according to the derivation in Section 6.1.2. It is not clear if this term is considered negligible or if it is for simplification reasons. It leaves the pressure diffusion term D_ω^p, expressed with Eq. (6.34), as the only new term in the model to impose the correct sqrt-law behaviour. Moreover, they propose

$$\sigma_\omega^p = a_1^2 \sigma_\omega, \tag{6.77}$$

corresponding to half the analytical solution Eq. (6.45), *i.e.* the pressure diffusion for ω is doubled, without further justifications. Similarly to Knopp's $k-\omega$ model, the additional term is blended using f_{b2} and f_{b3}, given by Eqs. (6.74) & (6.75) respectively.

Since it has been proved in Section 6.1.2 that the Reynolds-stress transport equations are not compatible with the square-root region, this recalibration of σ_ω^p can be seen as a compensation for the incompatibility in Eq. (6.60). Indeed, in the boundary layer, the pressure diffusion terms for k and ω defined in Section 6.1.2 can be simplified of the form

$$D_k^p = -\frac{\mathrm{d}}{\mathrm{d}y}\left(\frac{\nu_t}{\sigma_k^p k}\,\overline{uv}\frac{\mathrm{d}P}{\mathrm{d}x}\right) \tag{6.78}$$

$$D_\omega^p = -\frac{\omega}{k}\frac{\mathrm{d}}{\mathrm{d}y}\left(\frac{\nu_t}{\sigma_\omega^p k}\,\overline{uv}\frac{\mathrm{d}P}{\mathrm{d}x}\right) \tag{6.79}$$

The proposed correction therefore yields a local decrease of k, as $\overline{uv} < 0$ and $\sigma_k^p < 0$ hence $D_k^p < 0$, and a local increase of ω, $\sigma_\omega^p > 0$ (*cf.* Eq. (6.45)) hence $D_\omega^p > 0$. Neglecting

D_k^p as in [52] can then be compensated by a further increase of D_ω^p. Indeed, a larger pressure diffusion term in the ω-equation results in a larger specific dissipation rate ω, and thus a reduction of the diagonal Reynolds stresses, due to the isotropic dissipation model Eq. (3.48), $\varepsilon_{ij} = \frac{2}{3}0.09k\omega\,\delta_{ij}$, of the SSG/LRR-$\omega$ RSM. The shear-stress is indirectly affected, its production being moderated by the local reduction of the wall-normal stress $\overline{v^2}$. Consequently, at the edge of the inner layer, the mixing of the lower-momentum layers, closer to the wall, and the higher-momentum layers, closer to the free-stream region, becomes less efficient and the velocity profile steepens.

In [52], the new RSM accounting for the sqrt-law, denoted here 'SSG/LRR-ω-dP Knopp', is benchmarked against the original SSG/LRR-ω RSM with the DLR VicToria experiment, described in [52]. The set-up consists in a wind-tunnel with a deflecting wall, to study a high-Reynolds-number flow with a slowly increasing adverse pressure gradient. High-resolution profiles are captured using 2D2C-PIV (2-Dimensional 2-Component Particle Image Velocimetry) and Lagrangian 3D3C-PTV (Particle Tracking Velocimetry). Presenting velocity profiles under strong APG (up to $p^+ = 0.163$, $\beta_p = 151.1$) and the C_f-distribution, Knopp *et al.* [52] show that the pressure diffusion term greatly improves the overlap region prediction, as well as the skin friction.

To assess the performance of the SSG/LRR-ω-dP Knopp in this thesis, the model has been implemented in Aether. However, the dependence on the boundary layer thickness δ in the expression of f_{b3} (Eq. (6.75)) requires further developments in Aether to estimate δ at each point of the boundary layer. The solver must indeed detect the boundary layer thickness above each wall-node and propagate these values into the computational domain. Using the data structure introduced in Chapter 5 to define fluid columns above the wall-nodes, a detection algorithm has been implemented to compute δ in the volume, based on the fluid entropy. The algorithm is detailed in Appendix B.2.

6.2.3 Application to the Skåre & Krogstad test case

The SSG/LRR-ω-dP Knopp model is now assessed against the original SSG/LRR-ω RSM on the Skåre & Krogstad case. To prevent an uncontrolled behaviour in the corners and on the lateral wall, where the sqrt-law correction applies intermittently due to the δ-detection constrained in the corner (*cf.* Appendix B.2.4), the pressure diffusion term is simply deactivated in the half of the computation domain on the side of the lateral wall.

Figure 6.3 shows the significant improvement of the inner layer brought by Knopp's correction on the SSG/LRR-ω model to the velocity profiles in the equilibrium region of the Skåre & Krogstad wind-tunnel.

The profiles in wall-units plotted in Figure 6.3(a) point out the clear localisation of the correction in the inner layer, as the models coincide below $y^+ \leqslant 200$. It corresponds to the wall distance above which the correction starts to affect the velocity profile and inserts the sqrt-law behaviour before the outer layer.

The outer region in wall-units, in Figure 6.3,(a) rises higher and closer to the reference. The model improvement is also observed in Figure 6.3(b), presenting the velocity profiles in physical dimensions for $y < 0.04\,\mathrm{m}$, which corresponds to the inner layer. As a result, the SSG/LRR-ω-dP Knopp matches the wind-tunnel measurements close to the wall, which indicates an improved prediction of the skin friction. On the contrary, the model deviates

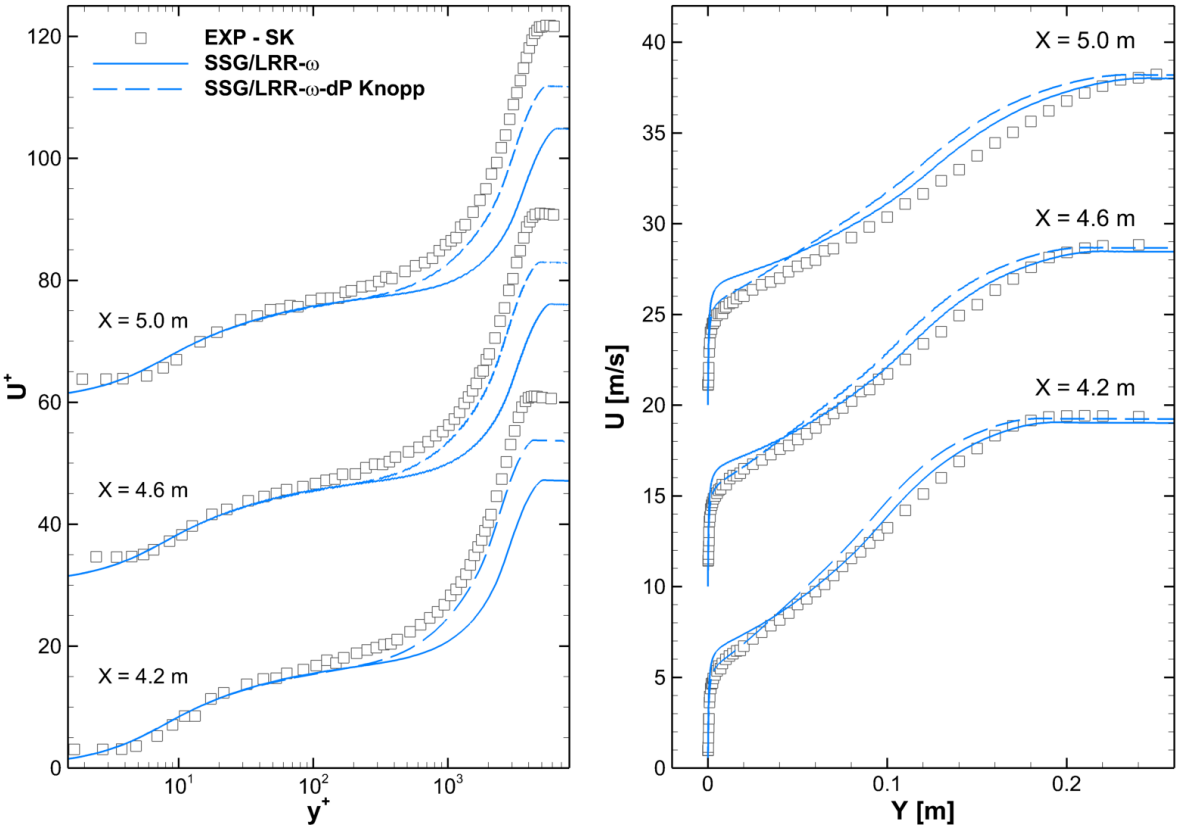

(a) *Wall-units* **(b)** *Dimensional quantities*

Figure 6.3: *Velocity profiles in the equilibrium region in the Skåre & Krogstad test case for the SSG/LRR-ω and the SSG/LRR-ω-dP Knopp models*

from the experimental profile in the outer region, as seen in Figure 6.3(b), which points out a reduction of the boundary layer thickness.

To further assess this sqrt-law correction, Figure 6.4 shows the diagnostic function Ξ_{sqrt} for the two models at $x = 5.0\,\text{m}$ and the corresponding velocity profiles using a sqrt-scale on the right. On these plots, the sqrt-law region should correspond to a constant Ξ_{sqrt} and a linear $U^+(\sqrt{y^+})$. The model improvement is well visible on both plots. For Ξ_{sqrt}, the corrected model noticeably reduces the overprediction returned by the original formulation in the inner layer for $\sqrt{y+} \leqslant 30$. The ability of the correction to yield a sqrt-law behaviour is more visible in the $U^+(\sqrt{y^+})$ plot, with a linear behaviour in the region delimited by the blending functions. This is less visible for the diagnostic function since no constant range is observed, despite an improvement of the agreement with experimental values.

It can be noted here that the inner blending function f_{b2} starts to switch exactly at the inner edge of the sqrt-law region observed on the reference. Besides, the outer blending function f_{b3} is already declining at the inner edge of the sqrt-law region. Consequently, the activation factor $f_{b2}f_{b3}$ never reaches unity, and the correction appears to be naturally damped in the entire extent of the correction range. Therefore, to improve the sqrt-law behaviour and enforce a plateau in the diagnostic function Ξ_{sqrt}, the transition locations of the blending functions f_{b2} and f_{b3} must be further separated.

These conclusion are confirmed for the evolution of the integral quantities in the boundary layer, in Figure 6.5. In particular, the outer layer is directly monitored by

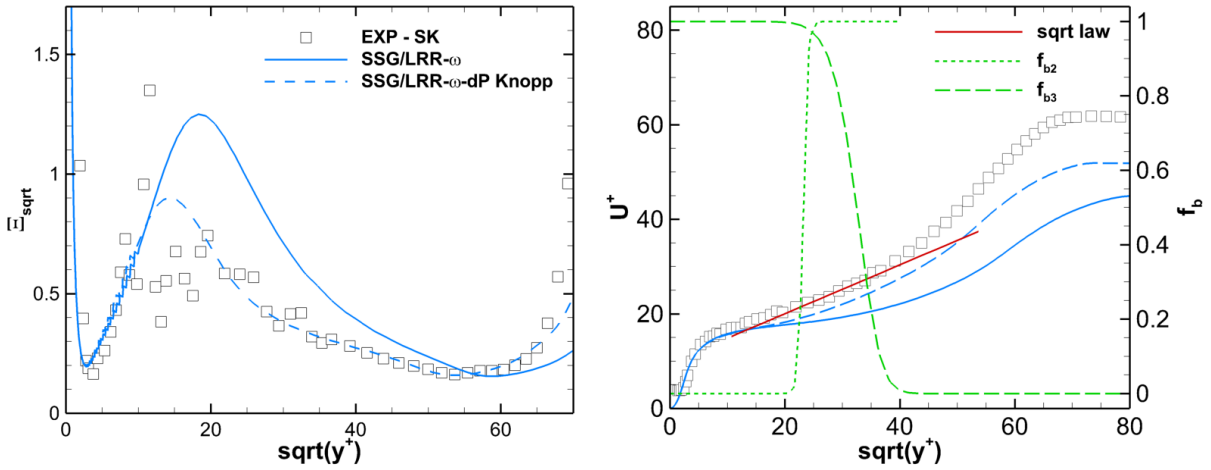

(a) *Diagnostic function* **(b)** *Velocity in sqrt-scale*

Figure 6.4: *Square-root behaviour in the Skåre & Krogstad test case at* $x = 5.0\,\mathrm{m}$ *for the SSG/LRR-ω and the SSG/LRR-ω-dP Knopp models*

the displacement and momentum thicknesses, plotted in Figure 6.5(a). It can be seen that the sqrt-law correction progressively reduces both thicknesses, which results in the deterioration of the outer layer. Conversely, the shape factor shown in Figure 6.5(b) is globally increased in the instrumented range, its values are closer to the experimental reference in the equilibrium region. This result is an expression of the correction of the shape of the velocity profile, as noted in Figure 6.3(b) where the profiles obtained with modified model are visually closer to the experiment.

The skin friction is shown in Figure 6.5(c) and confirms the reduction inferred from the velocity profiles in Figure 6.3. Indeed, after an abrupt decrease for $x \leqslant 3.0\,\mathrm{m}$, the friction appears almost constant in the area of interest, with a level significantly lower than the original model.

The improvement of C_f compensates for the reduction of δ^*, and results in an improved pressure-gradient parameter, shown in Figure 6.5(d). It can be observed that Clauser's parameter reaches a higher peak, increased from $\beta_p^{\max} \approx 12$ with the standard model to $\beta_p^{\max} \approx 14$, and decreases more slowly downstream until $x = 4.5\,\mathrm{m}$. An almost equilibrium region, where β_p is constant, can thus be recognised with the SSG/LRR-ω-dP Knopp model in the vicinity of $x \approx 4.0\,\mathrm{m}$. The equilibrium is actually still predicted too far upstream, which can be directly related to the inability of the corrected model to improve the boundary layer growth in this region.

To investigate in more detail the implications of the correction on the SSG/LRR-ω RSM, its impact on the dissipation rate ε is presented in Figure 6.6. On the left, Figure 6.6(a) presents the budget of the ω-equation for the original and the modified models, the latter including the pressure diffusion term D_ω^p. The other terms correspond to production P_ω, dissipation ε_ω, viscous diffusion D_ω^ν and turbulent transport D_ω^T of ω respectively.

Despite its restricted range of activation, D_ω^p significantly affects the balance of the budget terms of the corrected model (dashed line) in the sqrt layer, highlighted by the presence of the additional term. Its magnitude indeed exceeds the production and the turbulent transport of the original model, and forces the balance of the terms to adjust. In particular, it results in an almost doubling of P_ω and ε_ω, with a bump in the vicinity of the

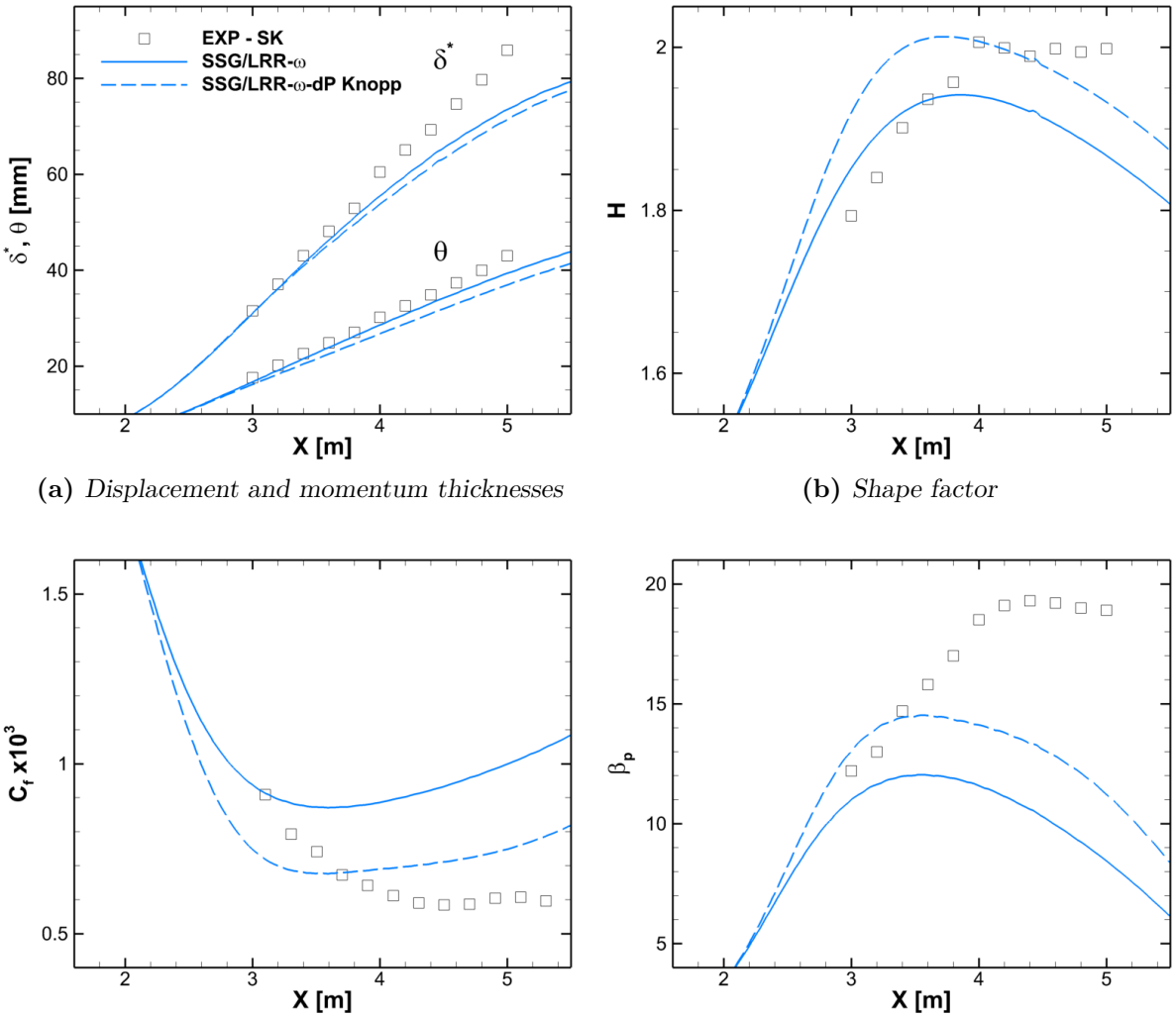

(a) *Displacement and momentum thicknesses*

(b) *Shape factor*

(c) *Skin friction coefficient*

(d) *Clauser's pressure-gradient parameter*

Figure 6.5: *Integral quantities in the Skåre & Krogstad test case for the SSG/LRR-ω and the SSG/LRR-ω-dP Knopp models*

pressure diffusion peak. This translates into a growth of the dissipation rate, observed in Figure 6.6(b), as expected from the model presentation in Section 6.2.2, to locally steepen the mean velocity profile. Moreover, the drop in turbulent transport points out the change in the structure of the profile of ω and ε across the boundary layer.

These profiles are shown in Figure 6.6(b) at $x = 5.0\,\mathrm{m}$, in wall-units. The velocity profile is added for reference to help to distinguish the different regions of the boundary layer. In the sqrt layer, ω^+ and ε^+ are increased by half, with ω^+ displaying a slow decrease up to $y^+ \approx 2{,}500$, in the middle of the outer region of the boundary layer.

Conversely, the new model keeps in this region an almost constant difference in the dissipation rate $\Delta\varepsilon^+ \approx 0.02$ compared to the original model. This indicates that the turbulent kinetic energy grows in the outer layer, and thus that the outer peak of k increases, as expected.

The SSG/LRR-ω-dP Knopp exhibits significant improvements to the original SSG/LRR-ω RSM in the Skåre & Krogstad test case. Although it does not exactly enforce a sqrt

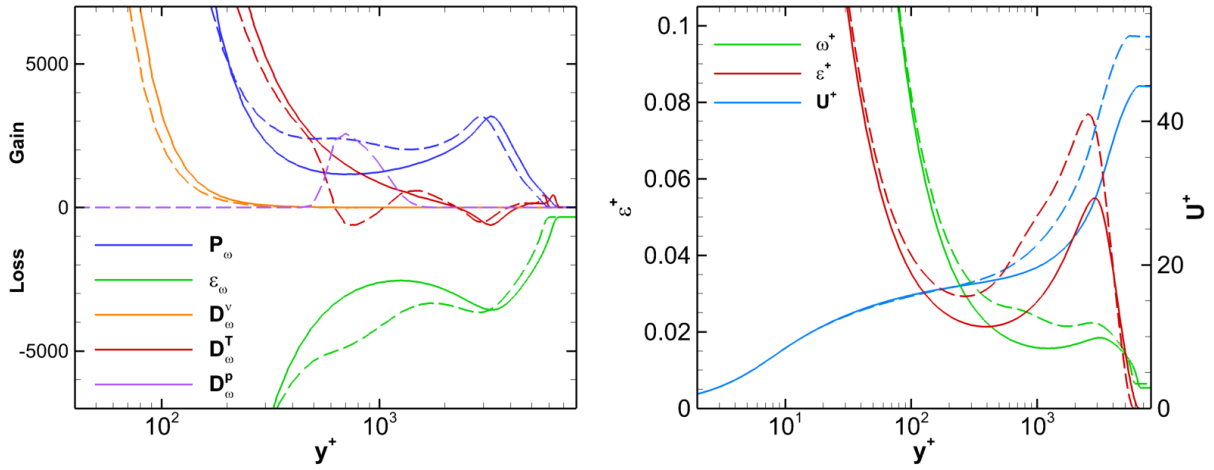

(a) *Budget of the ω-equation* **(b)** *ω and ε profiles*

Figure 6.6: *Effect of the sqrt-law correction on the dissipation rate in the Skåre & Krogstad test case at $x = 5.0\,\mathrm{m}$. Solid lines, SSG/LRR-ω; dashed lines, SSG/LRR-ω-dP Knopp.*

layer according to the diagnostic function Ξ_{sqrt}, the new pressure diffusion term D^p_ω locally impacts the inner layer of the velocity profile, especially enabling a better level of skin friction in the equilibrium region. However, the correction also slows the growth of the boundary layer.

6.3 New developments to account for the adverse-pressure-gradient effects

6.3.1 Modification of Knopp's inner blending function

In the previous section, it has been seen that the sqrt-law behaviour is not correctly enforced in the SSG/LRR-ω-dP Knopp model, due to a too narrow activation region of the correction resulting in a partial application the pressure diffusion term with $f_{b2}f_{b3} < 1$. This could be improved by adjusting Knopp's blending functions and broadening the activation range.

Moreover, Knopp's inner blending function f_{b2}, Eq. (6.74), is strongly dependent on experimental cases considered for calibration, and especially on the Reynolds number. Indeed, its transition zone has been calibrated with high-Reynolds-number APG flows to switch on beyond the log layer and results in a region that only depends on pressure-gradient parameter p^+, defined by Eq. (6.73). During the VicToria project final meeting [28], Knopp highlighted this issue and showed two additional calibrations of $y^+_{\mathrm{log,max}}$ for lower-Re reference data sets. The function f_{b2} should however directly account for the variable extent of log layer for a large range of Reynolds numbers to ensure a satisfactory correction on the whole span of the wing and on the tail of an aircraft.

There is also room for improvement for the outer blending function f_{b3}: deactivating the correction above $y = 0.15\delta$ appears also rigid. This limit corresponds to a general observation for ZPG flows, and varies between $0.1\delta \sim 0.2\delta$ in the literature and could be

flow dependent. Therefore, f_{b3} would benefit from being rather defined on the local flow quantities, but will be left unaltered for now.

To replace f_{b2}, a new blending function f_{b2^*} is introduced, inspired from Menter's BSL function F_1 [71], Eq. (3.17), recalled below

$$F_1 = \tanh\left(\arg_1^4\right), \qquad \arg_1 = \min\left[\max\left(\underbrace{\frac{\sqrt{k}}{\beta^*\omega d}}_{\xi}; \underbrace{\frac{500\mu}{\rho\omega d^2}}_{\zeta}\right); \underbrace{\frac{4\sigma_{\omega 2}k}{\mathrm{CD}_{k\omega}\, d^2}}_{\chi}\right]. \tag{6.80}$$

In $\arg_1$, ξ is constant in the overlap region and decreases in the outer region so that the F_1 switches after the inner layer. The last term, χ, ensures that F_1 remains at zero close to the boundary layer edge and prevents the ω-equation from yielding a free-stream-dependent solution. Finally, ζ is a near-wall shielding term that ensures that F_1 remains at one in the inner layer down to the wall.

As f_{b2}^* is expected to switch below the sqrt region, the argument is reduced to ζ, with a recalibration to adjust the switch localisation. Moreover, contrary to F_1, the new blending function is expected to be zero at the wall and one remote from the wall. Thus, the blending function f_{b2}^* is expressed as

$$f_{b2}^* = 1 - \tanh\left(\zeta^4\right), \qquad \zeta = C\frac{\nu}{\omega y^2} = \frac{C}{\omega^+ y^{+2}} \tag{6.81}$$

The value $C = 500$, used in [71], is inappropriate for the present purpose and a calibration on the Skåre & Krogstad test case yields $C = 4{,}000$.

Note that f_{b2}^* still depends on the Reynolds number, due to its dependence on y^+. However, contrary to f_{b2}, the new blending function uses a parameter based on the specific dissipation rate and the wall distance, similarly to the SSG-ω ATAAC RSM (see Eqs. (3.66) & (3.68)). Therefore, the switch localisation also account for the local flow features of the considered case, rather than to depend on the experiments used for calibration.

Figure 6.7 shows the new blending function f_{b2}^*, computed *a priori* with the SSG/LRR-ω-dP Knopp model, along with Knopp's f_{b2}. The apparent log-law is displayed for reference. The calibrated f_{b2}^* with $C = 4{,}000$ switches closer to the wall and closer to the log layer edge $y^+_{\log,\max}$ compared to f_{b2}. Figure 6.7(a) shows that the correction with Knopp's blending is hardly activated at $x = 2.0\,\mathrm{m}$ despite the adverse pressure gradient ($p^+ \approx 0.007$). This can be related to the low local Reynolds number and the rigidity of the inner layer definition used in f_{b3}, resulting in a inner blending switch far from the log-layer outer edge and a transition region for the outer blending already starting towards the end of the log layer. Although it does not here fully activate either, it can be deduced that $f_{b2}^* f_{b3}$ increases the upstream extent of the activation region compared to $f_{b2}f_{b3}$, as it switches closer to the wall and thus at lower Reynolds numbers.

A new version of the SSG/LRR-ω-dP Knopp is implemented by replacing Knopp's blending function f_{b2} with the f_{b2}^*, referred to as the SSG/LRR-ω-dP v2 model. To assess the impact of the new blending function on the correction, the results are presented below.

Figure 6.8 shows the velocity profiles of the original SSG/LRR-ω model and the two APG-sensitised versions. The wall-units profiles in Figure 6.8(a) are slightly improved by the new model. As targeted, the velocity departs closer to the wall, resulting in a steeper log-law slope that more closely matches the reference.

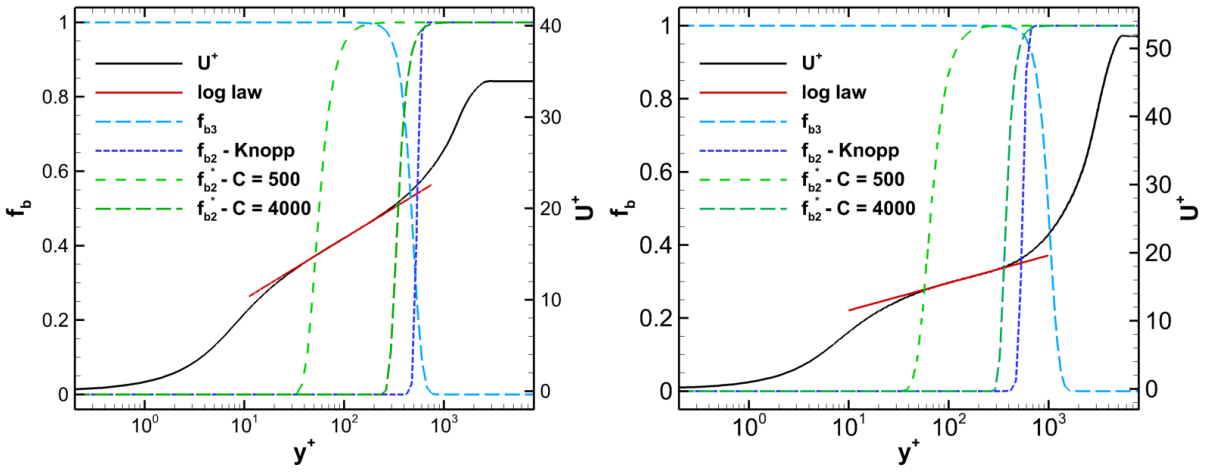

(a) $x = 2.0\,\mathrm{m}$ **(b)** $x = 5.0\,\mathrm{m}$

Figure 6.7: A priori *blending functions for the Skåre & Krogstad test case using the SSG/LRR-ω-dP Knopp model*

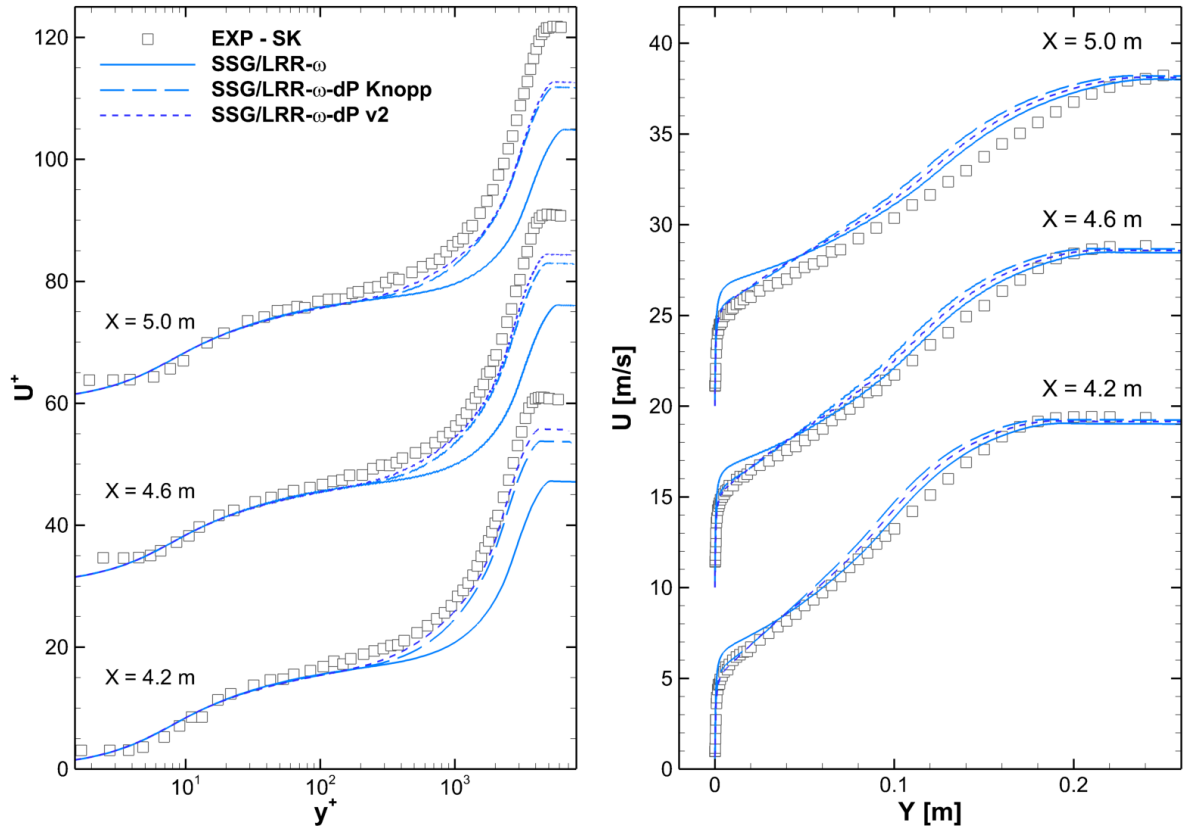

(a) *Wall-units* **(b)** *Dimensional quantities*

Figure 6.8: *Velocity profiles in the equilibrium region in the Skåre & Krogstad test case for the SSG/LRR-ω model variants*

The sqrt-law behaviour is further analysed with Figure 6.9, presenting the diagnostic functions and the velocity profiles in sqrt-scaling. In particular, the new blending function shown in Figure 6.9(b) activates closer to the wall, as expected. The smooth transition in f_{b2}^* prevents it to fully activate before the outer blending starts to decrease, but insures a broader activation range with $f_{b2}^* f_{b3} \geqslant 0.8$ for an extent of $\Delta\sqrt{y^+} \approx 8$, as compared to Knopp's function, which extends on $\Delta\sqrt{y^+} \approx 5.5$. As a consequence, the new velocity profile displays a slightly improved sqrt-law behaviour, seen as a linear range for $\sqrt{y^+} \in [20\,;35]$. This is confirmed by the diagnostic function Ξ_{sqrt} in Figure 6.9(a), which indicates a flatter range and an inflexion point.

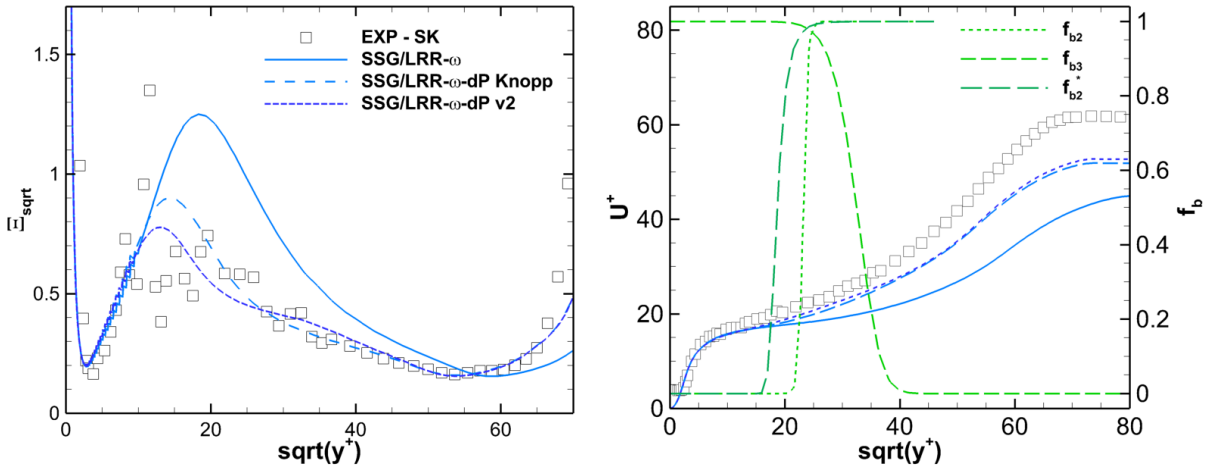

(a) *Diagnostic function* **(b)** *Velocity in sqrt-scale*

Figure 6.9: *Square-root behaviour in the Skåre & Krogstad test case at* $x = 5.0\,\text{m}$ *for the SSG/LRR-ω model variants*

Improvements can also be seen for the velocity profiles in physical dimensions, plotted in Figure 6.8(b). Despite a broader activation range, the new correction makes the v2 model reduce its deviation on the outer layer, while the inner layer still coincides with the SSG/LRR-ω-dP Knopp model.

This implies an overall improvement of the integral quantities, confirmed in Figure 6.10. The adverse effect of the 'dP' correction on δ^* and θ is significantly reduced by the v2 version in Figure 6.10(a). This reflects the velocity profile improvement in the outer layer, while keeping an almost coinciding inner layer velocity profile, as seen in Figure 6.8(b). The shape factor presented in Figure 6.10(b) is hardly altered, the effects on δ^* and θ compensating each other.

The larger activation region of the pressure diffusion term also amplifies the skin friction reduction shown in Figure 6.10(c), leading to further reduction for $x \leqslant 0.4$, but improves the skin friction level downstream. As a result, Figure 6.10(d) shows that the pressure-gradient parameter is now overpredicted upstream of the experimental equilibrium range but the maximum value is increased to $\beta_p^{\max} = 16.5$ due to the increased δ^* combined with the lower friction and becomes closer to the experiment. As observed for the shape factor and the skin friction in Figures 6.10(b) & (c), the new blending function causes β_p to decrease steeper after its maximum. The equilibrium state, characterised by a range with a constant value of β_p is less visible with the v2 version.

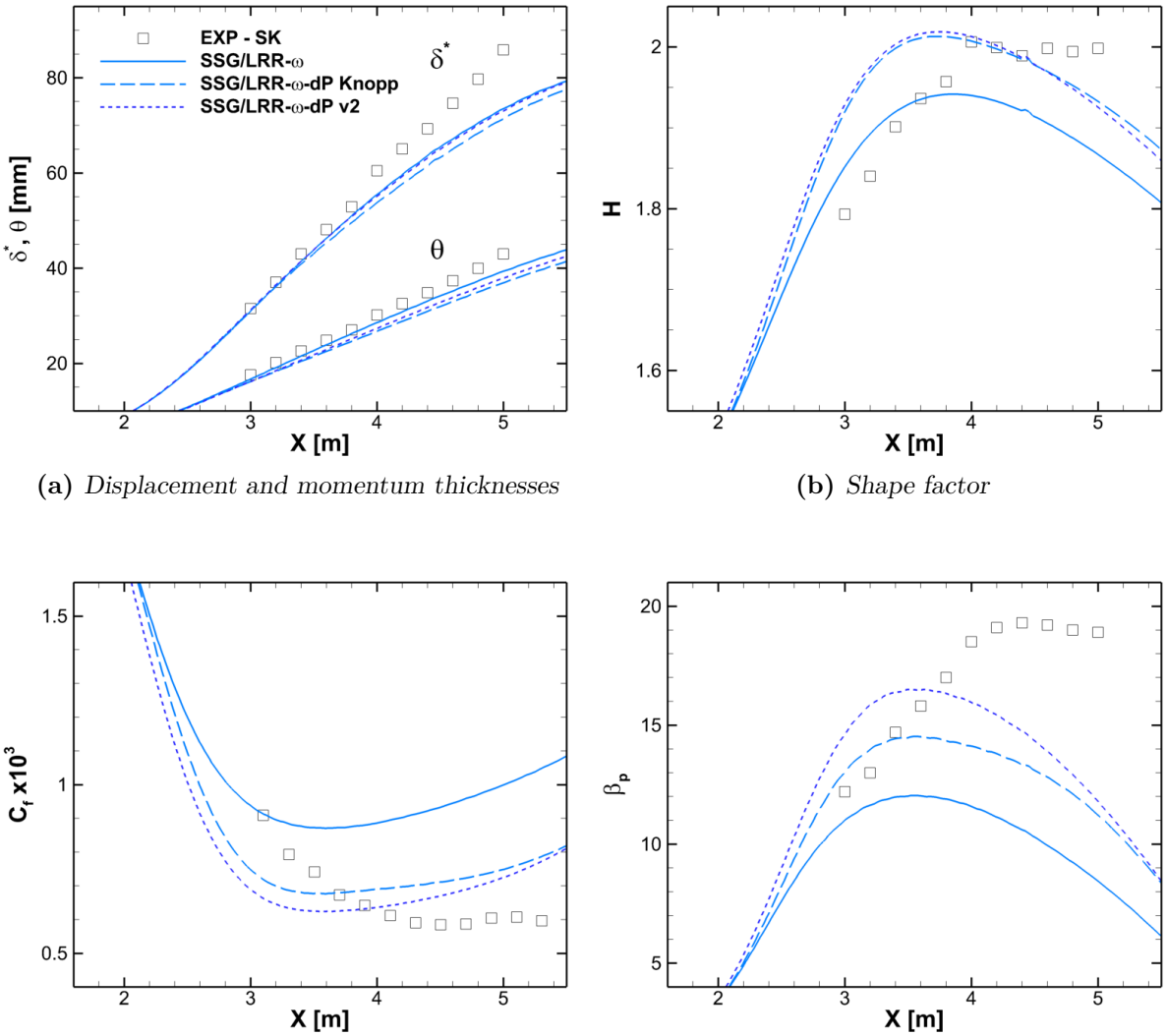

(a) *Displacement and momentum thicknesses*

(b) *Shape factor*

(c) *Skin friction coefficient*

(d) *Clauser's pressure-gradient parameter*

Figure 6.10: *Integral quantities in the Skåre & Krogstad test case for the SSG/LRR-ω model variants*

Figure 6.11 presents the impact of the new sqrt-law correction on the dissipation rate prediction compared to the SSG/LRR-ω-dP Knopp. In the ω-equation budget in Figure 6.11(a), the new blending function f_{b2}^{*} activates the pressure diffusion term closer to the walls compared to Knopp's function f_{b2}. The sqrt layer, as considered by the model, leads to a D_{ω}^{p} more than 50 % stronger than in the SSG/LRR-ω-dP Knopp. As a consequence, the turbulent transport drops closer to the wall and moderates ω in the whole sqrt layer.

Figure 6.11(b) shows the resulting dissipation rate profiles in wall-units for the new model. The increased pressure diffusion term intensifies ω^{+} by 30 % and ε^{+} by 50 % in the sqrt-law region compared to Knopp's correction. It can be noted that the new ω-profile decreases faster down to its outer layer value in the correction range. As for the comparison between the SSG/LRR-ω-dP Knopp and the original model, the increase of ε^{+} in the sqrt layer for the new SSG/LRR-ω-dP v2 is propagated to the outer layer, indicating once again an intensification of the outer peak in the turbulent kinetic energy in the new model.

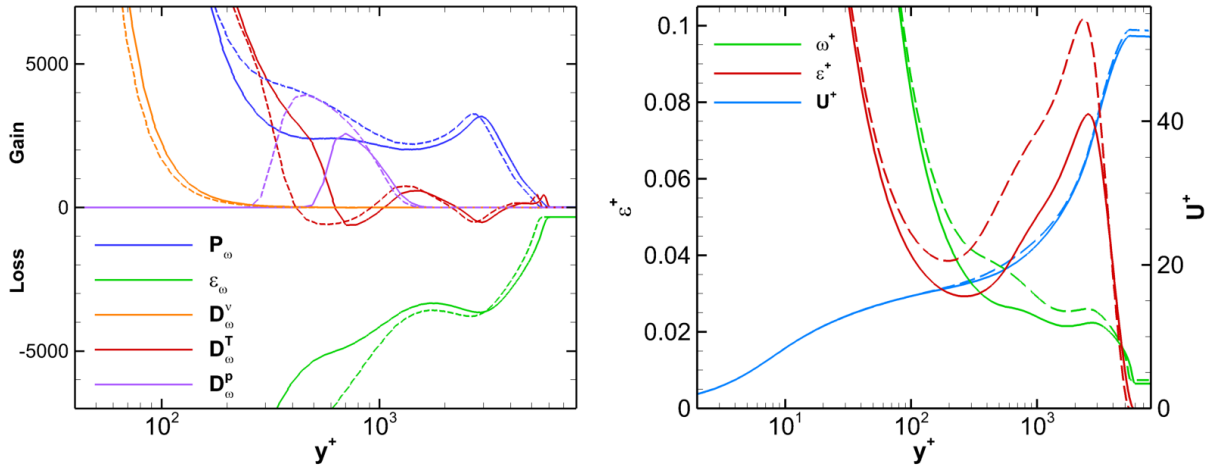

(a) *Budget of the ω-equation* **(b)** *ω and ε profiles*

Figure 6.11: *Effect of the correction on the dissipation rate in the Skåre & Krogstad test case at $x = 5.0\,\mathrm{m}$. Solid lines, SSG/LRR-ω-dP Knopp; dashed lines, SSG/LRR-ω-dP v2.*

The streamwise Reynolds-stress profiles in wall-units are shown in Figure 6.12(a). They confirm the intensification of the turbulence in the outer region due to the new blending with a higher outer peak, and thus show a better agreement to the reference. It can be noted however that the peak height declines faster with the streamwise position, compared to the one predicted by SSG/LRR-ω-dP Knopp model at $\overline{uu}^+ \approx 40$, which can be related to the steeper slope of β_p in Figure 6.10(d). Figure 6.12(b) presents the profiles in physical dimensions and especially highlights the underprediction of the boundary layer thickness by the models.

Overall, the SSG/LRR-ω-dP v2 brings the sqrt-law correction of the SSG/LRR-ω-dP Knopp model one step further, improving prediction of velocity profiles, boundary layer thickness and β_p.

6.3.2 Application of the Knopp correction to the EB-RSM

Chapter 4 has pointed out the enhanced accuracy of the EB-RSM over the standard SSG/LRR-ω RSM. In particular, on the Skåre & Krogstad test case, the EB-RSM behaves better in the outer region of the boundary layer, yielding much improved predictions of the boundary layer thicknesses and skin friction coefficient. To benefit from the significant improvement of the sqrt-law correction, whose effectiveness has been demonstrated in the previous sections for the SSG/LRR-ω model, the approach is here converted to the EB-RSM and its ε-equation.

Using the analysis of Section 6.1.2, the new EB-RSM-dP model adds a pressure diffusion term D^p_ε and an additional cross-diffusion term $D^{\mathrm{cd2}}_\varepsilon$ in the dissipation rate equation. To restrict the correction to the sqrt-law region, these terms are blended with f_{b3}, defined by Eq. (6.75), and the newly introduced function f^*_{b2}, which is here adjusted to depend on ε instead of ω

$$f^*_{b2} = 1 - \tanh\left(\zeta^4\right), \qquad \zeta = C\frac{\nu C_\mu k}{\varepsilon y^2} \tag{6.82}$$

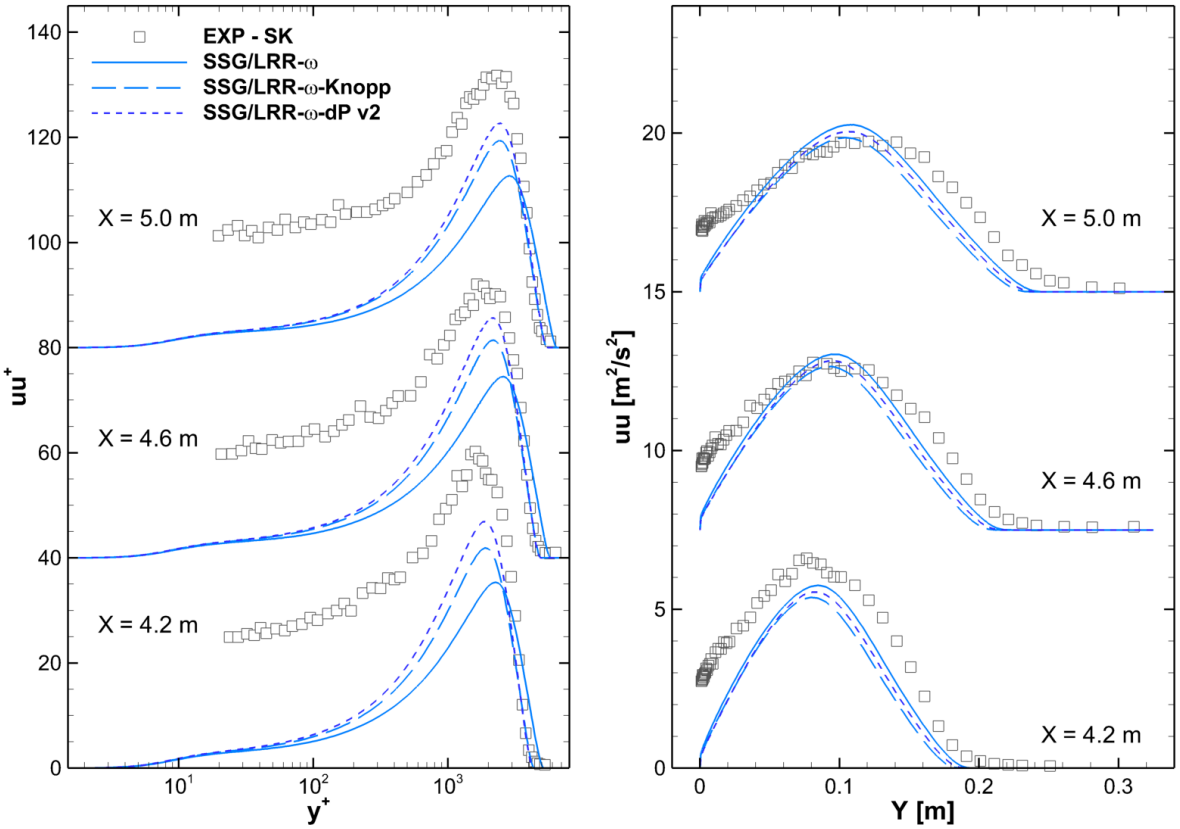

(a) *Wall-units* **(b)** *Dimensional quantities*

Figure 6.12: *Streamwise Reynolds-stress profiles in the Skåre & Krogstad test case for the SSG/LRR-ω model variants*

where $C = 4{,}000$, as in the SSG/LRR-ω-dP v2 model.

Similarly to the model of Knopp *et al* [52], the Reynolds-stress transport equations are left unaltered. To compensate for these unchanged transport equations (*cf.* Section 6.2.2), and following [52], the constant σ_ε^p found in Eq. (6.46) is halved, *i.e.* the pressure diffusion term in the ε-equation is doubled. The constants of the EB-RSM-dP are therefore

$$\sigma_\varepsilon^p = \frac{2}{3}a_1^2\sigma_\varepsilon, \qquad C_{k\varepsilon} = -\frac{5}{4\sigma_\varepsilon}. \tag{6.83}$$

The final form of the model is exactly that described in Section 3.3 with the only modification being the following ε-equation

$$\begin{aligned}\rho\frac{\mathrm{D}\varepsilon}{\mathrm{D}t} &= \rho P_\varepsilon - \rho\varepsilon_\varepsilon + \rho D_\varepsilon^\nu + \rho D_\varepsilon^T \\ &\quad + f_{b2}^* f_{b3}\left[\frac{\partial}{\partial x_l}\left(\frac{C_s}{\sigma_\varepsilon^p}\rho T\,\overline{u_l u_m}\frac{\partial P}{\partial x_m}\right) + C_{k\varepsilon}\frac{\mu_t}{k}\frac{\partial k}{\partial x_j}\frac{\partial \varepsilon}{\partial x_j}\right]\end{aligned} \tag{6.84}$$

with $\mu_t = \rho C_s \overline{u_m u_l} n_m n_l T$ in order to remain consistent with the GGDH modelling of the diffusion terms.

6.3.3 Results

The EB-RSM-dP has been assessed on the Skåre & Krogstad test case. Its results are presented with the original EB-RSM to highlight the effects of the correction. The SSG/LRR-ω-dP v2 is displayed for reference.

Figure 6.13 shows the velocity profiles across the experimental equilibrium region. The wall-units profiles in Figure 6.13(a) displays an improved shape of the log region, with reduced extent and slightly steeper slope. However, the comparison to the reference values is biased due to an overprediction of u_τ, used in the scaling, as will be seen later.

Figure 6.13(b) shows the dimensioned velocity profiles: the correction makes the EB-RSM-dP coincide with the SSG/LRR-ω-dP v2 and the experimental measurements in the inner layer ($y \leqslant 0.04\,\mathrm{m}$). Moreover, the outer layer is hardly affected so that the EB-RSM-dP combines the improvement of the pressure diffusion term with the satisfactory prediction of the original model for the outer region to yield an overall excellent agreement with the experiment.

As for the previous APG-sensitised models, the sqrt-law is analysed with the diagnostic function at $x = 5.0\,\mathrm{m}$, plotted in Figure 6.14(a). The EB-RSM-dP clearly improves the original model Ξ_{sqrt} on the entire range and defines a plateau as expected for $\sqrt{y^+} \in [20\,;35]$. Hence, contrary to the two SSG/LRR-ω-dP models, the EB-RSM-dP actually enforces a sqrt-law region. Figure 6.14(b) shows the corresponding velocity profile in sqrt-scale, with the blending functions delimiting a correction extent that matches the plateau extent of Ξ_{sqrt}. In this figure, the linear behaviour of the EB-RSM-dP highlights the sqrt layer as expected from the diagnostic function.

The integral quantities are gathered in Figure 6.15. It can be seen in Figure 6.15(a) that the displacement thickness is hardly affected by the correction, indicating that the reduction of the velocity in the inner layer is compensated by a slightly accelerated flow in the outer region, visible in Figure 6.13(b). The correction in the inner layer however affects the momentum thickness, but at a lesser extent compared to the SSG/LRR-ω-dP Knopp model. Therefore, the shape factor plotted in Figure 6.15(b) is increased to $H \approx 2$, which is the same level as reference data.

Figure 6.15(c) confirms the overprediction of C_f for the EB-RSM-dP as noticed with the wall-units scaling of Figure 6.13(a). However, it also points out a clear improvement compared to the original model, with a reduction of more than 10 % for $x \in [3.0\,\mathrm{m}\,;5.0\,\mathrm{m}]$, which suggests a significant improvement regarding the friction drag. Contrary to the SSG/LRR-ω-dP models, the correction in the EB-RSM-dP does not exaggerate the skin friction reduction upstream of $x = 4.0\,\mathrm{m}$. Similarly, the pressure-gradient parameter in Figure 6.15(d) shows a visible improvement, with a peak of $\beta_p^{\max} = 15$ at $x \approx 3.8\,\mathrm{m}$.

The budget of the ε-equation for both the original and the APG-sensitised EB-RSMs are presented in Figure 6.16(a). As for the ω-equation budget, it can be seen that the additional pressure diffusion term stimulates production P_ε, both of them being balanced by an intensified dissipation of ε. The EB-RSM-dP also includes a cross-diffusion term, $D_\varepsilon^{\mathrm{cd2}}$, which slightly feeds dissipation at the inner edge of the sqrt layer. It can be noted that the EB-RSM-dP tends to recover the original budget from both sides of the activation zone. This points out the localisation of the correction, which is essential to ensure that the correction is not detrimental in regions where it is not intended to be active.

Figure 6.16(b) shows the increase of ε^+ due to the additional terms in the sqrt layer, forming a bump for $y^+ \in [300\,;1300]$ in the dissipation profile. As a result, the turbulent

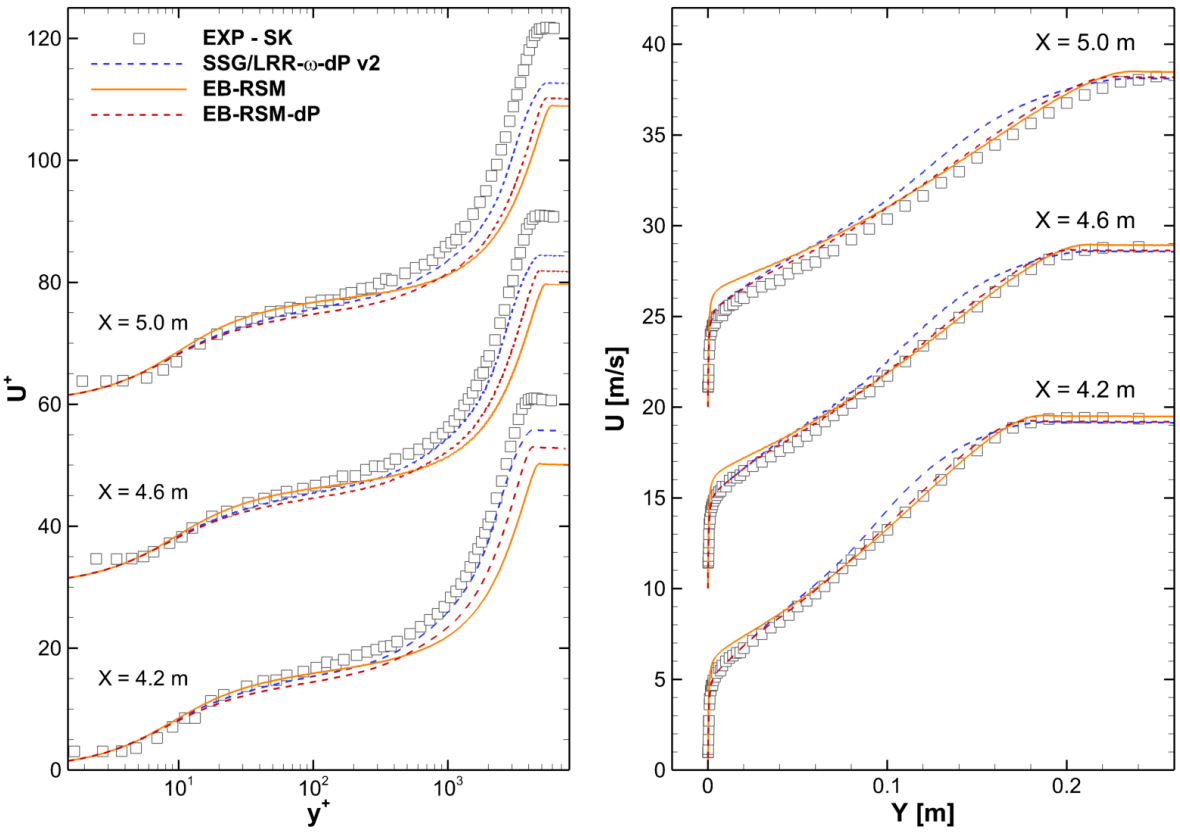

(a) *Wall-units* **(b)** *Dimensional quantities*

Figure 6.13: *Velocity profiles in the equilibrium region in the Skåre & Krogstad test case for the EB-RSM and the APG-sensitised models*

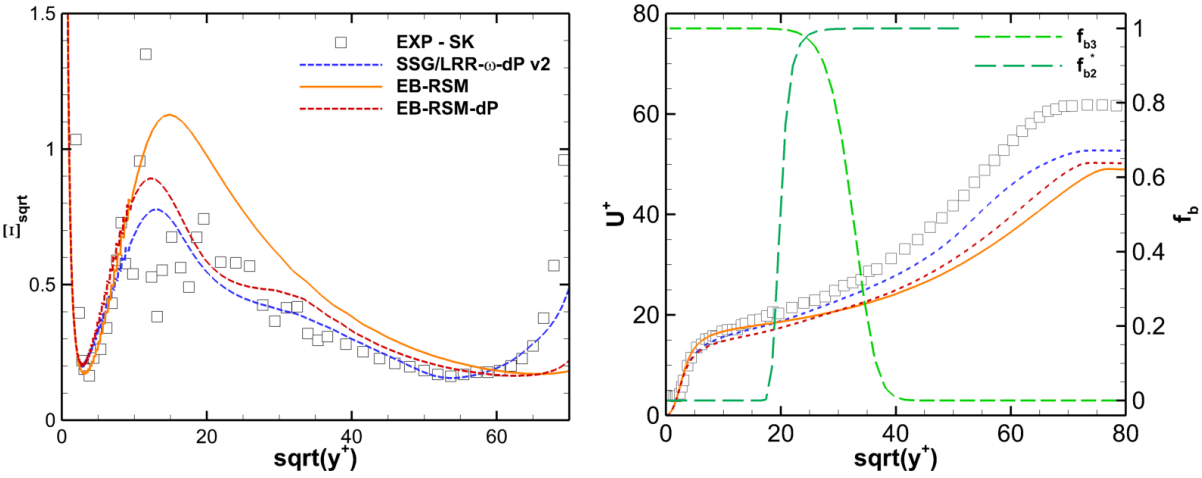

(a) *Diagnostic function* **(b)** *Velocity in sqrt-scale*

Figure 6.14: *Square-root behaviour in the Skåre & Krogstad test case for the EB-RSM and the APG-sensitised models at* $x = 5.0\,\mathrm{m}$

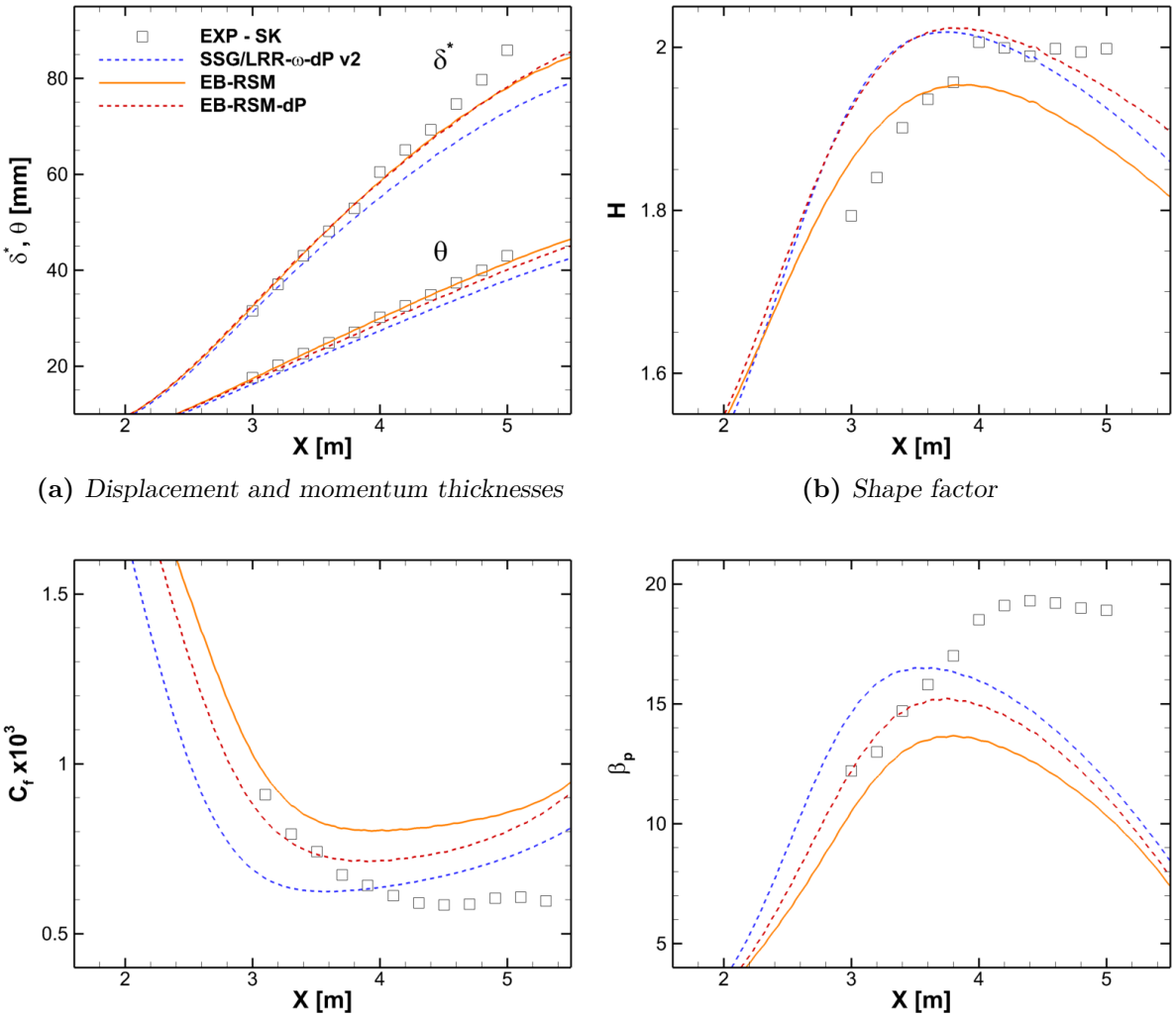

(a) *Displacement and momentum thicknesses*

(b) *Shape factor*

(c) *Skin friction coefficient*

(d) *Clauser's pressure-gradient parameter*

Figure 6.15: *Integral quantities in the Skåre & Krogstad test case for the EB-RSM and the APG-sensitised models*

mixing is damped and the velocity profile steepened. Contrary to the SSG/LRR-ω variants, the dissipation peak is only slightly increased for the EB-RSM. However it can be noted that the original model dissipation rate is more intense than the one from the SSG/LRR-ω, the latter dropping down to 0.02 in the log-law region, instead of 0.03 for the EB-RSM.

The streamwise Reynolds stress profiles are presented in Figure 6.17, respectively in wall-units and log-scale on the left, and in physical dimensions and sqrt-scale on the right. In Figure 6.17(a), the amplitude of the outer peak compared to the inner layer plateau is increased, by reducing the dimensionless turbulent intensity in the inner layer.

Figure 6.17(b) presents a zoom on the sqrt-law region for the dimensional quantities. Similarly to the dimensioned velocity profiles in Figure 6.13(b), the EB-RSM-dP displays a better agreement to the experiment, especially at the wall, where the original model predicts stresses twice as large as the wind-tunnel measurements. The reduction of $\overline{u^2}$ with the dP correction is a clear illustration of the role of the extra source terms in the ε-equation, reducing turbulence level and mixing, hence steepening the velocity profile.

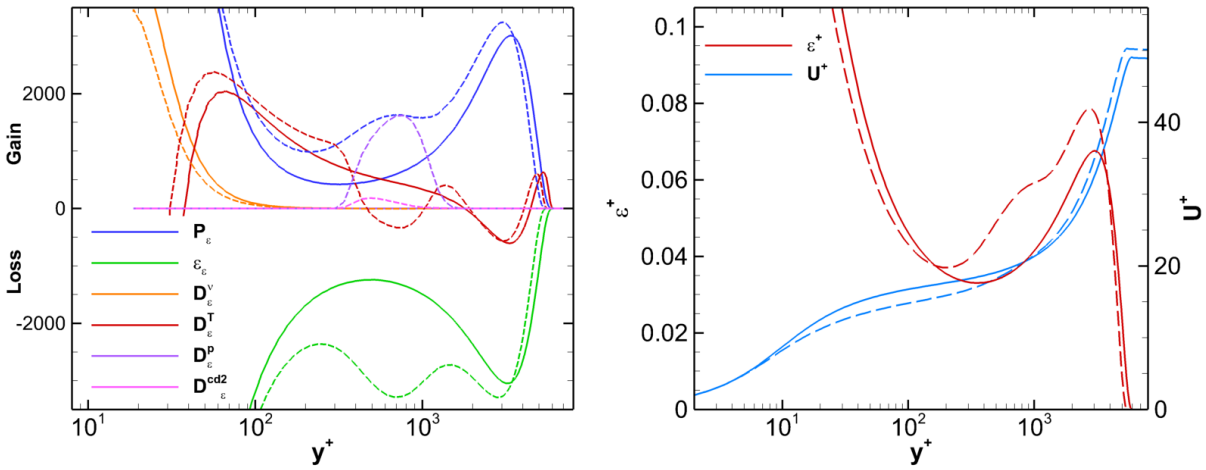

(a) *Budget of the ε-equation* **(b)** *Dissipation rate profile*

Figure 6.16: *Effect of the correction on the dissipation rate in the Skåre & Krogstad test case at $x = 5.0\,\mathrm{m}$. Solid lines, EB-RSM; dashed lines, EB-RSM-dP.*

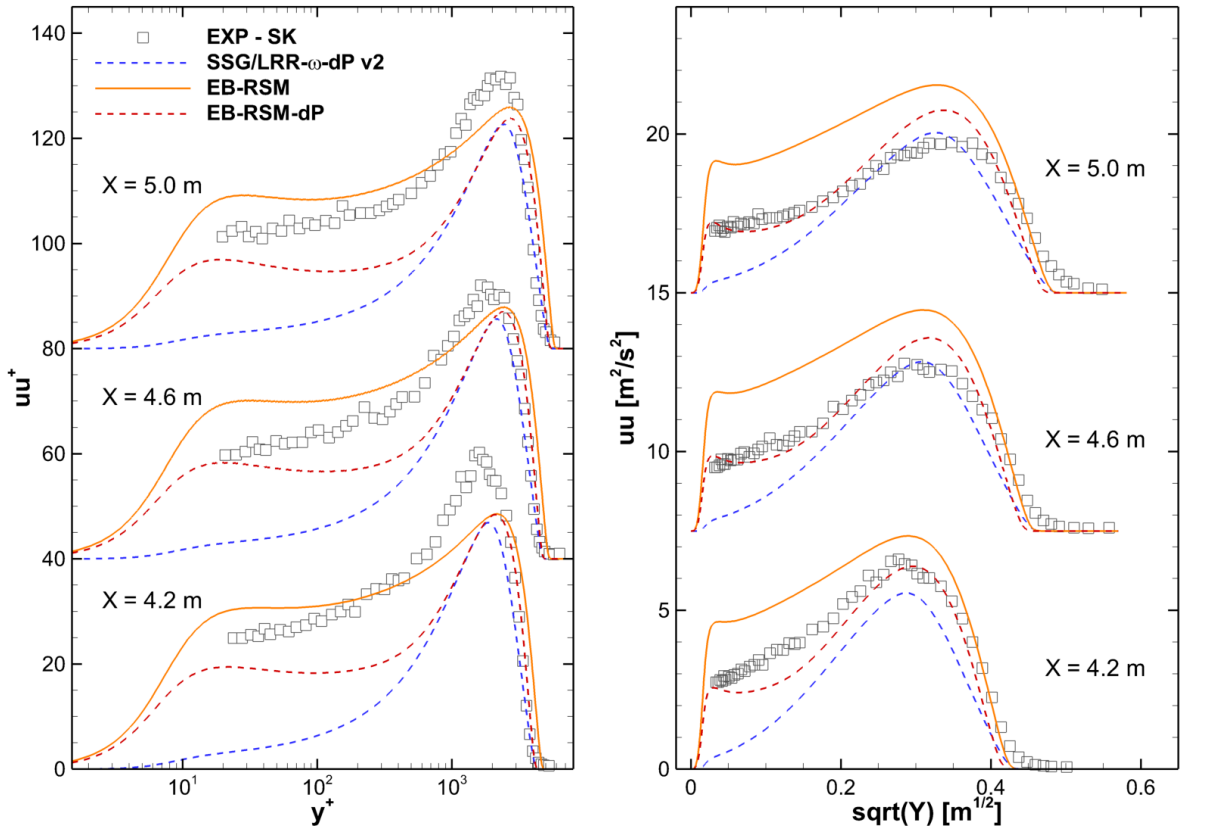

(a) *Wall-units* **(b)** *Dimensional quantities*

Figure 6.17: *Streamwise Reynolds-stress profiles in the Skåre & Krogstad test case for the EB-RSM and the APG-sensitised models*

This section has shown the effectiveness of the square-root region correction applied to the EB-RSM, by locally adding source terms in the ε-equation. The EB-RSM-dP successfully enforces the sqrt-law in the activation region, delimited by the newly defined inner blending function f_{b2}^* (Eq. (6.81)) and Knopp's outer blending function f_{b3} (Eq. (6.75)).

6.4 Conclusions

This chapter presented the analyses of the transport equations for two-equation models proposed in the literature in the overlap region defined by the generalised sqrt-law Eq. (2.49) and extended the analysis to any two-equation model. It also offered an insight of its application to Reynolds-stress transport equations, and the limits of this approach. After a short review of the existing models to account for the sqrt-law region, the proposed APG-sensitised SSG/LRR-ω model from Knopp *et al.* [52] was benchmarked and improved on the Skåre & Krogstad test case. Finally the approach was applied to the EB-RSM, whose original formulation returns enhanced results compared to the standard SSG/LRR-ω (see Chapter 4).

The resulting model, the EB-RSM-dP, displays satisfactory results. In particular, the diagnostic function displays an improved level in the inner layer, with a distinguishable plateau in the corrected region proving the effectiveness of the additional terms to impose a sqrt-law behaviour to the velocity profile, whose prediction in the inner layer is also greatly improved. Similarly, the correction improves the Reynolds-stress profiles, with a better agreement to the reference, observed with $\overline{u^2}$ for both the buffer layer peak level as well as for the outer peak, being correctly predicted. Moreover, the overall improvement of H and C_f are expected to reduce the overpredictions in form and friction drags respectively.

Chapter 7

Application: Common Research Model

The Reynolds-stress models implemented in AETHER are assessed on the Common Research Model (CRM), a public-domain geometry representative of a transonic wide-body commercial transport aircraft. This chapter first presents the results of the original RSMs presented in Chapter 3, then the improvements of the modified models ensuring consistency with the sqrt-law region: the SSG/LRR-ω-dP Knopp [52] and the EB-RSM-dP, developed in Chapter 6.

The aircraft model has been developed by NASA to build a high-quality and industry-relevant experimental database[1], and was tested in different wind-tunnel facilities. In particular, it is the reference model in the AIAA CFD Drag Prediction Workshop (DPW) series, which aims to assess state-of-the-art CFD methods as aerodynamic tools for the prediction of forces and moments, and gathers participants from academia, governments labs and industry worldwide.

7.1 Case presentation

7.1.1 Geometry

The CRM is available in different configurations, with or without a nacelle-pylon group (*i.e.* motorisation under the wing) and a horizontal tail. The 'wing-body' configuration, illustrated in Figure 7.1, is selected in the present study to keep the case simple and more representative of aircraft designed at Dassault Aviation, whose engines are located at the rear on the fuselage.

The geometry, detailed by Vassberg *et al.* [114], is designed for a cruise Mach number of $M = 0.85$ with a nominal lift of $C_L = 0.5$ at a reference-chord Reynolds number of $Re_c = 40\,\mathrm{M}$. The wing is characterised by an aspect ratio of $\mathit{AR} = 9.0$ and a leading edge sweep angle of 37.3°. Its supercritical transonic profile is shown in Figure 7.2. Noting η the normalised semi-spanwise coordinate, the wing root is located at $\eta = 0.1$ and the change in the trailing edge angle occurs at $\eta = 0.37$. The reference chord is $c_{\mathrm{ref}} = 275.8\,\mathrm{in} \approx 7.0\,\mathrm{m}$.

[1] https://commonresearchmodel.larc.nasa.gov/

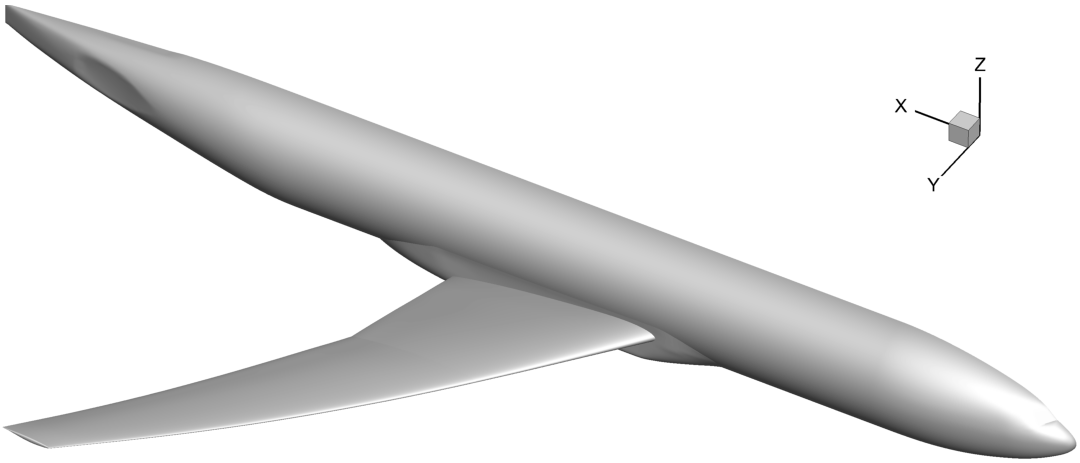

Figure 7.1: *The CRM 'Wing-Body' configuration*

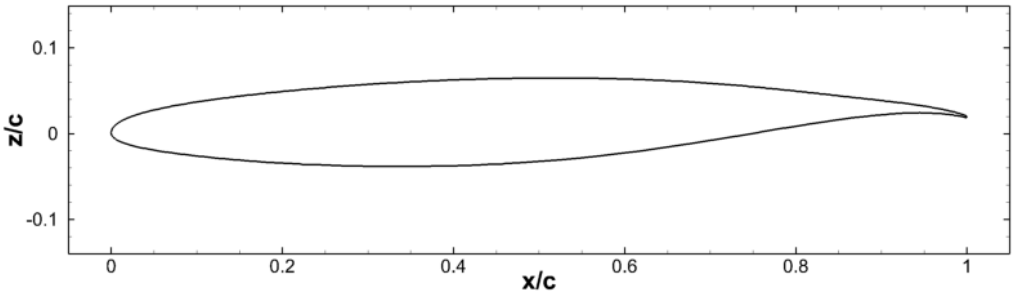

Figure 7.2: *The CRM wing supercritical transonic profile at* $\eta = 0.5$

7.1.2 Computational details

The CRM is investigated at two different Reynolds numbers considered during wind-tunnel tests, respectively $Re_c = 5\,\mathrm{M}$ and $Re_c = 30\,\mathrm{M}$. Although they are not run at the design Reynolds number ($Re_c = 40\,\mathrm{M}$), both cases are run at the design cruise Mach number $M = 0.85$.

To improve the correspondence with the experimental data, the CRM geometry is deformed according to the static aeroelastic deflections observed in wind-tunnels. Deformed CAD geometries have been provided for the 6$^{\text{th}}$ DPW [110] using measurements of the European Transonic Wind-tunnel (ETW) at $M = 0.85$, $Re_c = 5\,\mathrm{M}$ for seven angles of attack ($\alpha^{\text{exp}} \in [2.50°\,; 4.00°]$ with a step of 0.25°) [48].

For the present study, the low Reynolds number computations are performed on the deformed geometry provided by ETW for $\alpha^{\text{exp}} = 2.75°$, which corresponds to $C_L^{\text{exp}} = 0.5$.

For the high-Reynolds number case, no deformed geometry is available from ETW and the geometry deformation measured at $Re_c = 5\,\mathrm{M}$ for 3.50° is used. This corresponds to a lift at $Re_c = 5\,\mathrm{M}$ of $C_{L,5} = 0.6$ and a lift at $Re_c = 30\,\mathrm{M}$ of $C_{L,30} = C_{L,5} q_5/q_{30} = 0.4$, where q is the dynamic pressure. This extrapolation relies on the assumption that for a given value of lift $L = qC_L A_L$ (Eq. (2.7)) corresponds a unique deformation distribution which is only true if the distribution of aerodynamic forces and material properties, particularly elasticity, remain unchanged between low-Re and high-Re cases. This is no longer the case for strong aerodynamic load (*e.g.* due to buffeting), hence the analysis is restricted to $C_L \leqslant 0.4$ for the high-Reynolds number case.

In the results presented therein, the computed shape is only consistent with the

aerodynamic load of the experiment, $C_L = 0.5$ for the low-Re case and $C_L = 0.4$ for the high-Re case respectively. However, for results at lower lift coefficient, the error in calculated shape does not change the hierarchy of models variants with respect to reference data. To confirm the present conclusions on model performance, polar calculations have been repeated with a more accurate account of geometry deflection, the results of which are presented for the EB-RSM in Section 7.3.3.

The computations are performed on unstructured meshes with a first-cell height of $y^+ < 1$ on the wing. As a result, they consist in 17.3 M nodes for the first case at $Re_c = 5$ M and 20 M nodes for the second at $Re_c = 30$ M. The mesh convergence was confirmed with the Spalart-Allmaras QCR model, by comparison with the results from the participants of the 6$^{\text{th}}$ DPW [110]. The geometry and mesh characteristics of the cases are summarised in Table 7.1.

Table 7.1: *Characteristics of the application cases*

Case	Re_c	Deflected geometry	C_L	Mesh size
Low-Re	$5 \cdot 10^6$	$\alpha^{\text{exp}} = 2.75°$	0.5	$17.3 \cdot 10^6$
High-Re	$30 \cdot 10^6$	$\alpha^{\text{exp}} = 3.50°$	0.4	$20.0 \cdot 10^6$

In the following sections, pressure coefficient distributions and drag polars for the different turbulence models are compared to the corresponding measurements from the 'Test 197' wind-tunnel campaign carried out at the National Transonic Facility (NTF)[2]. The experimental data include wall corrections to account for the wind-tunnel walls in the test section.

To ensure a consistent comparison, the C_p-distributions are presented at the lift coefficient corresponding to the deformed geometry. To that end, the angle of attack α is iteratively adjusted by the solver to converge towards the target lift, after an initial convergence at constant α.

7.2 Original models

The three Reynolds-stress models presented in Section 3.3, namely the SSG/LRR-ω RSM, the SSG-ω ATAAC RSM and the EB-RSM, are benchmarked against the experimental data. In this section, the models are considered in their original formulation, *i.e.* without any modification. The Spalart-Allmaras model with the QCR correction is indicated as a reference to the prediction level of what is commonly used in engineering.

7.2.1 Pressure coefficient

The pressure coefficient distributions are presented in Figure 7.3 for both Reynolds numbers at three different spanwise positions, respectively close to the fuselage ($\eta = 0.201$), at the middle of the wing ($\eta = 0.502$) and close to the wing tip ($\eta = 0.846$). The predictions of the RSMs are globally close to the Spalart-Allmaras model and to the reference. This can be expected from the fact that the results are here compared at matching lift coefficients. The

[2] https://commonresearchmodel.larc.nasa.gov/home-2/high-speed-crm/

corresponding angles of attack are gathered in Table 7.2 and display noticeable differences to the experiment. Note that since the wind-tunnel measurements include wall-corrections, it can be assumed that the experimental angles of attack are free from the influence of the wind-tunnel. The EB-RSM yields the closest α, yet with a relative error of 6 % for the low-Re case and 15 % for the high-Re one. Therefore, considering the C_p-distribution at a given angle of attack would probably result in the EB-RSM yielding the best predictions, ahead of the SSG-ω ATAAC RSM, the SSG/LRR-ω and finally the Spalart-Allmaras.

Table 7.2: *Angles of attack yielding the target C_L*

	Low-Re	High-Re
EXP	2.75°	1.92°
EB-RSM	2.58°	1.64°
SSG-ω ATAAC RSM	2.53°	1.58°
SSG/LRR-ω RSM	2.52°	1.58°
SA-QCR	2.48°	1.55°

In the present comparison at given C_L, the models still tend to underestimate the aerodynamic load upstream of the shock wave and overestimate it downstream. This is especially visible for the three stations at $Re_c = 30$ M, in Figures 7.3(b), (d) & (f).

The largest differences amongst models are located at the shock, the EB-RSM returning a shock position closest to the experiment for most of the considered stations, for both Reynolds numbers. The comparison with the experiments is however more difficult for some positions in the vicinity of the shock wave, due to the coarse resolution of the pressure probes, particularly at $\eta = 0.502$, where the supersonic flow upstream of the shock is barely measured.

A major contributor to the discrepancies between CFD and experiment is the depression occurring after the shock on the suction side, characterised by a 'rebound' on the C_p plot, and largely overpredicted by models. This rebound grows from negligible at the body side into a second shock towards the wing tip. The rebound is amplified at high-Re, the depression becoming stronger than the leading edge depression at the wing tip in Figure 7.3(f). It can be noted that the reduction of this overprediction for both cases follows the ranking of the models observed in Table 7.2, the EB-RSM yielding the smallest overprediction of the rebound and thus being the closest to the experiment.

The pressure coefficients of the APG flow at the trailing edge, on both sides of the wing, are better predicted with RSMs, the EB-RSM yielding once again the closest distribution to the reference. However, the differences between models are very small and are mainly located at the suction-side bump around $x/c = 0.9$.

The leading edge pressure level on the suction side is also slightly improved, as it can be seen especially in Figure 7.3(d). It is directly related to the shock wave position shift since the models yield the same lift coefficient. Indeed in that case, assuming the same load distribution in the spanwise direction for all the models, the area inside the C_p-distribution is expected to be the same. The improvement of the leading edge pressure level exhibits therefore the same model ranking as the shock wave shifting, the EB-RSM being distinguishable from the others.

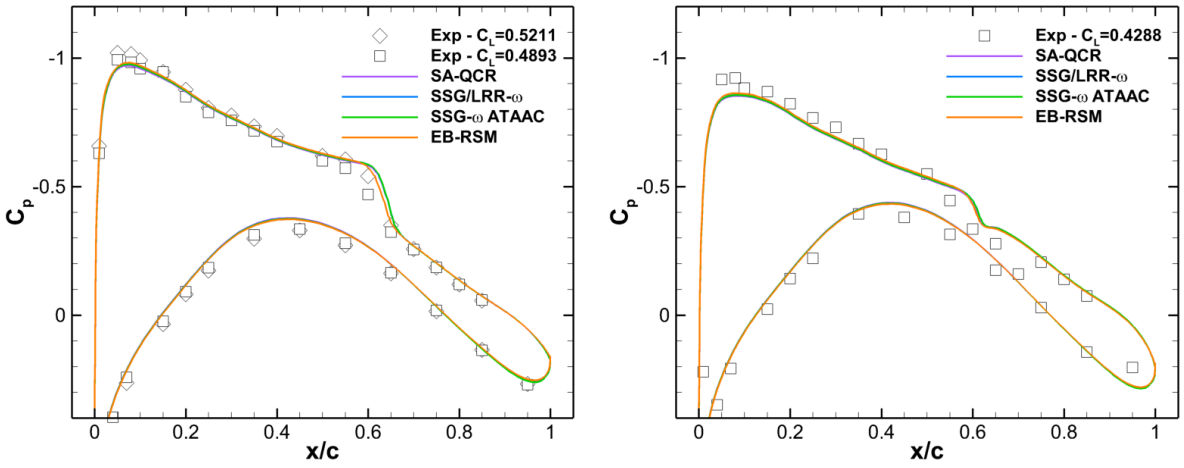

(a) $Re = 5\,\mathrm{M}$, $\eta = 0.201$

(b) $Re = 30\,\mathrm{M}$, $\eta = 0.201$

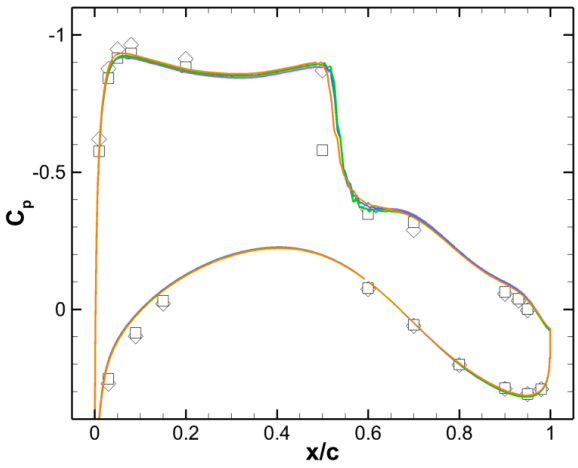

(c) $Re = 5\,\mathrm{M}$, $\eta = 0.502$

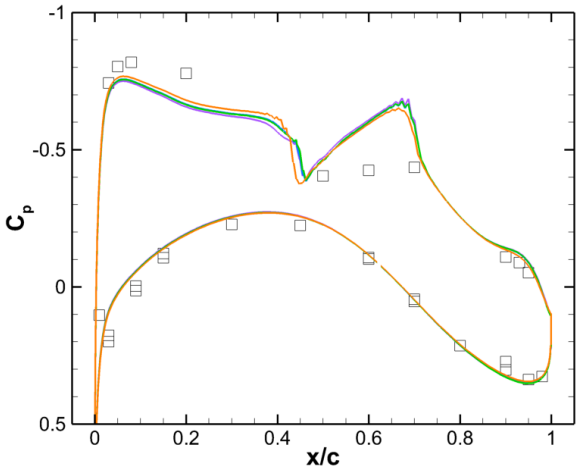

(d) $Re = 30\,\mathrm{M}$, $\eta = 0.502$

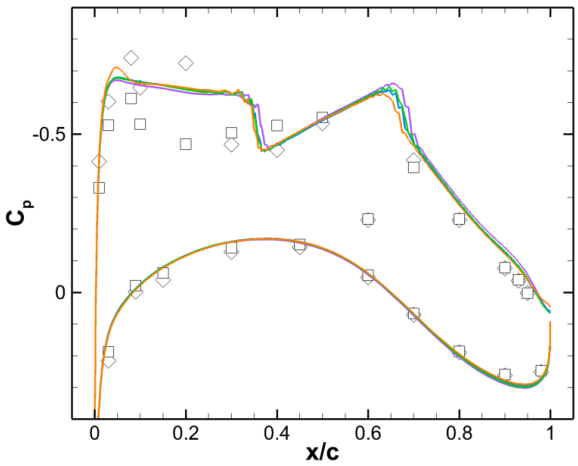

(e) $Re = 5\,\mathrm{M}$, $\eta = 0.846$

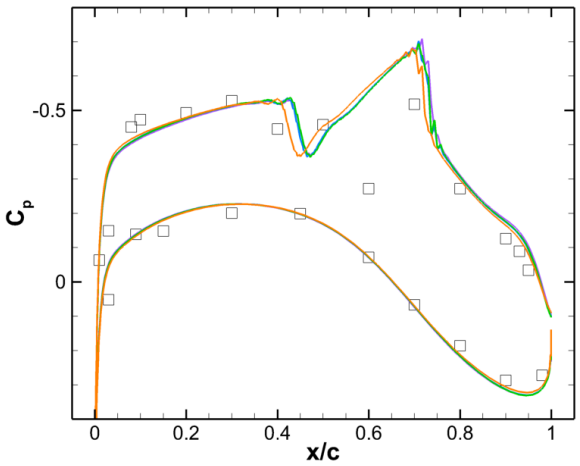

(f) $Re = 30\,\mathrm{M}$, $\eta = 0.846$

Figure 7.3: *Pressure coefficients on the CRM*

7.2.2 Drag polars

Polars have been computed between $C_L = 0.2$ and the nominal lift coefficient of the cases, to analyse the predicted variations of the aerodynamic load on the aircraft during cruise. Indeed, the aircraft gets lighter as it burns fuel, which decreases the lift required to sustain a level flight but also the resulting drag, and thus, the required thrust and the fuel consumption. To correctly predict the performance of the designed aircraft geometry and its overall fuel consumption, lift and drag variations must therefore be accurately anticipated, using drag polars.

In particular, these polars make it possible here to assess the accuracy of the response in drag to a given lift variation for the considered models. Contrary to Dassault Aviation standards to study the far-field drag, the drag presented here has been computed with the near-field method, as presented in Section 2.1.1. The far-field drag post-processing tools indeed require a specific recalibration for each model, which has not yet been carried out for the recently implemented RSMs.

Moreover, the computations do not account for the aircraft aeroelasticity, as the considered geometries are those measured at ETW for the highest C_L of the polar. The impact of the aeroelasticity of the aircraft model on the drag polars will be assessed in Section 7.3.3 for the EB-RSM and its sqrt-law corrected version.

Figures 7.4 & 7.5 present the lift and drag coefficients as functions of the angle of attack for all four models and the NTF test, respectively for $Re_c = 5\,\mathrm{M}$ and $Re_c = 30\,\mathrm{M}$.

Figures 7.4(a) & 7.5(a) illustrate the shift in the angles of attack indicated in Table 7.2, the amplitude of the deviation being amplified by the Reynolds number. Consequently, the lift is overpredicted by over 6 % at $\alpha = 2.5°$ in low-Re case and by over 10 % at $\alpha = 1.5°$ in the high-Re. As for the C_p-distribution, the EB-RSM is distinguishable from the other models for both cases and confirms its better predictions. The SSG/LRR-ω and the SSG-ω models also improve the predicted lift compared to the Spalart-Allmaras model at $Re_c = 5\,\mathrm{M}$. Note that the slopes of the lift coefficient computed by AETHER are steeper than the wind-tunnel measurements. This can be justified by the rigidity of the numerical geometry considered and is expected to be improved by accounting for aeroelasticity.

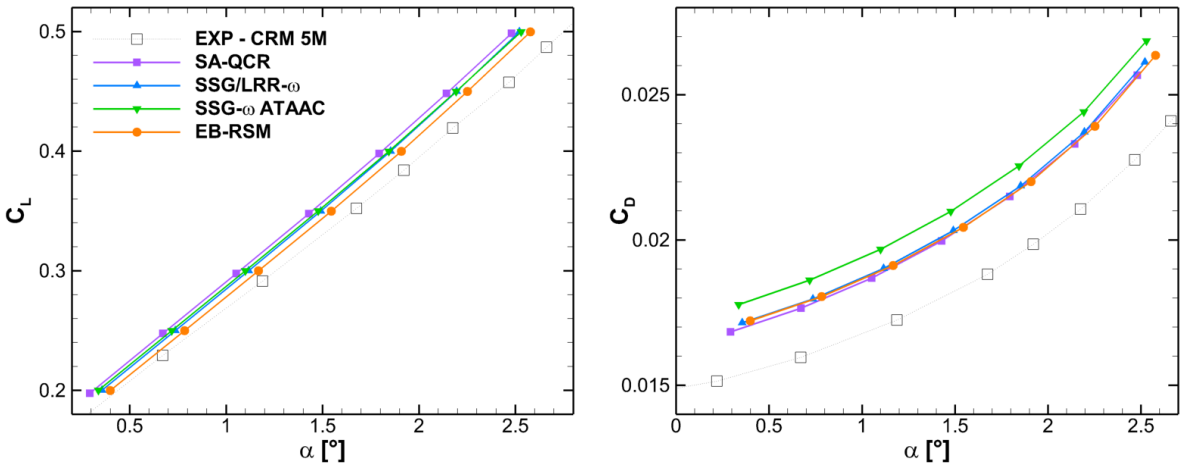

(a) *Lift* **(b)** *Drag*

Figure 7.4: *Aerodynamic forces on the CRM at* $Re_c = 5\,\mathrm{M}$ *with the standard models*

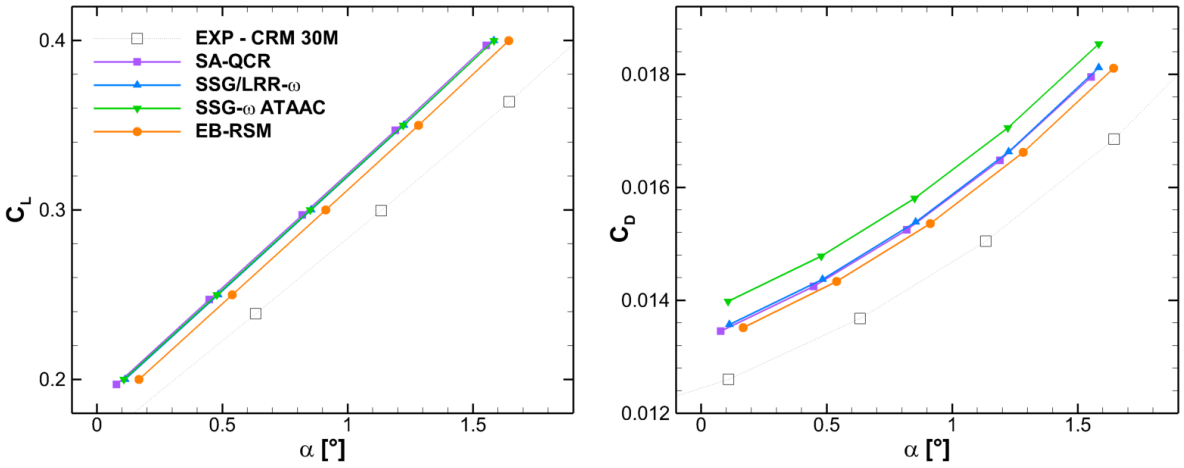

(a) *Lift* **(b)** *Drag*

Figure 7.5: *Aerodynamic forces on the CRM at* $Re_c = 30\,\mathrm{M}$ *with the standard models*

As seen in Figure 7.4(b), the models overestimate the drag by 12 % at $Re_c = 5\,\mathrm{M}$. The relative error is increased to 16 % for the SSG-ω ATAAC model, as expected from the flat plate benchmark. Indeed, its systematic overprediction of the skin friction observed in Section 4.1 leads to an extra friction drag. For the high-Re case, Figure 7.5(b), the same conclusions can be drawn, with an average relative error of 7 % for the Spalart-Allmaras and the SSG/LRR-ω models, increased to 11 % for the SSG-ω ATAAC model. The EB-RSM here stands out from the others, as for the lift coefficient in Figure 7.5(a), and improves the drag prediction with a relative error of 6 % to reference.

The drag polars plotted in Figures 7.6(a) & 7.7(a) show the evolution of drag with lift

$$C_D = C_{D,0} + C_{D,L}\,(C_L) \tag{7.1}$$

where $C_{D,0}$ is the drag remaining in zero-lift conditions and $C_{D,L}$ the drag due to lift, which includes the induced drag and the lift-dependent parts of friction, form and wave drags. Drag polars make it possible to distinguish the zero-lift drag $C_{D,0}$, corresponding essentially to the constant parts of the friction and form drags and appearing as a lateral shift in the figures, from $C_{D,L}$ regardless of the angle of attack.

Although all the models overpredict the drag, mostly the friction drag according to the Skåre & Krogstad benchmark in Section 4.2, where an overprediction of the skin friction coefficient was observed with all models, the increase of drag with lift is underpredicted. In particular, the shift of the SSG-ω ATAAC model polar indicates that the extra friction observed in the flat plate benchmark mostly impacts $C_{D,0}$, hence the constant component of the friction drag. Besides, it can be observed that the Spalart-Allmaras model better predicts the zero-lift drag compared to the Reynolds-stress models for the low-Re case.

At $Re_c = 30\,\mathrm{M}$, the EB-RSM, the SSG/LRR-ω and the Spalart-Allmaras model coincide. For the EB-RSM, whereas $C_L(\alpha)$ and $C_D(\alpha)$ are improved, $C_D(C_L)$ is no better than for other models, reflecting a misprediction of either the form drag or the friction drag. From the results of the Skåre & Krogstad test case presented in Section 4.2 and showing the discrepancies of the model in APG flows, it can be expected to be friction drag. Indeed, in that case, the displacement thickness was very well predicted and the

skin friction overpredicted. However, such a distinction of drag parts is not available in the experimental data to formally conclude.

In engineering applications, the drag polars are readjusted for a given polar point to compensate for the extra zero-lift drag due to wind-tunnel settings and aircraft excrescences, such as antenna and Pitot tubes. In the following, such readjusted drag polar is considered, with a reference point for the readjustment taken at $C_L = 0.2$. However, to focus on the error of drag due to lift, the absolute error of the readjusted drag polar to the experimental values is presented here rather than the readjusted drag polar itself.

Hence, Figures 7.6(b) & 7.7(b) exhibit such a drag-error polar

$$\mathrm{d}C_D = C_D - C_D^{\mathrm{exp}} - \left(C_D|_{C_L=0.2} - C_D^{\mathrm{exp}}|_{C_L=0.2}\right). \tag{7.2}$$

Although the geometry accounts for the static deformation at the highest lift point, the origin error is set at $C_L = 0.2$ to rather point out the dispersion of the models in the range where the slope becomes milder and the error more significant.

These figures highlight the better $C_{D,L}$ prediction from the RSMs over the Spalart-Allmaras model. It can be noted that the previous model ranking is retrieved. Indeed, in Figure 7.6(b), the Spalart-Allmaras error at $C_L = 0.45$ for the low-Re case is reduced by 25 % with the SSG/LRR-ω model, by almost 40 % with the SSG-ω ATAAC model and by more than half with the EB-RSM. The same conclusions apply to the high-Re case shown in Figure 7.7(b), with however a narrower amplitude, the EB-RSM still reducing the error down by 20 %.

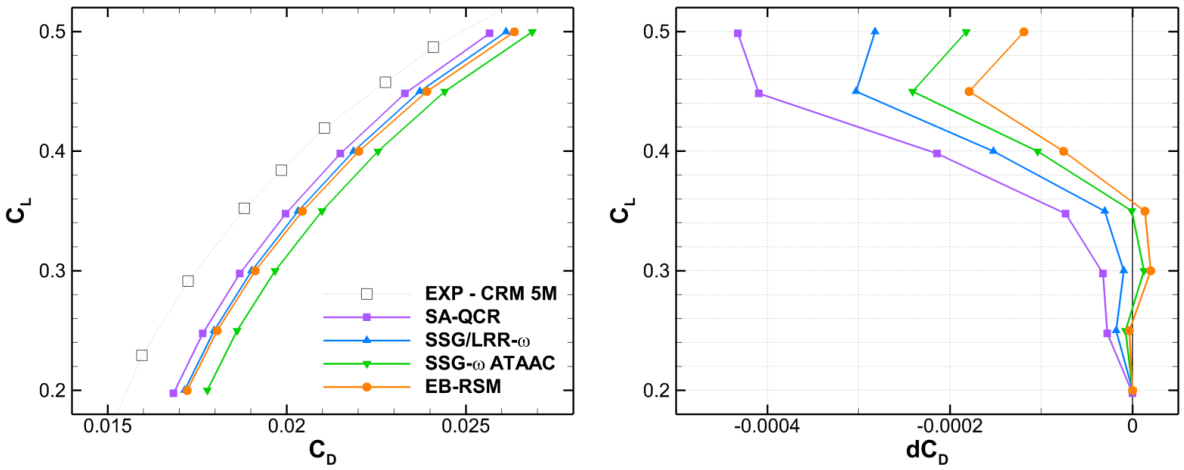

(a) $C_L = f(C_D)$ **(b)** *Absolute error of the drag-due-to-lift*

Figure 7.6: *Drag polars on the CRM at* $Re_c = 5\,\mathrm{M}$ *with the standard models*

7.2.3 Conclusions

Both the pressure-coefficient distributions and the drag polars pointed out the improved accuracy of the Reynolds-stress models on an industrial aeronautical application compared to today's default model in the industry, the Spalart-Allmaras model.

Despite the ω-equation being supposed to improve mild APG flow predictions, the computations on the CRM show here that the best results are achieved with the EB-RSM,

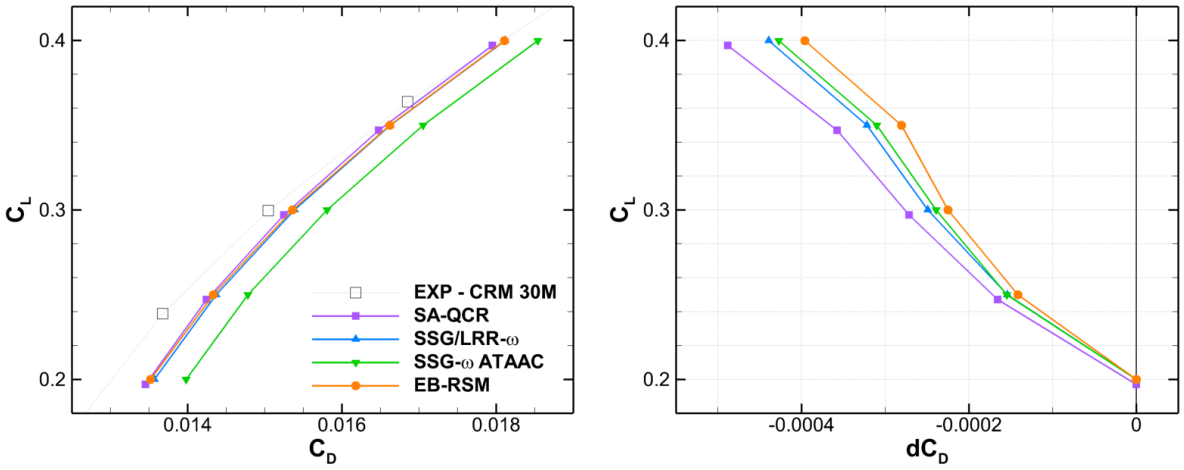

(a) $C_L = f(C_D)$ **(b)** *Absolute error of the drag-due-to-lift*

Figure 7.7: *Drag polars on the CRM at* $Re_c = 30\,\mathrm{M}$ *with the standard models*

relying on the ε-equation. This might be directly related to its near-wall modelling, as the results point out that both RSMs using such an approach, the EB-RSM and the SSG-ω ATAAC model, exhibit improved predictions compared to the SSG/LRR-ω model. The SSG-ω ATAAC model is however penalised by the overprediction of the skin friction, observed on the flat plate.

7.3 APG-sensitised models

To highlight the benefits of the sqrt-law correction presented in Chapter 6, two Reynolds-stress models using an additional pressure-diffusion term in their length-scale providing equations are compared to their original models.

- The SSG/LRR-ω-dP Knopp [52] is benchmarked as the reference APG-sensitised RSM from the literature.
- To build on the best predictions offered by the EB-RSM in the Skåre & Krogstad test case and in the CRM application case in the previous section, the suggested model from this work is the EB-RSM-dP, relying on a new blending function to define the activation region of the correction.

7.3.1 High Reynolds number case

Pressure coefficient

The pressure coefficients are shown in Figure 7.8 for $Re_c = 30\,\mathrm{M}$. The corrected models are drawn in dark dashed lines against the baseline formulations in solid lines at the same inner, mid-span and wing tip stations as in Section 7.2.1.

The pressure-diffusion correction clearly improves both the standard SSG/LRR-ω RSM and the EB-RSM, and amplifies the difference already observed between the models in the previous section. For both models, the correction reduces the underprediction of the aerodynamic load upstream of the shock, and the overprediction downstream, especially

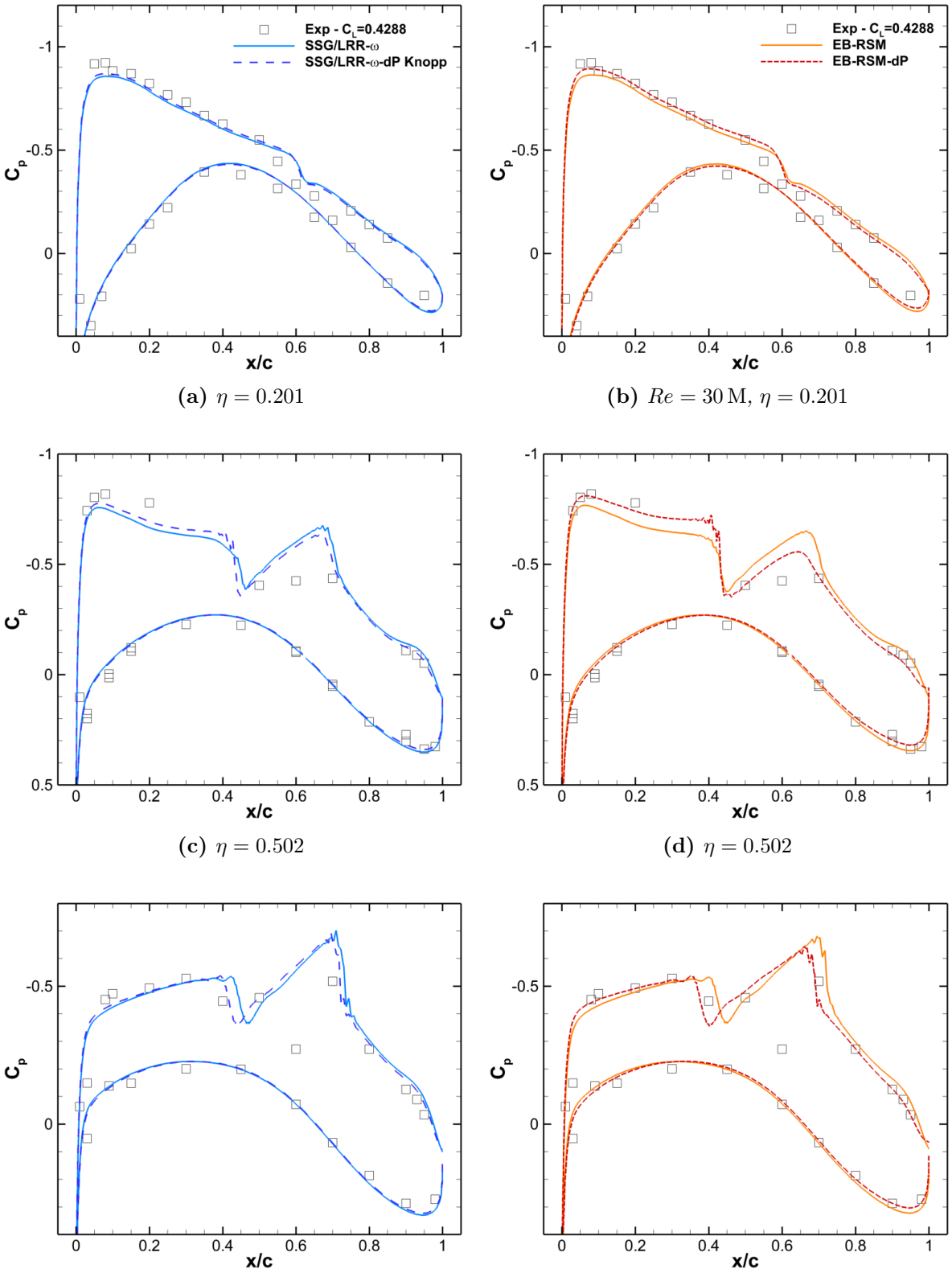

(a) $\eta = 0.201$ **(b)** $Re = 30\,\mathrm{M}$, $\eta = 0.201$

(c) $\eta = 0.502$ **(d)** $\eta = 0.502$

(e) $\eta = 0.846$ **(f)** $\eta = 0.846$

Figure 7.8: *Pressure coefficients on the CRM at* $Re = 30\,\mathrm{M}$ *for the APG-sensitised RSMs*

visible at midspan, Figures 7.8(c) & (d). It results in a stronger shock wave, which progressively drifts upstream with the spanwise distance, up to 6 % for the model from Knopp *et al.* [52] and 10 % for the new model. The rebounds are softened and the APG on the trailing edge more accurately rendered.

In particular, it can be seen that the amplitude of the correction is larger for the EB-RSM-dP model in Figures 7.8(b), (d) & (f), resulting in significant improvement compared to the other models. Indeed, its pressure distributions stands out and closely follows the experimental points, even for the body-side position in Figure 7.8(b). At this station, the correction has little effect on the SSG/LRR-ω model.

Moreover, the angles of attack yielding the target $C_L = 0.4$ at $Re_c = 30\,\mathrm{M}$ get better with the modified models. The resulting angle of attack for the SSG/LRR-ω model goes from 1.58° with the original model to 1.69° with the correction, and the EB-RSM goes from 1.64° to 1.90°, only 1.2 % below the experimental value $\alpha^{\mathrm{exp}} = 1.92°$.

The increased amplitude of the correction of the EB-RSM-dP over the model from Knopp *et al.* [52] can be explained by the increased zone of the pressure diffusion activation. Figure 7.9 shows this region, corresponding to the product of the inner and outer blending functions, at the trailing edge of the wing profile for $\eta = 0.502$, and highlights the thin APG boundary layers developing on both sides of the wing. As in the Skåre & Krogstad test case, the activation region for the SSG/LRR-ω-dP Knopp never reaches one, because the blending functions switch simultaneously. For instance, on the suction side, $f_{b2} f_{b3} \leqslant 0.9$, the maximum value being reached in a very thin layer. As a result, the additional pressure diffusion is damped and does not entirely correct the specific dissipation rate budget.

On the contrary, the new inner blending function f^*_{b2} activates closer to the wall for the EB-RSM-dP, and allows the corrective terms to be fully active in the budget of the ε-equation with $f^*_{b2} f_{b3} = 1$ in the sqrt-law region. It also makes the activation region extend on a larger part of the wing, and correct milder APG regions compared to the SSG/LRR-ω-dP Knopp model. This demonstrates the improved sensitivity to the local

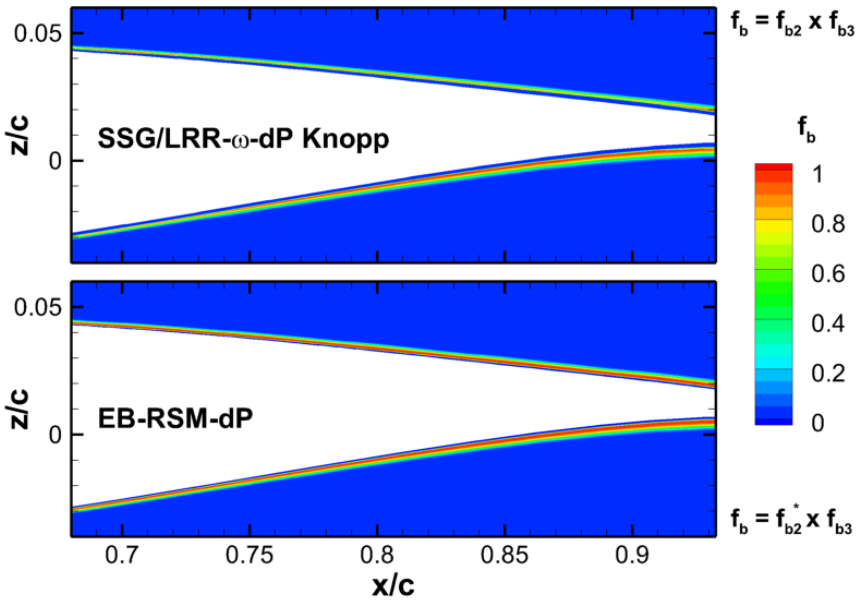

Figure 7.9: *Activation zone of the pressure-diffusion term for the APG-sensitised RSMs on the CRM at* $Re_c = 30\,\mathrm{M}$, $\eta = 0.502$

Reynolds number of the new function f_{b2}^* over the function f_{b2} experimentally inferred by Knopp.

Drag polars

In line with the conclusions for the predictions of the pressure coefficient, the lift and drag polars confirm the satisfactory behaviour of the modified models for the configurations at different flow angles of attack.

Figure 7.10 shows in particular the great agreement of the new EB-RSM version with the wind-tunnel test. Lift and drag are strongly reduced at a given α to coincide with the experimental measurements at $C_L = 0.4$, for which the computed geometry has been deformed. As for the models in Section 7.2.2, the inaccuracy in the lift slope is expected from the limitation of the rigid-body approach. Consequently, it can be anticipated that lift and drag will increase for the lower angles of attack with aeroelasticity.

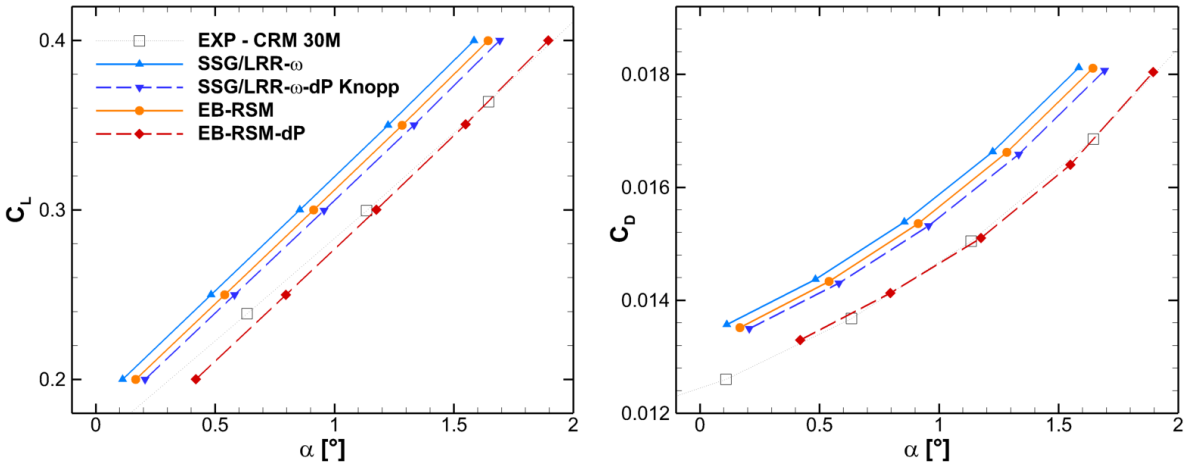

(a) *Lift* **(b)** *Drag*

Figure 7.10: *Aerodynamic forces on the CRM at* $Re_c = 30\,\mathrm{M}$ *for the APG-sensitised RSMs*

With the additional pressure-diffusion terms in the sqrt-law region, the EB-RSM-dP corrects both the zero-lift drag $C_{D,0}$, resulting especially from an improved friction prediction according to the Skåre & Krogstad test case Figure 6.15(c), and the drag due to lift, as seen in Figure 7.11(a). Regarding the SSG/LRR-ω-dP Knopp, the improvement observed for $C_L(\alpha)$ and $C_D(\alpha)$ is less visible on the $C_L(C_D)$ plot. It can be assumed that the friction drag reduction arising from the improved prediction of the skin friction, observed with the Skåre & Krogstad experiment in Section 6.2.3, is balanced with the degradation of the outer region of the boundary layer, impacting the form drag negatively.

Nevertheless, the modified RSM proposed by Knopp *et al.* yields a progressive improvement of the recalibrated polar $\mathrm{d}C_D$, achieving a reduction in the absolute error of 6 % at $C_L = 0.4$ in Figure 7.11(b). On the contrary, the figure shows an irregular impact of the sqrt-law correction on $\mathrm{d}C_D$ for the EB-RSM. Indeed, before reducing it by almost 40 % at $C_L = 0.4$, it deteriorates the error at $C_L = 0.3$ by 15 %. Note that this error corresponds to a drag increment of less than half a drag count[3] ΔC_D, which remains negligible. This

[3] a drag count is a unit drag used to measure the change in C_D and is equal to $\Delta C_D = 10^{-4}$

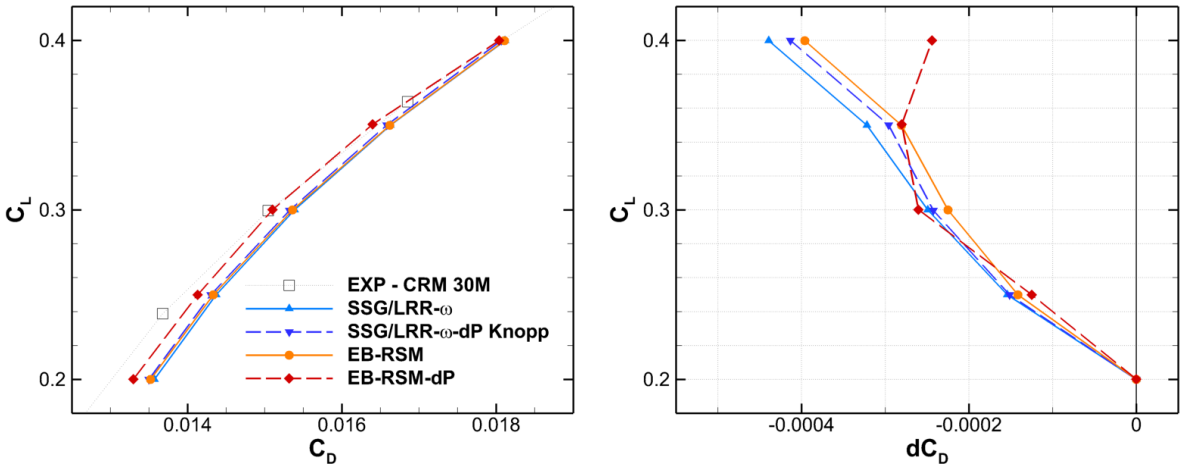

(a) $C_L = f(C_D)$ **(b)** *Absolute error of the drag-due-to-lift*

Figure 7.11: *Drag polars on the CRM at* $Re_c = 30\,\mathrm{M}$ *for the APG-sensitised RSMs*

odd behaviour might be due to numerical artefacts, and could be assessed by including more incidence points in the drag polar study.

7.3.2 Low Reynolds number case

Pressure coefficient

At $Re_c = 5\,\mathrm{M}$, the impact of the sqrt-law correction is hardly visible on the pressure distributions. Indeed, Figure 7.12 shows that the APG-sensitised RSMs coincide with their original models.

They mostly differ in their prediction of the shock wave position at the wing tip. The shock wave is indeed moved upstream by the correction of the SSG/LRR-ω-dP Knopp by 2 % in Figure 7.12(c), and by 3.5 % for the EB-RSM-dP in Figure 7.12(d). This can be compared to the 6 % and 10 % observed at $Re_c = 30\,\mathrm{M}$ respectively.

More generally, the same trend as in the high-Re case is to be noticed here, with a smaller amplitude. For instance at the mid-span station, the depression level increases upstream of the shock wave, especially for the EB-RSM in Figure 7.12(d), whereas the APG trailing edge on the suction side is slightly improved.

Paradoxically, the correction has a less significant impact at the wing tip trailing edge, where the pressure coefficient is clearly shifted outwards compared to the reference, than close to the fuselage, where the original models are already close to the reference. In Figures 7.12(e) & (f) the curves of the two modified models exactly coincide, despite the strong pressure gradient after the rebound downstream the shock wave, for $x/c \geqslant 0.6$, on both sides of the wing. Noting that the chord length is locally shorter, it results in a Reynolds number Re_θ restricted by the distance on which the boundary layer develops, in addition to the lower Reynolds number of the case, which already reduces Re_θ by decreasing the ratio U_∞/ν.

More globally, the reduced influence of the correction at low Reynolds number for both models was expected. Indeed, the blending functions have been calibrated on high-Reynolds-number APG flows, such as in the VicToria experiments [52] and the Skåre & Krogstad experiment [99], where $Re_\theta \in [40{,}000\,;\,50{,}000]$. At $Re_c = 30\,\mathrm{M}$, Re_θ ranges

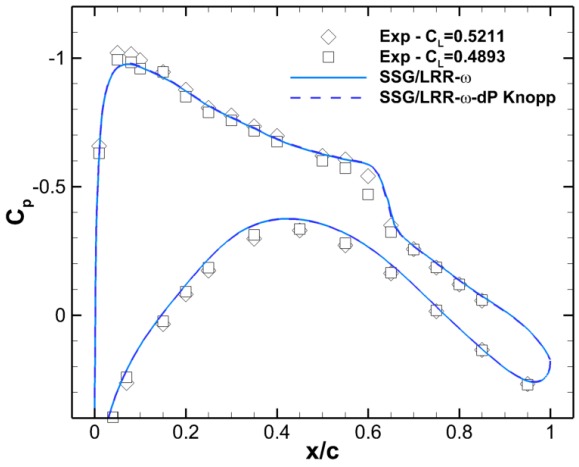

(a) $\eta = 0.201$

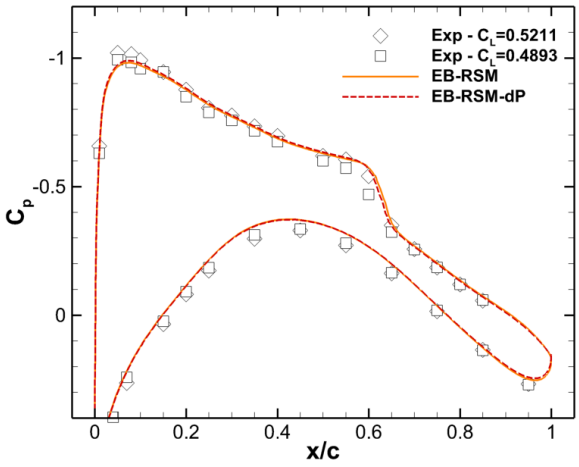

(b) $\eta = 0.201$

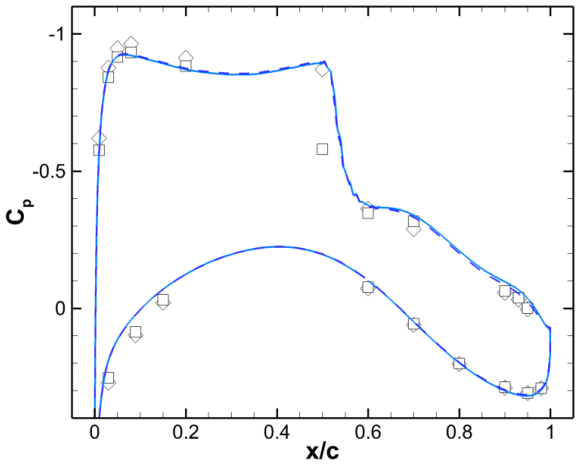

(c) $\eta = 0.502$

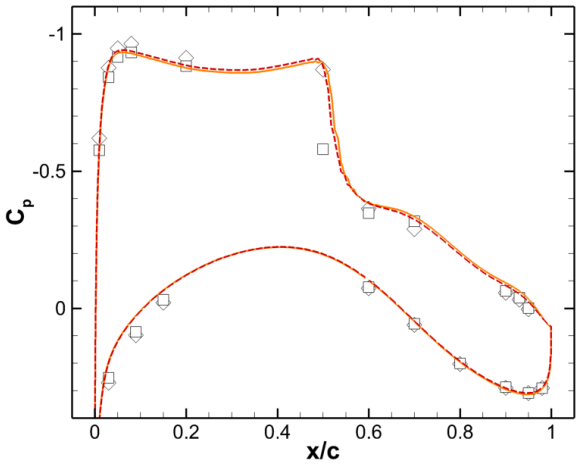

(d) $\eta = 0.502$

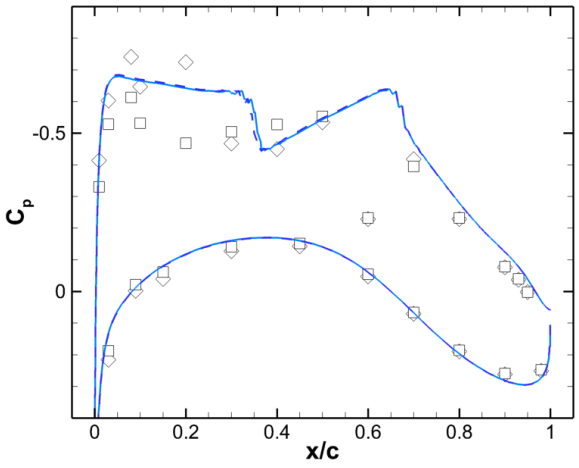

(e) $\eta = 0.846$

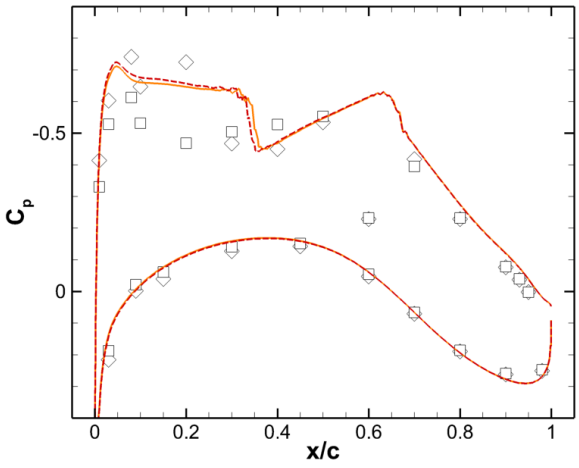

(f) $\eta = 0.846$

Figure 7.12: *Pressure coefficients on the CRM at $Re = 5\,\mathrm{M}$ for the APG-sensitised RSMs*

between 25,000 and 80,000 in the APG region, corresponding to the downstream half of the wing. For the low-Re case, it is restricted to $Re_\theta \leqslant 15{,}000$, thus significantly less than the other considered cases. The resulting activation regions for both models are therefore strongly reduced, as shown in Figure 7.13. In particular, the SSG/LRR-ω-dP Knopp barely alters the original model, whereas the activation region of the EB-RSM-dP remains below $f^*_{b2} f_{b3} \leqslant 0.8$ down to the trailing edge.

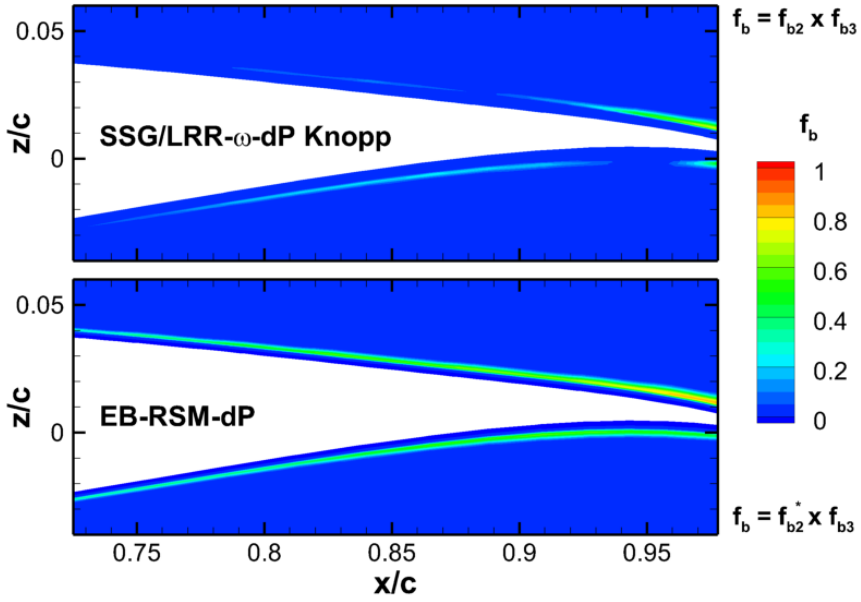

Figure 7.13: *Activation zone of the pressure-diffusion term for the APG-sensitised RSMs on the CRM at* $Re_c = 5\,\mathrm{M}$, $\eta = 0.502$

Although less efficient in this low-Re case, corrections still impact the angle of attack required to yield $C_L = 0.5$, which grows from 2.52° to 2.54° for the SSG/LRR-ω RSM and from 2.58° to 2.65° for the EB-RSM, thus closer to the experimental value $\alpha^{\mathrm{exp}} = 2.75°$. Contrary to the high-$Re$ case, Knopp's correction appears to have less impact on the model than a change of near-wall modelling approach. On the other hand, the EB-RSM-dP manages to almost halve the difference to the reference $\alpha^{\mathrm{exp}} = 2.75°$.

Drag polars

Similarly to the high-Re case, the predictions of lift and drag in Figure 7.14 are improved due to the sqrt-law correction. However, as noticed for the pressure coefficient distributions, the amplitude of this correction is more restricted, due to a damped activation of the pressure diffusion term. As a consequence, the dP correction has no noticeable effect on the SSG/LRR-ω model. The EB-RSM-dP stands out but reduces the drag relative error to the experiment by less than 3 %, resulting in an average relative error to the reference of 9 %.

The drag polars in Figure 7.15(a) shows a slight improvement of the new EB-RSM version, especially regarding $C_{D,0}$. Despite being less active in the low-Re case, the correction still results in an improvement of the drag due to lift. At $C_L = 0.45$, Figure 7.15(b) indicates that the correction leads to a 7 % reduction of the absolute error dC_D of the SSG/LRR-ω model, and a 35 % reduction for the EB-RSM. At $C_L = 0.5$, the absolute error further drops by 25 % and 118 % respectively, *i.e.* the EB-RSM-dP overestimates the

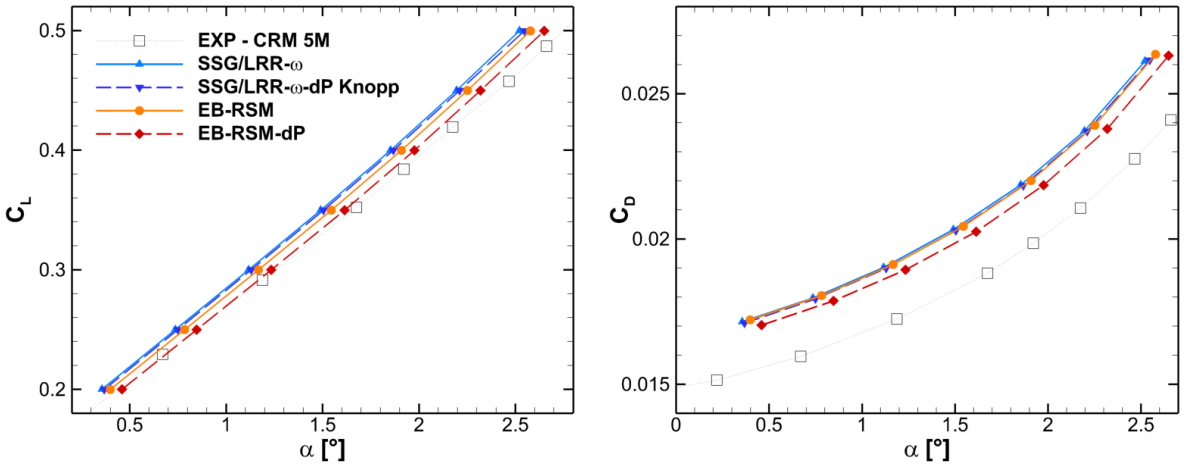

(a) *Lift* **(b)** *Drag*

Figure 7.14: *Aerodynamic forces on the CRM at $Re_c = 5\,\mathrm{M}$ for the APG-sensitised RSMs*

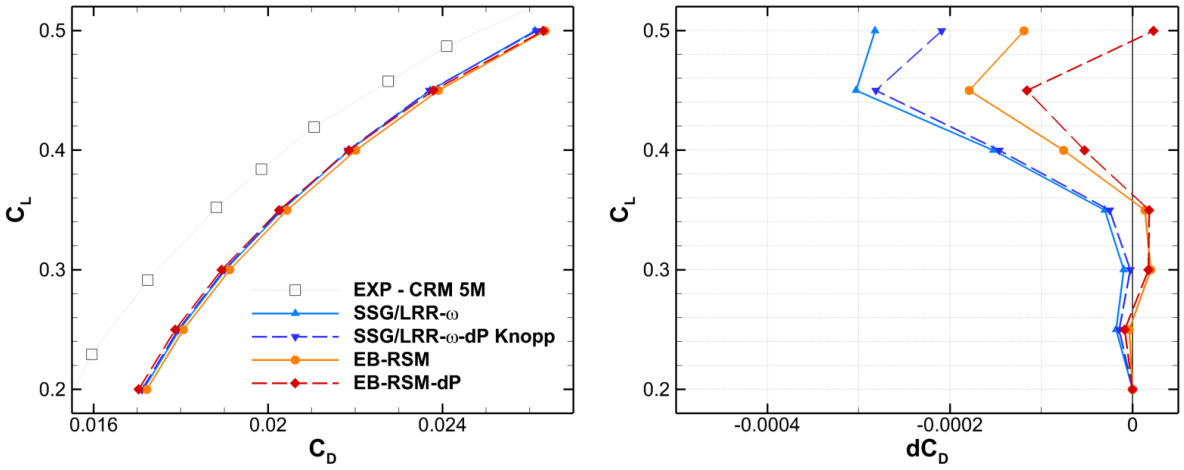

(a) $C_L = f(C_D)$ **(b)** *Absolute error of the drag-due-to-lift*

Figure 7.15: *Drag polars on the CRM at $Re_c = 5\,\mathrm{M}$ for the APG-sensitised RSMs*

drag due to lift. This slight overestimation, less than $\mathrm{d}C_D = 0.2\Delta C_D$, can also be seen for both version of the EB-RSM for $C_L \in [0.3\,;0.35]$. Although it is negligible, it should be monitored in future work aiming at improving the Reynolds-number sensitivity of the model.

7.3.3 Accounting for aeroelasticity

In this section, the effects of aeroelasticity have been investigated at $Re_c = 30\,\mathrm{M}$ for the EB-RSM and the EB-RSM-dP.

Computations have been run on a second geometry of the CRM provided by NASA, denoted 'shape 2' and corresponding to the aircraft model at $C_L^{\text{shape 2}} = 0$. The drag polars are computed at the same target lift coefficients as for the deformed geometry of ETW used in the previous sections, denoted here 'shape 1' with $C_L^{\text{shape 1}} = 0.4$, and consist thus

in five polar points with $C_L \in [0.2\,;0.4]$. With the lift increasing linearly with the angle of attack, the geometry is assumed to be deformed linearly as well. The progressive deflection of the aircraft model is therefore accounted for by simply interpolating drag and incidence between the results obtained with the two shapes for each lift coefficient C_L in the drag polar,

$$C_D^{\text{aeroelastic}} = f\, C_D|_{\text{shape 1}} + (1-f)\, C_D|_{\text{shape 2}}, \tag{7.3}$$

$$\alpha^{\text{aeroelastic}} = f\, \alpha|_{\text{shape 1}} + (1-f)\, \alpha|_{\text{shape 2}}, \tag{7.4}$$

with $f = \left(C_L - C_L^{\text{shape 2}}\right) / \left(C_L^{\text{shape 1}} - C_L^{\text{shape 2}}\right)$.

The results are presented in Figures 7.16 & 7.17. The lift slope is correctly reproduced in Figure 7.16(a): aeroelasticity increases the lift for the smallest angles of attack. Therefore, while the standard EB-RSM drifts away, the EB-RSM-dP very well predicts the experimental curve. Figure 7.16(b) shows that the drag at a given α also slightly increases with the flexible geometry. Since the modified model coincides with the wind-tunnel points with the rigid geometry, the aeroelasticity leads to an overestimation of the drag at small incidences.

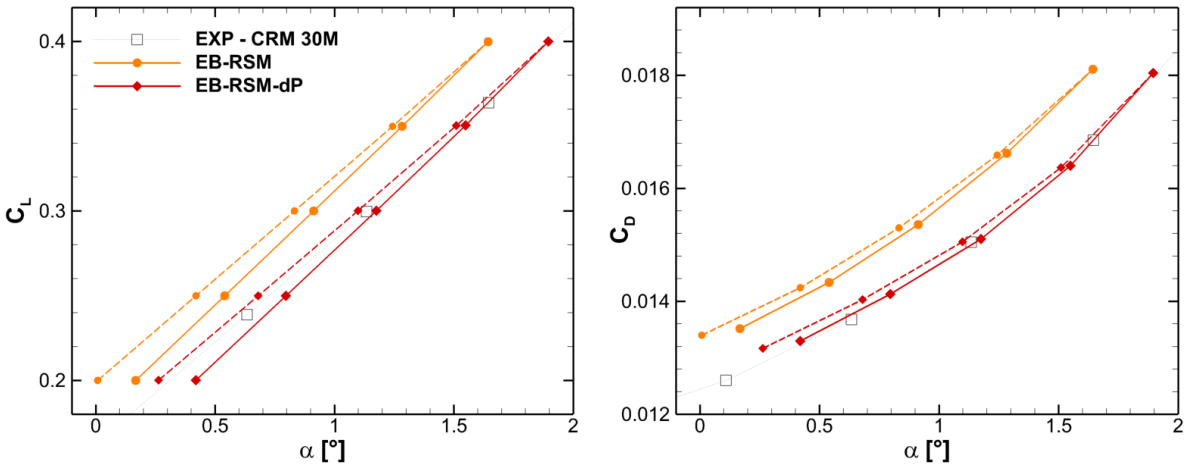

(a) *Lift* **(b)** *Drag*

Figure 7.16: *Effect of aeroelasticity on aerodynamic forces on the CRM at* $Re_c = 30\,\text{M}$. *Solid lines, rigid geometry; Dashed lines, aeroelastic geometry.*

The drag polars $C_L = f(C_D)$ are shown in Figure 7.17(a). The correction of the angle of attack deviation in the lift and drag profiles results in the zero-lift drag $C_{D,0}$ decreasing. Therefore it indicates that the increase of C_D for a given α observed in Figure 7.16(b) comes with a reorganisation of the drag between its part due to $C_{D,L}$ and $C_{D,0}$. Figure 7.17(b) shows a progressive improvement in the absolute $C_{D,L}$ error compared to the reference. Both models are shifted by $\mathrm{d}C_D \approx 1.2\Delta C_D$, corresponding to a 30 % correction for the original model and 50 % for the new one.

The aeroelastic polars for the Spalart-Allmaras model have also been computed and are shown in Figure 7.18, alongside the aeroelastic polars of the EB-RSM-dP. The figure displays the improvement of the corrected RSM over the industrial reference EVM. In particular, the EB-RSM-dP noticeably corrects the absolute $C_{D,L}$ error compared to the Spalart-Allmaras model at every polar point in Figure 7.18(b), with a reduction of 70 % at $C_L = 0.4$ ($\mathrm{d}C_D \approx 2.7\Delta C_D$).

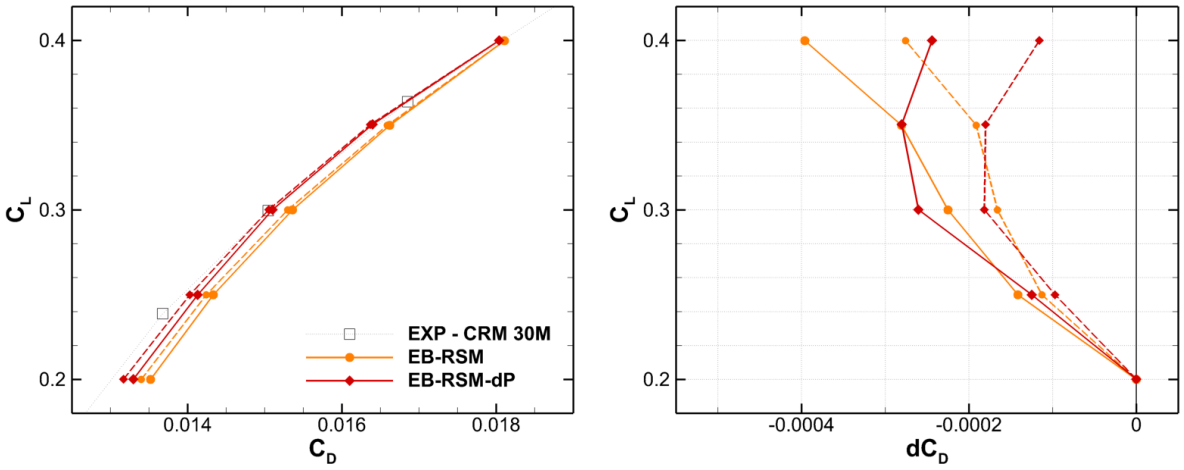

(a) $C_L = f(C_D)$ **(b)** *Absolute error of the drag-due-to-lift*

Figure 7.17: *Effects of aeroelasticity on drag polars on the CRM at* $Re_c = 30\,\mathrm{M}$. *Solid lines, rigid geometry; Dashed lines, aeroelastic geometry.*

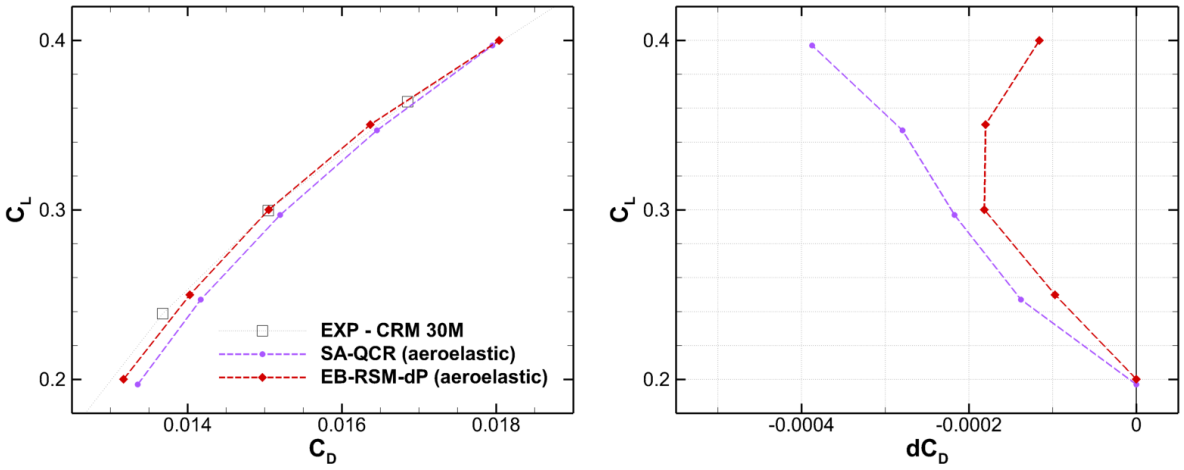

(a) $C_L = f(C_D)$ **(b)** *Absolute error of the drag-due-to-lift*

Figure 7.18: *Comparison of aeroelastic drag polars on the CRM at* $Re_c = 30\,\mathrm{M}$ *for the Spalart-Allmaras model and the EB-RSM-dP*

7.3.4 Conclusions

The sqrt-law correction presented in Chapter 6 has been shown to greatly improve the results of the Reynolds-stress models on an industrial aeronautical configuration, which further improves the somewhat better predictions of the RSMs compared to the Spalart-Allmaras model, as discussed in Section 7.2. In particular, the high-Re case demonstrates the effectiveness of this correction by making the EB-RSM-dP globally coincide with the experimental data.

It also highlights the restriction of Knopp's function, which fails to entirely activate the pressure-diffusion, and confirms its strong Reynolds-number dependency. This dependency also affects the proposed blending function f_{b2}^* based on Menter's BSL function, which also suffers from limitations in the low-Re case. A new blending function accounting for

the local Reynolds number appears therefore necessary to broaden the application range of the pressure diffusion approach.

The impact of the aeroelasticity of the aircraft model on the drag polars has been investigated using an interpolation method that has proven to yield satisfactory results, and further improved the predictions of the proposed APG-sensitised model.

To correctly calibrate the activation zone of the sqrt-law correction and confirm the improved behaviour of the EB-RSM-dP model, new configurations at various Reynolds numbers and with increased geometric complexity, for instance the CRM with tail and nacelle-pylon, could be considered.

Conclusions

This thesis has investigated the use of Reynolds-stress models in an industrial CFD code and their benefits over the one-equation Spalart-Allmaras model, which is today's state-of-the-art turbulence model in the aerospace industry. Corrections have been explored to improve the behaviour of these models in strong adverse pressure-gradient flows that occur on aircraft.

In particular, the EB-RSM-dP model was developed, based on the EB-RSM [69, 67], which integrates a pressure diffusion correction term in its dissipation rate transport equation to improve the predictions in the so-called square-root region of the boundary layer. The model has been successfully assessed on NASA's Common Research Model, an industrial configuration representative of a transonic commercial transport aircraft.

In Chapter 4, three Reynolds-stress models recently implemented in Dassault's in-house code Aether were benchmarked on academic ZPG and APG cases against the Spalart-Allmaras model: the EB-RSM, the SSG/LRR-ω RSM and the SSG-ω ATAAC RSM, which involve different near-wall modelling approaches and different length-scale providing equations.

The ZPG flat plate case pointed out the difference between the RSMs and the accuracy of the near-wall approach used in the EB-RSM and the SSG-ω ATAAC model regarding the physics of the Reynolds stresses in the boundary layer. The equilibrium APG boundary layer developing in the Skåre & Krogstad wind-tunnel [99] showed the superiority of RSMs over the Spalart-Allmaras model in the prediction of the boundary layer growth. It also highlighted their shortcomings in APG flows regarding the velocity gradient in the log region, which is under-predicted, and their skin friction coefficients, which are exaggerated.

In Chapter 5, a first approach consisting in ensuring the correct velocity gradient in the logarithmic layer for APG boundary layers was investigated. It was shown in particular that the challenges raised by the local recalibration of the von Kármán constant to comply with Nickels's APG log-law [77] in two-equation and Reynolds-stress models are coupled to a strong natural deviation [45, 15, 25] of the models relying on ε and ω as length-scale providing quantities, which should be compensated first.

Due to its relative simplicity, the one-equation Spalart-Allmaras model was selected for the application of the correction. An empirical law was introduced to account for its natural deviation and combined to the pressure-gradient sensitised von Kármán parameter κ_p to make the model correctly reproduce the log-law slope in strong APGs. The locality of the correction, restricted to the inner layer, and its limitations, especially regarding its impact on the outer region of the boundary layer, were highlighted with the new model, denoted SA(κ_c).

This approach was the occasion to implement a new data structure in Aether and a parallel algorithm to relate volume-nodes to their wall-projections, enabling more efficient simulations with mesh adaptation.

In Chapter 6, the sqrt-law behaviour of two-equation and Reynolds-stress models, which progressively replaces the log-law from its outer edge, was assessed. The analytical work from Knopp [51] was extended to any $k-\phi$ models, and under stricter assumptions ($p^+y^+ \gg 1$), to the Reynolds-stress transport equations. The correction suggested by Rao & Hassan [86] and Knopp [51] to add a pressure diffusion term was further analysed and applied to any ϕ-equation.

The corrected RSM proposed by Knopp *et al.* [52], denoted SSG/LRR-ω-dP Knopp, was implemented in AETHER along with a new algorithm it requires, based on the new data structure developed for Chapter 5, to estimate the boundary layer thickness during computation. The benefits of the correction was then benchmarked on the Skåre & Krogstad test case and its inner blending function f_{b2} improved. Finally, the correction using the new f_{b2}^* was applied to the EB-RSM, yielding the EB-RSM-dP, to build on the enhanced performances of this model and validated on the same test case.

Finally, in Chapter 7, the three standard RSMs were compared to the Spalart-Allmaras model on the CRM, an industrial application case, which demonstrated their relevance for the aeronautical industry, with improved pressure distribution on the wing and reduced errors in the drag-due-to-lift predictions.

The sqrt-law correction, developed in Chapter 6, was also validated on the CRM for the SSG/LRR-ω-dP Knopp and the EB-RSM-dP, and its impact on the original formulation of these models. In particular, the additional pressure diffusion term greatly improved the aerodynamic load on the wing as well as both the lift and drag predictions for the highest Reynolds number configuration. On the other hand, the low Reynolds number case pointed out the dependence on the Reynolds number of the activation functions.

Perspectives

The present work would benefit from further developments to improve the correction efficiency, especially in low-Re configurations.

The last chapter has shown that the activation range of the additional pressure diffusion term remains strongly dependent on the Reynolds number, despite the new inner blending function f_{b2}^*. This issue, also mentioned by Knopp in the final VicToria project meeting [28], should be addressed by improving the definition of f_{b2}^* and sensitising it to Reynolds-number effects.

Besides, the outer blending function f_{b3} could also be replaced to identify the outer edge of the square-root region based on local flow features rather than on an empirical definition of the inner layer thickness. This would not only simplify the model implementation, by dispensing with computing the boundary layer thickness, but also let the activation adapt to non-equilibrium boundary layers for which the empirical definition does not hold. For instance, the transition location of f_{b3} could adjust with respect to the detected location of the secondary peak of turbulent kinetic energy, which rises with the pressure gradient just beyond the square-root region.

The extent of the activation range and the intensity of the pressure diffusion term could be more finely tuned, to improve for example the impact on the Reynolds-stress profiles. Indeed, Section 6.3.3 has shown that the EB-RSM-dP tends to predict too strong gradients in the corrected range of the $\overline{u^2}$-profiles. Alternatively, additional pressure diffusion terms

could be directly integrated in the Reynolds-stress transport equations, which would result in a calibration closer to the asymptotic analysis for the correction in the ϕ-equation.

The calibration could take advantage of recent experiments and DNS of adverse-pressure-gradient boundary layers at different Reynolds numbers, carried out as part of projects such as WALLTURB, EuHit, VicToria and HiFi-Turb projects. In particular, considering strong APG flows at low-Re could demonstrate the benefits of combining the log-law recalibration, presented in Chapter 5, to the square-root region correction as suggested by Knopp [51] and Knopp *et al.* [52].

Finally, this work paves the way for sensitising other turbulence models to adverse pressure gradients. The analyses have been carried out for a generic $k - \phi$ model, and in particular the sqrt-law correction has proven to also apply satisfactorily to Reynolds-stress models using transport equations for either ε or ω. The correction could thus be extended to other RSMs or EVMs and applied in hybrid RANS-LES methods.

Appendix A

AETHER: numerical formulation

A.1 Matrix formulation

Using Cartesian coordinates and Einstein summation convention, the full Navier-Stokes equation system (1.12) in conservative form reads

$$\frac{\partial \rho}{\partial t} + \frac{\partial \rho U_j}{\partial x_j} = 0 \tag{A.1a}$$

$$\frac{\partial \rho U_i}{\partial t} + \frac{\partial \rho U_j U_i}{\partial x_j} = -\frac{\partial P}{\partial x_i} + 2\frac{\partial \mu S_{ij}^D}{\partial x_j} \tag{A.1b}$$

$$\frac{\partial \rho E}{\partial t} + \frac{\partial \rho U_j E}{\partial x_j} = -\frac{\partial P U_j}{\partial x_j} + 2\frac{\partial \mu S_{ij}^D U_i}{\partial x_j} - \frac{\partial q_j}{\partial x_j} \tag{A.1c}$$

which can be written in matrix form as

$$\frac{\partial}{\partial t}\underline{\boldsymbol{\mathcal{U}}} + \frac{\partial}{\partial x_j}\underline{\boldsymbol{\mathcal{F}}}_j = \frac{\partial}{\partial x_j}\underline{\boldsymbol{\mathcal{F}}}_j^{\text{diff}} \tag{A.2}$$

where $\underline{\boldsymbol{\mathcal{U}}}$, $\underline{\boldsymbol{\mathcal{F}}}$ and $\underline{\boldsymbol{\mathcal{F}}}^{\text{diff}}$ are respectively the conservative variables, the Euler fluxes and the diffusive fluxes, identified as

$$\underline{\boldsymbol{\mathcal{U}}} = \rho \begin{pmatrix} 1 \\ U_1 \\ U_2 \\ U_3 \\ E \end{pmatrix}, \qquad \underline{\boldsymbol{\mathcal{F}}}_j = \begin{pmatrix} \rho U_j \\ \rho U_j U_1 + P\delta_{1j} \\ \rho U_j U_2 + P\delta_{2j} \\ \rho U_j U_3 + P\delta_{3j} \\ \rho U_j E + P U_j \end{pmatrix}, \qquad \underline{\boldsymbol{\mathcal{F}}}_j^{\text{diff}} = \begin{pmatrix} 0 \\ 2\mu S_{1j}^D \\ 2\mu S_{2j}^D \\ 2\mu S_{3j}^D \\ 2\mu S_{ij}^D U_i - q_j \end{pmatrix}. \tag{A.3}$$

This can be equivalently written

$$\frac{\partial}{\partial t}\underline{\boldsymbol{\mathcal{U}}} + \underline{\underline{\mathbf{A}}}_i \frac{\partial}{\partial x_i}\underline{\boldsymbol{\mathcal{U}}} = \frac{\partial}{\partial x_i}\left(\underline{\underline{\mathbf{K}}}_{ij}\frac{\partial}{\partial x_j}\underline{\boldsymbol{\mathcal{U}}}\right) \tag{A.4}$$

with $\underline{\underline{\mathbf{A}}}_i = \underline{\nabla_{\boldsymbol{\mathcal{U}}}\boldsymbol{\mathcal{F}}}_j$ the i-th Jacobian matrix of the Euler fluxes and $\underline{\underline{\mathbf{K}}}_{ij}$ the diffusivity matrix defined as $\underline{\underline{\mathbf{K}}}_{ij}\partial_j\underline{\boldsymbol{\mathcal{U}}} = \underline{\boldsymbol{\mathcal{F}}}_j$. However, due to the non-linear nature of the Navier-Stokes equations, these matrices are dependent on the conservative variable vector $\underline{\boldsymbol{\mathcal{U}}}$.

A.2 Entropic formulation

To improve the mathematical properties of Eq. (A.4), Hughes *et al.* [46] and Mallet [65] introduced the generalized entropy function $\mathcal{H}$ defined as

$$\mathcal{H}\left(\underline{\boldsymbol{\mathcal{U}}}\right) = -\rho s \tag{A.5}$$

where $s = c_v \ln\left(P\rho^{-\gamma}\right) + s_0$ is the specific entropy and γ the specific heat ratio. Using this function, they proceed to a change of variable $\mathcal{S} : \mathcal{U} \rightarrow \mathcal{V}$ given by

$$\underline{\boldsymbol{\mathcal{V}}} = \mathcal{S}\left(\underline{\boldsymbol{\mathcal{U}}}\right) = \left(\underline{\nabla}_{\underline{\boldsymbol{\mathcal{U}}}}\mathcal{H}\right)^T = \frac{1}{T}\begin{pmatrix} \mu - E_c \\ U_1 \\ U_2 \\ U_3 \\ -1 \end{pmatrix}. \tag{A.6}$$

Here $\mu = E + P/\rho - Ts$ corresponds to the specific chemical potential for the considered species in the gas and $E_c = \frac{1}{2}U_iU_i$ the mean flow kinetic energy.

The conservative matrix Navier-Stokes system (A.4) becomes then

$$\widetilde{\underline{\underline{\mathbf{A}}}}_0 \frac{\partial}{\partial t}\underline{\boldsymbol{\mathcal{V}}} + \widetilde{\underline{\underline{\mathbf{A}}}}_i \frac{\partial}{\partial x_i}\underline{\boldsymbol{\mathcal{V}}} = \frac{\partial}{\partial x_i}\left(\widetilde{\underline{\underline{\mathbf{K}}}}_{ij}\frac{\partial}{\partial x_j}\underline{\boldsymbol{\mathcal{V}}}\right) \tag{A.7}$$

where

$$\widetilde{\underline{\underline{\mathbf{A}}}}_0 = \underline{\nabla}_{\underline{\boldsymbol{\mathcal{V}}}}\underline{\boldsymbol{\mathcal{U}}}, \qquad \widetilde{\underline{\underline{\mathbf{A}}}}_i = \underline{\underline{\mathbf{A}}}_i\widetilde{\underline{\underline{\mathbf{A}}}}_0, \qquad \widetilde{\underline{\underline{\mathbf{K}}}}_{ij} = \underline{\underline{\mathbf{K}}}_{ij}\widetilde{\underline{\underline{\mathbf{A}}}}_0. \tag{A.8}$$

The matrices $\widetilde{\underline{\underline{\mathbf{A}}}}_0$, $\widetilde{\underline{\underline{\mathbf{A}}}}_i$ and $\widetilde{\underline{\underline{\mathbf{K}}}} = \left[\underline{\underline{\mathbf{K}}}_{ij}\right]$ are symmetric, $\widetilde{\underline{\underline{\mathbf{A}}}}_0$ is positive-definite and $\widetilde{\underline{\underline{\mathbf{K}}}}$ is positive-semidefinite (their explicit definitions can be found in [63] and [121]). The matrix equation (A.7) in entropic formulation offers therefore nice mathematical properties for its numeric resolution, such as symmetry and efficient preconditioning. The entropy formulation has also a true physical sense since the stability condition associated to a finite element solution of Eq. (A.7) corresponds exactly to the Clausius-Duhem inequality (see [46]).

Appendix B

AETHER: developments

B.1 Accessing wall variables in the volume

The use of wall quantities, such as the friction velocity u_τ and the pressure-gradient parameter p^+ for the corrections developed in Chapter 5, makes it necessary to propagate a variable defined on the wall-nodes to the volume-nodes in the entire computational domain, at each step of the iterative resolution process.

The existing algorithm in AETHER, briefly presented below, has been upgraded as part of the development of the κ-correction, in order to improve the accuracy of the propagated values and reduce the memory and computational cost.

B.1.1 Upgrades

Before the present developments, AETHER already included a wall-to-volume propagation algorithm, necessary for the roughness corrections in turbulence models (Aupoix [2]). This initial algorithm associated each volume-node to the nearest wall-node, and the volume-nodes simply use the wall quantity v_w, for instance u_τ, calculated at the associated wall-node.

This algorithm has been improved as follow:

Accuracy

- Old algorithm:

  The simple association to the nearest wall-node is equivalent to assuming the wall quantity v_w piecewise constant ($\mathbb{P}_0$) on the domain boundary. Indeed, all the volume-nodes that are projected in the vicinity of the wall-node n (green area in Figure B.1(a)) have the same value $v_w(n)$.

- New algorithm:

  On the contrary, the wall quantities in AETHER are $\mathbb{P}_1$, *i.e.* they are continuous and piecewise linear on the domain boundary. The value of v_w for a given volume-node i is therefore interpolated at its projection point p on the wall. Noting f the wall-element on which i is projected, so that p is inside f, the interpolation coefficients correspond to the shape functions N of f for each wall-node j constituting f, evaluated at the

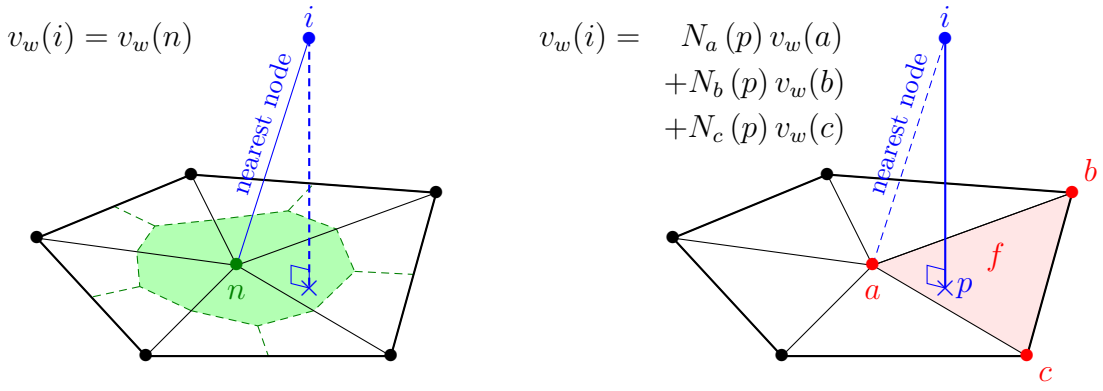

(a) *Old algorithm* **(b)** *New algorithm*

Figure B.1: *Propagation of the wall variable v_w to the volume-node i*

coordinates of p (see Figure B.1(b))

$$v_w(i) = v_w(p) = \sum_{j \in f} N_j(p)\, v_w(j). \tag{B.1}$$

CPU cost

- Old algorithm:

  To find the nearest wall-node to a given volume-node i, the distance from i to each of the wall-nodes in the domain is computed and the wall-node yielding the smallest distance is kept. This results in a large CPU cost and poor scaling performance.

- New algorithm:

  The nearest wall-node is efficiently found using a RTree structure from the C++ `boost` library, which enables fast mapping and indexation of the wall-elements. The projection of a given volume-node is then restricted to the stencil of wall-elements which contain the nearest wall-node to i, greatly reducing the number of distance computations and the resulting CPU cost.

Memory footprint

- Old algorithm:

  The computations are performed on a parallel architecture, using MPI (Message-Passing Interface), so that the computational domain is divided into as many blocks as there are cores. Consequently, all the blocks do not necessarily contain the nearest solid wall and the nearest wall-nodes on which their volume-nodes depend. Therefore, to access the nearest wall-node in the entire computational domain, an array containing all the wall-nodes is first locally allocated in each MPI block, yielding poor memory scaling performance.

  Moreover, these local arrays are updated at every iteration, which requires a large MPI communication between the blocks to transmit all the wall-nodes values. Hence, this also results in poor time performance.

- New algorithm:

  The memory footprint is reduced by storing, locally to a given block B, only the wall-data needed in B to interpolate v_w at the volume-nodes, and by creating dedicated MPI communicators. A communicator consists of a wall-block B_w, emitting wall-elements, and of all the 'recipient' blocks that require at least one of the wall-elements of B_w for the computation of v_w at their volume-nodes. Note that an MPI block can be part of several communicators.

  The communications are then carried for each communicator, one at the time, yielding reduced data transmissions, *i.e.* reduced buffer memory and time needs.

Note that due to its improved performance for wall-distance computations (see Table B.1), this algorithm can be used with limited CPU overhead for applications where the mesh is adapted within AETHER, such as mesh morphing and optimisation processes and requiring wall-distance updates during the simulation.

B.1.2 Implementation

The wall-variable propagation algorithm is split into two phases

1. the *communication structures preparation*: carried out once at the simulation initialisation, or after any change of the mesh during the simulation, this phase is the most time-consuming part of the algorithm,

2. the *variable propagation*: fast and carried out at each iteration.

Communication structures

In this first phase, the blocks containing wall-elements are identified. A communication structure is allocated in every MPI block to associate the volume-nodes to the corresponding projections on the solid walls. To restrict the communications between blocks to the values of v_w on the wall-nodes, the structure of a given block B provides:

- a wall-block array $\mathcal{B}$ associating each volume-node of B to the wall-block containing its projection,

- a wall-element array $\mathcal{F}$ associating each volume-node to the wall-nodes constituting the wall-element, in which it is projected

- an interpolation array $\mathcal{I}$ yielding, for each volume-node, the interpolation coefficients, which correspond to the coordinates of its projection in the wall-element.

Finally, the MPI communicators are created, by gathering a wall-block B_w and all the blocks for which the local association array $\mathcal{B}$ contain references to B_w.

Propagation

The propagation of a wall variable v_w is straightforward:

1. each wall-block B_w broadcasts the values of v_w on its wall-nodes through its dedicated MPI communicator $\mathcal{C}(B_w)$,

2. each recipient block within $\mathcal{C}(B_w)$ uses its local wall-element and interpolation arrays, $\mathcal{F}$ and $\mathcal{I}$, to interpolate the received values v_w accordingly to each volume-node associated to B_w with the wall-block array $\mathcal{B}$.

B.1.3 Results

Figure B.2 shows the friction velocity u_τ, computed at the wall and broadcasted in the volume using the new parallel algorithm. It can be seen that the interpolation process enables the algorithm to provide results independent from the mesh and the multi-block division.

Regarding its performance, Table B.1 provides the computational time of the algorithm on two meshes of different sizes. On the large mesh, including 22 M nodes, the *communication structure preparation* phase that yields the structures, communicators and wall-distances, is carried out in 73 s. Due to its parallel implementation and the C++ `boost` library, this is far below the 20 min ($\approx$ 1,200 s) required by the old wall-distance algorithm, which projects the volume-nodes on every wall-elements in the entire domain to determine the smallest distance. Table B.1 also highlights the incompressible time needed for MPI communications in small meshes in the preparation phase, becoming significantly larger than the wall-distance computation used to find the closest wall-elements.

Table B.1: *Algorithm time performance*

Mesh size	Wall-data communication	Wall-distance computation	Communicators creation	Skin variable propagation
$42 \cdot 10^3$	0.7 s	0.02 s	0.6 s	40 µs
$22 \cdot 10^6$	28 s	31 s	14 s	40 ms

Moreover, the new algorithm is more memory-efficient, as it only loads the wall-elements of one wall-block at a time for the projection step, instead of loading them all from the entire domain.

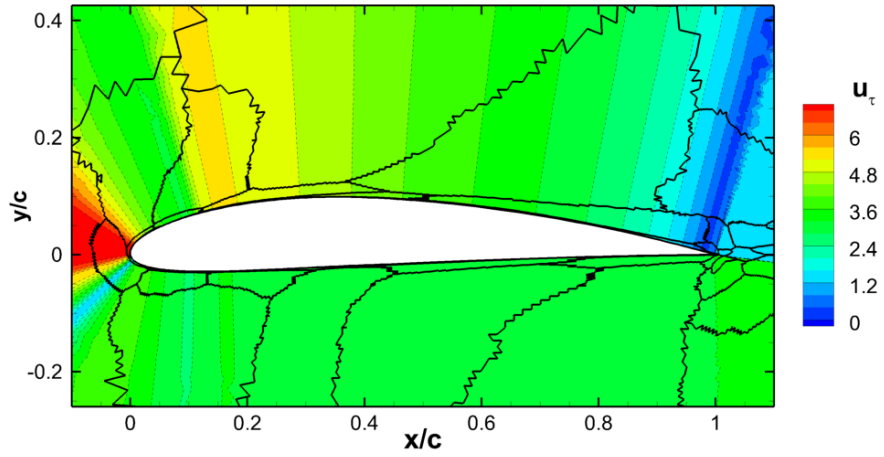

Figure B.2: *Fields of u_τ around the NACA 4412 profile using the Spalart-Allmaras model. The black solid lines indicate the borders of the domain blocks.*

B.2 Estimating the boundary layer thickness

The Knopp correction (Sections 6.2.1 & 6.2.2) depends on the boundary layer thickness δ through the blending function f_{b3}, Eq. (6.75), recalled below

$$f_{b3} = \left(1 + 5.5\left(\frac{y}{0.35\delta}\right)^6\right)^{-4}. \tag{B.2}$$

However, δ is an integral quantity that is not available as a volume or wall variable. Indeed, due to its non-local definition (Section 2.1.2), it is measured by probing the boundary layer to determine the distance yielding 99 % of the edge velocity U_e. This is usually carried out with post-processing tools, which interpolate the volume variables in the fluid above the wall-nodes. Probing the boundary layer during computations requires performing the same operation and thus to use a specific data structure, linking the volume-nodes to the wall nodes above which they are located.

Such a structure is available in the TAU-Code used by Knopp [51] and Knopp *et al.* [52] and makes it possible to find the closest volume-nodes to the wall that achieve $0.99\,U_e$, hence located at the distance δ from the wall. It has been implemented for DES applications and is further described by Probst *et al.* [85] and Reuß [87].

This section presents the probing algorithm developed in AETHER to detect δ and implement the SSG/LRR-ω-dP Knopp and the new 'dP' models. It relies on the communication structures, introduced in Section B.1, to define fluid columns above the wall, find the volume-nodes at the threshold v_v^δ defined for the volume variable v_v and collect the wall-distance of these nodes at the wall-nodes, as illustrated in Figure B.3. To comply with the multi-block domain computation, this algorithm relies on MPI `min` and `max` functions to determine the volume-nodes at the boundary layer edge in each fluid column.

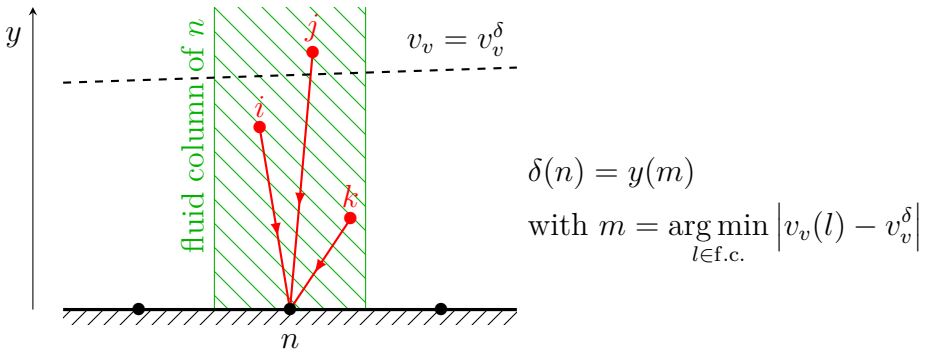

Figure B.3: *Detection of the thickness δ with a threshold v_v^δ of the volume variable v_v in a fluid column (f.c.)*

B.2.1 Edge velocity

To ensure a good estimation of the boundary layer thickness, the solver must be able to detect the threshold at $0.99\,U_e$ in the velocity field. The solver thus requires the edge velocity U_e, also to be estimated.

Knopp *et al.* [52] estimate U_e at the wall using the local pressure. Indeed, it can be related to the far-field conditions with the compressible Bernoulli relation for a perfect gas in adiabatic conditions[1]

$$\frac{1}{2}U^2 + \frac{\gamma}{\gamma-1}\frac{P}{\rho} = cst. \tag{B.3}$$

Neglecting heat transfers in the boundary layer, the perfect gas law (1.13), $P = \rho R_{\text{air}} T$, results in a constant ratio P/ρ. Therefore, Eq. (B.3) leads to the Saint-Venant & Wantzel relation

$$U_e^{\text{SV-W}} = \sqrt{U_\infty^2 + 2\frac{\gamma}{\gamma-1}\left(1 - \left(\frac{P}{P_\infty}\right)^{\frac{\gamma-1}{\gamma}}\right)\frac{P_\infty}{\rho_\infty}}. \tag{B.4}$$

As shown in Figure B.4, Eq. (B.4) yields a reliable estimation, especially for simple low-Re cases such as the flat plate (a) and the NACA 4412 wing profile (b). However, on the other studied cases, the Skåre & Krogstad wind-tunnel (c) and the CRM, a high-Re transonic aircraft (d), U_e is slightly overestimated and unevenly deviates from the expected value, affecting the robustness of the detection of δ. In particular, if $0.99\,U_e^{\text{SV-W}}$ is greater than the actual edge velocity, the solver is unable to find the boundary layer thickness. This occurs for instance in the Skåre & Krogstad test case for the SSG/LRR-ω model and results in jumps in the boundary layer thickness detected by Aether using Eq. (B.4), as seen in Figure B.5.

Alternatively, U_e can be assessed by probing the first local maximum of the velocity from the wall. However this implies detecting and sorting all the velocity extrema in order to extract the value of the boundary layer threshold, and results in a sophisticated algorithm.

B.2.2 Entropy-based detection

To avoid the robustness issues from the Saint-Venant & Wantzel approach and keep the algorithm simple, a new detection approach based on entropy is proposed.

In the boundary layer, the strong viscosity effects produce entropy, resulting in an entropy layer. Below hypersonic velocities ($M < 5$), the entropy layer and the boundary layer can be assumed to grow similarly. On the contrary, in the hypersonic regime, the entropy layer becomes considerably thicker than the velocity boundary layer due to the strong energetic disequilibrium, which prevents the use of this approach.

The specific entropy is defined as

$$s = c_p \log(T) - R_{\text{gas}} \log(P) \tag{B.5}$$

with $c_p = \gamma R_{\text{gas}}/(\gamma - 1)$. Neglecting heat transfers, the free-stream flow can be assumed isentropic. As a result, the specific entropy outside the boundary layer is constant and at its absolute minimum value $s_e \equiv s_\infty$. Unlike U_e, no sorting is necessary and s_e is therefore easily estimated. This approach can be extended to confined configurations, where the free-stream entropy varies with the pressure loss and can be assumed constant at a given streamwise coordinate. Thus,

$$s_e = \min(s) \tag{B.6}$$

remains valid in the fluid column over a wall-node.

[1] this relation is also known as the 3rd form of the Barré de Saint-Venant equation

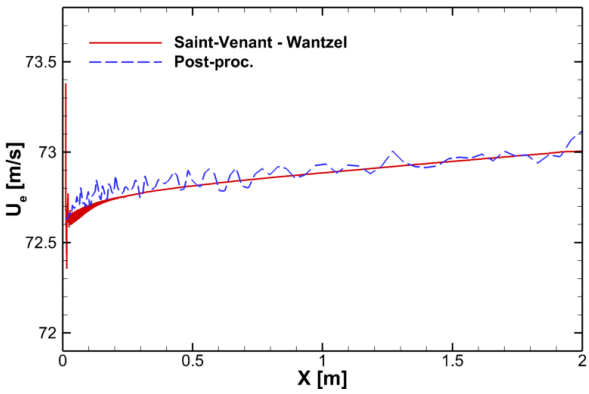

(a) *Flat plate* ($M = 0.2$, $Re_L = 5\,\mathrm{M}$)

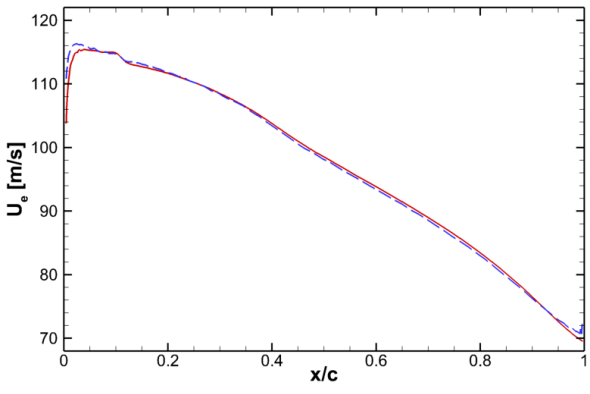

(b) *NACA 4412* ($Re_c = 1\,\mathrm{M}$, $\alpha = 5°$)

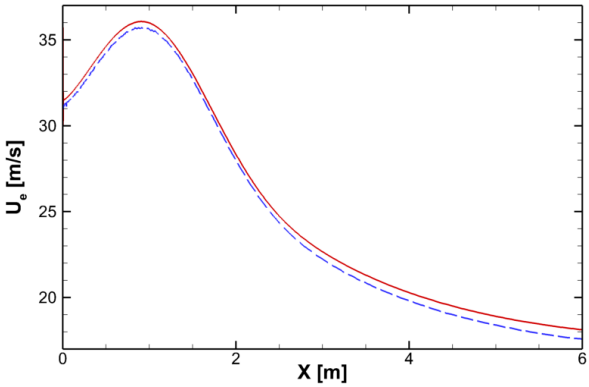

(c) *Skåre & Krogstad experiment*

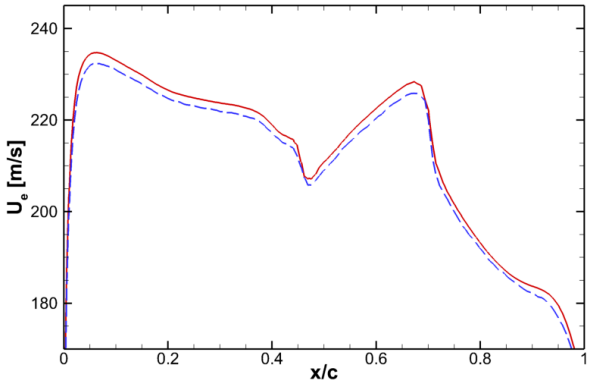

(d) *CRM* ($Re_c = 30\,\mathrm{M}$, $C_L = 0.40$, $\eta = 0.502$)

Figure B.4: *Comparison of U_e as predicted by Eq. (B.4) and the post-processing tool*

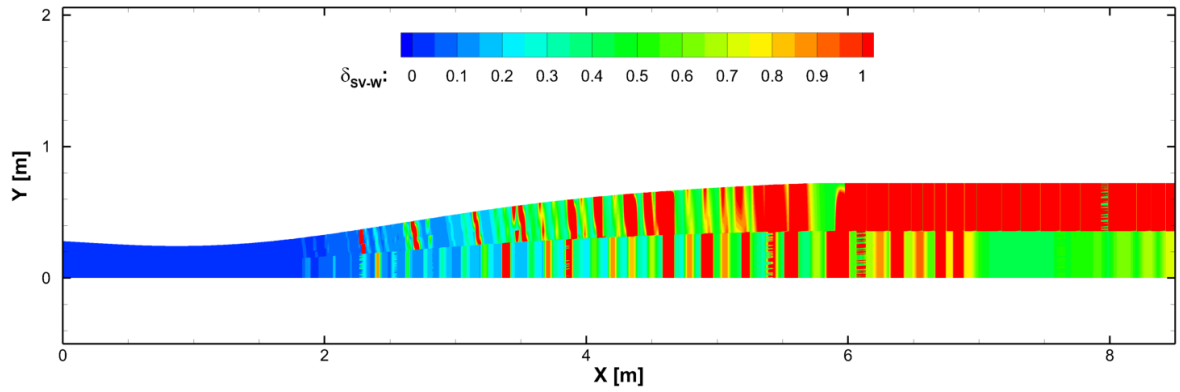

Figure B.5: *Detected δ in AETHER using Eq. (B.4) with the SSG/LRR-ω model in the Skåre & Krogstad configuration*

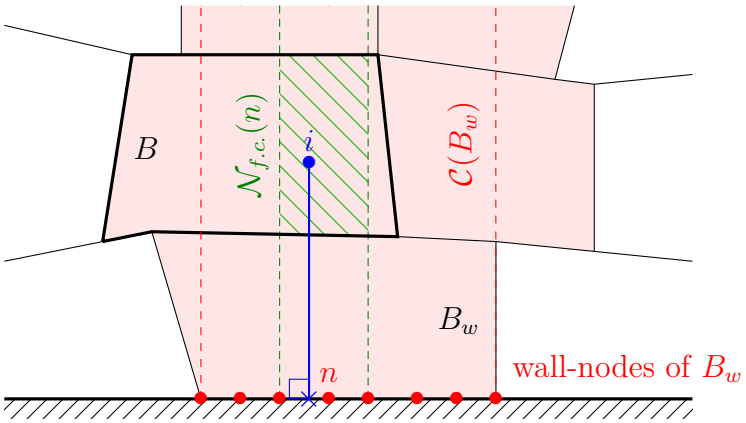

Figure B.6: *Fluid column in multi-block environment. The blocks in red are part of the communicator $\mathcal{C}(B_w)$.*

B.2.3 Algorithm description

Assimilating the entropy layer thickness δ_s to the boundary layer thickness, the new algorithm finds δ as the minimum distance achieving 99 % of the local free-stream entropy s_e, corresponding to the maximum entropy in the considered fluid column. The free-stream region can therefore be defined by

$$\left| \frac{s - s_e}{s_{\text{wall}} - s_e} \right| < 0.01. \tag{B.7}$$

As for the propagation algorithm introduced in Section B.1, the present algorithm works with a loop on the MPI communicators. Considering a wall-block B_w associated to its communicator $\mathcal{C}(B_w)$, the algorithm is here described locally to a block B, recipient block in the communicator $\mathcal{C}(B_w)$.

In the block B, the fluid column above the wall-node n of B_w is defined by a local array $\mathcal{N}_{f.c.}(n)$, which lists the volume-nodes of B that depend on n in the communication structure, *i.e.* each volume-node $i \in \mathcal{N}_{f.c.}(n)$ is projected on a wall-element of B containing n. The notation is illustrated in Figure B.6. Note that due to the communication structure, which associates the volume-nodes to the wall-elements rather than simply the wall-nodes, the volume-nodes are part of several fluid columns.

A second local array $\mathcal{N}_c$, named *communication nodes array*, is allocated with the size of the received wall-nodes of B_w to enable a communication from B back to B_w. Each communication node is a virtual node associated to a wall-node of B_w and the corresponding fluid column. The local array N_c hence makes it possible to send back to B_w a single value per fluid column determined in B, for instance a local estimation of the thickness δ.

The algorithm is split in three steps:

1. *Get the extreme values s_{wall} and s_e of the specific entropy*

   The wall entropy s_{wall} is easily propagated with the algorithm defined in Section B.1.

   The free-stream entropy s_e must be computed with Eq. (B.6) in each fluid column. Thus, on each fluid column $\mathcal{N}_{f.c.}(n)$, the minimum entropy is computed and stored on the communication node corresponding to the wall-node n. The `MPI_AllReduce` function is then used to broadcast the minimum value of s found on the different blocks of the communicator $\mathcal{C}(B_w)$, directly to the other blocks of $\mathcal{C}(B_w)$.

2. *Compute the thickness above each wall-element*

   The minimum wall-distance satisfying condition Eq. (B.7) in B is stored on the communication nodes. If no node in the considered fluid column satisfies Eq. (B.7), a large value is stored instead. As for s_e, the minimum value across the communicator $\mathcal{C}(B_w)$ is retained for each fluid column and broadcasted in $\mathcal{C}(B_w)$.

3. *Propagate a consistent value of δ in the volume*

   The values of δ stored on the wall-nodes of B_w are propagated with the communicator $\mathcal{C}(B_w)$ using the propagation algorithm in Section B.1, to take advantage of the interpolation at the wall and ensure a consistent value of δ across the volume.

B.2.4 Results and discussion

The results are presented in Figure B.7 for the Spalart-Allmaras model on the four studied configurations. The entropy-based detection of the boundary layer thickness δ in Aether is compared to the post-processing tool, in which both detection methods are implemented.

The entropy layer grows slightly faster than the boundary layer, being up to 10 % thicker. Its thickness is correctly computed in Aether, despite not being as smooth. This is due to the 'fluid column' approach. To improve this behaviour, the computed s_e would need to be interpolated depending on the alignment of the volume-nodes with respect to the wall-node.

Figure B.7(d) highlights the limits of the isentropy assumption, which is not valid at the leading edge of a transonic wing and results in Aether wrongly detecting the thickness δ. The post-processing tool relies on a more common method and probes progressively the entropy profile starting from the wall, until it detects the first minimum, corresponding to s_e, which is different from s_∞ if the flow is not isentropic. This limitation of the boundary layer thickness computation in Aether can however be neglected for the current use, which consists in restraining the APG correction domain with $f_{b3}(\delta)$ (Eq. (6.75)), since no adverse pressure gradient is expected at the wing leading edge.

Another limitation of the estimation appears in corner flows. Indeed, close to the corner, the fluid column on one side is limited to the intersection with the fluid column on the other side. As a consequence, in a perpendicular corner, the detected thickness δ_d is limited to the distance d to the corner edge (see Figure B.8). To overcome this issue, the thickness computation would need a new structure that yields fluid columns oriented along the distance gradient.

The limitation more broadly affects flows between parallel walls with asymmetrical boundary layers, if one of them grows larger than half the distance separating the walls. However, such flows are not encountered in external aerodynamics, the context of this work.

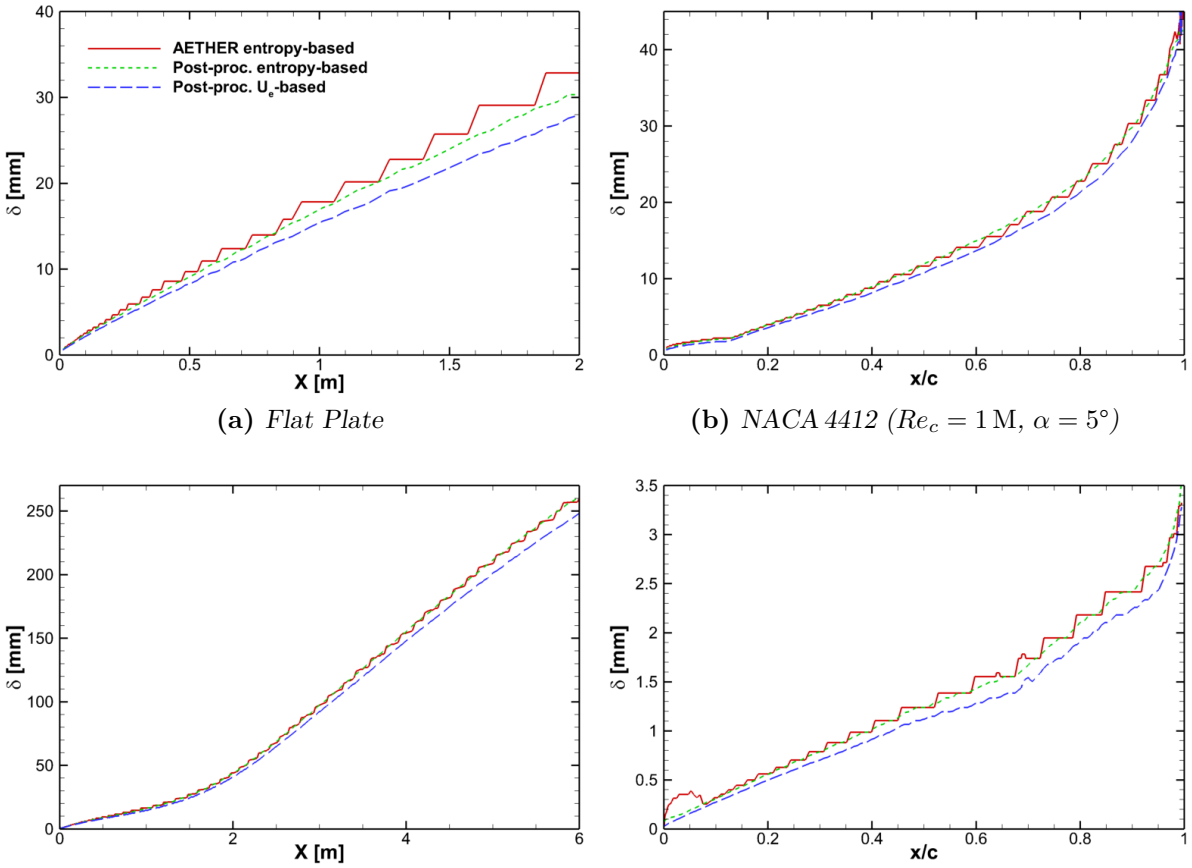

(a) *Flat Plate* **(b)** *NACA 4412 ($Re_c = 1\,\mathrm{M}$, $\alpha = 5°$)*

(c) *Skåre & Krogstad experiment* **(d)** *CRM ($Re_c = 30\,\mathrm{M}$, $C_z = 0.40$, $\eta = 0.502$)*

Figure B.7: *Comparison of δ as predicted by* AETHER *and the post-processing tool*

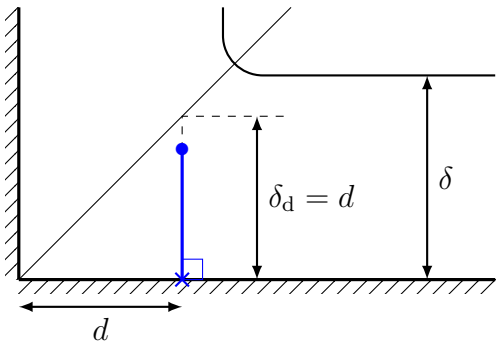

Figure B.8: *Detected thickness δ_d in a corner flow*

Appendix C

Article presented at: 55^{th} 3AF International Conference on Applied Aerodynamics (AERO2020+1)

Association Aéronautique et Astronautique de France

55th 3AF International Conference on Applied Aerodynamics
23 — 25 March 2020, Poitiers – France

FP87-AERO2020-sporschill

TURBULENCE MODELLING IMPROVEMENTS FOR APG FLOWS ON INDUSTRIAL CONFIGURATIONS

Gustave Sporschill[(1),(2),*] **Flavien Billard**[(1)] **Michel Mallet**[(1)] **Rémi Manceau**[(2)]

[(1)]*Dassault Aviation, 78 quai Marcel Dassault, 92552 Saint-Cloud Cedex, France,*
gustave.sporschill@dassault-aviation.com

[(2)]*CNRS, Université de Pau et des Pays de l'Adour, E2S UPPA, INRIA, project-team CAGIRE, Laboratory of Mathematics and Applied Mathematics (LMAP), Pau, France*

ABSTRACT

A new version of the Spalart-Allmaras model is presented to improve adverse pressure gradient flow predictions. High fidelity numerical simulations confirmed the sensitivity of the log-law region to the pressure gradient, for both its slope and its intercept. The study is limited to the correction of the slope by tuning the von Kármán constant according to the local dimensionless pressure gradient p^+ and is a first step towards better approach to account for pressure gradients. A new model is calibrated on a NACA 4412 wing section at $Re_c = 1M$ and then applied to 3D cases, including a simplified aircraft configuration. The new model displays encouraging results regarding the inner layer but exhibits limitations in the outer layer and the need for another kind of correction.

NOMENCLATURE

Latin symbols

p^+	Pressure gradient parameter
U^+	Dimensionless streamwise velocity (U/u_τ)
u_τ	Wall friction velocity
u_T	Turbulent friction velocity
x/c	Fraction of wing section chord
y^+	Dimensionless wall-distance (yu_τ/ν)

Greek symbols

β_p	Clauser pressure gradient parameter
κ_0	von Kármán constant
κ_p	Nickels p^+-sensitive von Kármán const. (Eq. (5))
κ_{corr}	corrected von Kármán constant (Eq. (14))
$\overline{\kappa}$	apparent von Kármán constant
η	Fraction of wing semi-span

1. INTRODUCTION

Turbulence modelling directly impacts the accuracy of the numerical simulations and its improvement allows reducing design margins of the studied products. In the aeronautical industry, dimensioning conditions are defined by the limits of flight domain, where the boundary layer is strongly slowed down by adverse pressure gradients (APG), leading to separation and stall. However the response to APG in the turbulent boundary layer remains one of the challenges in turbulence modelling, that affects turbulent boundary layer behaviour and separation point predictions, and thus the lift and drag estimates for the aircraft.

Many authors have studied the effects of pressure gradients on the boundary layer structure. In the inner layer, Nagano *et al.* [9], Huang and Bradshaw [4] and Catris and Aupoix [2] observed that pressure gradients do not affect the log-law slope. However, recent theoretical [11] and experimental works [6] showed the slope is steepened and the intercept value is decreased with increasing APG. Besides, Perry [13] and Townsend [19] describe the existence of a half-power region, also called sqrt-law region, replacing progressively the log-law region from its far-end. The pressure gradients also affect the outer layer [7].

All these effects should therefore be taken into account in the turbulent models. Although turbulent models are calibrated using zero pressure gradient (ZPG) configurations, some models implicitly behave better in APG conditions than others, including the Spalart-Allmaras model [16] and ω-based models, *e.g.* Wilcox's [21] and Menter's [8] models. Catris [1] showed that among usual models, only the Spalart-Allmaras tends to predict

a square-root behaviour. Recently, Knopp [5] presented improvements to the $k-\omega$ model by modifying the von Kármán constant and adding a pressure diffusion terms in order to comply with the sqrt-law.

In this article, the Spalart-Allmaras model will be considered with focus on its log-law prediction.

2. THEORETICAL BACKGROUND

2.1 Turbulent boundary layer

In a 2D steady turbulent boundary layer, the Navier-Stokes streamwise-momentum equation simplifies into

$$U\partial_x U + V\partial_y U = -\frac{1}{\rho}\frac{dP}{dx} + \partial_y \underbrace{(\nu\partial_y U - \overline{uv})}_{\tau}. \quad (1)$$

In the inner part of the boundary layer, convection can be neglected and noting that pressure is constant across the boundary layer in the normal direction, the total shear stress τ is constant as well. Neglecting the viscous diffusion (outside the viscous sublayer) and using the wall units, it yields

$$\frac{\tau}{\tau_w} = -\overline{uv}^+ = 1 + p^+ y^+, \quad (2)$$

with $p^+ = \dfrac{\nu}{\rho u_\tau^3}\dfrac{dP}{dx}$ the dimensionless pressure gradient.

2.2 Slope variation

The inner part of the turbulent boundary layer can be divided into the viscous sublayer, where viscosity is dominating and the velocity is linear, and the log region, where the velocity follows the log-law , written in wall units

$$U^+ = \frac{1}{\kappa_0}\log y^+ + B, \quad (3)$$

with $\kappa_0 = 0.41$ and $B \approx 5$.

Considering the viscous sublayer as a laminar region and the buffer layer as a transition-to-turbulence region, Nickels [11] introduces a new velocity scale corresponding to a "turbulent friction velocity" to study the log-law region. He defines it as the friction velocity at the transition point y_c between laminar and turbulent layers

$$u_T = \sqrt{\tau(y=y_c)/\rho} = u_\tau\sqrt{1+p^+ y_c^+}. \quad (4)$$

Using the log-law development with the new scales, the relation becomes:

$$\frac{dU}{dy} = \frac{u_T}{\kappa_0 y} \quad \Rightarrow \quad \frac{dU}{dy} = \frac{u_\tau}{\kappa_p y} \quad \Rightarrow \quad \frac{dU^+}{dy^+} = \frac{1}{\kappa_p y^+},$$

where

$$\kappa_p = \frac{\kappa_0}{\sqrt{1+p^+ y_c^+}} \quad (5)$$

is the modified coefficient of the log-law. Note that without pressure gradient ($p^+ = 0$), the turbulent friction velocity equals the wall friction velocity, meaning the classical wall law is unchanged and κ_p equals the von Kármán constant κ_0.

In order to find y_c, Nickels defines a critical Reynolds number R_c corresponding to the transition between the viscous sublayer and the log-law region

$$R_c = \frac{u_T y_c}{\nu} = 12. \quad (6)$$

When replacing u_T by Eq. (4) in Eq. (6) and squaring the relation, it becomes

$$p^+\left(y_c^+\right)^3 + \left(y_c^+\right)^2 - R_c^2 = 0. \quad (7)$$

The solution corresponds to the smallest positive root of Eq. (7). This equation shows that the sublayer thickness reduces with increasing p^+, and therefore the modified κ_p (Eq. (5)) only depends on the pressure-gradient parameter.

2.3 Reference data analysis

In [5], Knopp showed that relation (5) holds for several experimental data sets, up to $p+ \approx 0.055$.

A similar analysis has been performed using the LES data of a NACA 4412 wing section at a chord-Reynolds $Re_c = 1M$ and angle of attack $\alpha = 5^\circ$ provided by Vinuesa *et al.* [20], where the slope of the log-law is found to vary in the strong pressure gradient region close to the trailing edge. Fig. 1 shows the velocity profile on the suction side of the wing section, at four different chord-wise positions and therefore, four different pressure gradients. It can be observed that the log-law region is best fitted by the modified log-law as suggested by Nickels, instead of using the classical von Kármán constant value $\kappa_0 = 0.41$.

3. NUMERICAL METHOD

The numerical simulations have been carried out with Dassault Aviation CFD code AETHER [17]. It is an unstructured finite element solver for the compressible Navier-Stokes equations, stabilised using the Streamline Upwind Petrov-Galerkin (SUPG) method. AETHER is written using the entropy formulation which offers many advantages, in particular symmetric operators with positivity properties and efficient preconditioning.

The present article focuses on the Spalart-Allmaras model [16], described by Eq. (8)

$$\frac{D\hat{\nu}}{Dt} = c_{b1}\hat{S}\hat{\nu} - c_{w1}f_w\left(\frac{\hat{\nu}}{d}\right)^2 + \frac{1}{\sigma}\left[\nabla\left((\nu+\hat{\nu})\nabla\hat{\nu}\right) + c_{b2}\left(\nabla\hat{\nu}\right)^2\right], \quad (8)$$

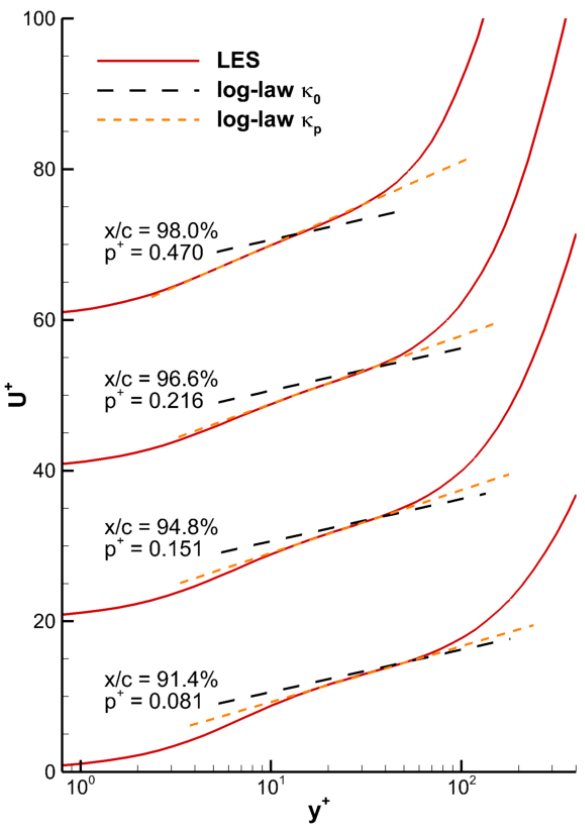

Figure 1: Velocity profiles on the NACA 4412 wing section at different chordwise positions (LES [20] $Re_c = 1M$, α =5°)

where $\hat{\nu}$ is related to the eddy viscosity as $\nu_t = \hat{\nu} f_{v1}$. The von Kármán constant κ_0 appears directly in the model through the definitions of $\hat{S}$ and the constant c_{w1}:

$$\hat{S} = \Omega + \frac{\hat{\nu}}{\kappa_0^2 d^2} f_{v2}, \tag{9}$$

$$c_{w1} = \frac{c_{b1}}{\kappa_0^2} + \frac{1 + c_{b2}}{\sigma}. \tag{10}$$

Ω is the magnitude of the vorticity, d the distance to the nearest wall, f_{v2} a blending function active close to the wall and c_{b1}, c_{b2} and σ are the model constants.

The model has been calibrated to render the log-law slope with $\kappa_0 = 0.41$ in a ZPG case. However, the slope becomes inaccurate in a APG case. The Spalart-Allmaras model has therefore been modified by implementing Nickels von Kármán parameter $\kappa_p(p^+)$ in place of the κ_0 constant, transposing a part of Knopp's work on the $k-\omega$ model [5]. The pressure gradient parameter p^+ is computed in the volume, using the wall friction velocity u_τ at the nearest wall and the local pressure gradient along the streamline $\nabla P \cdot \mathbf{U}$ where $\mathbf{U}$ is the velocity vector. It is clipped to positive values, the focus of the correction applying to APG. The different Spalart-Allmaras models are named SA(κ) where κ is the von Kármán value involved in Eq. (8).

4. RESULTS ON THE NACA 4412 WING SECTION

4.1 Prediction and influence of κ_0 in the Spalart-Allmaras model under pressure gradient

The LES case by Vinuesa *et al.* (α =5°, $Re_c = 1M$) has been reproduced using the industrial CFD code AETHER on a 2D mesh. The laminar-turbulent transition is imposed at $x/c = 10\%$ as in the LES, by deactivating the production term of the turbulent model in the laminar region. The simulations were performed using the SA(κ_0) and the SA(κ_p) models.

Figs. 2 and 3 show the influence of p^+ on the log-law prediction. The reference LES data as well as the two models are compared at the same p^+ value, thus not necessarily at the same chordwise position as indicated on Tab. 1.

Table 1: Pressure gradient p^+ – chordwise position x/c correspondance for the Spalart-Allmaras models and the LES reference at $Re_c = 1M$, α =5°

p^+	LES	SA(κ_0)	SA(κ_p)
0.470	98.3 %	94.8 %	84.8 %
0.216	96.6 %	93.2 %	83.8 %
0.151	94.8 %	92.1 %	83.1 %
0.106	93.1 %	90.8 %	82.6 %
0.061	89.7 %	88.0 %	80.8 %
0.024	81.0 %	80.8 %	76.7 %
0.008	60.0 %	62.2 %	59.1 %

The apparent log-law slope is determined with the mean velocity slope diagnostic function for the log-law region, defined in Eq.(11), see *e.g.* Österlund *et al.* [12] and Knopp [5]

$$\Xi_{log} = \left(y^+ \frac{dU^+}{dy^+} \right)^{-1}. \tag{11}$$

The log-law region corresponds to the vicinity of an inflexion point of the velocity profile, which is expressed by the local maximum in the Ξ_{log} function above $y^+ \approx 10$. The apparent von Kármán constant $\overline{\kappa}$ will be defined as this local maximum for the studied models.

Fig. 2 shows that the models at $p^+ = 0.151$ both predict the wrong slope, the apparent von Kármán constant $\overline{\kappa}$ for each curve being indicated in the figure and highlighted in Fig. 3. Note that as Fig. 1 above, the latter also confirms Nickels theoretical κ_p value. These observations can be extended to all values of p^+.

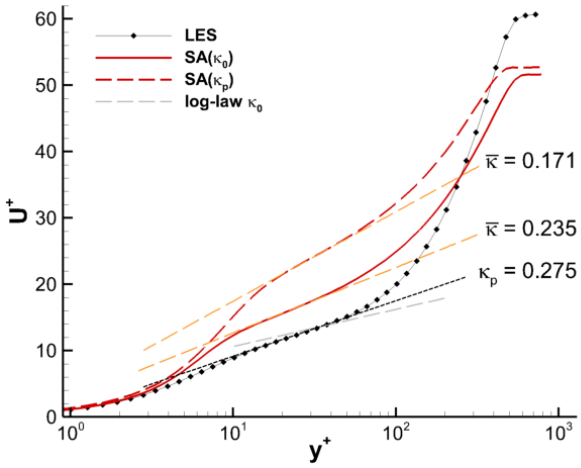

Figure 2: SA(κ_0) and SA(κ_p) models velocity profiles on the NACA 4412 wing section at $p^+ = 0.151$

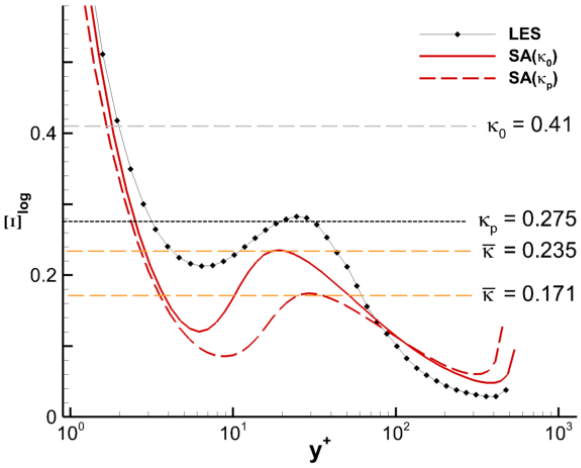

Figure 3: SA(κ_0) and SA(κ_p) models apparent $\overline{\kappa}$ on the NACA 4412 wing section at $p^+ = 0.151$

The original SA(κ_0) does predict a reduction of $\overline{\kappa}$ as p^+ increases, but to a stronger extent as what is returned by Nickels relation and the LES, indicating that the model log-law slope is implicitly affected. Expectedly, this natural response of the Spalart-Allmaras model amplifies the $\overline{\kappa}$ reduction of the modified model SA(κ_p).

However, it can be also observed in Fig. 4 that the SA(κ_p) correctly responds to the new target κ value in the model equation, as the ratio $\overline{\kappa}\,[SA(\kappa_p)]\,/\,\overline{\kappa}\,[SA(\kappa_0)]$ follows the theoretical law Eq. (5). This figure also gathers data computed with a higher Reynolds number, $Re_c = 4M$, all others parameters unchanged.

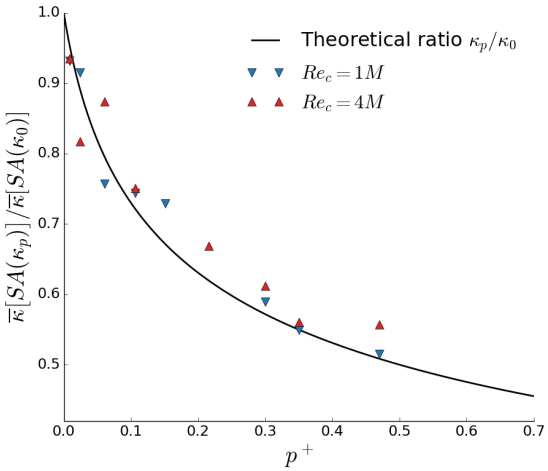

Figure 4: Response to the implemented κ-value in the Spalart-Allmaras model on the NACA 4412 wing section

4.2 Correction of the slope prediction in the Spalart-Allmaras model

The effect of the pressure gradient p^+ on $\overline{\kappa}$ for both SA(κ_0) and SA(κ_p) models, given their target κ (κ_0 and κ_p resp.), are shown in Fig. 5. As it has been shown in the previous section that the Spalart-Allmaras model correctly responds to the target changes, $\overline{\kappa}$ can be corrected to yield the κ_p slope by anticipating the natural deviation of the model.

The correction law, Eq. (12), has been obtained using a regression on the data computed at $Re_c = 1M$ and $Re_c = 4M$ for both SA(κ_0) and SA(κ_p).

$$r(\kappa) = \frac{\overline{\kappa}}{\kappa} = a\log(p^+ + c) + b. \tag{12}$$

The best fit is obtained with a coefficient of determination $r^2 = 0.98$ for

$$a \simeq -0.135, \qquad b \simeq 0.344,$$
$$c = \exp\left(\frac{1-b}{a}\right) \simeq 0.0077,$$

where the constant c is chosen to ensure

$$r(\kappa)|_{p^+=0} = 1. \tag{13}$$

A new version SA(κ_{corr}) of the model has been implemented, using the target value κ_{corr} defined by

$$\kappa_{corr} = \frac{\kappa_0}{r(\kappa_0)\sqrt{1 + p^+ y_c^+}}. \tag{14}$$

Results are shown in Figs. 6 and 7 for $p^+ = 0.061$. The slope of the new model SA(κ_{corr}) corresponds well to Nickels value. As can be observed in Fig. 7, its peak

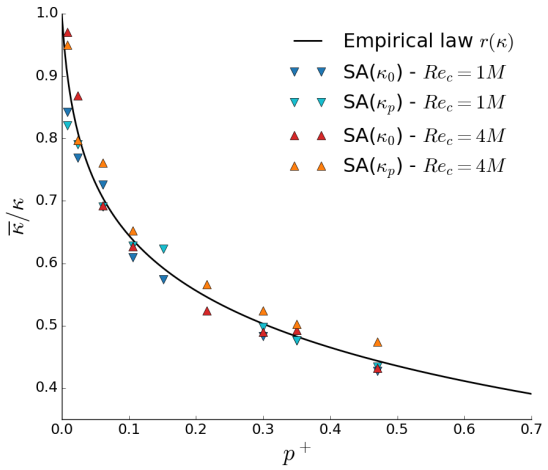

Figure 5: Apparent-to-target κ ratio for the Spalart-Allmaras model

value is closer to the LES reference, but is reached for smaller y^+, highlighting the shift of the log-law region towards the wall. The diagnostic plot once again points out the correct response to the change in the implemented κ value.

The corrected model SA(κ_{corr}) offers improved results compared to the SA(κ_0), as it pushes the separation point back downstream, knowing that no separation occurs in the LES. This is directly linked to the p^+ distribution on the wing section, which fits the LES results longer and diverges for larger pressure gradient, as shown in Fig. 8.

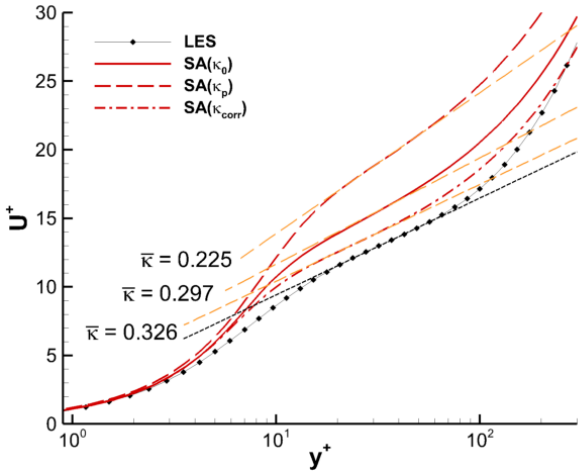

Figure 6: SA(κ_0), SA(κ_p) and SA(κ_{corr}) models velocity profiles on the NACA 4412 wing section at $p^+ = 0.061$

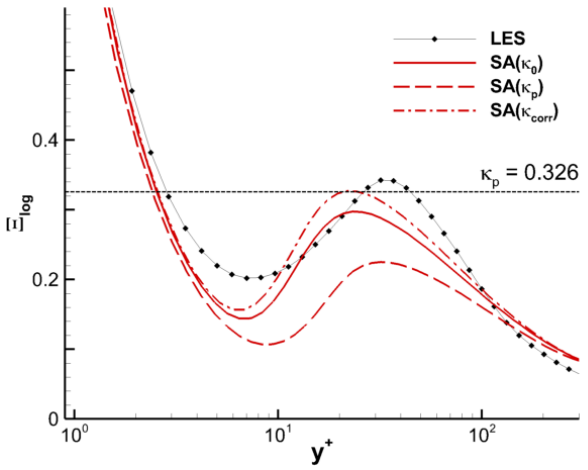

Figure 7: SA(κ_0), SA(κ_p) and SA(κ_{corr}) models apparent $\overline{\kappa}$ on the NACA 4412 wing section at $p^+ = 0.061$

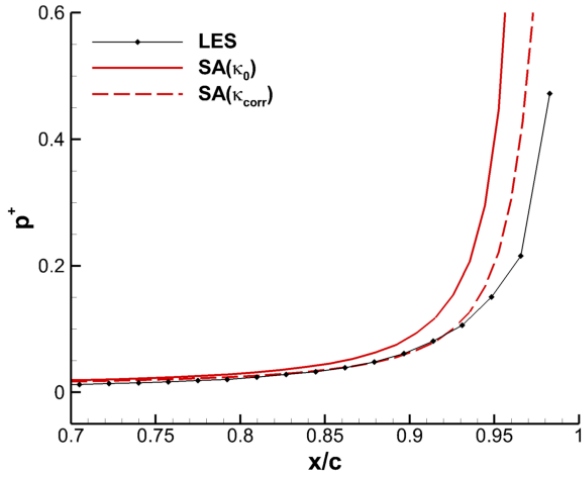

Figure 8: Pressure gradient distribution on the NACA 4412 trailing edge

4.3 Log-law intercept deviation

Figs. 2 and 6 show that the intercept value of the log-law is shifted upward with the Spalart-Allmaras models, compared with LES. These values have been gathered in Tab. 2.

In this table, the LES confirms the experimental observations by Clauser [3] and Nagano *et al.* [9] of the downward shift of the velocity in the log-law region with increasing adverse pressure gradient. The intercepts predicted by the SA models are little affected, except at very large p^+ (over $p^+ \approx 0.15$).

The LES results comply with the empirical relation (15) for the apparent intercept $\overline{B}$ introduced by Nagib & Chauhan [10], shown in Fig. 9.

$$\overline{\kappa}\overline{B} = 1.6\left(\exp(0.1663\overline{B}) - 1\right) \qquad (15)$$

Table 2: Apparent log-law intercept $\overline{B}$ at given pressure gradient p^+ positions for the Spalart-Allmaras models and the LES reference at $Re_c = 1M$, $\alpha = 5°$

p^+	LES	SA(κ_0)	SA(κ_{corr})
0.470	-1.1	2.6	2.9
0.216	-0.2	2.5	2.6
0.151	0.8	2.9	3.3
0.106	1.5	2.8	2.7
0.061	2.4	3.9	3.4
0.024	3.7	3.4	3.7
0.008	4.6	3.8	3.9

This figure also shows that the SA(κ_{corr}) model improves the $\overline{B}$ for small p^+, corresponding to the closest points to the empirical relation, but indicates a drift for the other points.

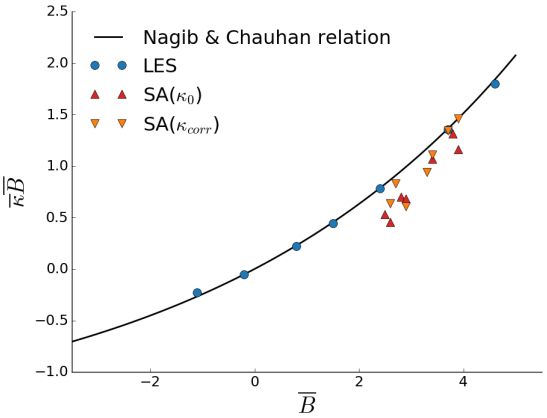

Figure 9: Variation of $\overline{\kappa}\overline{B}$ with $\overline{B}$ for the LES and the SA models

This is confirmed in Fig. 10. Indeed, the log-law region of the corrected model SA(κ_{corr}) starts drifting from the reference above $p^+ \approx 0.03$.

From Fig. 11, the intercept upward shift is to be expected from an overestimation of the viscous sublayer thickness. The SA(κ_{corr}) reduces it slightly, resulting in a smaller log-law region upward shift with respect to LES. To further improve this behaviour, the pressure gradient effects on the Spalart-Allmaras viscous sublayer must be taken into account.

4.4 Slope-correction effects on the wake region

The wake region seems barely affected by the change in the von Kármán constant value. Fig. 10 shows that it is slightly steepened by the correction in order to reach the same free-stream velocity as in the SA(κ_0). However, the

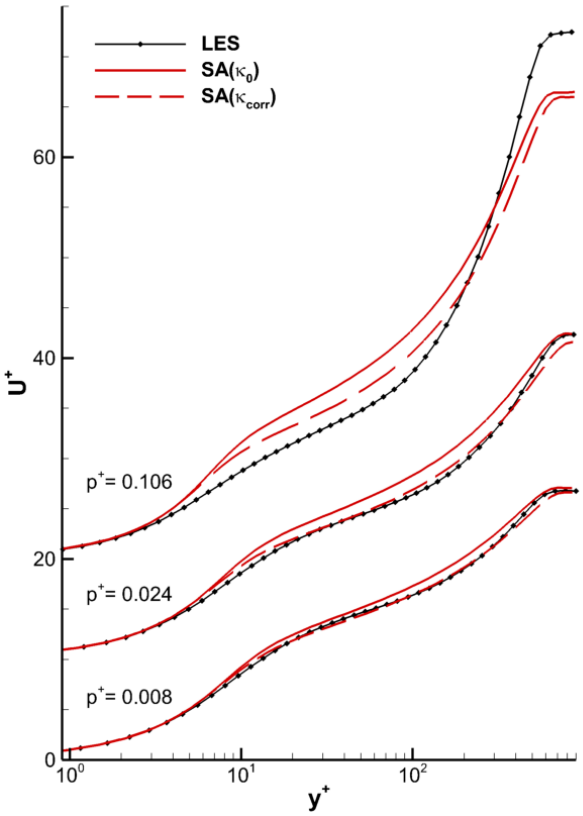

Figure 10: SA(κ_0)) and SA(κ_{corr}) models velocity profiles on the NACA 4412 wing section for different mild to strong pressure gradients

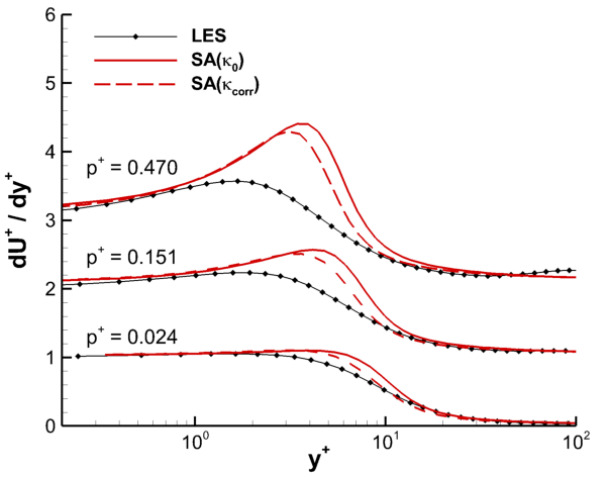

Figure 11: SA(κ_0)) and SA(κ_{corr}) models dU^+/dy^+ profiles in the viscous sublayer on the NACA 4412 wing section for three pressure gradients (the profiles are shifted incrementally)

wake region adds a smaller ΔU^+ than in the LES, leading to a smaller free-stream velocity in the wall units. The small effect of the slope correction on the wake behaviour

implies that another correction must be found to properly render the outer layer.

5. 3D CASES APPLICATIONS

5.1 Skåre & Krogstad wind-tunnel

The SA(κ_{corr}) has been compared to the original model SA(κ_0) on the Skåre & Krogstad experimental configuration. The experiment consists in a diverging wind-tunnel with an APG turbulent boundary layers in equilibrium developing on the wall. The setup is shown in Fig. 12.

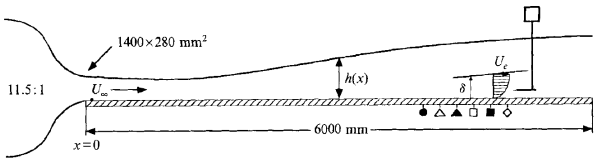

Figure 12: Skåre & Krogstad experiment configuration [14]

Due to three-dimensional effects, the numerical simulation has to be carried in a 3D domain with the quadratic constitutive relation (QCR) for the Spalart-Allmaras model [15] to correctly reproduce the pressure coefficient C_p distribution of the experiment (shown in Fig. 13) while preventing large vortices in the corners.

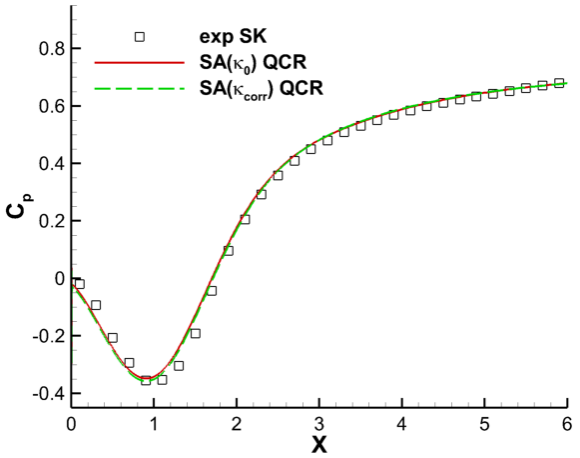

Figure 13: Pressure coefficient C_p compared with experiment

In [14], Skåre and Krogstad used the Clauser gradient parameter $\beta_p = (\delta^*/\tau_w)dP/dx$ to characterise the equilibrium APG flow. As it can be observed in Fig. 14, the numerical simulations fail to achieve the experimental value $\beta_p = 20$, while the p^+ parameter is just slightly underestimated. This can be explained by the deviation observed in the displacement thickness δ^* distribution, plotted in Fig. 15, which indicates that the boundary layer growth is underestimated and thus the outer layer wrongly predicted.

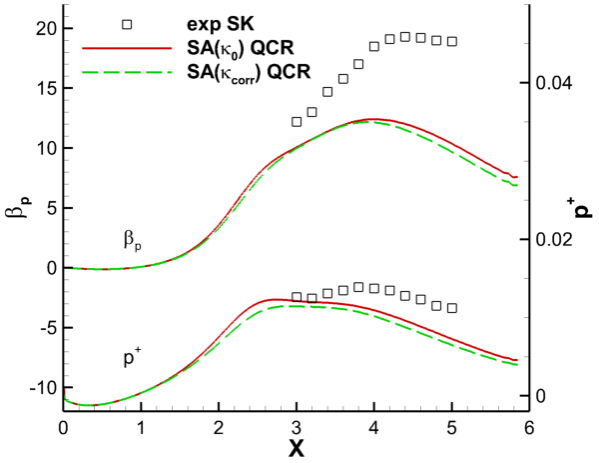

Figure 14: Distribution of the pressure gradient parameters in the wind-tunnel

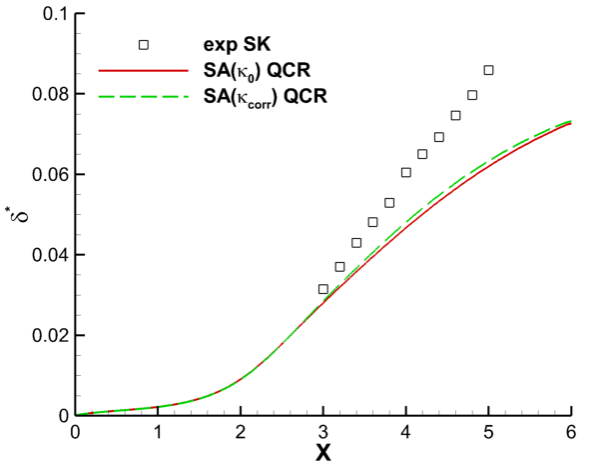

Figure 15: Distribution of the displacement thickness δ^* in the wind-tunnel

Therefore, Fig. 16 shows as expected that the SA(κ_{corr}) model performs better in the inner layer but fails in the outer layer identically to the SA(κ_0) model, as for the NACA 4412 case (Fig. 10). This case points out once again the need for an outer layer correction. Moreover, though the intercept is well estimated (due to the small value of p^+), it can be seen that the log-law region predicted by both models starts slightly closer to the wall compared with the experiment. This behaviour could already be seen in Sec. 4.2.

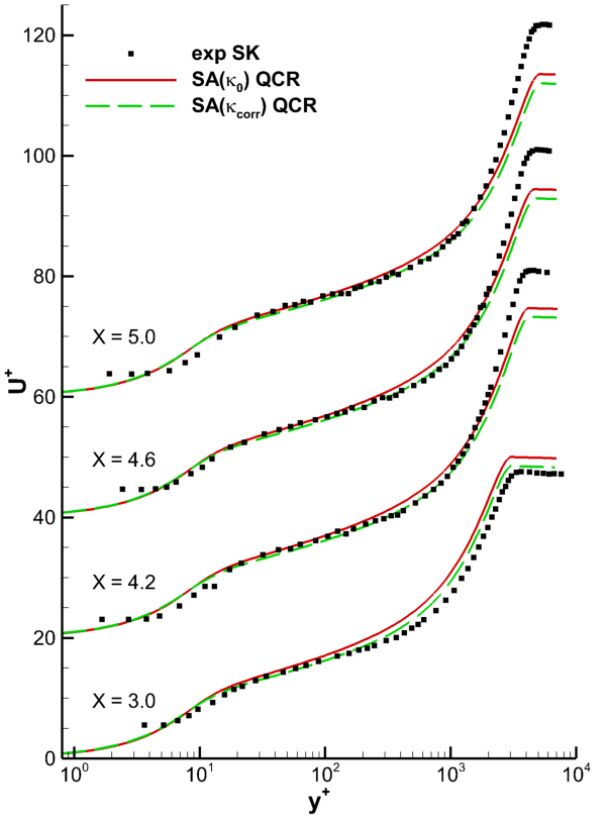

Figure 16: Velocity profiles at 4 different positions

5.2 Common Research Model

The model SA(κ_{corr}) is now applied to the Common Research Model (CRM) used in the AIAA Drag Prediction Workshop [18], in its "wing and body" without nacelle–pylons configuration, see Fig. 17. It represents a generic commercial aircraft, without tail and motorisation.

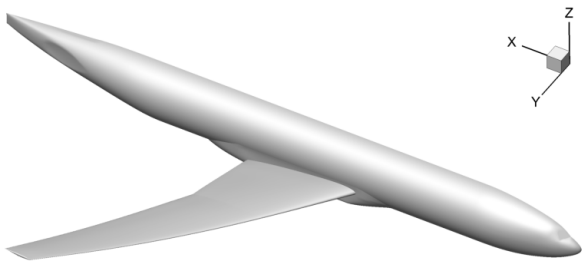

Figure 17: The CRM "Wing and Body" configuration

The QCR correction is once again used to improve the juncture flow prediction at the wing-root and the side-of-body separation. The case has been run for $M = 0.85$ and $Re_c = 5M$. The angle of attack α is adapted during computation to yield a target lift of $C_L = 0.609$, in order to obtain results comparable to the available experimental data, consisting in pressure coefficient measurements at several spanwise positions η. The converged angle of attack for both models is α =3.27°, whereas the experiment results were obtained for $\alpha_{\exp} \approx 3.7°$.

The predicted p^+ distributions for the models are given in Fig. 18 for $\eta = 60.3\%$. The shock position is clearly illustrated through the peak at $x/c = 55\%$, the pressure gradient on the aft part of the wing being limited to relatively smaller values ($p^+ < 0.01$).

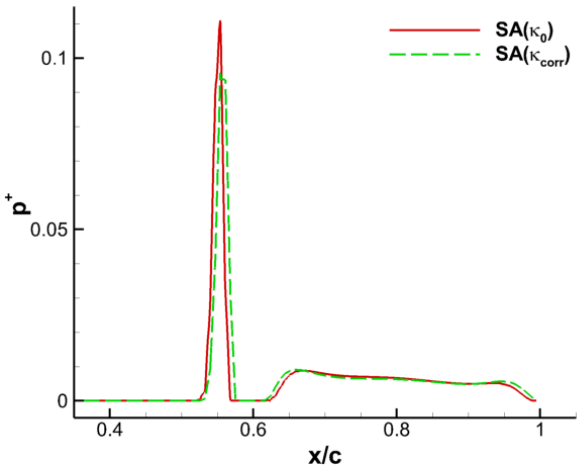

Figure 18: Pressure gradient parameter p^+ at the spanwise position $\eta = 60.3\%$ on the upper side of the wing

Figs. 19–20 show that the model correction has little effects on the pressure coefficient, with only a small shift of the shock position and of the C_p-level at the trailing edge on the suction side for $\eta = 60.3\%$. The differences in Fig. 20 between the experimental data and the models results might be due to a misprediction of the boundary layer growth, as observed in Sec. 5.1 for the Skåre & Krogstad case, or to three-dimensional effects.

Figs. 21–24 highlight the locality of the correction in the SA(κ_{corr}) model. The friction coefficients C_f and the boundary layer parameters δ^* and H are identical on the first half of the wing section for both models, however the influence of the correction is clearly visible where p^+ is positive (*cf.* Fig. 18).

6. CONCLUSION

This article presented a first attempt to improve the Spalart-Allmaras model response to an adverse pressure gradient, commonly encountered in aeronautical applications. Firstly, the assumption of a pressure gradient sensitive log-law was confirmed on LES results. Based on the observation that the model wrongly predicted the log-law region in strong APG cases, the model was modified to yield the correct slope. This was done by correcting

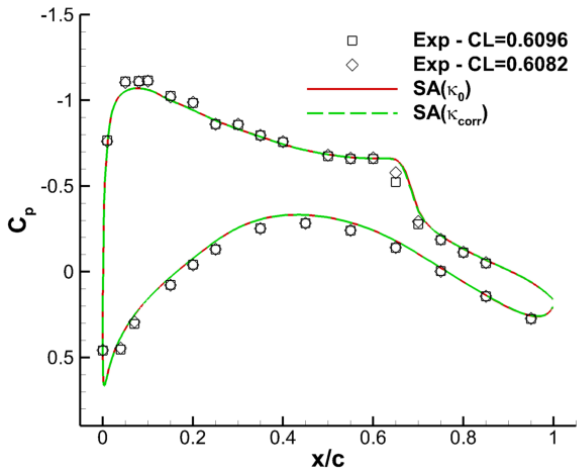

Figure 19: Pressure coefficient C_p at the spanwise position $\eta = 20.1\%$

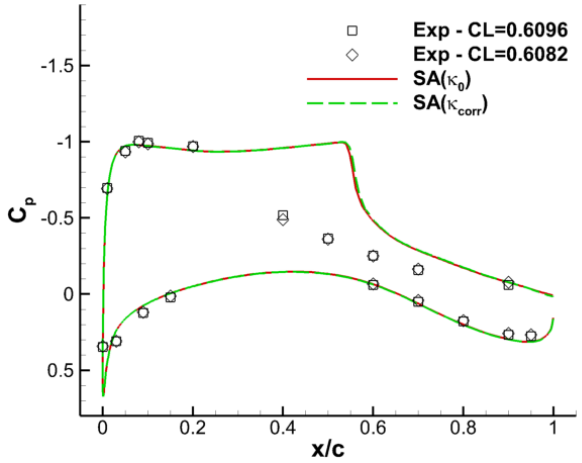

Figure 20: Pressure coefficient C_p at the spanwise position $\eta = 60.3\%$

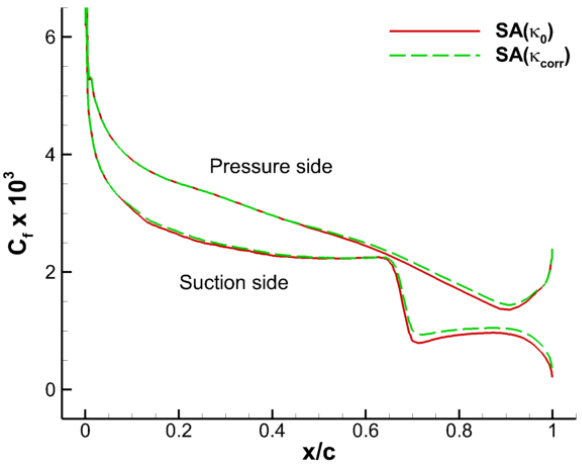

Figure 21: Friction coefficient C_f at the spanwise position $\eta = 20.1\%$

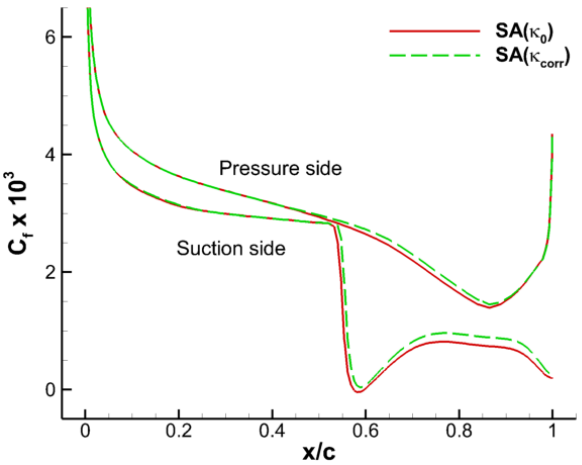

Figure 22: Friction coefficient C_f at the spanwise position $\eta = 60.3\%$

the natural deviation of the apparent slope to the implemented value before targeting the theoretical value defined by Nickels.

The correction introduced is however limited for now to the slope of the log-law region and does not actively take into account the log-law downward shift in the velocity profile, which appears for strong APG ($p^+ > 0.03$). Noting that the viscous sublayer thickness is overestimated in the Spalart-Allmaras model, this second correction should focus on the model viscous sublayer thickness response to the pressure gradient.

The slope correction also barely affects the outer layer. As a result, the turbulent boundary layer growth is unchanged and still mispredicted, leading to little effects on the pressure coefficient C_p for an aircraft. This implies that another correction improving the outer layer behaviour is also needed.

REFERENCES

[1] S. Catris. *Étude de contraintes et qualification de modèles à viscosité turbulente*. PhD thesis, ENSAE, Toulouse, 1999.

[2] S. Catris and B. Aupoix. Towards a calibration of the length-scale equation. *Int. J. Heat Fluid Fl.*, 21(5):606–613, 2000.

[3] F.H. Clauser. Turbulent boundary layers in adverse pressure gradients. *J. Aeronaut. Sci.*, 21(2):91–108, 1954.

[4] P.G. Huang and P. Bradshaw. Law of the wall for turbulent flows in pressure gradients. *AIAA J.*, 33(4):624–632, 1995.

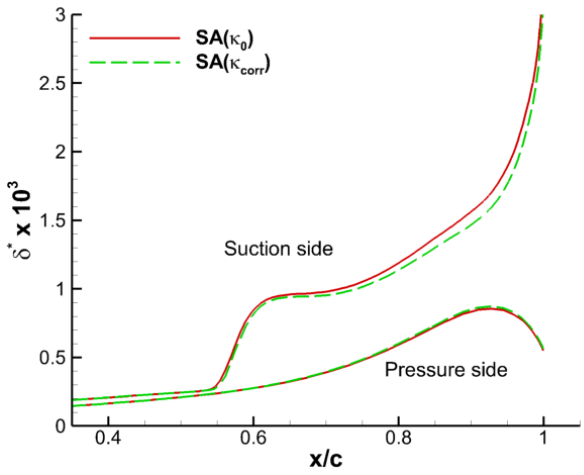

Figure 23: Displacement thickness δ^* at the spanwise position $\eta = 60.3\%$

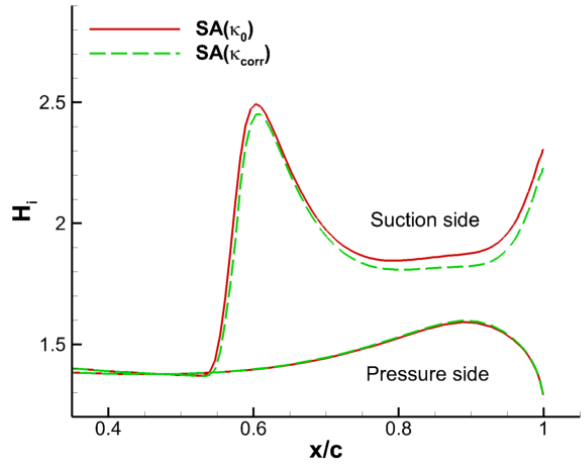

Figure 24: Form factor $H = \delta^*/\theta$ at the spanwise position $\eta = 60.3\%$

[5] T. Knopp. A new wall-law for adverse pressure gradient flows and modification of k-omega type RANS turbulence models. In *54th AIAA Aerospace Sciences Meeting*, page 0588, 2016.

[6] T. Knopp, D. Schanz, A. Schröder, M. Dumitra, Ch. Cierpka, R Hain, and C.J. Kähler. Experimental investigation of the log-law for an adverse pressure gradient turbulent boundary layer flow at Re θ= 10000. *Flow Turbul. Combust.*, 92(1-2):451–471, 2014.

[7] Y. Maciel, K.-S. Rossignol, and J. Lemay. Self-similarity in the outer region of adverse-pressure-gradient turbulent boundary layers. *AIAA J.*, 44(11):2450–2464, 2006.

[8] F. R. Menter. Two-equation eddy-viscosity turbulence models for engineering applications. *AIAA J.*, 32(8):1598–1605, 1994.

[9] Y. Nagano, M. Tagawa, and T. Tsuji. Effects of adverse pressure gradients on mean flows and turbulence statistics in a boundary layer. In *Turbulent Shear Flows 8*, pages 7–21. Springer, 1993.

[10] H.M. Nagib and K.A. Chauhan. Variations of von Kármán coefficient in canonical flows. 20(10):101518, 2008.

[11] T.B. Nickels. Inner scaling for wall-bounded flows subject to large pressure gradients. *J. Fluid Mech.*, 521:217–239, 2004.

[12] J.M. Österlund, A.V. Johansson, H.M. Nagib, and M.H. Hites. A note on the overlap region in turbulent boundary layers. *Phys. Fluids*, 12(1):1–4, 2000.

[13] A.E. Perry. Turbulent boundary layers in decreasing adverse pressure gradients. *J. Fluid Mech.*, 26(3):481–506, 1966.

[14] P.E. Skåre and P.-Å. Krogstad. A turbulent equilibrium boundary layer near separation. *J. Fluid Mech.*, 272:319–348, 1994.

[15] P.R. Spalart. Strategies for turbulence modelling and simulations. *Int. J. Heat Fluid Fl.*, 21(3):252–263, 2000.

[16] P.R. Spalart and S.R. Allmaras. One-equation turbulence model for aerodynamic flows. *La Recherche Aerospatiale*, 1:5–21, 1994.

[17] E. Stein, R. de Borst, and T.J.R. Hughes, editors. *Encyclopedia of Computational Mechanics*, volume 3: Fluids. John Wiley & Sons, Ltd., 2004. Chap. 12, sec. 4.

[18] E.N. Tinoco, O.P. Brodersen, S. Keye, K.R. Laflin, E. Feltrop, J.C. Vassberg, M. Mani, B. Rider, R.A. Wahls, J.H. Morrison, D. Hue, C.J. Roy, D.J. Mavriplis, and M. Murayama. Summary Data from the Sixth AIAA CFD Drag Prediction Workshop: CRM Cases. *J. Aircraft*, 55(4):1352–1379, 2018.

[19] A.A. Townsend. *The Structure of Turbulent Shear Flow*. Second edition, 1976.

[20] R. Vinuesa, P.S. Negi, M. Atzori, A. Hanifi, D.S. Henningson, and P. Schlatter. Turbulent boundary layers around wing sections up to Re_c = 1,000,000. *Int. J. Heat Fluid Fl.*, 72:86–99, 2018.

[21] D. C. Wilcox. *Turbulence Modeling for CFD*. DCW industries, Inc., La Cañada, California, third edition, 2006.

Appendix D

Article submitted to: International Journal of Heat and Fluid Flow

Reynolds-Stress Models for Aeronautical Applications

Gustave Sporschill[a,b,*], Flavien Billard[a], Michel Mallet[a], Rémi Manceau[b], Hervé Bézard[c]

[a] *Dassault Aviation, Saint-Cloud, France*
[b] *CNRS, Université de Pau et des Pays de l'Adour, E2S UPPA, INRIA, project-team CAGIRE, Laboratory of Mathematics and Applied Mathematics (LMAP), Pau, France*
[c] *ONERA, Toulouse, France*

Abstract

Three recent Reynolds-Stress Models (RSMs) have been benchmarked on industrial configurations with aeronautical applications. The models are first compared on a zero-pressure-gradient boundary layer, which highlights the differences in the near-wall approaches of the models. Results are then analyzed for the Skåre & Krogstad adverse-pressure-gradient boundary layer and the Common Research Model (CRM) aircraft for two Reynolds numbers. Both cases display improvements in using RSMs over the eddy-viscosity Spalart-Allmaras model. The considered second-moment closures better predict the boundary layer growth and its shape factor in the Skåre & Krogstad test case, and greatly improve the drag-due-to-lift in the CRM case.

Keywords: Turbulence modeling, Boundary layer, Turbulence budget, Adverse pressure gradient, Aeronautical applications, Common Research Model

1. Introduction

Turbulence modeling is a key feature of CFD design tools, the improvement of which directly impacts the design margin of aeronautical products. Second-moment closures of the Reynolds-Averaged Navier-Stokes (RANS) equations, also called Reynolds-Stress Models (RSMs), reduce the empiricism of the Eddy-Viscosity Models (EVMs). They inherently render the anisotropy of turbulence for 3D and wall-bounded cases, and are therefore well-adapted to the 3D highly anisotropic flows encountered in aeronautical applications. Their spreading in the industry has mainly suffered for a long time from numerical stiffness, due to their many coupled equations. Recent models have been developed with emphasis on their robustness in order to be implemented in industrial CFD codes.

Three of them are assessed in the present work: the elliptic blending Reynolds-stress model (EB-RSM) (Manceau, 2015), the SSG/LRR-ω model (Cécora et al., 2012) and the SSG-ω model from the European ATAAC project (Schwamborn and Strelets, 2012; Aupoix, 2012). The SSG/LRR-ω and the SSG-ω ATAAC models both use the specific dissipation rate ω as the length-scale providing quantity, due to its improved performance in adverse-pressure-gradient (APG) flow, and thus in aeronautical applications. This behavior, observed for the two-equation $k-\omega$ models, has been explained by Huang and Bradshaw (1995) and Catris and Aupoix (2000) by the mathematical ability of the ω-equation to preserve the log-law prediction in APG, compared to the ε-equation. The SSG-ω ATAAC model also uses a specific near-wall approach to correctly reproduce the asymptotic behavior of the turbulent quantities at the wall, including the near-wall model of Manceau and Hanjalić (2002) developed for the EB-RSM.

They are investigated alongside the Spalart-Allmaras model, a widely applied EVM in the aeronautical industry, on cases of industrial interests, including the Common Research Model (CRM) used in the AIAA Drag Prediction Workshop (Tinoco et al., 2018).

2. Reynolds-stress models

2.1. General formulation

For compressible flow, the Reynolds-averaged Navier-Stokes equations are written using both the Reynolds decomposition $f = \overline{f} + f'$ and the density-weighted average decomposition $f = \widetilde{f} + f''$, where $\widetilde{f} = \overline{\rho f}/\overline{\rho}$,

$$\frac{\partial \overline{\rho}}{\partial t} + \frac{\partial \overline{\rho}\widetilde{U}_i}{\partial x_i} = 0 \tag{1}$$

$$\frac{\partial \overline{\rho}\widetilde{U}_i}{\partial t} + \frac{\partial \overline{\rho}\widetilde{U}_j\widetilde{U}_i}{\partial x_j} = -\frac{\partial \overline{P}}{\partial x_i} + \frac{\partial}{\partial x_j}\left(2\overline{\mu S^*_{ij}} - \overline{\rho}R_{ij}\right) \tag{2}$$

where $\overline{\rho}R_{ij} = \overline{\rho u_i'' u_j''}$, and $S^*_{ij} = S_{ij} - S_{kk}\delta_{ij}/3$ is the deviatoric part of the strain-rate tensor $S_{ij} = (\partial_j U_i + \partial_i U_j)/2$. The energy equation is not presented in this paper, which focuses on the different approaches for the modeling of the Reynolds-stress tensor R_{ij} and not on the turbulent heat fluxes[1]. The latter are here simply modeled with a Simple Gradient Diffusion Hypothesis.

Second-moment closures solve transport equations for the Reynolds stresses R_{ij} directly, without relying on the Boussinesq

*Corresponding author: gustave.sporschill@gmail.com

[1] details on the energy equation closure can be found on the TMR website https://turbmodels.larc.nasa.gov/implementrans.html

hypothesis that assumes a linear relation between Reynolds-stress and strain-rate tensors. Using Morkovin's hypothesis (Morkovin, 1962), the compressibility terms can be neglected, so that the transport equations read

$$\underbrace{\frac{\partial \overline{\rho} R_{ij}}{\partial t} + \frac{\partial \overline{\rho} \widetilde{U}_k R_{ij}}{\partial x_k}}_{\overline{\rho} C_{ij}} = \underbrace{-\overline{\rho}\left(R_{ik}\frac{\partial \widetilde{U}_j}{\partial x_k} + R_{jk}\frac{\partial \widetilde{U}_i}{\partial x_k}\right)}_{\overline{\rho} P_{ij}} + \underbrace{\frac{\partial}{\partial x_k}\left(\overline{\mu}\frac{\partial R_{ij}}{\partial x_k}\right)}_{\overline{\rho} D^{\nu}_{ij}} + \overline{\rho} D^{T}_{ij} + \overline{\rho}\phi^{*}_{ij} - \overline{\rho}\varepsilon_{ij} \quad (3)$$

where C_{ij}, P_{ij}, D^{ν}_{ij}, D^{T}_{ij}, ϕ^{*}_{ij}, and ε_{ij} denote convection, production, viscous diffusion, turbulent transport, velocity pressure-gradient correlation and dissipation, respectively. The first four terms are exact as they only depend on the mean flow velocity and the Reynolds stresses, solved by the equation system. On the contrary, the last three terms involve unknown correlations

$$\overline{\rho} D^{T}_{ij} = -\frac{\partial \overline{\rho u_i'' u_j'' u_k''}}{\partial x_k}, \quad (4)$$

$$\overline{\rho}\phi^{*}_{ij} = -\left(\overline{u_i''\frac{\partial p'}{\partial x_j}} - \overline{u_j''\frac{\partial p'}{\partial x_i}}\right), \quad (5)$$

$$\overline{\rho}\varepsilon_{ij} = 2\,\mu\,\overline{\frac{\partial u_i''}{\partial x_k}\frac{\partial u_j''}{\partial x_k}}. \quad (6)$$

The next section describes the different models used to close Eq. (3) at second-moment level.

2.2. Considered models

Three RSMs are investigated in this study and are shortly described and compared in this section:

- the elliptic blending Reynolds-stress model (EB-RSM) (Manceau and Hanjalić, 2002; Manceau, 2015)
- the SSG/LRR-ω RSM (Cécora et al., 2012; Eisfeld et al., 2016)
- the SSG-ω RSM from the European ATAAC project (Schwamborn and Strelets, 2012; Aupoix, 2012)

Different formulations of the SSG/LRR-ω RSM have been proposed and are detailed on NASA's Turbulence Modeling Resource website[2], the one considered here is referred to as `SSG/LRR-RSM-w2012-SD`. The SSG-ω ATAAC model is detailed in Appendix A.

2.2.1. Length-scale providing equation

As for two-equation eddy-viscosity models, the Reynolds-stress transport equation set is closed by adding a length-scale providing transport equation.

The EB-RSM model relies on an ε-equation,

$$\overline{\rho}\frac{\mathrm{D}\varepsilon}{\mathrm{D}t} = \frac{\overline{\rho}}{T}\left(C'_{\varepsilon 1}P_k - C_{\varepsilon 2}\varepsilon\right) + \frac{\partial}{\partial x_j}\left(\overline{\mu}\frac{\partial \varepsilon}{\partial x_j}\right) + \overline{\rho} D^{T}_{\varepsilon}. \quad (7)$$

[2] https://turbmodels.larc.nasa.gov/rsm-ssglrr.html

where $T = \max\left(k/\varepsilon; C_T\,(\nu/\varepsilon)^{1/2}\right)$ is the local turbulent time scale, bounded by the Kolmogorov time scale to prevent a singularity at the wall, as k vanishes. To correctly reproduce the peak of production of ε in the buffer layer, the production term is amplified in this region by replacing the constant $C_{\varepsilon 1}$ by a variable coefficient $C'_{\varepsilon 1}$. Several formulations have been suggested (see Manceau, 2015) and the following expression has been retained here

$$C'_{\varepsilon 1} = C_{\varepsilon 1}\left(1 + A_1\left(1-\alpha^3\right)\sqrt{\frac{k}{R_{ij}n_i n_j}}\right). \quad (8)$$

The SSG/LRR-ω and the SSG-ω ATAAC models both use the specific dissipation rate $\omega = \varepsilon/(\beta^* k)$. Indeed, they solve the BSL equation, defined by Menter (1994) as a blending of a Wilcox ω-equation at the wall with the standard ε-equation at the edge of the boundary layer, motivated by the good predictions of Menter's $k-\omega$ model in aeronautical applications and in APG flows

$$\overline{\rho}\frac{\mathrm{D}\omega}{\mathrm{D}t} = \gamma\overline{\rho}\frac{\omega}{k}P_k - \beta\overline{\rho}\omega^2 + \frac{\partial}{\partial x_j}\left(\overline{\mu}\frac{\partial \omega}{\partial x_j}\right) + \overline{\rho} D^{T}_{\omega} + 2\,(1-F_1)\,\frac{\sigma^{(\varepsilon)}_{\omega}}{\omega}\frac{\partial k}{\partial x_j}\frac{\partial \omega}{\partial x_j} \quad (9)$$

The blending is carried out on the coefficients according to $c = F_1\,c^{(\omega)} + (1-F_1)\,c^{(\varepsilon)}$, where the baseline function F_1 is unity at the wall and zero in the free-stream region (Eq. (A.15)).

To improve its prediction in the vicinity of the wall, the SSG-ω ATAAC model corrects the dissipation rate ε used in the Reynolds-stress transport equations by adding a damping function and a clipping to an asymptotic behavior in its conversion from ω

$$\varepsilon = f_{\varepsilon}\max\left(0.09\omega k; \left(\frac{k}{k_0^{+}}\right)^{3/2}\frac{1}{\kappa y}\right), \quad (10)$$

$$f_{\varepsilon} = \frac{5}{18} + \frac{13}{18}\tanh\left(\left[\frac{y}{42}\left(\frac{\omega k}{\nu^3}\right)^{1/4}\right]^3\right), \quad (11)$$

where y corresponds to the wall distance. The clipping corresponds to a Yap-type correction to prevent the deviation of the log-law slope in APG flows (see for instance Catris and Aupoix, 2000), whereas the damping function ensures the correct asymptotic behavior of k close to the wall.

2.2.2. Turbulent transport

The EB-RSM uses the Generalized Gradient Diffusion Hypothesis (GGDH) to account for the anisotropy of the turbulent transport in the boundary layer

$$D^{T}_{ij} = \frac{\partial}{\partial x_l}\left(C_s\,T\,R_{lm}\frac{\partial R_{ij}}{\partial x_m}\right), \quad (12)$$

$$D^{T}_{\varepsilon} = \frac{\partial}{\partial x_l}\left(\frac{C_s}{\sigma_{\varepsilon}}\,T\,R_{lm}\frac{\partial \varepsilon}{\partial x_m}\right), \quad (13)$$

whereas the ω-based RSMs are implemented with the Simple Gradient Diffusion Hypothesis (SGDH)

$$D_{ij}^T = \frac{\partial}{\partial x_l}\left(\frac{2}{3}\frac{C_s}{\beta^*}\nu_t\frac{\partial R_{ij}}{\partial x_l}\right), \tag{14}$$

$$D_{\omega}^T = \frac{\partial}{\partial x_l}\left(\sigma_w\nu_t\frac{\partial \omega}{\partial x_l}\right), \tag{15}$$

with $\nu_t = k/\omega$. It corresponds to the turbulent transport model used in eddy-viscosity models, with an isotropic diffusion coefficient. In the case of the SSG-ω ATAAC model, the eddy viscosity used in D_{ij}^T is damped in the near-wall region to account for the wall-blocking effect and bounded as for ε above, see Eq. (A.4) in appendix.

2.2.3. Velocity pressure-gradient correlation

The velocity pressure-gradient correlation ϕ_{ij}^* is a critical term to model in second-moment closures. It can be decomposed into a traceless term ϕ_{ij} and a pressure diffusion D_{ij}^p, the traceless term representing a redistribution of the turbulent kinetic energy among the Reynolds stresses. The pressure diffusion is generally assumed to globally contribute to turbulent diffusion, such that D_{ij}^p and D_{ij}^T are modeled as a whole.

The RSMs here use the high-Reynolds-number model proposed by Speziale, Sarkar and Gatski (SSG) (Speziale et al., 1991) for the redistribution far from the wall. It is expressed by

$$\begin{aligned}\phi_{ij} =& -\left(C_1\varepsilon + C_1^* P_k\right) b_{ij} \\ &+ C_2\varepsilon\left(b_{il}b_{jl} - \frac{1}{3}b_{mn}b_{mn}\delta_{ij}\right) \\ &+ \left(C_3 - C_3^*\sqrt{b_{mn}b_{mn}}\right) kS_{ij}^* \\ &+ C_4 k\left(b_{il}S_{jl} + b_{jl}S_{il} - \frac{2}{3}b_{mn}S_{mn}\delta_{ij}\right) \\ &+ C_5 k\left(b_{il}\Omega_{jl} + b_{jl}\Omega_{il}\right).\end{aligned} \tag{16}$$

The constant are given in Table 1. In the EB-RSM, the nonlinear return C_2 term is suppressed to prevent numerical stiffness.

The SSG-ω ATAAC model also uses the SSG model, including the C_2 term. However, as the SSG model has been calibrated alongside an ε-equation, the coefficients of the BSL ω-equation are slightly recalibrated to improve the model behavior where the ω-equation is solved (see Appendix A). Both the EB-RSM and the SSG-ω ATAAC model rely on a specific near-wall model, presented in Sec. 2.2.5, that activates close to the wall.

In the SSG/LRR-ω RSM, the redistribution term is modeled with a blending of both the SSG and the LRR (Launder et al., 1975) models. Indeed, Wilcox (2006) showed that the ω-equation provides a better behavior in association with the LRR model. The SSG/LRR-ω model thus switches from the SSG model in the free-stream region to the LRR model close to the wall when the BSL equation switches from the ε to the ω-equation. Since both redistribution models can be cast into the same mathematical expression, Eq. (16), the blending is simply applied on their coefficients, similarly to the BSL ω-equation,

$$C = F_1\, C^{(\omega)} + (1 - F_1)\, C^{(\varepsilon)} \tag{17}$$

where F_1 is the baseline function defined in Menter's model (Menter, 1994).

Table 1: Constants for ϕ_{ij} models ($c_2^{\mathrm{LRR}} = 0.52$)

	C_1	C_1^*	C_2	C_3	C_3^*	C_4	C_5
SSG	3.4	1.8	4.2	0.8	1.3	1.25	0.4
LRR	3.6	0	0	0.8	0	$\frac{18c_2^{\mathrm{LRR}}+12}{11}$	$\frac{-14c_2^{\mathrm{LRR}}+20}{11}$

2.2.4. Dissipation rate

Considering the deviatoric contribution of ε_{ij} modeled as part of the SSG and the LRR models, the presented RSMs reduce the dissipation rate tensor to its isotropic part

$$\varepsilon_{ij} = \frac{2}{3}\varepsilon\delta_{ij} \tag{18}$$

However, this assumption is no longer valid in the vicinity of the wall, where the flow is strongly anisotropic. As for the redistribution term, the EB-RSM and the SSG-ω ATAAC model therefore rely on a specific near-wall model.

2.2.5. Near-wall modeling

The presence of a solid wall implies an amplified damping of the wall-normal Reynolds stress R_{22} due to the blocking effect of the wall, asymptotically leading to a two-component turbulence. The Taylor-series expansion of the Reynolds stresses yields

$$R_{11} \sim y^2, \qquad R_{22} \sim y^4, \qquad R_{33} \sim y^2. \tag{19}$$

To reproduce this physical phenomenon, the EB-RSM and the SSG-ω ATAAC model use a specific near-wall modeling for ε_{ij} and ϕ_{ij} ensuring the correct asymptotic behavior. They both rely on Rotta's near-wall dissipation model ε_{ij}^w (Rotta, 1951) and Manceau & Hanjalić asymptotic redistribution model ϕ_{ij}^w (Manceau and Hanjalić, 2002)

$$\varepsilon_{ij} = (1 - f_b)\;\varepsilon_{ij}^w + f_b\,\frac{2}{3}\varepsilon\delta_{ij}, \qquad \varepsilon_{ij}^w = \frac{R_{ij}}{k}\varepsilon, \tag{20}$$

$$\begin{aligned}&\phi_{ij} = (1 - f_b)\;\phi_{ij}^w + f_b\,\phi_{ij}^{SSG}, \\ &\phi_{ij}^w = -5\frac{\varepsilon}{k}\left(R_{ik}n_jn_k + R_{jk}n_in_k - \frac{1}{2}R_{kl}n_kn_l\left(n_in_j + \delta_{ij}\right)\right).\end{aligned} \tag{21}$$

However, these two models differ in their blending functions f_b. The SSG-ω ATAAC model uses an analytic function, depending on the wall-distance y

$$f_b = 1 - \exp\left(-\left[\frac{1}{225}\left(\frac{\omega y^2}{\nu} - \frac{6}{\beta}\right)\right]^2\right), \tag{22}$$

with $\beta = 3/40$.

On the other hand, the EB-RSM is based on the elliptic blending to avoid any direct dependence on the wall-distance. As a simplification of Durbin's elliptic relaxation (Durbin, 1991)

Table 2: Differences between the considered models in the near-wall region

	EB-RSM	SSG-ω RSM ATAAC	SSG/LRR-ω RSM
Length-scale	ε	ω BSL (recalibrated) near-wall corrected ε	ω BSL $\varepsilon = \beta^* \omega k$
ε_{ij}^w	Rotta, Eq. (20)	Rotta, Eq. (20)	isotropic
ϕ_{ij}^w	Manceau & Hanjalić, Eq. (21)	Manceau & Hanjalić, Eq. (21)	LRR
D_{ij}^T	GGDH	SGDH	SGDH
f_b	elliptic blending	analytic blending	BSL function F_1

down to only one additional equation, the elliptic blending (Manceau and Hanjalić, 2002) let the EB-RSM sense the distance to the wall from a characteristic local length scale L to adapt the transition between near-wall and free-stream modeling

$$\alpha - L^2 \nabla^2 \alpha = 1, \tag{23}$$

$$L = C_L \max\left(\frac{k^{3/2}}{\varepsilon}; C_\eta \left(\frac{\nu^3}{\varepsilon}\right)^{1/4}\right). \tag{24}$$

For an optimal behavior, the blending function is set to $f_b = \alpha^3$ (Manceau, 2015).

2.2.6. Summary

In the free-stream region, all three RSMs behave similarly. Indeed, they all rely on the SSG model for the velocity pressure-gradient modeling, with an isotropic dissipation and the use of an ε-equation to transport the dissipation rate.

However, they differ in their near-wall modeling. Both the SSG/LRR-ω model and the SSG-ω ATAAC model switch to a ω-equation, but the ATAAC model uses a specific relation for the ω-to-ε conversion to ensure a correct behavior in the vicinity of the wall. While the SSG/LRR-ω model switches ϕ_{ij}^* models only out of reason of compatibility with the BSL ω-equation, the others ensure a correct asymptotic behavior for ε_{ij} and ϕ_{ij}^* by using a specific asymptotic near-wall model. Finally, all models have their own blending functions to activate their near-wall modeling. Table 2 sums up the near-wall differences.

These models have been implemented at Dassault Aviation in the in-house CFD code Aether (Stein et al., 2004). It is an unstructured continuous finite element solver for the compressible Navier-Stokes equations, stabilized using the Streamline Upwind Petrov-Galerkin (SUPG) method. Aether is written using the entropy formulation which offers many advantages, in particular symmetric operators with positivity properties and efficient preconditioning.

3. Zero-pressure-gradient boundary layer

The models are first assessed in the case of a flat plate, zero-pressure-gradient boundary layer to analyze the fundamental differences between the Reynolds-stress models implemented. The computations are run for $M = 0.2$, $Re = 5\,\mathrm{M}$ on a mesh provided by NASA[3]. A uniform velocity profile is imposed at the inlet, upstream of the leading edge.

The results are compared with empirical correlations, the DNS data of Schlatter et al. (2010) and the results given by the Spalart-Allmaras model used as a reference.

3.1. Integral quantities

The evolution of the integral quantities in the boundary layer is assessed using empirical laws. Using the von Kármán integral equation without pressure gradient, $\mathrm{d}\theta/\mathrm{d}x = C_f/2$, with an experimentally calibrated $1/7^{\text{th}}$-power-law velocity profile (Schlichting, 1979), the displacement and the momentum thicknesses are expressed as

$$\delta^* = \int_0^\infty \left(1 - \frac{U}{U_\infty}\right) \mathrm{d}y \approx \frac{0.048x}{Re_x^{1/5}}, \tag{25}$$

$$\theta = \int_0^\infty \frac{U}{U_\infty}\left(1 - \frac{U}{U_\infty}\right) \mathrm{d}y \approx \frac{0.037x}{Re_x^{1/5}}, \tag{26}$$

and are valid for $Re_x < 10^7$ for a boundary layer turbulent from the leading edge.

Fig. 1 shows the good agreement of the Reynolds-stress models with these empirical laws. In particular, the ω-based RSMs satisfactorily predicts δ^*, whereas the EB-RSM slightly overpredicts it towards the end of the domain. Regarding the momentum thickness, the RSMs seem to better predict θ compared to the Spalart-Allmaras model, which slightly underpredicts the integral thicknesses. Here, the SSG/LRR-ω model still underpredicts θ by about 2.5 %.

The local skin friction is shown in Fig. 2. The models are benchmarked against the Kármán-Schoenherr relation (Schoenherr, 1932)

$$C_f = \frac{1}{17.08\,(\log_{10} Re_\theta)^2 + 25.11 \log_{10} Re_\theta + 6.012}, \tag{27}$$

for $4{,}000 < Re_\theta < 13{,}000$ as suggested by NASA.

Both the EB-RSM and the SSG/LRR-ω model improve the predictions over the Spalart-Allmaras model on a large range of Reynolds numbers. In Fig. 2, they closely follow the empirical relation. The Spalart-Allmaras model recovers to the target

[3] https://turbmodels.larc.nasa.gov/flatplate_grids.html

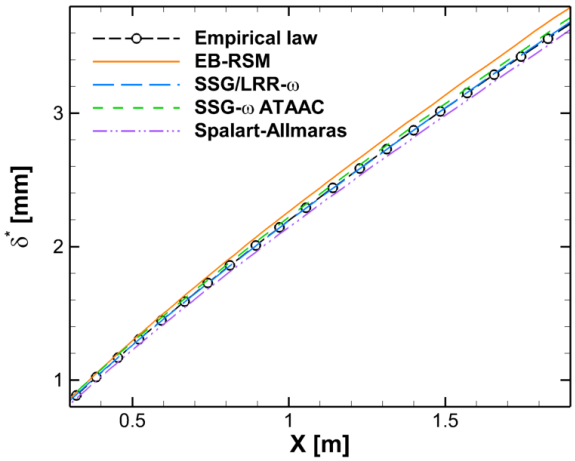

(a) Displacement thickness

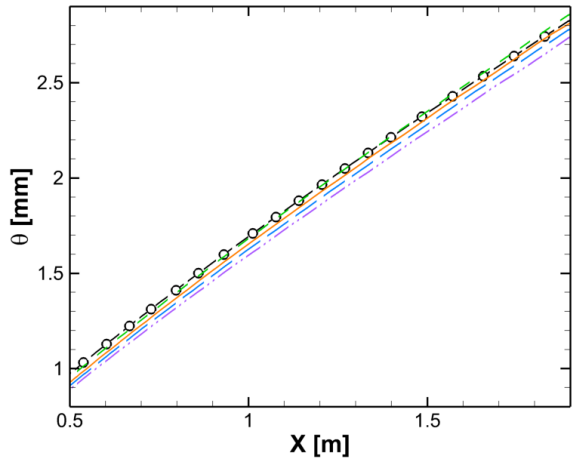

(b) Momentum thickness

Figure 1: Boundary layer thicknesses on the flat plate

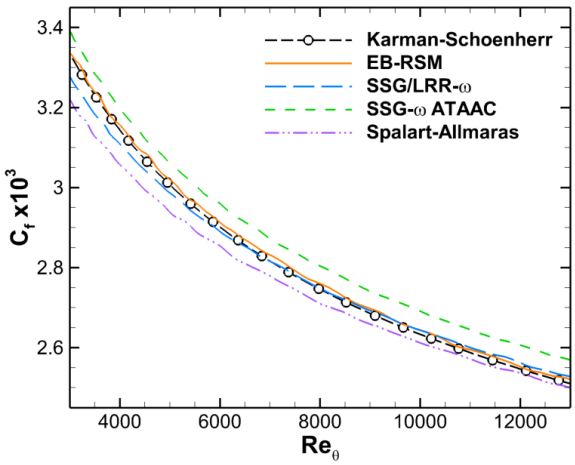

Figure 2: Skin friction coefficient on the flat plate

skin friction at the highest Re_θ, reducing the relative error from 2.8 % at Re_θ = 4,000 down to 0.4 % at Re_θ = 12,000. Despite a correct trend over the entire flat plate, the SSG-ω ATAAC model systematically overestimates the skin friction of about 2 %.

3.2. *Profiles at Re_θ = 4060*

The results are compared with the flat plate DNS of Schlatter et al. (2010). The profiles are extracted at the same Reynolds numbers Re_θ as in the DNS.

Fig. 3 shows the profiles in wall-units for Re_θ = 4,060, the highest Reynolds number available in the reference. As expected, the mean velocity profile is correctly predicted by all the models in Fig. 3(a). It can be noted though that the SSG-ω ATAAC model underestimates the velocity in the wake region, whereas the EB-RSM and the SSG/LRR-ω model tend to underestimate the buffer layer velocity. These observations are confirmed by the turbulent shear-stress, which directly affects the mean velocity. Fig. 3(b) indeed shows good overall predictions, but the SSG-ω ATAAC model returns to zero in the free-stream region more gradually than the DNS, and the other RSMs amplify the shear-stress in the vicinity of $y^+ \approx 10$ by 10 % with a slightly steeper gradient. The stronger shear-stress in these regions increases the mixing between the low-momentum fluid closer to the wall and the higher-momentum fluid further away, resulting in an underestimation of the mean velocity where $|R_{12}|$ is too large compared to the DNS.

Figs. 3(c)–(e) highlight the difference in the modeling approaches. Both the EB-RSM and the SSG-ω ATAAC model correctly reproduce the two-component turbulence at the wall by means of the near-wall model Eq. (21) of Manceau and Hanjalić (2002), with R_{11} and R_{33} decreasing in y^2 whereas R_{22} decreases in y^4. They also predict the peaks in the buffer layer for R_{11} and R_{33}. This can be related to the ε-equation in the EB-RSM and the improved ω-to-ε conversion Eq. (10) of the SSG-ω ATAAC model, whose effectiveness is evidenced here by the fact that it yields a non-zero constant dissipation rate in the viscous sublayer, as shown in Fig. 3(f).

This behavior is to be compared to the vanishing dissipation rate with the SSG/LRR-ω model and its exaggerated peak in the buffer layer. Indeed, without the corrected conversion, the SSG/LRR-ω model is unable to reproduce any peak for R_{11} and R_{33}. Moreover, due to the lack of near-wall modeling, the model fail to predict the two-component turbulence at the wall, with all the Reynolds stresses decreasing in y^3.

3.3. *Turbulence budgets*

The models can be further analyzed by looking at the budget of the Reynolds stresses. Figs. 4 & 5 compares the different source terms of the transport equations for R_{11} and R_{22}.

The vanishing of ε at the wall for the SSG/LRR-ω model shown in Fig. 3(f) results in the component ε_{11} of the dissipation tensor to tend to zero as well in Fig. 4(b). Since the dissipation term balances the viscous diffusion at the wall, the fact that it tends to zero with this model is at the origin of the cancellation of viscous diffusion D^ν_{11}. As a consequence, since its secondary derivative is zero, R_{11} behaves as y^3 in the vicinity of the wall as mentioned above.

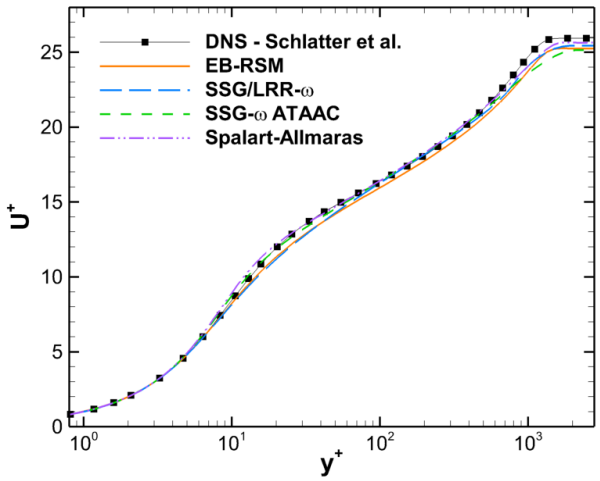

(a) Mean velocity

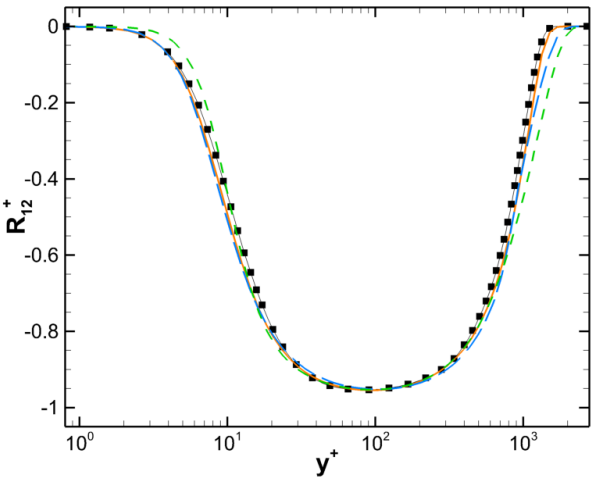

(b) Turbulent shear-stress

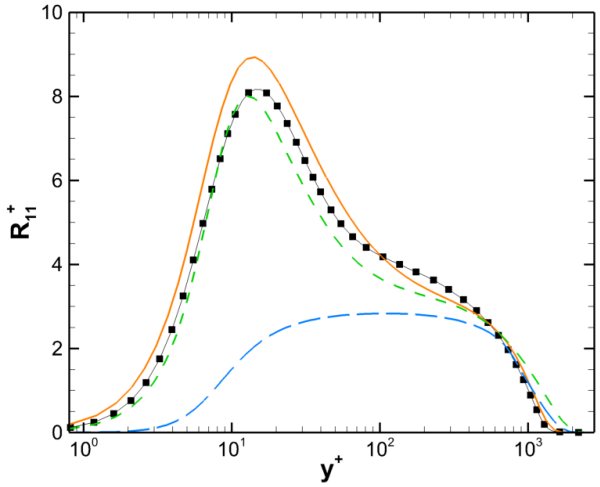

(c) Streamwise Reynolds stress

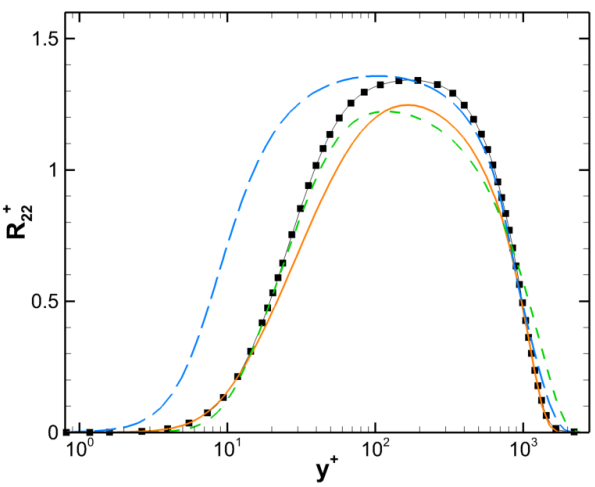

(d) Wall-normal Reynolds stress

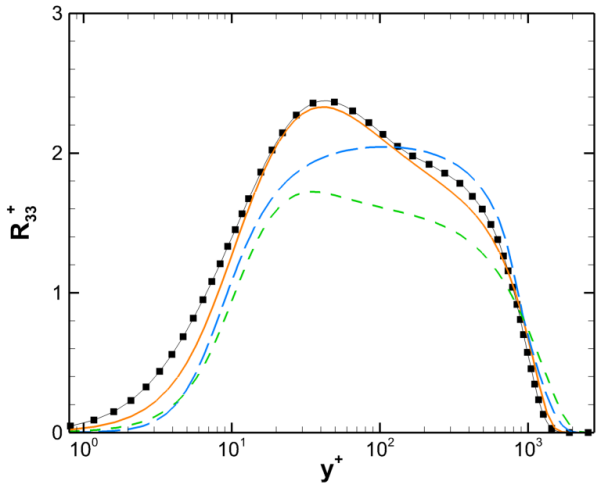

(e) Spanwise Reynolds stress

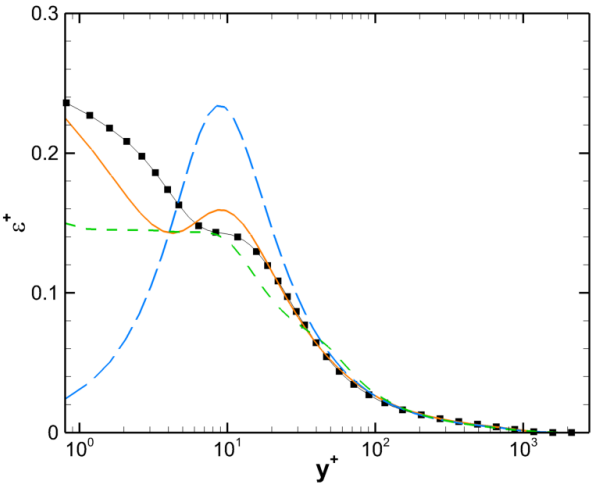

(f) Dissipation rate

Figure 3: Profiles on the flat plate at Re_θ = 4,060

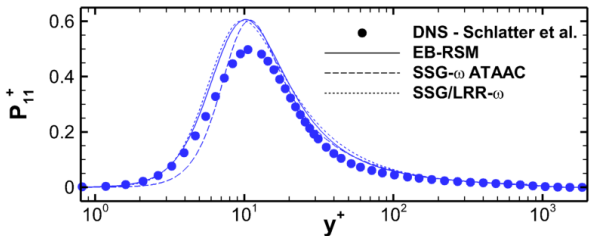

(a) Production of R_{11}

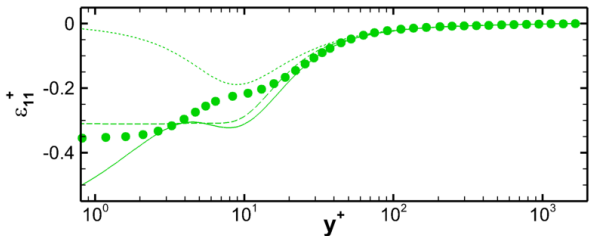

(b) Dissipation of R_{11}

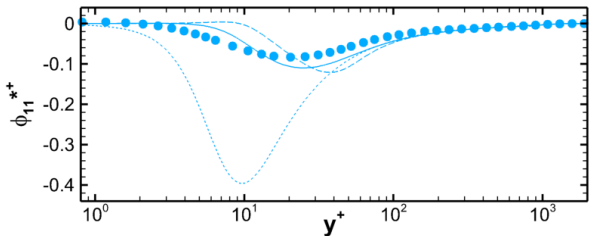

(c) Redistribution of R_{11}

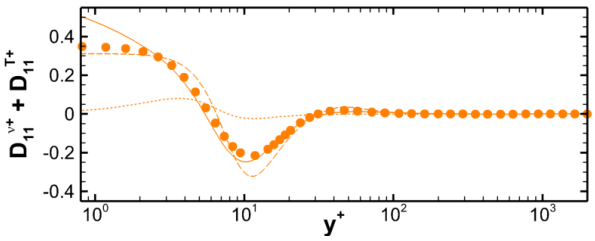

(d) Total diffusion of R_{11}

Figure 4: Reynolds-stress source terms of R_{11} on the flat plate at $Re_\theta = 4{,}060$

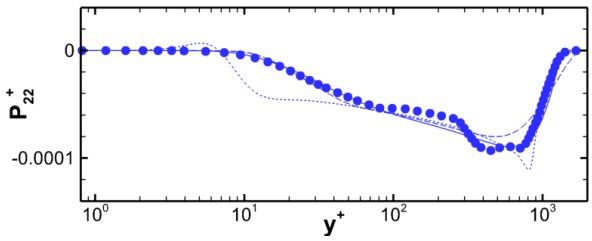

(a) Production of R_{22}

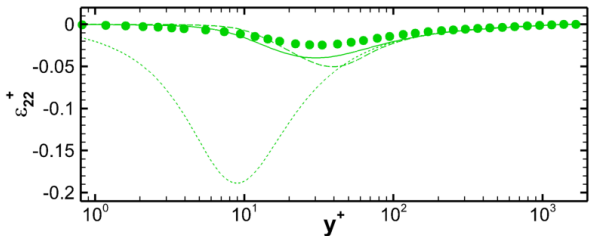

(b) Dissipation of R_{22}

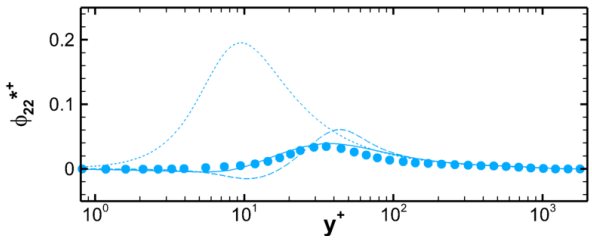

(c) Redistribution of R_{22}

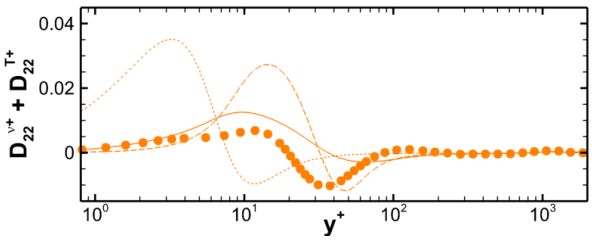

(d) Total diffusion of R_{22}

Figure 5: Reynolds-stress source terms of R_{22} on the flat plate at $Re_\theta = 4{,}060$

The near-wall modeling in the EB-RSM and the SSG-ω ATAAC model improves this behavior. In particular, the blending of the SSG model with the near-wall model Eq. (21) of Manceau and Hanjalić (2002) corrects the amplitude of their redistribution terms ϕ^*_{11} and ϕ^*_{22}. The near-wall modeling also damps the source terms for R_{22} in the viscous sublayer and in the buffer layer, so that the wall-normal stress correctly decreases as $\propto y^4$ at the wall.

Figs. 4(d) & 5(d) highlight the differences between the GGDH model used in the EB-RSM and the SGDH in the other RSMs. In particular, the SGDH overpredicts the peaks of turbulent transport in the buffer layer. Despite an improved amplitude, the GGDH does not correctly predict the negative diffusion of R_{22} for $y^+ \approx 30$.

To analyze the relative amplitude of the different terms as they vanish, Fig. 6 presents the budgets in a proportional way, as proposed by Billard (2012). The terms are decomposed into their positive and negative contributions, so that the transport equation can be written

$$\frac{\partial R_{ij}}{\partial t} = \sum_k T_k^+ + \sum_k T_k^-, \tag{28}$$

with $T_k^+ = \max(T_k, 0)$, $T_k^- = \min(T_k, 0)$.

The flow considered is stationary, thus $\partial_t R_{ij} = 0$ and the balance of the transport equation imposes $\sum_k T_k^+ = -\sum_k T_k^-$. The terms are then rescaled according to the budget amplitude $\sum_k T_k^+$ at each point of the boundary layer to indicate the proportion of each term at a given distance to the wall.

Using a DNS, this presentation enables to gain understanding of the physical phenomena at play. It also illustrates the ability of the Reynolds-stress models to reproduce these phenomena. Fig. 6 especially highlights the main regions of the boundary

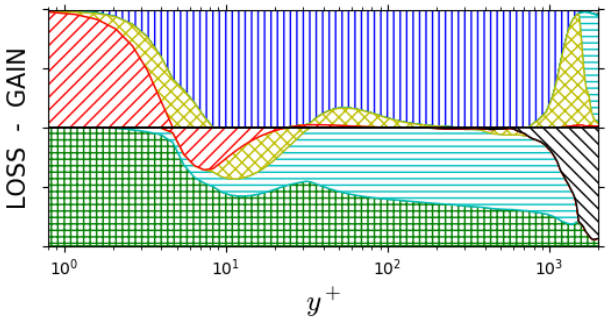

(a) Budget of R_{11}, DNS – Schlatter *et al.* (Schlatter et al., 2010)

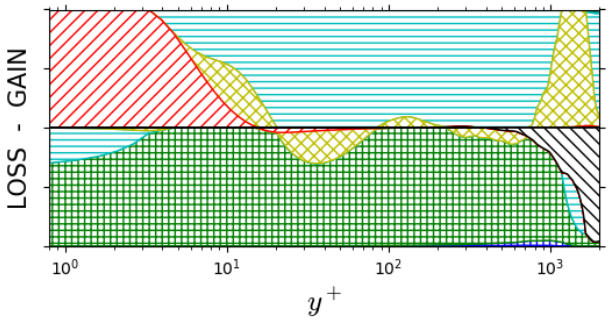

(b) Budget of R_{22}, DNS – Schlatter *et al.* (Schlatter et al., 2010)

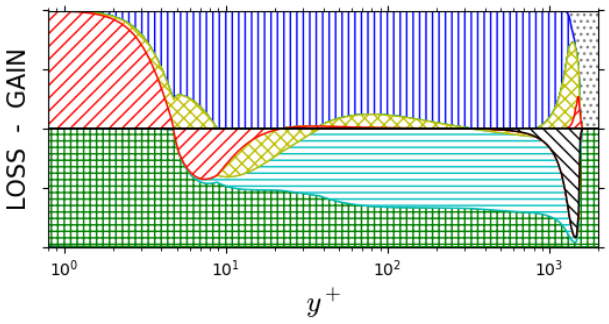

(c) Budget of R_{11}, EB-RSM

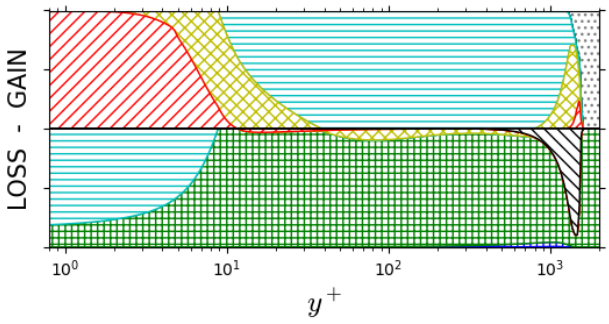

(d) Budget of R_{22}, EB-RSM

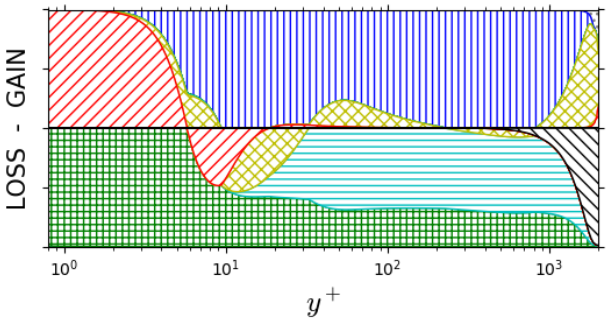

(e) Budget of R_{11}, SSG-ω ATAAC

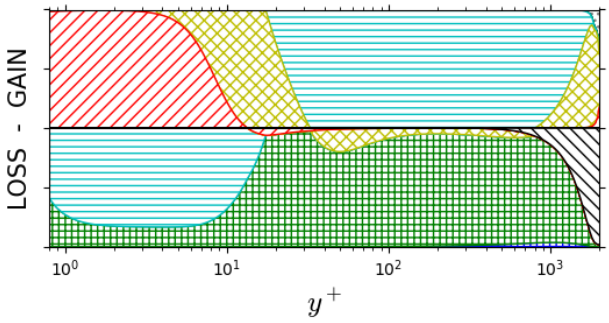

(f) Budget of R_{22}, SSG-ω ATAAC

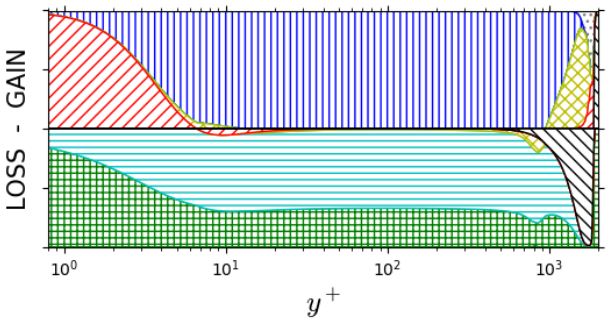

(g) Budget of R_{11}, SSG/LRR-ω

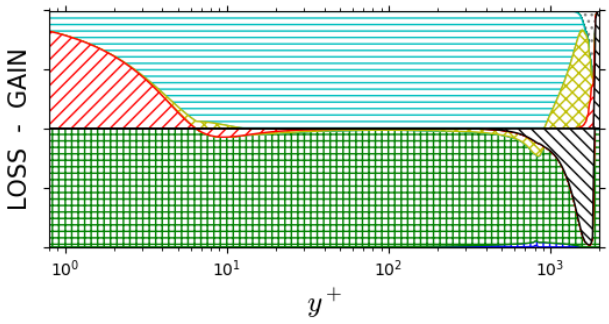

(h) Budget of R_{22}, SSG/LRR-ω

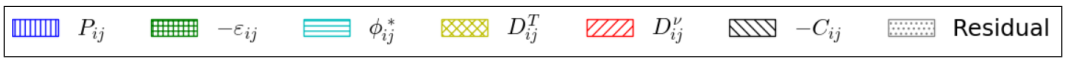

Figure 6: Proportional budgets on the flat plate at Re_θ = 4,060

layer.

The logarithmic layer corresponds to the range where the molecular diffusion D^{ν}_{ij} vanishes and the convection C_{ij} is not yet involved. For infinite Reynolds numbers, turbulent transport is also expected to vanish, which is not entirely the case in the considered DNS with $Re_\theta = 4{,}060$. One third of the production of R_{11} is dissipated, whereas the rest is redistributed to the other stresses. In particular, this redistribution feeds R_{22} and is almost entirely dissipated in the log layer. This behavior is well reproduced by all models. Similarly, the models correctly predict the balance between turbulent transport and convection in the outer region, as observed in the DNS, Figs. 6(a) & (b).

The main discrepancies appear as expected in the near-wall region. The viscous sublayer in the SSG/LRR-ω displays an erroneous redistribution: ϕ^*_{11} is taking energy from R_{11} at the wall to feed R_{22}, in the continuation of the log layer behavior for which the LRR model has been calibrated. Consequently, ϕ^*_{22} does not reproduces the wall-blockage effect, which leads to redistribute the energy of the wall-normal stress towards all others stresses.

This phenomenon is on the contrary visible for the EB-RSM (d) and the SSG-ω ATAAC model (f). The relative contributions of ϕ^*_{22} and ε_{22} is however different from the $^2/_5 - {}^3/_5$ distribution in the DNS. As explained in Manceau and Hanjalić (2002), the near-wall model aims at correctly predicting the difference $\phi^*_{22} - \varepsilon_{22}$ at the wall, which is involved in the budget, rather than each term individually, and compensates especially for the asymptotic shortcomings of Rotta's near-wall dissipation Eq. (20) (Rotta, 1951). For these two models, the spatial extent of the negative ϕ^*_{22} is larger than what is observed for the DNS (b). This region extended towards the buffer layer balances the turbulent transport D^T_{22} and is all the larger for the SSG-ω ATAAC model as the SGDH exaggerates the turbulent transport D^T_{22} in the buffer layer, as observed in Fig. 5(d).

This section highlighted the difference between Reynolds-stress models enforcing the correct near-wall stress behavior through an asymptotic approach, and the SSG/LRR-ω model, which does not. The near-wall modeling greatly improves the Reynolds-stress profiles, and especially helps the models to reproduce the physical features of turbulence at the wall, such as the two-component limit and the peaks in the buffer layer. However, the lack of this specific modeling does not prevent the SSG/LRR-ω RSM to yield satisfactory results regarding the mean flow, close to the other RSMs.

4. Application cases

4.1. Adverse-pressure-gradient boundary layer

The Skåre & Krogstad wind-tunnel experiment (Skåre and Krogstad, 1994) aimed at gathering data on an adverse-pressure-gradient (APG) turbulent boundary layer at equilibrium. The setup, shown in Fig. 7, consists in a diverging wind-tunnel with a 6 m long test section, which upper-wall profile $h(x)$ was adjusted to let the lower boundary layer reach an equilibrium state under APG, defined as a region where the velocity profiles are

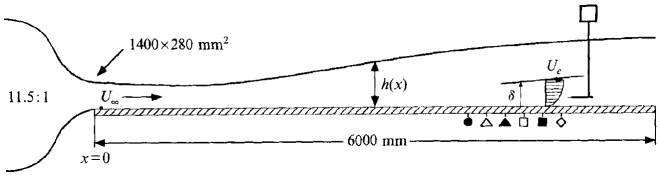

Figure 7: Skåre & Krogstad experiment configuration (reproduced from Skåre and Krogstad (1994))

self-similar. The streamwise evolution of the boundary layer becomes independent of the flow history, thus simplifying the study of the impact of the pressure-gradient on the flow. The equilibrium is characterized by a constant pressure-gradient parameter β_p introduced by Clauser (1954)

$$\beta_p = \frac{\delta^*}{\tau_w}\frac{\mathrm{d}P_w}{\mathrm{d}x}. \tag{29}$$

The equilibrium region is achieved for $4.0\,\mathrm{m} \leqslant x \leqslant 5.0\,\mathrm{m}$, with $Re_\theta \in [39{,}000\,;51{,}000]$ and $\beta_p = 20$. This experiment is a case relevant to the aeronautical industry as it is representative of the strong pressure gradients and high Reynolds numbers found at the trailing edge of wings, as shown for instance in Fig. 8 for NASA's Common Research Model.

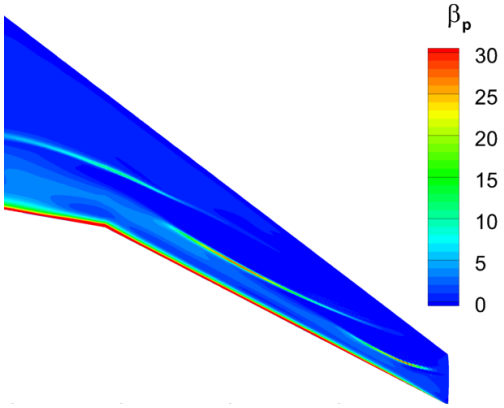

Figure 8: Predicted β_p on the wing of the CRM with the Spalart-Allmaras model ($Re_c = 30\,\mathrm{M}$, $C_L = 0.4$)

The numerical simulations have been carried out on the 3D geometry of the wind-tunnel, to account for the non-negligible three-dimensional effects, including a strong recirculation that develops in the upper corner and compresses the flow in the symmetry plan, as shown in Fig. 9 for the Spalart-Allmaras model. This ensures a correct prediction of the pressure coefficient distribution, hence a correct pressure-gradient. Moreover, the geometry is extended with a straight channel up to $x = 9.0\,\mathrm{m}$ with constant pressure outlet.

The Spalart-Allmaras model is here completed with the Quadratic Constitutive Relation (QCR) (Spalart, 2000), which adds anisotropy to the Boussinesq hypothesis to improve the behavior of the model, especially in corner flows. The SSG-ω ATAAC model severely overpredicts the recirculation in the upper corner and fails to converge. Its results on this case will therefore not be presented.

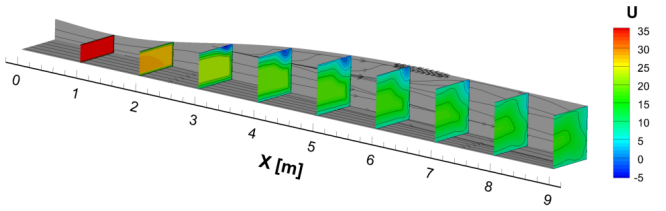

Figure 9: Flow topology for the Spalart-Allmaras QCR model. The lines indicate the skin friction direction.

4.1.1. *Integral quantities*

The boundary layer quantities are shown in Fig. 9. The experimental equilibrium region is clearly visible in Figs. 9(a)–(b), displaying a constant pressure-gradient parameter β_p within $x \in [4.0\,\mathrm{m}\,; 5.0\,\mathrm{m}]$.

On the other hand, none of the models achieve the equilibrium flow, according to Fig. 9(b). Instead of a plateau of β_p starting from $x = 4.0\,\mathrm{m}$, all three models decrease after reaching a peak between $x = 3.5\,\mathrm{m}$ and $x = 4.0\,\mathrm{m}$. The β_p-distribution upstream of the peak for the RSMs is consistent with the upstream experimental measurements.

Both RSMs yield good predictions of the skin friction at $x = 3.0\,\mathrm{m}$ but overpredict it downstream, resulting in a relative error to the experiment of 42 % and 67 % at $x = 5.0\,\mathrm{m}$ for the EB-RSM and the SSG/LRR-ω model respectively. The Spalart-Allmaras model here exhibits a better prediction of C_f in the equilibrium region, despite the exaggerated drop in the upstream region, for $x \leqslant 3.0\,\mathrm{m}$.

The discrepancy observed with the pressure-gradient parameter is explained by the deviation of the displacement thickness, which enters the definition (29) of the parameter. Fig. 9(c) shows indeed that for the RSMs, δ^*, and to a lesser extent θ, progressively deviate from the measurements around the predicted peak of β_p. The figure also highlights the correct growth of their boundary layers upstream, as they reach the experimental values for $x = 3.0\,\mathrm{m}$. In contrast, the Spalart-Allmaras model underpre-

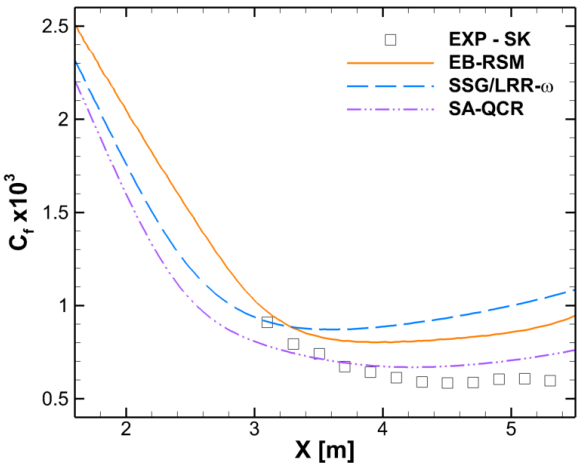

(a) Skin friction coefficient

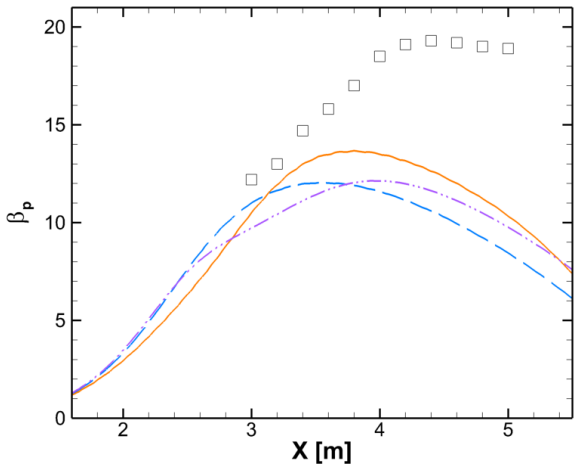

(b) Clauser's pressure-gradient parameter

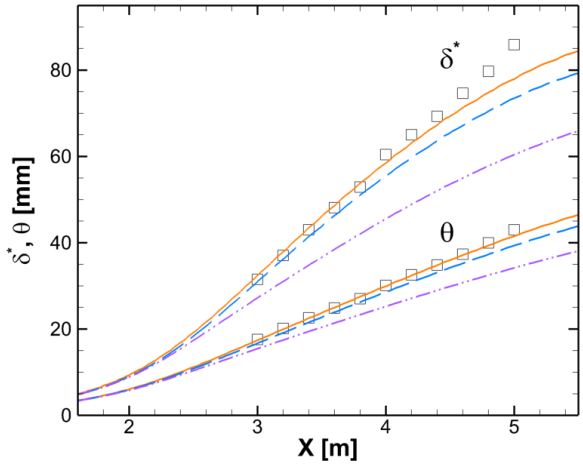

(c) Displacement and momentum thicknesses

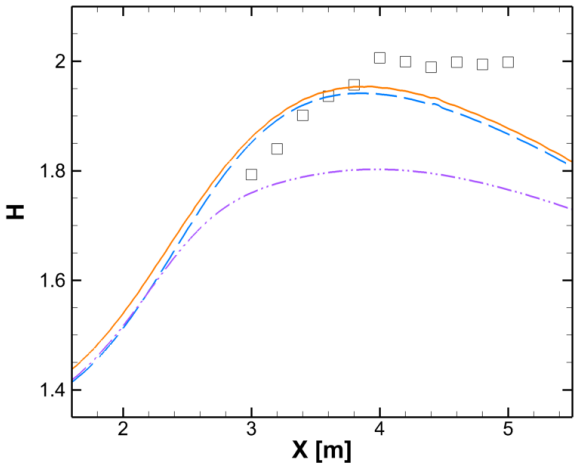

(d) Shape factor

Figure 9: Integral quantities in the instrumented region of the Skåre & Krogstad wind-tunnel

dicts both thicknesses downstream of $x = 3.0\,\mathrm{m}$, which explains the poor prediction of the pressure-gradient parameter despite a C_f prediction closer to the reference.

The underprediction of the boundary layer growth of the Spalart-Allmaras model also results in a less accurate shape factor $H = \delta^*/\theta$, plotted in Fig. 9(d). The RSMs improve the minimum relative error of H to the measurements in the equilibrium region from about 10 % for the Spalart-Allmaras model down to 2.5 %–5 %.

4.1.2. *Profiles*

Three profiles in the experimental equilibrium region are compared in Fig. 10, for $x \in \{4.2\,\mathrm{m}; 4.6\,\mathrm{m}; 5.0\,\mathrm{m}\}$. Fig. 10(a) shows the mean velocity profiles in wall-units, which indicate a better agreement of the Spalart-Allmaras model to the experiment. Indeed, the EB-RSM and the SSG/LRR-ω model both predict a thick and abnormally flat logarithmic layer, with an apparent von Kármán constant of $\kappa \approx 0.60$, to be compared to the experimental value of $\kappa = 0.38$. Conversely, the velocity profiles in Fig. 10(b), plotted in a linear scale, support the RSMs against the one-equation model. Keeping the dimension of the quantities here make it possible to combine the information of the outer boundary layer shape with the accuracy of the boundary layer thickness. Therefore, as expected from the previous section, the RSMs correctly predict the outer layer, especially the EB-RSM which offers a satisfactory behavior at the boundary layer edge. The decrease of H seen in Fig. 9(d) is explained here by an upward shift of the velocity profile in the inner region ($y < 0.05\,\mathrm{m}$). This reflects the inability of these models to correctly slow down the flow in the inner layer, and is related by the overprediction of the skin friction in Fig. 9(a).

4.2. *Common Research Model*

The Reynolds-stress models are applied to the Common Research Model (CRM), used in the AIAA Drag Prediction Workshop (Vassberg et al., 2008; Tinoco et al., 2018). It represents a generic commercial aircraft and its 'wing-body' configuration is here selected to keep the case simple and more representative of aircraft designed at Dassault Aviation, whose engines are located at the rear of the fuselage.

The case is run at $M = 0.85$ for $Re_c = 5\,\mathrm{M}$ and $Re_c = 30\,\mathrm{M}$. The turbulence models are compared to wind-tunnel measurements of the NTF (National Transonic Facility), which include wall corrections to account for the wind-tunnel walls in the test section. The geometries used account for the aeroelastic deformation at $C_L = 0.5$ for $Re_c = 5\,\mathrm{M}$ and at $C_L = 0.4$ for $Re_c = 30\,\mathrm{M}$, using deflection measurements of the ETW (European Transonic Wind-tunnel) facility (Keye and Gammon, 2016). The mesh convergence was confirmed with the Spalart-Allmaras QCR model, by comparison with the results from the workshop participants.

4.2.1. *Pressure coefficient*

To ensure a consistent comparison, the pressure coefficient distributions are presented at the lift coefficient corresponding to the deformed geometry. To that end, the angle of attack α is

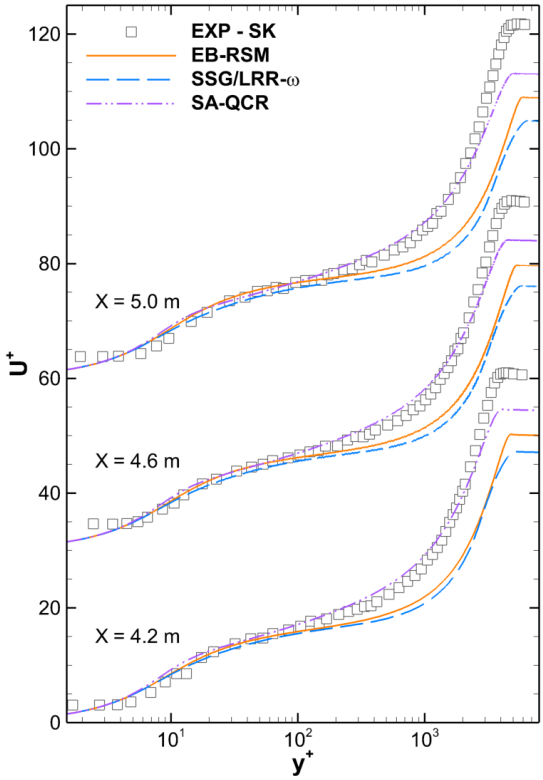

(a) Wall-units

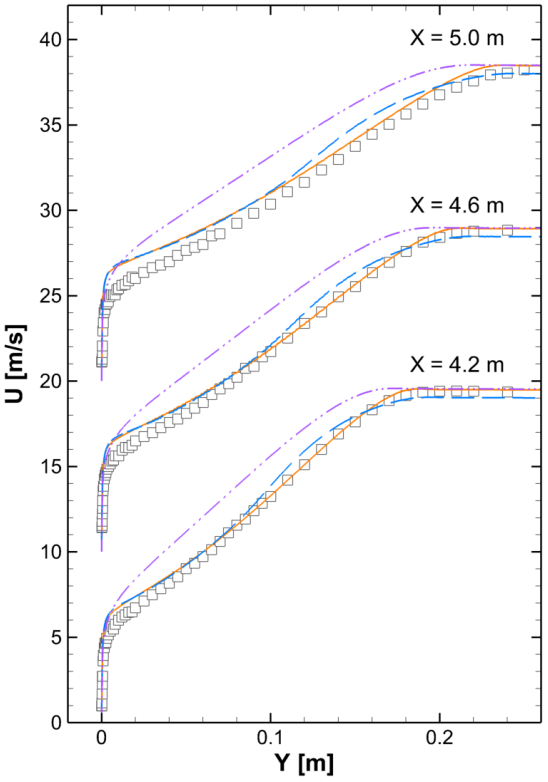

(b) Physical quantities

Figure 10: Mean velocity profiles in the equilibrium region for the Skåre & Krogstad wind-tunnel

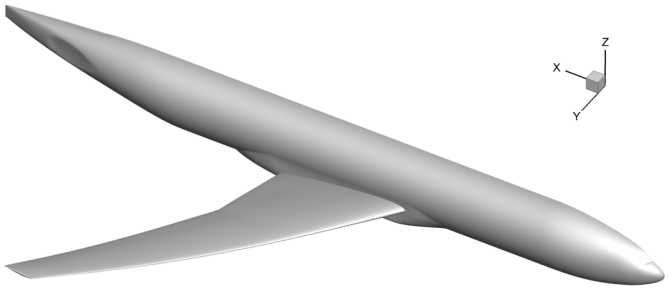

Figure 11: The CRM 'Wing-Body' configuration

iteratively adjusted by the solver to converge towards the target lift, after an initial convergence at constant α.

Fig. 12 shows the C_p-distribution for both Reynolds numbers at three different spanwise positions, respectively close to the fuselage ($\eta = 0.201$), at the middle of the wing ($\eta = 0.502$) and close to the wing tip ($\eta = 0.846$). The predictions of the RSMs are globally close to the Spalart-Allmaras model and to the reference. This can be expected from the fact that the results are here compared at matching lift coefficients. The corresponding angles of attack are gathered in Table 3 and display noticeable differences to the experiment. Note that since the wind-tunnel measurements include wall-corrections, it can be assumed that the experimental angles of attack are free from the influence of the wind-tunnel. The EB-RSM yields the closest α, yet with a relative error of 6 % for the low-*Re* case and 15 % for the high-*Re* one.

Table 3: Angles of attack yielding the target C_L

	$Re_c = 5\,\mathrm{M}$ $C_L = 0.5$	$Re_c = 30\,\mathrm{M}$ $C_L = 0.4$
EXP	2.75°	1.92°
EB-RSM	2.58°	1.64°
SSG-ω ATAAC RSM	2.53°	1.58°
SSG/LRR-ω RSM	2.52°	1.58°
SA-QCR	2.48°	1.55°

In the present comparison at given C_L, the models still tend to underestimate the aerodynamic load upstream of the shock wave and overestimate it downstream. This is especially visible for the three stations at $Re_c = 30\,\mathrm{M}$, in Figs. 12(b), (d) & (f).

The largest differences among models are located at the shock, the EB-RSM returning a shock position closest to the experiment for most of the considered stations, for both Reynolds numbers. The comparison with the experiments is however more difficult for some positions in the vicinity of the shock wave, due to the coarse resolution of the pressure probes, particularly at $\eta = 0.502$, where the supersonic flow upstream of the shock is barely measured.

A major contributor to the discrepancies between CFD and experiment is the depression occurring after the shock on the suction side, characterized by a 'rebound' on C_p, and largely overpredicted by models. This rebound grows from negligible at the body side into a second shock towards the wing tip. The rebound is amplified at high-*Re*, the depression becoming stronger than the leading edge depression at the wing tip in Fig. 12(f). It can be noted that the reduction of this overprediction for both cases follows the ranking of the models observed in Table 3, the EB-RSM yielding the smallest overprediction of the rebound and thus being the closest to the experiment.

The pressure coefficients of the APG flow at the trailing edge, on both sides of the wing, are better predicted with RSMs, the EB-RSM yielding once again the closest distribution to the reference. However, the differences between models are more restrained and are mainly located at the suction-side bump around $x/c = 0.9$.

The leading edge pressure level on the suction side is also slightly improved, as can be seen especially in Fig. 12(d). It is directly related to the shock wave position shift since the models yield the same lift coefficient. Indeed in that case, assuming the same load distribution in the spanwise direction for all the models, the area inside the C_p-distribution is expected to be the same. The improvement of the leading edge pressure level exhibits therefore the same model ranking as the shock wave shifting, the EB-RSM being distinguishable from the others.

4.2.2. *Drag polars*

To assess the benefits of Reynolds-stress models in aircraft design more generally, the lift and drag predictions have been investigated. Polars have been computed between $C_L = 0.2$ and the nominal lift coefficient of the cases presented above, to analyze the predicted variations of the aerodynamic load on the aircraft during flight. To correctly predict the performance of the designed aircraft geometry and its overall fuel consumption, lift and drag variations must therefore be accurately anticipated, using drag polars. In particular, these polars make it possible here to assess the accuracy of the response in drag to a given lift variation for the considered models.

To account for the aircraft aeroelasticity, computations have been run on a second geometry of the CRM provided by NASA, denoted 'shape 2' and corresponding to the aircraft model at $C_L^{\text{shape 2}} = 0$. The drag polars are computed at the same target lift coefficients as for the deformed geometry of ETW used in the previous sections, denoted here 'shape 1' with $C_L^{\text{shape 1}} = 0.4$, and consist thus in five polar points with $C_L \in [0.2\,;0.4]$. In the considered range of computation, the lift increases linearly with the angle of attack, so that the geometry is assumed to be deformed linearly as well. The progressive deflection of the aircraft model is therefore accounted for by simply interpolating drag and incidence between the results obtained with the two shapes for each lift coefficient C_L in the drag polar,

$$C_D^{\text{aeroelastic}} = f\, C_D|_{\text{shape 1}} + (1-f)\, C_D|_{\text{shape 2}}, \tag{30}$$

$$\alpha^{\text{aeroelastic}} = f\, \alpha|_{\text{shape 1}} + (1-f)\, \alpha|_{\text{shape 2}}, \tag{31}$$

$$\text{with } f = \left(C_L - C_L^{\text{shape 2}}\right) / \left(C_L^{\text{shape 1}} - C_L^{\text{shape 2}}\right).$$

Figs. 13 & 14 present the lift and drag coefficients as functions of the angle of attack for all four models and the NTF measurements, respectively for $Re_c = 5\,\mathrm{M}$ and $Re_c = 30\,\mathrm{M}$.

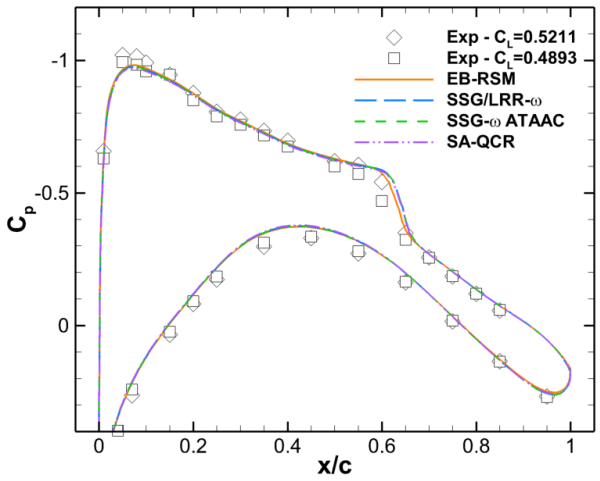

(a) $Re = 5\,\mathrm{M}$, $\eta = 0.201$

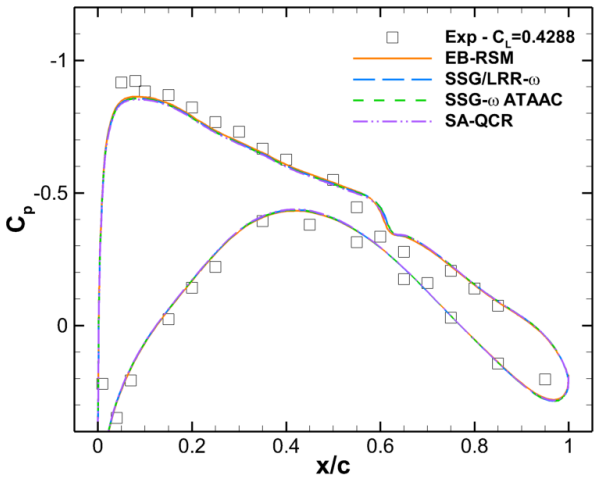

(b) $Re = 30\,\mathrm{M}$, $\eta = 0.201$

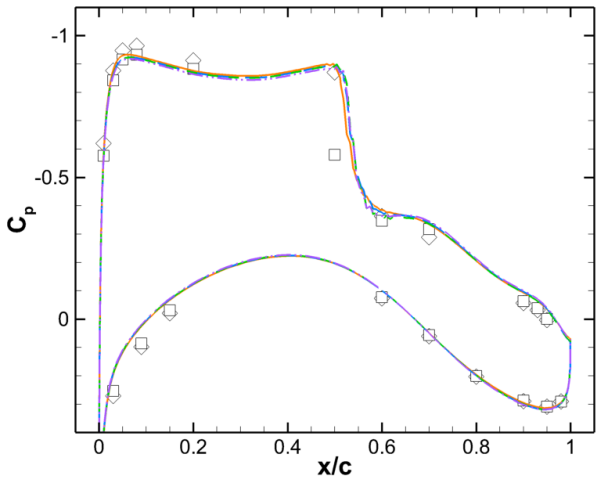

(c) $Re = 5\,\mathrm{M}$, $\eta = 0.502$

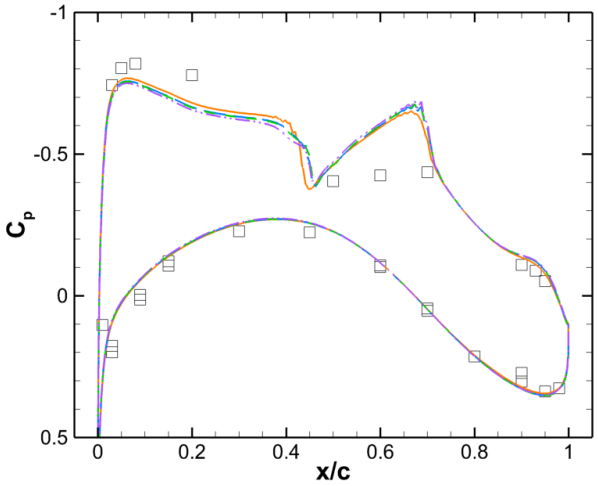

(d) $Re = 30\,\mathrm{M}$, $\eta = 0.502$

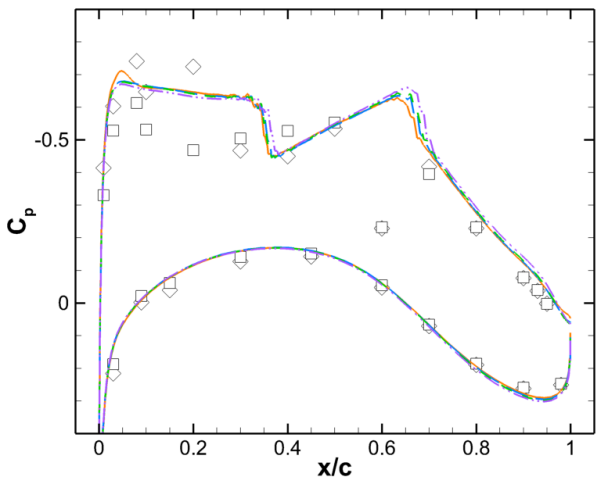

(e) $Re = 5\,\mathrm{M}$, $\eta = 0.846$

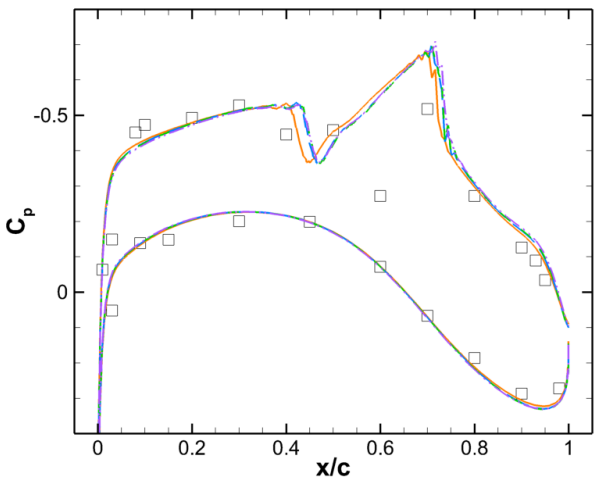

(f) $Re = 30\,\mathrm{M}$, $\eta = 0.846$

Figure 12: Pressure coefficients on the CRM

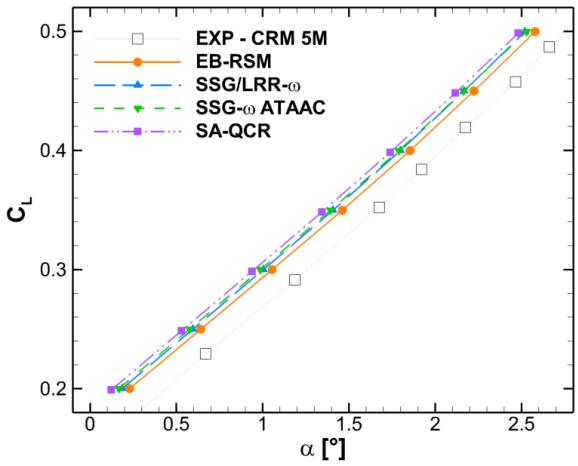

(a) Lift

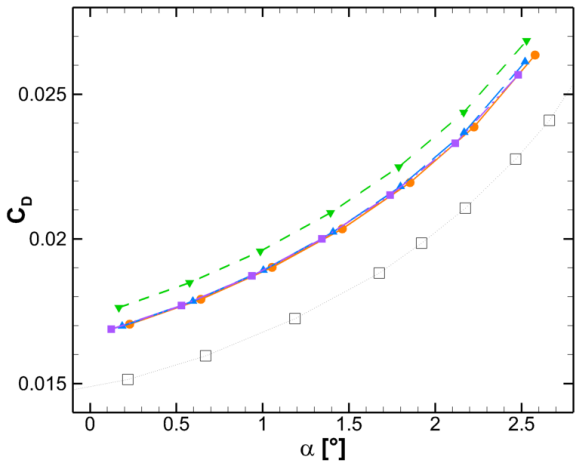

(b) Drag

Figure 13: Aerodynamic forces on the CRM at $Re_c = 5\,\mathrm{M}$

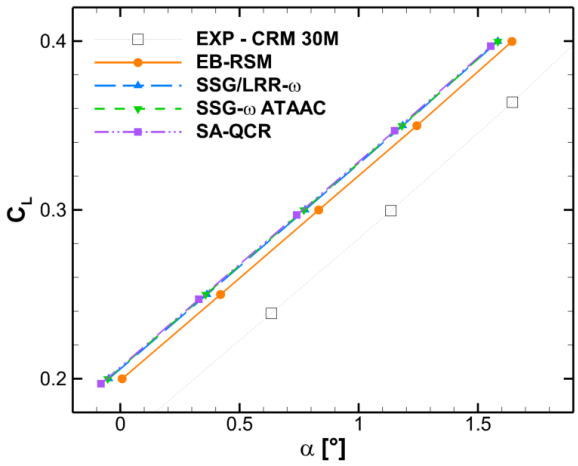

(a) Lift

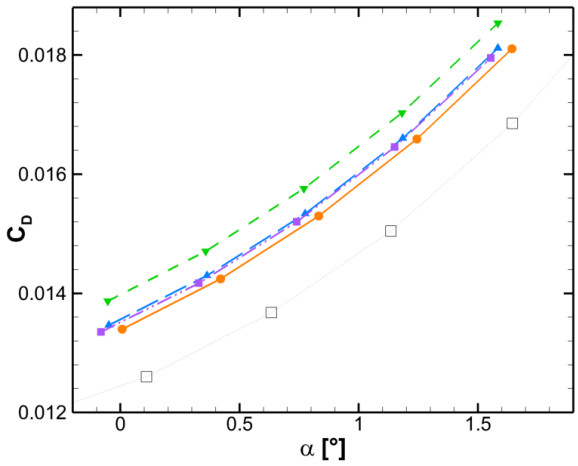

(b) Drag

Figure 14: Aerodynamic forces on the CRM at $Re_c = 30\,\mathrm{M}$

Figs. 13(a) & 14(a) illustrate the shift in the angles of attack indicated in Table 3, the deviation being amplified by the Reynolds number. Consequently, the lift is overpredicted by over 6 % at $\alpha = 2.5°$ in low-*Re* case and by over 10 % at $\alpha = 1.5°$ in the high-*Re*. As for the C_p-distribution, the EB-RSM is distinguishable from the other models for both cases and confirms its better predictions. The SSG/LRR-ω and the SSG-ω models also improve the predicted lift compared to the Spalart-Allmaras model at $Re_c = 5\,\mathrm{M}$.

As seen in Fig. 13(b), the models overestimate the drag by 12 % at $Re_c = 5\,\mathrm{M}$. The relative error is increased to 16 % for the SSG-ω ATAAC model, as expected from the flat plate benchmark. Indeed, its systematic overprediction of the skin friction observed in Sec. 3 leads to an extra friction drag. For the high-*Re* case, Fig. 14(b), the same conclusions can be drawn, with an average relative error of 9 % for the Spalart-Allmaras and the SSG/LRR-ω models, increased to 12 % for the SSG-ω ATAAC model. The EB-RSM here stands out from the others, as for the lift coefficient in Fig. 14(a), and improves the drag prediction with a relative error below 8 % to reference.

The drag polars plotted in Figs. 15(a) & 16(a) show the evolution of drag with lift

$$C_D = C_{D,0} + C_{D,L}\,(C_L) \tag{32}$$

where $C_{D,0}$ is the drag remaining in zero-lift conditions and $C_{D,L}$ the drag due to lift, which includes the induced drag and the lift-dependent parts of friction, form and wave drags. Drag polars make it possible to distinguish the zero-lift drag $C_{D,0}$, corresponding essentially to the constant parts of the friction and form drags that appears as a lateral shift in the figures, from $C_{D,L}$ regardless of the angle of attack.

All the models overpredict the drag, and mostly the friction drag according to the Skåre & Krogstad benchmark in previous section, where an overprediction of the skin friction coefficient was observed with all models. However, the increase of drag with lift is underpredicted, resulting in the total drag being less overpredicted for the highest values of C_L. It can be observed that the Spalart-Allmaras model better predicts the zero-lift drag compared to the Reynolds-stress models for the low-*Re* case. In particular, the shift of the SSG-ω ATAAC model polar indicates

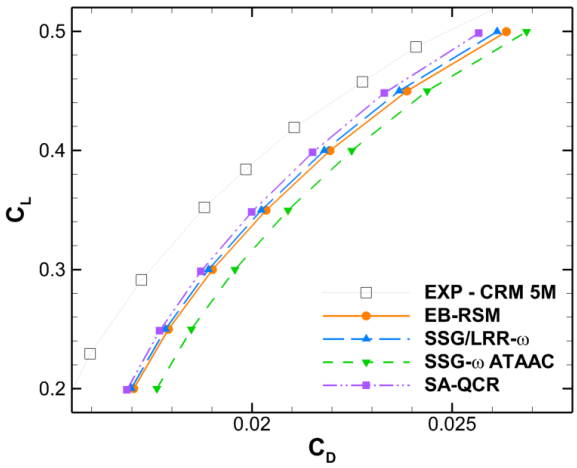

(a) $C_L = f(C_D)$

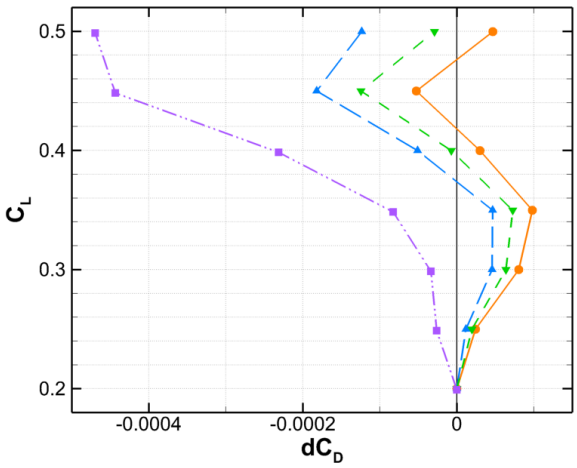

(b) Absolute error of the drag-due-to-lift

Figure 15: Drag polars on the CRM at $Re_c = 5\,\mathrm{M}$

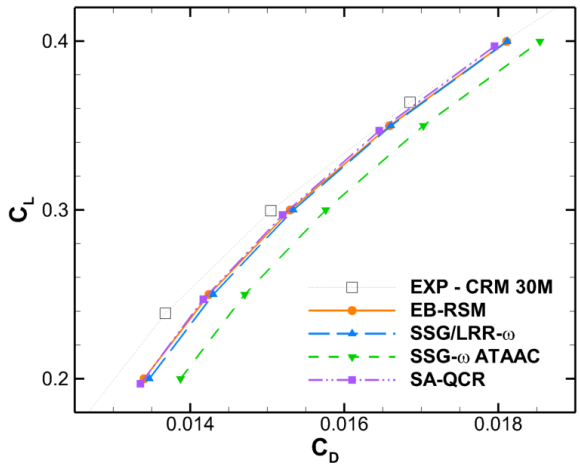

(a) $C_L = f(C_D)$

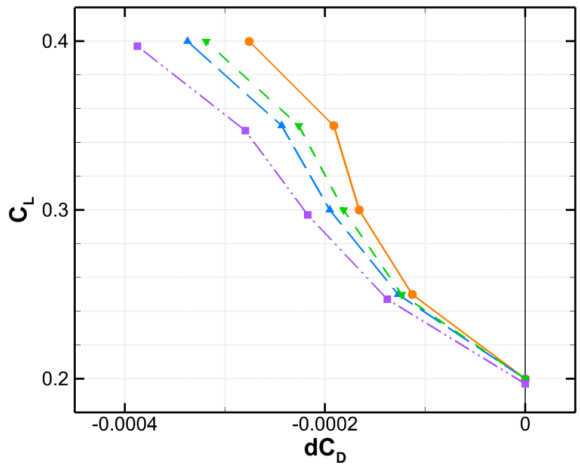

(b) Absolute error of the drag-due-to-lift

Figure 16: Drag polars on the CRM at $Re_c = 30\,\mathrm{M}$

that the extra friction observed in the flat plate benchmark mostly impacts $C_{D,0}$, hence the constant component of the friction drag. At $Re_c = 30\,\mathrm{M}$, the EB-RSM, the SSG/LRR-ω and the Spalart-Allmaras model almost coincide. For the EB-RSM, whereas $C_L(\alpha)$ and $C_D(\alpha)$ are improved, $C_D(C_L)$ is no better than for other models, reflecting a misprediction of the zero-lift drag.

In engineering applications, the drag polars are readjusted for a given polar point to compensate for the extra zero-lift drag due to wind-tunnel settings and aircraft excrescences, such as antenna and Pitot tubes. In the following, such readjusted drag polar is considered, with a reference point for the readjustment taken at $C_L = 0.2$. However, to focus on the error of drag due to lift, the absolute error of the readjusted drag polar to the experimental values is presented here rather than the readjusted drag polar itself. Hence, Figs. 15(b) & 16(b) show the polar of the drag error, defined as

$$\mathrm{d}C_D = C_D - C_D^{\mathrm{exp}} - \left(C_D|_{C_L=0.2} - C_D^{\mathrm{exp}}|_{C_L=0.2}\right). \tag{33}$$

These figures highlight the better $C_{D,L}$ prediction from the RSMs over the Spalart-Allmaras model, with an error that remains below one drag count ΔC_D[4] for the EB-RSM, and below $2\Delta C_D$ for the the ω-based RSMs. In particular in Fig. 15(b), the Spalart-Allmaras error at $C_L = 0.45$ for the low-Re case is reduced by 60 % with the SSG/LRR-ω model, by almost 75 % with the SSG-ω ATAAC model and 90 % with the EB-RSM. The same conclusions apply to the high-Re case shown in Fig. 16(b), with however a reduced improvement, the EB-RSM still reducing the error by 30 %.

4.2.3. Conclusions

Both the pressure-coefficient distributions and the drag polars demonstrated the improved accuracy of the Reynolds-stress models on an industrial aeronautical application compared to today's reference model in the industry, the Spalart-Allmaras model.

Despite the ω-equation being supposed to improve mild APG flow predictions, the computations on the CRM show here

[4] a drag count is defined as $\Delta C_D = 10^{-4}$

that the best results are achieved with the EB-RSM, relying on the ε-equation. This might be directly related to its near-wall modeling, as the results point out that both RSMs using such an approach, the EB-RSM and the SSG-ω ATAAC model, exhibit improved predictions compared to the SSG/LRR-ω model. The SSG-ω ATAAC model is however penalized by the overprediction of the skin friction, observed on the flat plate.

5. Conclusions

This study aimed at assessing the relevance of second-moment closures of the RANS equation to aeronautical applications. Three Reynolds-stress models that differ in their near-wall modeling and in their length-scale providing equation, namely the EB-RSM, the SSG/LRR-ω RSM and the SSG-ω ATAAC RSM, were assessed on two academic test cases, a flat plate case and the Skåre & Krogstad case (Skåre and Krogstad, 1994) providing an APG flow at equilibrium, and one application case, the CRM aircraft case, against the Spalart-Allmaras model and empirical, DNS and experimental data.

The academic cases highlighted the fundamental differences between the models, regarding integral quantities and profiles in the boundary layer. In particular, the turbulence budgets in the flat plate test case demonstrated the effectiveness of near-wall modeling. The near-wall modeling also proved to be beneficial for high-Reynolds-number aeronautical cases, improving further the superior predictions of RSMs over the Spalart-Allmaras model on the CRM aircraft, especially regarding the prediction of drag due to lift. In this application case, the RSMs also improved the predictions of pressure coefficients and the lift and drag polars with respect to the angle of attack. This should strengthen the attractiveness of these models in the aeronautical industry.

However, the Skåre & Krogstad test case showed that despite a satisfactory prediction of the boundary layer growth, the RSMs still need improvements regarding the skin friction prediction in strong APG flows. Further assessments of Reynolds-stress models could also be carried out on different aeronautical cases, such as high-lift configurations and intake flow distortion predictions, where more complex flow phenomena can be expected, such as boundary layer-wake interactions and rotational flows.

Appendix A. SSG-ω RSM 'ATAAC'

Appendix A.1. Equations

Model equations:

$$\overline{\rho}\frac{\mathrm{D}R_{ij}}{\mathrm{D}t} = \overline{\rho}P_{ij} + \overline{\rho}D^{\nu}_{ij} + \overline{\rho}D^{T}_{ij} + \overline{\rho}\phi^{*}_{ij} - \overline{\rho}\varepsilon_{ij}, \tag{A.1}$$

$$\begin{aligned}\overline{\rho}\frac{\mathrm{D}\omega}{\mathrm{D}t} &= \gamma\overline{\rho}\frac{\omega}{k}P_k - \beta\overline{\rho}\omega^2 + \frac{\partial}{\partial x_j}\left(\overline{\mu}\frac{\partial\omega}{\partial x_j}\right)\\ &\quad + \frac{\partial}{\partial x_l}\left(\sigma_\omega\frac{\overline{\rho}k}{\omega}\frac{\partial\omega}{\partial x_l}\right) + 2\left(1-F_1\right)\frac{\sigma^{(\varepsilon)}_\omega}{\omega}\frac{\partial k}{\partial x_j}\frac{\partial\omega}{\partial x_j},\end{aligned} \tag{A.2}$$

Turbulent transport:

$$D^{T}_{ij} = \frac{\partial}{\partial x_l}\left(\frac{2}{3}\frac{C_s}{\beta^*}\nu_t\frac{\partial R_{ij}}{\partial x_l}\right), \tag{A.3}$$

$$\nu_t = f_w \min\left[\frac{k}{\omega}\,;k_0^{+3/2}\kappa\sqrt{k}y\right], \tag{A.4}$$

Velocity pressure-gradient correlation:

$$\phi^{*}_{ij} = f_b\,\phi^{SSG}_{ij} + \left(1-f_b\right)\,\phi^{w}_{ij}, \tag{A.5}$$

$$\begin{aligned}\phi^{SSG}_{ij} &= -\left(C_1\varepsilon + C^{*}_1P_k\right)b_{ij}\\ &\quad + C_2\varepsilon\left(b_{il}b_{jl} - \frac{1}{3}b_{mn}b_{mn}\delta_{ij}\right)\\ &\quad + \left(C_3 - C^{*}_3\sqrt{b_{mn}b_{mn}}\right)kS^{*}_{ij}\\ &\quad + C_4k\left(b_{il}S_{jl} + b_{jl}S_{il} - \frac{2}{3}b_{mn}S_{mn}\delta_{ij}\right)\\ &\quad + C_5k\left(b_{il}\Omega_{jl} + b_{jl}\Omega_{il}\right),\end{aligned} \tag{A.6}$$

$$\phi^{w}_{ij} = -5\frac{\varepsilon}{k}\left(R_{ik}n_jn_k + R_{jk}n_in_k - \frac{1}{2}R_{kl}n_kn_l\left(n_in_j + \delta_{ij}\right)\right), \tag{A.7}$$

$$b_{ij} = \frac{R_{ij}}{2k} - \frac{1}{3}\delta_{ij}, \qquad S_{ij} = \frac{1}{2}\left(\frac{\partial\widetilde{U}_i}{\partial x_j} + \frac{\partial\widetilde{U}_j}{\partial x_i}\right), \tag{A.8}$$

$$S^{*}_{ij} = S_{ij} - \frac{1}{3}S_{kk}\delta_{ij}, \qquad \Omega_{ij} = \frac{1}{2}\left(\frac{\partial\widetilde{U}_i}{\partial x_j} - \frac{\partial\widetilde{U}_j}{\partial x_i}\right), \tag{A.9}$$

Dissipation rate:

$$\varepsilon_{ij} = f_b\,\frac{2}{3}\varepsilon\delta_{ij} + \left(1-f_b\right)\,\frac{R_{ij}}{k}\varepsilon, \tag{A.10}$$

$$\varepsilon = f_\varepsilon \max\left(\beta^*k\omega\,;\left(\frac{k}{k_0^{+}}\right)^{3/2}\frac{1}{\kappa_0 y}\right), \tag{A.11}$$

Blending functions:

$$f_b = 1 - \exp\left(-\left[\frac{1}{225}\left(\frac{\omega y^2}{\nu} - \frac{6}{\beta^{(\omega)}}\right)\right]^2\right), \tag{A.12}$$

$$f_w = 1 - \exp\left(-\left[\frac{\omega y^2}{250\nu}\right]^{2.5}\right), \tag{A.13}$$

$$f_\varepsilon = \frac{5}{18} + \frac{13}{18}\tanh\left(\left[\frac{y}{42}\left(\frac{\omega k}{\nu^3}\right)^{1/4}\right]^3\right), \tag{A.14}$$

$$F_1 = \tanh\left(\arg_1^4\right), \tag{A.15}$$

$$\arg_1 = \min\left[\max\left(\frac{\sqrt{k}}{\beta^*\omega y}; \frac{500\overline{\mu}}{\overline{\rho}\omega y^2}\right); \frac{4\sigma_\omega^{(\varepsilon)} k}{\mathrm{CD}_{k\omega} y^2}\right], \tag{A.16}$$

$$\mathrm{CD}_{k\omega} = \max\left(\frac{2\sigma_\omega^{(\varepsilon)}}{\omega}\frac{\partial k}{\partial x_j}\frac{\partial \omega}{\partial x_j}; 10^{-20}\right). \tag{A.17}$$

Appendix A.2. Coefficients

The coefficients in the BSL ω-equation are blended according to $c = F_1\, c^{(\omega)} + (1 - F_1)\, c^{(\varepsilon)}$

$\gamma^{(\omega)} = 5/9$; $\beta^{(\omega)} = 0.075$; $\sigma_\omega^{(\omega)} = 0.605$;
$\gamma^{(\varepsilon)} = 0.664$; $\beta^{(\varepsilon)} = 0.0828$; $\sigma_\omega^{(\varepsilon)} = 0.65$; $\beta^* = 0.09$

$C_s = 0.22$; $k_0^+ = 3.118556$; $\kappa = 0.41$
$C_1 = 3.4$; $C_1^* = 1.8$; $C_2 = 4.2$; $C_3 = 0.8$;
$C_3^* = 1.30$; $C_4 = 1.25$; $C_5 = 0.40$

References

Aupoix, B., 2012. Improving the coupling of the Speziale, Sarkar and Gatski differential Reynolds stress model with an ω scale equation. Technical Report 13929. ONERA. Unpublished.

Billard, F., 2012. Development of a robust elliptic-blending turbulence model for near-wall, separated and buoyant flows. Ph.D. thesis. University of Manchester.

Catris, S., Aupoix, B., 2000. Towards a calibration of the length-scale equation. Int. J. Heat Fluid Fl. 21, 606–613.

Cécora, R.D., Eisfeld, B., Probst, A., Crippa, S., Radespiel, R., 2012. Differential Reynolds stress modeling for aeronautics, in: 50th AIAA Aerospace Sciences Meeting including the New Horizons forum and aerospace exposition, p. 465.

Clauser, F.H., 1954. Turbulent boundary layers in adverse pressure gradients. J. Aeronaut. Sci. 21, 91–108.

Durbin, P.A., 1991. Near-Wall Turbulence Closure Modeling Without "Damping Functions". Theor. Comput. Fluid Dyn. 3, 1–13.

Eisfeld, B., Rumsey, C.L., Togiti, V., 2016. Verification and validation of a second-moment-closure model. AIAA J. 54, 1524–1541.

Huang, P.G., Bradshaw, P., 1995. Law of the wall for turbulent flows in pressure gradients. AIAA J. 33, 624–632.

Keye, S., Gammon, M., 2016. Development of Deformed CAD Geometries of NASA's Common Research Model for the Sixth AIAA CFD Drag Prediction Workshop, in: 34th AIAA Applied Aerodynamics Conference, p. 3431.

Launder, B.E., Reece, G.J., Rodi, W., 1975. Progress in the development of a Reynolds-stress turbulence closure. J. Fluid Mech. 68, 537–566.

Manceau, R., 2015. Recent progress in the development of the Elliptic Blending Reynolds-stress model. Int. J. Heat Fluid Fl. 51, 195–220. doi:10.1016/j.ijheatfluidflow.2014.09.002.

Manceau, R., Hanjalić, K., 2002. Elliptic Blending Model: A New Near-Wall Reynolds-Stress Turbulence Closure. Phys. Fluids 14, 744–754. doi:10.1063/1.1432693.

Menter, F.R., 1994. Two-equation eddy-viscosity turbulence models for engineering applications. AIAA J. 32, 1598–1605.

Morkovin, M.V., 1962. Effects of compressibility on turbulent flows. Mécanique de la Turbulence 367, 380.

Rotta, J.C., 1951. Statistische Theorie nichthomogener Turbulenz. Z. Phys. 129, 547–572.

Schlatter, P., Li, Q., Brethouwer, G., Johansson, A.V., Henningson, D.S., 2010. Simulations of spatially evolving turbulent boundary layers up to $Re_\theta = 4{,}300$. Int. J. Heat Fluid Fl. 31, 251–261.

Schlichting, H., 1979. Boundary-Layer Theory. 7th edition ed., McGraw-Hill.

Schoenherr, K.E., 1932. Resistance of flat surfaces moving through a fluid. Soc. Nav. Arch. and Marine Eng. Trans. 40, 279–313.

Schwamborn, D., Strelets, M., 2012. ATAAC – an EU-project dedicated to hybrid RANS/LES methods, in: Progress in Hybrid RANS-LES Modelling. Springer, pp. 59–75.

Skåre, P.E., Krogstad, P.Å., 1994. A turbulent equilibrium boundary layer near separation. J. Fluid Mech. 272, 319–348.

Spalart, P.R., 2000. Strategies for turbulence modelling and simulations. Int. J. Heat Fluid Fl. 21, 252–263.

Speziale, C.G., Sarkar, S., Gatski, T.B., 1991. Modeling the pressure-strain correlation of turbulence: an invariant dynamical system approach. J. Fluid Mech. 227, 245–272.

Stein, E., de Borst, R., Hughes, T.J.R. (Eds.), 2004. Encyclopedia of Computational Mechanics. volume 3: Fluids. John Wiley & Sons, Ltd. Chap. 12, sec. 4.

Tinoco, E.N., Brodersen, O.P., Keye, S., Laflin, K.R., Feltrop, E., Vassberg, J.C., Mani, M., Rider, B., Wahls, R.A., Morrison, J.H., Hue, D., Roy, C.J., Mavriplis, D.J., Murayama, M., 2018. Summary Data from the Sixth AIAA CFD Drag Prediction Workshop: CRM Cases. J. Aircraft 55, 1352–1379. doi:10.2514/1.C034409.

Vassberg, J., Dehaan, M., Rivers, M., Wahls, R., 2008. Development of a common research model for applied CFD validation studies, in: 26th AIAA applied aerodynamics conference, p. 6919.

Wilcox, D.C., 2006. Turbulence Modeling for CFD. Third ed., DCW industries, Inc., La Cañada, California.

Bibliography

[1] K. S. Abdol-Hamid. Assessments of $k - kl$ turbulence model based on Menter's modification to Rotta's two-equation model. *Int. J. Aerosp. Eng.*, 2013.

[2] B. Aupoix. A general strategy to extend turbulence models to rough surfaces: application to Smith's $k - l$ model. *J. Fluid Eng.-T. ASME*, 129:1245–1254, 2007.

[3] B. Aupoix. Improving the coupling of the Speziale, Sarkar and Gatski differential Reynolds stress model with an ω scale equation. Technical Report 13929, ONERA, 2012. Unpublished.

[4] B. Aupoix, H. Bézard, S. Catris, and T. Daris. Towards a calibration of the length-scale equation. *Fluid Dynamics and Aeronautics New Challenges, CIMNE*, pages 327–349, 2003.

[5] G. I. Barenblatt. Scaling laws for fully developed turbulent shear flows. Part 1. Basic hypotheses and analysis. *J. Fluid Mech.*, 248:513—520, 1993.

[6] F. Billard. *Development of a robust elliptic-blending turbulence model for near-wall, separated and buoyant flows.* PhD thesis, University of Manchester, 2012.

[7] F. Billard and D. Laurence. A robust $k - \varepsilon - \overline{v^2}/k$ elliptic blending turbulence model applied to near-wall, separated and buoyant flows. *Int. J. Heat Fluid Fl.*, 33(1):45–58, 2012.

[8] A. Bobke, R. Vinuesa, R. Örlü, and P. Schlatter. History effects and near equilibrium in adverse-pressure-gradient turbulent boundary layers. *J. Fluid Mech.*, 820:667–692, 2017.

[9] P. Bradshaw. The turbulence structure of equilibrium boundary layers. *J. Fluid Mech.*, 29(4):625–645, 1967.

[10] P. Bradshaw, D. H. Ferriss, and N. P. Atwell. Calculation of boundary-layer development using the turbulent energy equation. *J. Fluid Mech.*, 28(3):593–616, 1967.

[11] J. Bredberg. On two-equation eddy-viscosity models. Technical report, Department of Thermo and Fluid Dynamics, Chalmers University of Technology, Göteborg,Sweden, 2001.

[12] K. C. Brown and P. N. Joubert. The measurement of skin friction in turbulent boundary layers with adverse pressure gradients. *J. Fluid Mech.*, 35(4):737–757, 1969.

[13] M. H. Buschmann and M. Gad-el-Hak. Generalized logarithmic law and its consequences. *AIAA J.*, 41(1):40–48, 2003.

[14] L. Castillo and W. K. George. Similarity analysis for turbulent boundary layer with pressure gradient: outer flow. *AIAA J.*, 39(1):41–47, 2001.

[15] S. Catris. *Étude de contraintes et qualification de modèles à viscosité turbulente.* PhD thesis, ENSAE, Toulouse, 1999.

[16] S. Catris and B. Aupoix. Towards a calibration of the length-scale equation. *Int. J. Heat Fluid Fl.*, 21(5):606–613, 2000.

[17] R.-D. Cécora, R. Radespiel, B. Eisfeld, and A. Probst. Differential Reynolds-stress modeling for aeronautics. *AIAA Journal*, 53(3):739–755, 2015.

[18] F. Chalot. Industrial aerodynamics. In E. Stein, R. de Borst, and T. J. R. Hughes, editors, *Encyclopedia of Computational Mechanics*, volume 3: Fluids, chapter 12. John Wiley & Sons, Ltd., 2004.

[19] F. Chalot, M. Mallet, and G. Rogé. Review of recent developments and future challenges for the simulation-based design of aircraft. In *27th Int. Congress of the Aeronautic Sciences (ICAS 2010), Nice, France*, pages 599–608, 2010.

[20] K.-Y. Chien. Predictions of Channel and Boundary-Layer Flows with a Low-Reynolds-Number Turbulence Model. *AIAA J.*, 20(1):33–38, 1982.

[21] F. H. Clauser. Turbulent boundary layers in adverse pressure gradients. *J. Aeronaut. Sci.*, 21(2):91–108, 1954.

[22] F. H. Clauser. The turbulent boundary layer. *Adv. Appl. MEch.*, 4:1–51, 1956.

[23] G. N. Coleman, C. L. Rumsey, and P. R. Spalart. Numerical study of turbulent separation bubbles with varying pressure gradient and Reynolds number. *J. Fluid Mech.*, 847:28, 2018.

[24] B. J. Daly and F. H. Harlow. Transport equations in turbulence. *Phys. Fluids*, 13(11):2634–2649, 1970.

[25] T. Daris. *Étude des modèles de turbulence à quatre équations de transport pour la prévision des écoulements turbulents faiblement chauffés.* PhD thesis, ENSAE, Toulouse, 2002.

[26] S. Deck, P.-É. Weiss, M. Pamies, and E. Garnier. Zonal detached eddy simulation of a spatially developing flat plate turbulent boundary layer. *Comput. Fluids*, 48(1):1–15, 2011.

[27] D. Destarac. Far-field/near-field drag balance and applications of drag extraction in CFD. In *CFD-Based Aircraft Drag Prediction and Reduction*, volume 2003-02 of *VKI Lecture Series*, pages 1–62. von Karman Institute for Fluid Dynamics, Nov. 2003.

[28] DLR. *VicToria, Virtual Aircraft Technology Integration Platform – Final Project Meeting*, Dec 2020.

[29] P. A. Durbin. Near-Wall Turbulence Closure Modeling Without "Damping Functions". *Theor. Comput. Fluid Dyn.*, 3:1–13, 1991.

[30] P. A. Durbin. A Reynolds stress model for near-wall turbulence. *J. Fluid Mech.*, 249:465–498, 1993.

[31] B. Eisfeld. Implementation of Reynolds stress models into the DLR-FLOWer code. Technical report, DLR Institute of Aerodynmaics and Flow Technology, 2004. Unpublished.

[32] A. Favre. Equations des gaz turbulents compressibles. *J. de Mecanique*, 4(3), 1965.

[33] E. M. Fernando and A. J. Smits. A supersonic turbulent boundary layer in an adverse pressure gradient. *J. Fluid Mech.*, 211:285–307, 1990.

[34] G. A. Gerolymos, C. Lo, I. Vallet, and B. A. Younis. Term-by-term analysis of near-wall second-moment closures. *AIAA J.*, 50(12):2848–2864, 2012.

[35] G. A. Gerolymos and I. Vallet. The dissipation tensor ε_{ij} in wall turbulence. *J. Fluid Mech.*, 807:386–418, 2016.

[36] M. M. Gibson and B. E. Launder. Ground effects on pressure fluctuations in the atmospheric boundary layer. *J. Fluid Mech.*, 86(3):491–511, 1978.

[37] S. Girimaji. Partially averaged Navier-Stokes (PANS) approach: A RANS to LES bridging model. *APS*, 56:EC–001, 2003.

[38] W. Glowacki and S. Chi. Effect of pressure gradient on mixing length for equilibrium turbulent boundary layers. In *10th Aerospace Sciences Meeting*, page 213, 1972.

[39] W. Haase, B. Aupoix, U. Bunge, and D. Schwamborn, editors. *FLOMANIA – A European Initiative on Flow Physics Modelling*, volume 94. Springer-Verlag Berlin Heidelberg, 2006.

[40] K. Hanjalić. Advanced turbulence closure models: a view of current status and future prospects. *Int. J. Heat Fluid Fl.*, 15(3):178–203, 1994.

[41] K. Hanjalic and B. E. Launder. A reynolds stress model of turbulence and its application to thin shear flows. *J. Fluid Mech.*, 52(4):609–638, 1972.

[42] Z. Harun, J. P. Monty, R. Mathis, and I. Marusic. Pressure gradient effects on the large-scale structure of turbulent boundary layers. *J. Fluid Mech.*, 715:477, 2013.

[43] A. Hellsten. *New two-equation turbulence model for aerodynamics applications*. PhD thesis, Helsinki University of Technology, 2004.

[44] S. M. Hosseini, R. Vinuesa, P. Schlatter, A. Hanifi, and D. S. Henningson. Direct numerical simulation of the flow around a wing section at moderate Reynolds number. *Int. J. Heat Fluid Fl.*, 61:117–128, 2016.

[45] P. G. Huang and P. Bradshaw. Law of the wall for turbulent flows in pressure gradients. *AIAA J.*, 33(4):624–632, 1995.

[46] T. J. R. Hughes, L. P. Franca, and M. Mallet. A new finite element formulation for computational fluid dynamics: I. Symmetric forms of the compressible Euler and Navier-Stokes equations and the second law of thermodynamics. *Comp. Methods Appl. Mech. Eng.*, 54(2):223–234, 1986.

[47] S. Jarkilić and K. Hanjalić. A new approach to modelling near-wall turbulence energy and stress dissipation. *J. Fluid Mech.*, 459:139, 2002.

[48] S. Keye and M. Gammon. Development of Deformed CAD Geometries of NASA's Common Research Model for the Sixth AIAA CFD Drag Prediction Workshop. In *34th AIAA Applied Aerodynamics Conference*, page 3431, 2016.

[49] V. Kitsios, C. Atkinson, J. A. Sillero, G. Borrell, A. G. Gungor, J. Jiménez, and J. Soria. Direct numerical simulation of a self-similar adverse pressure gradient turbulent boundary layer. *Int. J. Heat Fluid Fl.*, 61:129–136, 2016.

[50] V. Kitsios, A. Sekimoto, C. Atkinson, J. A. Sillero, G. Borrell, A. G. Gungor, J. Jiménez, and J. Soria. Direct numerical simulation of a self-similar adverse pressure gradient turbulent boundary layer at the verge of separation. *J. Fluid Mech.*, 829:392–419, 2017.

[51] T. Knopp. A new wall-law for adverse pressure gradient flows and modification of k-omega type RANS turbulence models. In *54th AIAA Aerospace Sciences Meeting*, page 0588, 2016.

[52] T. Knopp, M. Novara, D. Schanz, R. Geisler, F. Philipp, M. Schroll, C. Willert, and A. Schröder. Modification of the SSG/LRR-ω RSM for Turbulent Boundary Layers at Adverse Pressure Gradient with Separation Using the New DLR VicToria Experiment. In *Symposium der Deutsche Gesellschaft für Luft-und Raumfahrt*, pages 80–89. Springer, 2018.

[53] T. Knopp and N. Reuther. A wall-law for adverse pressure gradient flows and modification for k-ω models. In *17. STAB-Workshop*, Jahresbericht 2015, STAB-Mitteilung, pages 96–97, 2015.

[54] T. Knopp, D. Schanz, A. Schröder, M. Dumitra, C. Cierpka, R Hain, and C. J. Kähler. Experimental investigation of the log-law for an adverse pressure gradient turbulent boundary layer flow at $Re_\theta = 10{,}000$. *Flow Turbul. Combust.*, 92(1-2):451–471, 2014.

[55] A. N. Kolmogorov. The local structure of turbulence in incompressible viscous fluid for very large Reynolds numbers. *Cr Acad. Sci. URSS*, 30:301–305, 1941.

[56] A. N. Kolmogorov. Equations of motion of an incompressible fluid. *Izvestia Acad. Sci., URSS, Phys.*, 6(6):56–58, 1942.

[57] P.-Å. Krogstad and P. E. Skåre. Influence of a storng adverse pressure gradient on the turbulent structure in a boundary layer. *Phys. Fluids*, 7(8):2014–2024, 1995.

[58] B. E. Launder, G. J. Reece, and W. Rodi. Progress in the development of a Reynolds-stress turbulence closure. *J. Fluid Mech.*, 68(3):537–566, 1975.

[59] B. E. Launder and B. I. Sharma. Application of the Energy-Dissipation Model of Turbulence to the Calculation of Flow Near a Spinning Disc. *Letters in Heat and Mass Transfer*, 1:131–138, 1974.

[60] B. E. Launder and D. P. Tselepidakis. Contribution to the second-moment modelling of sublayer turbulent transport. *Zaric Memorial Intl Seminar on Near-Wall Turb., Dubrovnik, Yougoslavie*, pages 16–20, 1988.

[61] J.-P. Laval and M. Marquillie. Direct Numerical Simulations of converging–diverging channel flow. In *Progress in wall turbulence: understanding and modeling*, pages 203–209. Springer, 2011.

[62] M. Leschziner. *Statistical turbulence modelling for fluid dynamics-demystified: an introductory text for graduate engineering students*. World Scientific, 2015.

[63] V. Levasseur. *Simulation des grandes échelles en éléments finis stabilisés: une approche variationnelle multi-échelles*. PhD thesis, Université Paris 6, 2007.

[64] Y. Maciel, K.-S. Rossignol, and J. Lemay. Self-similarity in the outer region of adverse-pressure-gradient turbulent boundary layers. *AIAA J.*, 44(11):2450–2464, 2006.

[65] M. Mallet. *A finite element method for computational fluid dynamics*. PhD thesis, Stanford University, 1985.

[66] R. Manceau. *Modélisation de la turbulence. Prise en compte de l'influence des parois par relaxation elliptique*. PhD thesis, Université de Nantes, 1999.

[67] R. Manceau. Recent progress in the development of the Elliptic Blending Reynolds-stress model. *Int. J. Heat Fluid Fl.*, 51:195–220, 2015.

[68] R. Manceau. Progress in Hybrid Temporal LES (invited keynote paper). In Y. Hoarau, S.-H. Peng, D. Schwamborn, and A. Revell, editors, *Papers contributed to the 6th Symp. Hybrid RANS-LES Methods, 26–28 September 2016, Strasbourg, France*, volume 137 of *Notes on Numerical Fluid Mechanics and Multidisciplinary Design*, pages 9–25. Springer, 2018.

[69] R. Manceau and K. Hanjalić. Elliptic Blending Model: A New Near-Wall Reynolds-Stress Turbulence Closure. *Phys. Fluids*, 14(2):744–754, 2002.

[70] N. N. Mansour, J. Kim, and P. Moin. Reynolds-stress and dissipation-rate budgets in a turbulent channel flow. *J. Fluid Mech.*, 194:15–44, 1988.

[71] F. R. Menter. Two-equation eddy-viscosity turbulence models for engineering applications. *AIAA J.*, 32(8):1598–1605, 1994.

[72] J. P. Monty, Z. Harun, and I. Marusic. A parametric study of adverse pressure gradient turbulent boundary layers. *Int. J. Heat Fluid Fl.*, 32(3):575–585, 2011.

[73] M. V. Morkovin. Effects of compressibility on turbulent flows. *Mécanique de la Turbulence*, 367:380, 1962.

[74] Y. Nagano, M. Tagawa, and T. Tsuji. Effects of adverse pressure gradients on mean flows and turbulence statistics in a boundary layer. In *Turbulent Shear Flows 8*, pages 7–21. Springer, 1993.

[75] H. M. Nagib and K. A. Chauhan. Variations of von Kármán coefficient in canonical flows. *Phys. Fluids*, 20(10):101518, 2008.

[76] D Naot. Interactions between components of the turbulent velocity correlation tensor. *Isr. J. Technol.*, 8:259–269, 1970.

[77] T. B. Nickels. Inner scaling for wall-bounded flows subject to large pressure gradients. *J. Fluid Mech.*, 521:217–239, 2004.

[78] Netherlands Aerospace Centre NLR. Destination 2050 – A Route to Net Zero European Aviation, February 2020.

[79] J. M. Österlund, A. V. Johansson, H. M. Nagib, and M. H. Hites. A note on the overlap region in turbulent boundary layers. *Phys. Fluids*, 12(1):1–4, 2000.

[80] R. Paysant. Amélioration de la modélisation des écoulements turbulents. Technical report, ISAE-ENSICA, 2016.

[81] A. E. Perry. Turbulent boundary layers in decreasing adverse pressure gradients. *J. Fluid Mech.*, 26(3):481–506, 1966.

[82] S. Pirozzoli, F. Grasso, and T. B. Gatski. Direct Numerical Simulation and analysis of a spatially evolving supersonic turbulent boundary layer at $M = 2.25$. *Phys. Fluids*, 16(3):530–545, 2004.

[83] S. Pope. *Turbulent Flows*. Cambridge University Press, New-York, 2000.

[84] L. Prandtl. Über Flussigkeitsbewegung bei sehr kleiner Reibung. *Verhandl. III, Internat. Math.-Kong., Heidelberg, Teubner, Leipzig, 1904*, pages 484–491, 1904.

[85] A. Probst, R. Radespiel, and T. Knopp. Detached-eddy simulation of aerodynamic flows using a Reynolds-stress background model and algebraic RANS/LES sensors. In *20th AIAA Computational Fluid Dynamics Conference*, page 3206, 2011.

[86] M. Rao and H. Hassan. Modeling turbulence in the presence of adverse pressure gradients. In *14th Applied Aerodynamics Conference*, page 2429, 1996.

[87] S. Reuß. *A grid-adaptive algebraic hybrid RANS/LES method*. PhD thesis, Georg-August-Universität Göttingen, 2015.

[88] N. Reuther, D. Schanz, S. Scharnowski, R. Hain, A. Schröder, and C. Kähler. Experimental investigation of adverse pressure gradient turbulent boundary layers by means of large-scale PIV. In *11th International Symposium on Particle Image Velocimetry - PIV15* -, Conference Proceedings on USB-Stick, pages 1–8, 2015.

[89] C.-C. Rossow and L. Cambier. *100 Volulmes of 'Notes on Numerical Fluid Mechanics': 40 Years of Numerical Fluid Mechanics and Aerodynamics in Retrospect*, chapter European Numerical Aerodynamics Simulation Systems, pages 189–208. Springer Berlin Heidelberg, 2009.

[90] J. C. Rotta. Statistische Theorie nichthomogener Turbulenz. *Z. Phys.*, 129(6):547–572, 1951.

[91] C. L. Rumsey, J.-R. Carlson, T. H. Pulliam, and P. R. Spalart. Improvements to the Quadratic Constitutive Relation Based on NASA Juncture Flow Data. *AIAA J.*, 58(10):4374–4384, 2020.

[92] R. Schiestel and A. Dejoan. Towards a new partially integrated transport model for coarse grid and unsteady turbulent flow simulations. *Theor. Comput. Fluid Dyn.*, 18(6):443–468, 2005.

[93] P. Schlatter, Q. Li, G. Brethouwer, A. V. Johansson, and D. S. Henningson. Simulations of spatially evolving turbulent boundary layers up to $Re_\theta = 4{,}300$. *Int. J. Heat Fluid Fl.*, 31(3):251–261, 2010.

[94] P. Schlatter and R. Örlü. Turbulent boundar layer at moderate Reynolds numbers: inflow length and tripping effects. *J. Fluid Mech.*, 710:5, 2012.

[95] H. Schlichting. *Boundary-Layer Theory.* McGraw-Hill, 7th edition edition, 1979.

[96] K. E. Schoenherr. Resistance of flat surfaces moving through a fluid. *Soc. Nav. Arch. and Marine Eng. Trans.*, 40:279–313, 1932.

[97] D. Schwamborn and M. Strelets. ATAAC – an EU-project dedicated to hybrid RANS/LES methods. In *Progress in Hybrid RANS-LES Modelling*, pages 59–75. Springer, 2012.

[98] M. L. Shur, M. K. Strelets, A. K. Travin, and P. R. Spalart. Turbulence modeling in rotating and curved channels: assessing the Spalart-Shur correction. *AIAA J.*, 38(5):784–792, 2000.

[99] P. E. Skåre and P.-Å. Krogstad. A turbulent equilibrium boundary layer near separation. *J. Fluid Mech.*, 272:319–348, 1994.

[100] J. Slotnick, A. Khodadoust, J. Alonso, D. Darmofal, W. Gropp, E. Lurie, and D. Mavriplis. CFD Vision 2030 study: a path to revolutionary computational aerosciences, 2014.

[101] J. Smagorinky. General circulation experiments with the primitive equations. I. The basic experiment. *Mon. Weather Rev.*, 91:99, 1963.

[102] P. R. Spalart. Strategies for turbulence modelling and simulations. *Int. J. Heat Fluid Fl.*, 21(3):252–263, 2000.

[103] P. R. Spalart. Detached-eddy simulation. *Annu. Rev. Fluid Mech.*, 41:181–202, 2009.

[104] P. R. Spalart and S. R. Allmaras. One-equation turbulence model for aerodynamic flows. *La Recherche Aerospatiale*, 1:5–21, 1994.

[105] P. R. Spalart, S. Deck, M. Shur, K. Squires, M. Strelets, and A. Travin. A new version of detached-eddy simulation, resistant to ambiguous grid densities. *Theor. Comput. Fluid Dyn.*, 20:181–195, 2006.

[106] C. G. Speziale. Turbulence modeling for time-dependent RANS and VLES: a review. *AIAA J.*, 36(2):173–184, 1998.

[107] C. G. Speziale, S. Sarkar, and T. B. Gatski. Modeling the pressure-strain correlation of turbulence: an invariant dynamical system approach. *J. Fluid Mech.*, 227:245–272, 1991.

[108] B. S. Stratford. The prediction of separation of the turbulent boundary layer. *J. Fluid Mech.*, 1(5):1–16, 1959.

[109] H. Tennekes and J. L. Lumley. *A first course in turbulence*. MIT press, 2018.

[110] E. N. Tinoco, O. P. Brodersen, S. Keye, K. R. Laflin, E. Feltrop, J. C. Vassberg, M. Mani, B. Rider, R. A. Wahls, J. H. Morrison, D. Hue, C. J. Roy, D. J. Mavriplis, and M. Murayama. Summary Data from the Sixth AIAA CFD Drag Prediction Workshop: CRM Cases. *J. Aircraft*, 55(4):1352–1379, 2018.

[111] A. A. Townsend. Equilibrium layers and wall turbulence. *J. Fluid Mech.*, 11:97–120, 1961.

[112] A. A. Townsend. *The Structure of Turbulent Shear Flow*. Second edition, 1976.

[113] J. van der Vooren and J. W. Sloof. CFD-based drag prediction; State-of-the-art, theory, prospects. In *Lecture Notes of AIAA Professional Studies Series*. Portland, August 1990.

[114] J. Vassberg, M. Dehaan, M. Rivers, and R. Wahls. Development of a common research model for applied CFD validation studies. In *26th AIAA applied aerodynamics conference*, page 6919, 2008.

[115] R. Vinuesa, S. M. Hosseini, A. Hanifi, D. S. Henningson, and P. Schlatter. Pressure-gradient turbulent boundary layers developing around a wing section. *Flow Turbul. Combust.*, 99(3):613–641, 2017.

[116] R. Vinuesa, P. S. Negi, M. Atzori, A. Hanifi, D. S. Henningson, and P. Schlatter. Turbulent boundary layers around wing sections up to $Re_c = 1{,}000{,}000$. *Int. J. Heat Fluid Fl.*, 72:86–99, 2018.

[117] R. Vinuesa, R. Örlü, C. Sanmiguel Vila, A. Ianiro, S. Discetti, and P. Schlatter. Revisiting history effects in adverse-Pressure-Gradient turbulent boundary layers. *Flow Turbul. Combust.*, 99(3-4):565–587, 2017.

[118] T. von Kármán. Mechanische Ähnlichkeit und Turbulenz. *Nachr. Ges. Wiss.*, page 68, 1930.

[119] D. C. Wilcox. Reassessment of the scale-determining equation for advanced turbulence models. *AIAA journal*, 26(11):1299–1310, 1988.

[120] D. C. Wilcox. *Turbulence Modeling for CFD*. DCW industries, Inc., La Cañada, California, third edition, 2006.

[121] P. Yser. *Simulation numérique aéroacoustique d'écoulements par une approche LES d'ordre élevé en éléments finis non structurés*. PhD thesis, École Centrale Lyon, 2017.

[122] M. V. Zagarola, A. E. Perry, and A. J. Smits. Log laws or power laws: The scaling in the overlap region. *Phys. Fluids*, 9(7):2094–2100, 1997.

[123] M. V. Zagarola and A. J. Smits. Mean-flow scaling of turbulent pipe flow. *J. Fluid Mech.*, 373:33–79, 1998.